PHASE 2: QUANTITATIVE EVALUATION PROCESS FOR IMPROVED ROCKSLOPE SAFETY AND REDUCED MAINTENANCE

Final Report

SPR 864



Oregon Department of Transportation

PHASE 2: QUANTITATIVE EVALUATION PROCESS FOR IMPROVED ROCKSLOPE SAFETY AND REDUCED MAINTENANCE

Final Report

SPR 864

by

Michael J. Olsen
Ben A. Leshchinsky
Oregon State University

Joseph Wartman
Ground Zero Projects

for

Oregon Department of Transportation
Research Section
555 13th Street NE, Suite 1
Salem OR 97301

and

Federal Highway Administration
1200 New Jersey Avenue SE
Washington, DC 20590

August 2026

Technical Report Documentation Page

1. Report No. FHWA-OR-RD-27-07	2. Government Accession No.	3. Recipient's Catalog No.
4. Title and Subtitle Phase 2: Quantitative evaluation process for improved rockslope safety and reduced maintenance		5. Report Date September, 2026 6. Performing Organization Code
7. Author(s) Michael J. Olsen, Ben A. Leshchinsky, Joseph Wartman		8. Performing Organization Report No.
9. Performing Organization Name and Address Oregon Department of Transportation Research Section 555 13th Street NE, Suite 1 Salem, OR 97301		10. Work Unit No. (TRAIS) 11. Contract or Grant No.
12. Sponsoring Agency Name and Address Oregon Dept. of Transportation Research Section and Federal Highway Admin. 555 13th Street NE, Suite 1 1200 New Jersey Avenue SE Salem, OR 97301 Washington, DC 20590		13. Type of Report and Period Covered _____ Report 14. Sponsoring Agency Code
15. Supplementary Notes: ODOT Project Champion: Curran Mohney; ODOT Project Manager: Kira Glover-Cutter		

16. Abstract: Rockfalls pose serious risks to transportation infrastructure. The effectiveness of mitigation strategies is unclear. Short-term approaches such as scaling and blasting are costly and hazardous, requiring workers to operate on unstable slopes, while longer-term solutions such as rock bolting or nailing are often too expensive for widespread use. In addition, rockfall mitigation decisions are frequently subjective and ad hoc, making it difficult to evaluate the true effectiveness or durability of slope treatments. As a result, mitigated slopes may quickly return to hazardous conditions, leading to recurring maintenance and cleanup costs. To address these challenges, this research evaluates the use of quantitative, objective methods for assessing rockfall mitigation performance. Specifically, it investigates the application of a morphological classification framework—the Rockfall Activity Index—to measure mitigation effectiveness. A controlled field site was established and monitored over a two-year period following scaling using terrestrial laser scanning. Changes in magnitude–frequency relationships, activity rates, block sizes, precarious overhangs, and potential energy were analyzed to characterize post-mitigation slope behavior. The research supports more effective, sustainable rockfall mitigation strategies and improved long-term asset management.

17. Key Words Rockfall; lidar; monitoring; scaling; mitigation; rockfall activity index		18. Distribution Statement Copies available from NTIS, and online at http://www.oregon.gov/ODOT/TD/TP_RES/	
19. Security Classification (of this report) Unclassified	20. Security Classification (of this page) Unclassified	21. No. of Pages 259	22. Price

Technical Report Form DOT F 1700.7 (8-72) Reproduction of completed page authorized Printed on recycled paper

SI* (Modern Metric) Conversion Factors
Approximate Conversions to SI Units

Physical Quantity	Symbol	When You Know	Multiply By	To Find	Symbol
Length	n	inches	25.4	millimeters	mm
Length	ft	feet	0.305	meters	m
Length	yd	yards	0.914	meters	m
Length	mi	miles	1.61	kilometers	km
Area	in2	square inches	645.2	square millimeters	mm2
Area	ft2	square feet	0.093	square meters	m2
Area	yd2	square yard	0.836	square meters	m2
Area	ac	acres	0.405	hectares	ha
Area	mi2	square miles	2.59	square kilometers	km2
Volume	fl oz	fluid ounces	29.57	milliliters	mL
Volume	gal	gallons	3.785	liters **	L
Volume	ft3	cubic feet	0.028	cubic meters	m3
Volume	yd3	cubic yards	0.765	cubic meters	m3
Mass	oz	ounces	28.35	grams	g
Mass	lb	pounds	0.454	kilograms	kg
Mass	T	short tons (2000 lb)	0.907	megagrams (or "metric ton")	Mg (or "t")
Temperature (exact degrees)	oF	Fahrenheit	5 (F-32)/9 or (F-32)/1.8	Celsius	oC
Illumination	fc	foot-candles	10.76	lux	lx
Illumination	fl	foot-Lamberts	3.426	candela/m2	cd/m2
Force and Pressure or Stress	lbf	poundforce	4.45	newtons	N
Force and Pressure or Stress	lbf/in2	poundforce per square inch	6.89	kilopascals	kPa

*SI is the symbol for the International System of Measurement
** Volumes greater than 1000 L shall be shown in m^3

SI* (Modern Metric) Conversion Factors
Approximate Conversions from SI Units

Physical Quantity	Symbol	When You Know	Multiply By	To Find	Symbol
Length	mm	millimeters	0.039	inches	in
Length	m	meters	3.28	feet	ft
Length	m	meters	1.09	yards	yd
Length	km	kilometers	0.621	miles	mi
Area	mm2	square millimeters	0.0016	square inches	in2
Area	m2	square meters	10.764	square feet	ft2
Area	m2	square meters	1.195	square yards	yd2
Area	ha	hectares	2.47	acres	ac
Area	km2	square kilometers	0.386	square miles	mi2
Volume	mL	milliliters	0.034	fluid ounces	fl oz
Volume	L	liters	0.264	gallons	gal
Volume	m3	cubic meters	35.314	cubic feet	ft3
Volume	m3	cubic meters	1.307	cubic yards	yd3
Mass	g	grams	0.035	ounces	oz
Mass	kg	kilograms	2.202	pounds	lb
Mass	Mg (or "t")	megagrams (or "metric ton")	1.103	short tons (2000 lb)	T
Temperature (exact degrees)	oC	Celsius	1.8C+32	Fahrenheit	oF
Illumination	lx	lux	0.0929	foot-candles	fc
Illumination	cd/m2	candela/m2	0.2919	foot-Lamberts	fl
Force and Pressure or Stress	N	newtons	0.225	poundforce	lbf
Force and Pressure or Stress	kPa	kilopascals	0.145	poundforce per square inch	lbf/in2

For More Information see: https://www.fhwa.dot.gov/publications/convtabl.cfm

ACKNOWLEDGEMENTS

We gratefully acknowledge Dr. Kira Glover of Oregon DOT for her many contributions as the research coordinator guiding the project and Curran Mohney for his input and contributions as the project champion and directing the scaling operations at the rumble pit. Mike Tardif (ODOT), Casey Varnum (ODOT), Michael Zimmerman (GRI), Doug Haines (retired), and Ben Haines (FHWA) participated on the Technical Advisory Committee and provided guidance throughout the project. We thank Sarah Hunt (ODOT) for her assistance with access to the Iron Mountain Quarry. We appreciate the assistance of Jill Dekoekkoek (ODOT) with logistics for several of the scaling sites. Special thanks to Jonathan Rawlings and Rhonda Dodge at ODOT Geometronics for providing the mobile lidar datasets. Dr. Dimitrios Bolkas from Pennsylvania State University assisted with development of the RUMBLE PIT methodology and data collection efforts. Many people from OSU geomatics assisted in the field work and data processing including: Dr. Dae Kun Kang, Cole Hudnall, Mohsen Arjmand, Caleb Ogbeta, Susanna Eng, Bryce Berrett, Chase Simpson, Erik Fulmer, Sheng Tan, Sanjaya Paudel, Dr. Heidar Rastiveis, Heather Maran, Dana Lind, and Jaclyn Bohn. Bryce Berrett from OSU developed the UAS flight plan and procedure. Dr. Ezra Che from EZDataMD LLC performed code development to support the data analysis. EZDataMD LLC provided the Rambo, PointReg, EZVox, and EZPC software used to support the data analysis. Relevant information compiled for the project report SPR-809 including contributions by Dr. Andrew Senogles were adapted into this literature review.

DISCLAIMER

This document is disseminated under the sponsorship of the Oregon Department of Transportation and the United States Department of Transportation in the interest of information exchange. The State of Oregon and the United States Government assume no liability of its contents or use thereof.

The contents of this report reflect the view of the authors who are solely responsible for the facts and accuracy of the material presented. The contents do not necessarily reflect the official views of the Oregon Department of Transportation or the United States Department of Transportation.

The State of Oregon and the United States Government do not endorse products of manufacturers. Trademarks or manufacturers' names appear herein only because they are considered essential to the object of this document.

This report does not constitute a standard, specification, or regulation.

Dr. Olsen has financial interests in EZDataMD LLC, a company which commercializes technology related to this research (e.g., *Rambo* and *PointReg* software). The conduct, outcomes, or reporting of this research could benefit EZDataMD LLC and could potentially benefit the authors.

Disclosure of AI use:
ODOT Research accepts the responsible use of artificial intelligence as a supportive technology to strengthen the quality of research products and deliverables if risk of use is deemed acceptable by ODOT Research. To help ensure transparency, author accountability, and enhance public trust, AI tools and associated applications are listed below and/or in the relevant Research Methodology subsection. Author is accountable for scholarly and evaluative judgement herein.

- Claude – Manuscript language refinement

TABLE OF CONTENTS

LIST OF FIGURES ..... **XIII**
LIST OF TABLES ..... **XVII**
1.0 INTRODUCTION **1**
1.1 OVERVIEW 1
1.2 OBJECTIVES 2
1.3 POTENTIAL BENEFITS 2
2.0 LITERATURE REVIEW **1**
2.1 OVERVIEW 1
2.1.1 Key References and Resources *1*
2.2 ROCKFALL HAZARDS 1
2.2.1 Rockfall hazards *2*
2.2.2 Contributing Factors to Rockfall *2*
2.2.3 Rockslope Failure Modes *4*
2.3 ROCKSLOPE DESIGN 5
2.4 ROCKSLOPE INSPECTION PROCEDURES AND TOOLS 5
2.4.1 Rockfall Hazard Rating and Analysis Systems *5*
2.4.2 Remote Sensing Tools *10*
2.4.3 Magnitude-Frequency Relationships *23*
2.4.4 Rockfall Activity Index (RAI) *23*
2.4.5 Rambo *29*
2.5 ROCKFALL MODELING 34
2.5.1 RAMMS (Rockfall Analysis and Monitoring in Engineering and Mining Services) 34
2.5.2 RocFall *34*
2.5.3 GIS-based tools *35*
2.5.4 Modelling mitigation techniques using lidar derived surfaces *35*
2.6 MITIGATION TECHNIQUES 36
2.6.1 Slope Modifications *39*
2.6.2 Physical Barriers *41*
2.6.3 Rockslope Reinforcement *42*
2.6.4 Seismic mitigation strategies and design guidelines *43*
2.7 ROCKFALL MONITORING AND WARNING SYSTEMS 44
2.8 OTHER DATASETS 44
2.8.1 Oregon Sites *44*
2.8.2 New Zealand *47*
2.9 SUMMARY 47
3.0 DATA COLLECTION PROTOCOLS AND SITE CHARACTERIZATION **49**
3.1 OVERVIEW 49
3.2 TYPICAL WORKFLOW 49
3.3 SISKIYOU PASS 53
3.3.1 Site Geology *53*

3.3.2 Data Collection *54*
3.4 GREEN SPRING, OR66 57
3.5 YELLOW JACKET CREEK 60
3.6 EDDYVILLE 62
3.7 SR14 MP73, COLUMBIA RIVER GORGE, WASHINGTON 64
3.7.1 Site Geology *64*
3.7.2 Data Collection *65*

4.0 RUMBLE PIT - ROCKSLOPE UNDERSTANDING OF MORPHOLOGICAL BEHAVIOUR AND LONG-TERM EVOLUTION- PLACE OF INSTABILITY AND TRANSFORMATION 67

4.1 SITE GEOLOGY 67
4.2 ROCK MASS CHARACTERIZATION 70
4.3 PREPARATORY WORK 70
4.4 BASELINE SURVEY (9/29/2023) 72
4.5 SURVEYS 72
4.5.1 General Survey Plan *75*
4.5.2 Scaling *80*
4.5.3 Repeat monitoring plans *80*
4.5.4 Safety Plan *87*
4.5.5 Documentation required for each site *89*

5.0 DATA PROCESSING PROTOCOLS 91

5.1 PROJECT SETUP 91
5.2 GNSS PROCESSING 92
5.2.1 Setup procedure for workstation *92*
5.2.2 Processing *92*
5.3 TOTAL STATION PROCESSING 93
5.4 PRELIMINARY SCAN REGISTRATION 93
5.5 MOBILE LIDAR 94
5.6 UNMANNED AIRCRAFT SYSTEM DATA 95
5.7 MULTI-EPOCH, MULTI-SCAN, MULTI-SENSOR LEAST SQUARES ADJUSTMENT 96
5.7.1 CSV file setup *96*
5.7.2 Adjustment *97*
5.7.3 Adjustment Results *97*
5.8 MODELING AND ANALYSIS PROTOCOLS 103
5.9 SUMMARY OF PRODUCTS CREATED 104
5.10 ROCKFALL SITE VIEWER 105

6.0 ANALYSIS METRICS 109

6.1 GLOBAL METRICS 109
6.1.1 RAI Site Score *110*
6.1.2 Per-Class Instability Rates and Failure Depths *110*
6.1.3 Magnitude-Frequency Relationships *111*
6.2 MORPHOLOGICAL CLASSIFICATION / ROCK SLOPE SURFACE ASSESSMENT 112
6.3 SLOPE PERFORMANCE 113
6.4 ROCKSLOPE IMPROVEMENT PERFORMANCE PREDICTION 113

7.0 ROCKFALL TRAJECTORY ANALYSIS 115
7.1 CHANGE ANALYSIS 115
7.2 ROCKFALL TRAJECTORY MODEL METHODOLOGY 116
7.1 TRAJECTORY ANALYSIS AND VISUALIZATION TOOL 120
7.1.1 ROCKIT Analyzer 120
7.1.2 ROCKIT Visualizer 121
8.0 RUMBLE PIT ANALYSIS 123
8.1 SCALING SITE A 123
8.1.1 Scaling procedures 123
8.1.2 RAI Analysis 126
8.1.3 Rates and Volumes 128
8.1.4 Volume-Frequencies 131
8.1.5 Trajectory Analysis 132
8.2 SCALING SITE B 140
8.2.1 Scaling procedures 140
8.2.2 RAI Analysis 142
8.2.3 Rates and Volumes 144
8.2.4 Volume-Frequencies 147
8.2.5 Trajectory Analysis 149
8.3 SCALING SITE C 154
8.3.1 Scaling procedures 154
8.3.2 RAI Analysis 154
8.3.3 Rates and Volumes 156
8.3.4 Volume-Frequencies 159
8.3.5 Trajectory Analysis 160
9.0 OREGON SITE ANALYSIS 165
9.1 I-5 SISKIYOU PASS 165
9.1.1 RAI Analysis 165
9.1.2 8.1.2 Rates and Volumes 170
9.1.3 Volume-Frequencies 174
9.1.4 Trajectory Analysis 176
9.1.5 Summary 179
9.2 OR66 GREEN SPRING 180
9.3 SR14 MP73 (WASHINGTON) 182
9.3.1 RAI Analysis 182
9.3.2 Rates and Volumes 187
9.3.3 Summary 192
10.0 LONG-TERM MONITORING: GLITTER GULCH MILEPOST 241 (GG241) ..195
10.1 SITE OVERVIEW 195
10.2 SURVEY HISTORY 196
10.3 RAI ANALYSIS 197
10.3.1 Morphological Classification 197
10.3.2 RAI Site Score 202

10.4 PER-CLASS INSTABILITY RATES AND FAILURE DEPTHS....202
10.5 RATES AND VOLUMES....205
10.5.1 Cumulative Erosion Volume....205
10.5.2 Volume-Frequency Relationships....207
10.6 SLOPE PERFORMANCE....212
10.7 SYNTHESIS AND CROSS-METRIC ASSESSMENT....212
10.8 SUMMARY....214
11.0 CONCLUSIONS....215
11.1 KEY TAKEAWAYS....217
11.2 FUTURE RESEARCH....218
12.0 REFERENCES....221

LIST OF FIGURES

Figure 2-1: Classification scheme utilized for the RAI (Rockfall Activity Index) modified from Dunham et al. (2017) and Markus et al. (2023). 24
Figure 2-2: Graphical User Interface of *Rambo*. 29
Figure 2-3: Example change analyses for Eddyville, OR from 2013-2022. The top shows the magnitude of change between 2013-2017 and 2018-2022 while the bottom shows the failure rate between 2013-2022 for window sizes of 1 and 10 pixels, highlighting the hotspots on the cliff. 45
Figure 3-1: Site plan of the Siskiyou Pass showing position of the GNSS base and the TLS locations. 54
Figure 3-2: Example TLS setup at the Siskiyou Pass field site. 55
Figure 3-3: GNSS Base Station setup at the Siskiyou Pass field site. 56
Figure 3-4: Close-up of the GNSS base setup location. 57
Figure 3-5: Scan setup locations at the Green Spring field site (OR66 MP13.2). 58
Figure 3-6: Example RTC360 setup with the prototype custom GNSS mount. 58
Figure 3-7: Initial GNSS base station setup location. 59
Figure 3-8: Site plan of Yellow Jacket showing position of control points, TLS scan positions, TS setups and targets. 61
Figure 3-9: Overview of site plan of Eddyville showing position of control points and TLS scan positions. 62
Figure 3-10: Site plan of Pioneer Mt Eddyville showing position of control points, TLS scan positions, TS setups and targets. 63
Figure 3-11: Control point plan of SR14 MP73. 66
Figure 4-1. Geologic cross-section showing the Iron Mountain stock (i.e., the current "Rumble Pit" site; unit Ticf, intrusive Cape Foulweather Basalt) intruding through the Astoria Formation (Ta) and the Yaquina Formation (Tn) in the vicinity of the Rumble Pit site, Lincoln County, Oregon. Cross-section A–A' reproduced from Snavely et al. (1976), Geologic Map of the Yaquina and Toledo Quadrangles, Lincoln County, Oregon, USGS Miscellaneous Investigations Series Map I-867. (Not to scale) 69
Figure 4-2. Examples of vegetation obstructions to be cleared at the site. 71
Figure 4-3. Weather station installed at the site 71
Figure 4-4. GNSS Base Station setup over GCP#1. 78
Figure 4-5. Leica P50 setup with GNSS mount and total station setup. 78
Figure 4-6. Example GCP#4 and stake for identification. 79
Figure 4-7. Left: close-up of GCP#4 and Right: Closeup of GCP#5 with prism pole centered in the divet. 79
Figure 4-8. Stake to indicate the location of RTC Scan #10. 79
Figure 4-9. Gridded Smart Oblique flight plan of the Rumble Pit showing key parameters. More details and screenshots of the flight plan can be seen in Appendix B. 80
Figure 4-10. Scaling extents and control sections at the RUMBLE PIT 81
Figure 4-11. Scaling extents and control sections of section A at the RUMBLE PIT 82
Figure 4-12. Scaling extents and control sections of section B at the RUMBLE PIT 83
Figure 4-13. Scaling extents and control sections of section C at the RUMBLE PIT 84
Figure 4-14. Typical monitoring survey plan at the RUMBLE PIT 85

Figure 4-15. Example sparse point cloud rendering from first UAS survey depicting camera pose positions from the gridded optimized oblique flight path and additional manually collected photos.....86
Figure 5-1. Main interface of the SPR864 Rockfall Site Viewer, showing the location so the sites, geology, and unstable slopes.....106
Figure 5-2. Example potree viewer for the I-5 Siskiyou dataset. 107
Figure 7-1. Main GUI of the Rockit analyzer tool.....121
Figure 7-2. Main GUI of the Rockit visualizer tool.....122
Figure 8-1. Scaling Site A (a) before (September 29, 2023), (b) during (November 10, 2023), and (c) after (November 10, 2023) scaling operations. A scaler standing on the slope provides scale. 125
Figure 8-2. Changes in RAI classification resulting from the scaling operation for Scaling Site A and Control Site A. (11/10/2023 vs 9/29/2023).....126
Figure 8-3. Changes in RAI classification percent areas over time for scaling Site A. The blue vertical line represents the date of scaling (11/10/2023).....127
Figure 8-4. Changes in activity rates over time for scaling Site A compared with control site. (a) including baseline activity rates and (b) after scaling with regression functions. 129
Figure 8-5. Cumulative normalized erosion for Control Rockslope A (top), Scaled Rockslope A (center), and ratio of scaled to control (bottom). 131
Figure 8-6. Volume-frequency relationships for both scaled (green) and control (black) rockslopes for the six months following scaling at Site A. 132
Figure 8-7. Rockfall sources (top) and ending rockfall locations (bottom) for Site A for all epochs. 134
Figure 8-8. Probability of exceedance plots for Site A for POE vs (a) the ratio of reach length to drop height and (b) kinetic energy at the lowest elevation and the change in POE vs (c) the ratio of reach length to drop height and (d) kinetic energy at the lowest elevation. Green represents the control and red represents the pre-scaling. 136
Figure 8-9. PTA results showing starting/ending locations and trajectories for Scaled and Control Rockslope A (four panels). 137
Figure 8-10. PTA results for Scaled Rockslope A: (a) travel distance, (b) kinetic energy, (c) filtered high-hazard sources, and (d) impact heatmap.....139
Figure 8-11. PTA-derived probability of exceedance of normalized kinetic energy rate for Site A (top) and reduction in POE (bottom).....140
Figure 8-12. Scaling operation in progress at Scaling Site B.....141
Figure 8-13. Changes in RAI classification resulting from the scaling operation for Scaling Site B and Control Site B (11/10/2023 vs 9/29/2023).....143
Figure 8-14. Changes in RAI classification percent areas over time for Scaling Site B. The blue vertical line represents the date of scaling (11/10/2023).....144
Figure 8-15. Changes in activity rates over time for Scaling Site B compared with control site B. (a) Including baseline activity rates and (b) after scaling with regression functions.....146
Figure 8-16. Cumulative normalized erosion for Control Rockslope B (top), Scaled Rockslope B (center), and ratio of scaled to control (bottom). 147
Figure 8-17. Volume-frequency relationships for both scaled (green) and control (black) rockslopes for the six months following scaling for Rockslope B.....148
Figure 8-18. Rockfall sources (top) and ending rockfall locations (bottom) for Site B for all epochs. 150

Figure 8-19. Probability of exceedance plots for Site B for POE vs (a) the ratio of reach length to drop height and (b) kinetic energy at the lowest elevation and the change in POE vs (c) the ratio of reach length to drop height and (d) kinetic energy at the lowest elevation. Green represents the control and red represents the pre-scaling. 151
Figure 8-20. PTA-derived probability of exceedance of normalized kinetic energy rate for Site B (top) and reduction in POE (bottom). 153
Figure 8-21. Changes in RAI classification resulting from the scaling operation for Scaling Site C and Control Site C (11/10/2023 vs 9/29/2023). 154
Figure 8-22. Changes in RAI classification percent areas over time for Scaling Site C. The blue vertical line represents the date of scaling (11/10/2023). 156
Figure 8-23. Changes in activity rates over time for Scaling Site C compared with control site C. (a) Including baseline activity rates and (b) after scaling with regression functions. 157
Figure 8-24. Cumulative normalized erosion for Control Rockslope C (top), Scaled Rockslope C (center), and ratio of scaled to control (bottom). 158
Figure 8-25. Volume-frequency relationships for both scaled (green) and control (black) rockslopes for the six months following scaling for Rockslope C. 160
Figure 8-26. Rockfall sources (top) and ending rockfall locations (bottom) for Site C for all epochs. 162
Figure 8-27. Probability of exceedance plots for Site C for POE vs (a) the ratio of reach length to drop height and (b) kinetic energy at the lowest elevation and the change in POE vs (c) the ratio of reach length to drop height and (d) kinetic energy at the lowest elevation. Green represents the control and red represents the pre-scaling. 163
Figure 8-28. PTA-derived probability of exceedance of normalized kinetic energy rate for Site C (top) and reduction in POE (bottom). 164
Figure 9-1. Changes in slope gradient resulting from the scaling operation for a portion of the I-5 Siskiyou Pass site. (6/1/2023 vs 10/12/2023). 167
Figure 9-2. Changes in the RAI classification resulting from the scaling operation for a portion of the I-5 Siskiyou Pass site. (6/1/2023 vs 10/12/2023). 168
Figure 9-3. Changes in the distribution of RAI classes resulting from the scaling operation for a portion of the I-5 Siskiyou Pass site. (6/1/2023 vs 10/12/2023). 169
Figure 9-4. Changes in the RAI classification over time for the I-5 Siskiyou Pass site. 169
Figure 9-5. Changes to the rock slope resulting from the scaling operation. (6/1/2023 vs 10/12/2023). 171
Figure 9-6. Changes in the overall activity rate over time. 173
Figure 9-7. Changes in the activity rate over time by RAI class. 173
Figure 9-8. (Top Panel) Cumulative normalized erosion of Siskiyou Pass over period of monitoring. Each shaded area represents cumulative normalized erosion volume stemming from various rockfall sizes. (Bottom Panel) Ratio of cumulative volume from Scaled rockfall rates at Siskiyou Pass to post-scaling rates. 174
Figure 9-9. Volume-frequency relationships for both post-scaling (green) and scaled (black) rockfall for Siskiyou Summit. During this period, the scaled rockslope shows a modest decrease in the frequency of larger rockfalls. 175
Figure 9-10. Starting and ending rockfall locations for all rockfall sources and volumes for Siskiyou Pass for all epochs. 177
Figure 9-11. Top Left (a): Probability of exceedance of reach length to drop height ratio (m/m) for scaled conditions on Siskiyou Pass (green) and post-scaling conditions (black). Bottom

Left (b): Change in probability of exceedance of reach length to drop height ratio (m/m) for post-scaling conditions (black). Top Right (c): Probability of exceedance of kinetic energy at lowest elevation for pre-scaling for scaled conditions on Siskiyou Pass (green) and post-scaling conditions (black), where gray lines represent individual epochs, black line represents mean. Bottom Left (d): Change in probability of exceedance of kinetic energy at lowest elevation for scaled conditions on Siskiyou Pass (green).....178
Figure 9-12. Changes observed at the OR66 site during the monitoring period for a portion of the slope.....181
Figure 9-13. RAI classification map of the SR14 MP73 site (a) before and (b) after scaling. ...183
Figure 9-14. Slope map of the SR14 MP73 site (a) before and (b) after scaling. 184
Figure 9-15. Changes in RAI classifications due to scaling at SR14 MP73. 185
Figure 9-16. Changes in the percent area of RAI classes at site SR14 MP73 over time. 187
Figure 9-17. Change analysis of Site SR14 MP73 from scaling. 189
Figure 9-18. Changes in RAI classes over time at Site SR14 MP73. 190
Figure 9-19. Changes in activity rates over time at Site SR14 MP73 190
Figure 10-1. RAI classifications at Site GG241 before (a) and after (b) scaling operations. 199
Figure 10-2. Slope morphology at site GG241 before (a) and after (b) scaling operations. 200
Figure 10-3. Changes in RAI classifications due to scaling operations at site GG241. 201
Figure 10-4. Changes in percent area of RAI classes at site GG241 over time. The Blue Line is the approximate scaling date.....201
Figure 10-5. Activity rates for all RAI classes over time at site GG241. *Assuming significant changes of 0.014 m or larger.* 203
Figure 10-6. Overall activity rates over time at site GG241. *Assuming significant changes of 0.014 m or larger.* 204
Figure 10-7. Volume and significant volume change observed at site GG241 over time. *Assuming significant changes of 0.014 m or larger.* 204
Figure 10-8. (Top Panel) Cumulative normalized erosion of GG241 over period of monitoring. Each shaded area represents cumulative normalized erosion volume stemming from various rockfall sizes. (Bottom Panel) Ratio of cumulative volume from pre-scaled rockfall rates at GG241 to post-scaling rates. 206
Figure 10-9. Volume-frequency relationships for both post-scaling (green), scaled (black), and pre-scaling rockfall for GG241. During this period, the scaled rockslope shows a notable decrease in the frequency of larger rockfalls. 208
Figure 10-10. Ending rockfall locations for all rockfall sources and volumes GG241 for all epochs. 210
Figure 10-11. Top Left (a): Probability of exceedance of reach length to drop height ratio (m/m) for pre-scaling conditions on GG241 (green) and post-scaling conditions (black). Bottom Left (b): Change in probability of exceedance of reach length to drop height ratio (m/m) for post-scaling conditions (black). Top Right (c): Probability of exceedance of kinetic energy at lowest elevation for pre-scaling conditions on GG241 (green) and post-scaling conditions (black), where gray lines represent individual epochs, black line represents mean. Bottom Right (d): Change in probability of exceedance of kinetic energy at lowest elevation for scaled conditions on GG241 (green). 211

LIST OF TABLES

Table 2-1: Summary of different rockfall hazard rating systems (modified from Olsen et al., 2020). 7
Table 2-2: Summary of benefits and limitations of remote sensing for rockslope assessments (adapted from Bouali et al., 2017 to be applicable to broader remote sensing tools beyond lidar). 11
Table 2-3: Summary of capabilities, limitations, and example applications of common remote sensing technologies for rockslope assessment (modified from Olsen et al., 2020). 12
Table 2-4: Summary of common point cloud processing tasks for rockslope analysis (modified from content in Olsen et al., 2020). 16
Table 2-5: Summary of morphological parameters (modified from content in Olsen et al., 2020). 22
Table 2-6: Updated and original activity rates and assumed failure depths for each RAI classification, table modified from Markus, 2018 28
Table 2-7. Summary of features available in Rambo to analyze point clouds of rockslopes (modified from Olsen et al., 2022). 30
Table 2-8: Summary of the advantages and disadvantages of mitigation methods that can be used to reduce rockfall hazard (Modified from Olsen et al., 2020) 37
Table 2-9: Summary of MLS and TLS acquisition for each site (expanded from Olsen et al., 2020). 46
Table 3-1. Monitoring frequency for sites for rockfall activity in Oregon/Washington 51
Table 4-1. Summary of data acquisition at the Rumble Pit site. 73
Table 4-2. Project contact list. 87
Table 5-1. Summary of quality control metrics from the registration. 99
Table 5-2. Registration QC metrics for the Rumble Pit site 100
Table 5-3. Summary of registration QC metrics for Siskiyou Pass. 101
Table 5-4. Summary of registration QC metrics for the Green Spring site 101
Table 5-5. Summary of registration QC metrics from the Yellow Jacket site. 102
Table 5-6. Summary of registration QC metrics for the Eddyville Site 102
Table 5-7. Summary of registration QC metrics for Site SR14MP73. 103
Table 9-1. Summary of RAI class areas for SR14 MP73. 185
Table 9-2. Activity rates and failure depths observed for the SR14 MP73 Site 188
Table 10-1. Summary of quality control metrics from the registration for Site GG241 197
Table A-1: Detailed rating of rockslopes in the Rockfall Hazard Rating System (RHRS). (From Pierson, 1993). ..... **Error! Bookmark not defined.**
Table A-2: Evolved RHRS system to assess both rockfall risk and potential hazard levels (From ODOT, 2001). ..... **Error! Bookmark not defined.**
Table A-3: Slope mass rating (SMR) categories used in the IMS (from Budetta et al., 2004). ..... **Error! Bookmark not defined.**
Table A-4: Categories for the Italian modified system (IMS) adapted from the RHRS (from Budetta et al., 2004) ..... **Error! Bookmark not defined.**
Table B-1. Summary of data acquisition for the Siskiyou Pass Site ..... **Error! Bookmark not defined.**

Table B-2. Summary of data acquisition for the Green Spring (OR66 MP13) field site.....**Error! Bookmark not defined.**
Table B-3. Summary of data acquisition for Yellow Jacket Creek field site.....**Error! Bookmark not defined.**
Table B-4. Summary of data acquisition for Eddyville field site..**Error! Bookmark not defined.**
Table B-5. Summary of data acquisition for SR14 MP73 field site.....**Error! Bookmark not defined.**

1.0 INTRODUCTION

1.1 OVERVIEW

Thousands of problematic rockslopes adversely impact ODOT's infrastructure and will soon require substantial mitigation as Oregon's highway rockcuts near the end of their respective design life. This deterioration is predicted to be further exacerbated by increasing storms and adverse weather due to climate change and seismic activity. Many short-term mitigation techniques, such as scaling or blasting, are costly and dangerous as these techniques require personnel to physically scale the cliff, while longer-term mitigation solutions (e.g., nailing) are often too cost-prohibitive to deploy beyond a few select slopes. Rockfall mitigation efforts are further compounded by the subjective, ad-hoc nature of the mitigation process, which can lead to uncertainty regarding actual slope improvement and predicted improvement duration. It is also uncertain how effective mitigation efforts are in actuality, particularly with respect to the longevity of scaling before the eroding slopes return to a similar or even more precarious state. Further, when rockslopes are not clearly improved with mitigation, clean-up costs for rockfall accumulate for ODOT's district maintenance crews. Taken together, the lack of quantitative information regarding how mitigation efforts actually improve the overall activity of rock slopes runs counter to ODOT's aim for budget efficiency and transparency, with potential negative impacts on an already limited rockfall mitigation budget which could then in-turn negatively impact the safety of the traveling public. Quantitative, objective methods that better inform successful rockfall mitigation techniques, maintenance strategies, and overall asset management are needed.

Recently, ODOT Research invested in the development of a series of lidar-based tools for efficient and effective assessment and monitoring of rockfall events (SPR809). Specifically, SPR809 refined the Rockfall Activity Index (RAI) hazard screening tool (originally developed in research funded by PacTrans), analyzed seismic hazards, collected lidar and Uncrewed Aerial Systems (UAS) data for several rockslopes, and developed a user-friendly Graphical User Interface (GUI) software called *Rambo* for implementation (Olsen et al., 2020). RAI is a point cloud-derived, high-resolution, low-cost, morphology-based, objective approach for assessing rockslopes that can objectively and efficiently analyze large geographic regions. The RAI provides hazard scores based on rockslope morphology, falling height, classification-based activity rates and failure depths, all of which are based on change analysis from multiple epochs of lidar data. RAI may also be used to identify specific locations to target for mitigation by identifying morphology-associated activity rates and failure depths of the slope, as well as precarious overhangs and potential energy associated with failure. The *Rambo* software enables rapid assessment of multiple epochs of point cloud data to identify trends and patterns in rockslope activity. It not only performs the RAI classification and scoring analysis but also performs a detailed change analysis, including generation of magnitude-frequency curves to describe levels of rockfall activity between surveys.

This research project leverages these recently developed tools to create a new methodology and associated metrics for quantifying rockfall mitigation effectiveness that can also be used to direct future mitigation and maintenance efforts. Further, associated magnitude and frequency relationships describing rockfall block size over time for rockslopes may enable estimation of maintenance needs and potential uncertainties.

1.2 OBJECTIVES

This research will provide tools for quantitative, objective characterization of rockslopes for directed, effective mitigation efforts that optimize funding investments to improve safety through mountainous lifeline corridors. While many mitigation techniques exist (e.g., catch ditches, barrier walls, meshing, etc.), this research will focus on improvement techniques such as scaling that actively modify the rockslope itself. Leveraging research products and lidar data delivered from ODOT's SPR809 investment, analytical tools and methods will be developed that:

1. Enable strategic selection of active rockslope areas that would benefit from local mitigation across large rockslopes;

2. Enable verification and efficacy of slope improvement efforts with subsequent monitoring;

3. Evaluate the effectiveness of rockslope improvement techniques, and

4. Provide guidance for future rockslope improvement efforts.

The data collection for SPR864 was augmented with lidar data obtained by an OSU, UW, UAF, and GNS Science research team from mitigated slopes in Alaska, which have a longer history of observation. The most robust dataset, from Alaska, includes approximately 5 years of pre-mitigation data (i.e., "baseline") and 4 years of post-mitigation data, thus providing a comprehensive and rich longitudinal monitoring set for analysis.

1.3 POTENTIAL BENEFITS

Efficient and effective rockslope mitigation is critical to ODOT's mission to provide a safe and reliable multimodal transportation system because proactive management of highway slopes helps ensure safety and economic mobility, especially during emergency situations. While a small proportion of rockfall mitigation efforts only require partial closure, most require complete closure of the highway to ensure safety of motorists, bicyclists, and pedestrians as large quantities of debris fall from the slopes onto right-of-way (ROW) during scaling operations. As a result, mobility and economic activity in the region are significantly reduced due to the disproportionately high impact on traffic and the hazardous nature of the operation.

This research can 1) facilitate increased capacity for rapid assessment of rock slope activity by supplementing manual efforts with mobile and/or terrestrial lidar methods, 2) identify more detailed areas where rockslope mitigation is beneficial and feasible, reducing closure time and cost of mitigation, and 3) identify which in-situ rockslope mitigation techniques provide the most value, both in efficacy and design life. This work intersects and complements multiple ODOT

agency efforts including seismic lifeline and resiliency planning initiatives and the Unstable Slopes Program. It also provides another mechanism to obtain additional value out of mobile lidar scans being routinely performed by Geometronics that are already utilized for several purposes throughout ODOT. Importantly, guidelines from this research provide enhanced performance measures to assess management costs, optimize limited rockfall budgets, and ensure safer ROW.

2.0 LITERATURE REVIEW

2.1 OVERVIEW

The project team reviewed recent research related to rockslope mitigation and improvement practices. This section will summarize rockfall hazards, rockslope design practices, inspection procedures, remote sensing tools, performance measures, mitigation techniques, monitoring systems, and modeling approaches. It will then summarize the key findings relevant to the project objectives including gaps in knowledge to guide this research.

2.1.1 Key References and Resources

2.1.1.1 NCHRP Design Practices for Rock Slopes and Rockfall Management (2022)

This synthesis documents current DOT procedures for rockslope design and mitigation. A questionnaire administered to DOTs explored challenges with funding; communication between DOT technical staff, DOT management, stakeholders, contractors; and the benefits of well-developed rockslope inventories and data collection.

2.1.1.2 TRB Rockfall Characterization and Control (Turner and Schuster, 2012)

This textbook covers a variety of topics such as rockfall hazard identification and evaluation, investigation processes, quantitative modeling, mitigation options, and establishing maintenance and management programs. The book also contains a digital appendix with a variety of multi-media resources.

2.2 ROCKFALL HAZARDS

Rockfalls are a chronic, pervasive hazard that is important to consider during the planning, design, and management stages of infrastructure asset management for highways traversing steep and mountainous terrain (Turner and Jayaprakash, 2013). In mountainous terrains road cuts are often required to provide sufficient right of way. Rockfalls are especially precarious in freshly created road cuts compared with natural rock slopes that have formed and stabilized over a long period of time. Freshly exposed rock may be initially stable after construction, but weathering causes the slope to degrade and become unstable over time (Taherynia et al., 2014) without maintenance and mitigation efforts. Often mitigation measures focus on minimizing the entry of rocks to the highway rather than improving the slope.

DOTs have formally addressed rockslopes and rockfall hazards since the 1960's and have improved the state of practice through lessons learned and documented related to technical, contractual and geologic factors (NASEM, 2022). Limited understanding of rockfall hazards during the construction and maintenance of highways can result in substantial social, economic, and human losses. Notably, rockfalls can lead to significant delays to motorists, resulting in

increased carbon footprints from idling or substantially long detours. These events are frequent during the winter months in the Pacific Northwest. Holtan et al. (2021) explored relationships between rockfall volume and closure times in the Pacific Northwest and found a strong correlation. Mason et al. (2017) studied rockfall impacts on highway networks in New Zealand (related to the 2016 M7.8 Kaikoura earthquake) and found that rockfall was the most common cause of the road closures after this event. Mason et al. (2017) also highlighted that rockfall produces "disrupted rock masses along the slopes above the roadway [making] reconstruction efforts more difficult and [involving] a much longer duration for clearing of debris…therefore the outage periods were much longer."

2.2.1 **Rockfall hazards**

Rockfalls occur frequently throughout Oregon and regularly result in damage to roads and potentially lengthy road closures that require substantial detours. As an example, on February 16th, 2016 a large section of the Tyee Formation fell onto Tyee Road resulting in a 45 min detour (Campbell, 2016). The Tyee Formation in the Umpqua River region of southern Oregon is one of several formations that experiences frequent rockfall activity (see section 3.5). As another example, on May 7th, 2017, a large rockfall on U.S. Highway 30 occurred with an estimated volume greater than 670 yards^3 covering around 200 feet of the highway. This rockfall resulted in the road being closed for over two weeks (Fox 12, 2017). Holtan (2021) created the Rockfall Impacts on Mobility (RIM) database that documents many other similar type events in the PNW in recent years.

2.2.2 **Contributing Factors to Rockfall**

Many factors lead to rockslope instability, including: geology, cutslope design, and climatic environment\hydraulic conditions. These factors influence the modes of failure. Hence, improved understanding of these factors can help determine appropriate slope improvement techniques and methods to reduce rockfall risk in the design and maintenance of highway infrastructure.

2.2.2.1 Geology

Geologic factors such as depositional environment, time, cementation, environmental conditions have a substantial impact on the strength of the rock material as well as the presence, quantity, and size of joints, fracturing, and weathering. These are important factors for the stability of the slope controlling the magnitude and frequency of rockslopes. There is a wide range of rockslope geologies and failure modes, for example:

- Plutonic granites, such as those found in Yosemite National Park tend to be strong, stable rocks. Nevertheless, outward expansion from thermal gradients, overburden material, and other sources can cause exfoliation fractures (Keller, 2011). This process can result in sudden, massive rockfall events such as the 1996 Happy Isles rockfall event in Yosemite, which produced an estimated 23,000m^3 to 38,000m^3 of rockfall that generated seismic waves detected up to 200 km away (Wieczorek et al., 2000).

- Other sites consist of interbedding of a "soft" soluble unit with a "hard" insoluble unit such as the Tyee formation in the Coast Range of Oregon which consists of sandstone layers interbedded with thin mudstone layers. Such interbedding is typical in marine-derived sedimentary rocks and results from repeated sea level transgressions and regressions over time. Once these materials are exposed, the mudstone layers erode faster causing the sandstone layers to fail as cantilevered overhangs due to the undercutting (Keller, 2011). These types of failures result in smaller but more frequent collapse that produce debris and require frequent maintenance to minimize risk to motorists.

Tectonics also play a role in the formation and stability of rockslopes. Oregon is situated in a geologically active setting with the subduction of the Juan de Fuca plate below the North American plate resulting in local uplift rates of 0.05 to 0.33mm/yr in the Cascade Range (Mitchell et al., 2001; Reiners et al., 2003). Active uplift correlates with increases in both the erosion and rock weathering rates (Riebe et al., 2001; Hren et al., 2007; Gabet & Mudd, 2009). Massey et al. (2022) found that rockfall activity increased for substantial periods of time following major seismic events in addition to the large rockfalls triggered directly from the strong shaking. Uplift and periodic earthquake events destabilizing slopes, combined with high precipitation rates and freeze-thaw temperature ranges during the winter months, results in a nearly perfect breeding ground for rockfalls.

2.2.2.2 Rockslope Design

How a rockslope is originally designed (e.g., slope gradient, benches, presence of mitigation, etc.) and maintained are important factors related to rockfall activity (Vandewater et al., 2005). During design, in order to achieve an optimal benefit cost-ratio, a "design life" needs to be determined to guide the design. Design methodologies and considerations are described in more detail in Section 2.3. Potential mitigation techniques and appropriate scenarios will be discussed in Section 2.6.

2.2.2.3 Climate

Several climatic factors affect rates and types of weathering generating rockfall:

- **Precipitation**: the quantity and intensity of rainfall as well as the hydraulic conductivity of overlying soil and rock are important to quantify rockfall risk (Krautblatter & Moser, 2009). Sites with interbedded "soft" and "hard" layers (e.g., Eddyville) will weather much faster with precipitation compared to the same type of interbedding in an arid environment. In comparison, variations in precipitation rate are less likely to have an impact on other types of geology such as exfoliated granite, where temperature fluctuations are a more substantial cause of weathering (Keller, 2011).

- Freeze-thaw cycles or other sequences of rapid, repeated temperature changes can result in mechanical weathering of the rockmass (Matsuoka & Sakai, 1999; Mateos et al., 2012; Arosio et al., 2013). These effects tend to be most prominent in the winter months of high latitude locations. Rapid temperature changes not

only lead to thermal expansion and contraction of the rock but also cause expansion and contraction of water as it changes from liquid to solid state (Keller, 2011). Luo et al. (2017) utilized TLS with GNSS to study freeze/thaw induced slope deformations. These observations were linked with soil temperature and moisture sensors at 11 depths to provide the hydrological and thermal conditions of the active layers. Subsidence trends were observed during thaw settlements compared with uplifting trends during the freezing period, likely resulting from frost heaving. Deformations on the order of -0.2 to 0.2 m were observed. Cunningham et al. (2017) discussed the potential effects of climate change on rock slope stability, where they present a potential approach to assessing the connection between potential climate projections on freeze/thaw and propose a connection between future rockfall activity rates, freeze/thaw cycling, and precipitation. They also outline capturing the influence of climate through a rockslope evolution model based on the Rockfall Activity Index (RAI, Section 2.4.4).

- Likewise, seasonal variability (Matsuoka & Sakai, 1999; Krautblatter & Moser, 2009) can be a contributing factor. Temperatures, precipitation, and freeze thaw cycles vary throughout the year in many locations. Rockfall is often more frequent near the middle and end of a rainy season given that the water has penetrated the overlying strata and accelerated weathering (Krautblatter & Moser, 2009).

- Removal of vegetation from talus slopes via wildfire can contribute to rockfall by loosening up rock boulders, particularly for heavily fractured rock masses. Similarly, vegetation subject to significant wind loading may enhance crack growth on rockslopes, causing rockfall and debris fall hazards.

2.2.3 Rockslope Failure Modes

Generally, rockslope failures are classified with the definition below. However, it should be noted that many rockslope failures often consist of a combination of these mechanisms.

1. *Planar failure* – Failed material slides along a structural discontinuity (Raghuvanshi, 2017) such as joints, faults or bedding planes. These failures also can occur within the interface between the weaker, weathered rock at the surface and the intact rock below.

2. *Wedge failure* – Rock masses slide along two intersecting discontinuities such as joints, inclined bedding, foliation, and well-defined cleavages (Kulatilake et al., 2011).

3. *Toppling failure* – Toppling failures occur from steep discontinuities, resulting in columns of rock that slip outward and downward from the slope (Kulatilake et al., 2011).

4. *Rockfalls* – Small block failures resulting from surface instability due to weathering or freeze thaw (Hoek and Bray., 1981).

5. *Raveling* – very small (<1 cm^3) blocks or grains of material that regularly fall from the rockslope surface.

2.3 ROCKSLOPE DESIGN

Often, construction of highways in mountainous terrain requires the creation of cutslopes, which are often excavated in native bedrock. In some instances, the only available right-of-way is at the base of natural bluffs incised by fluvial processes. In both instances, rockslope design is required to mitigate rockfall and slope stability issues during construction and operation of the adjacent highway. Rockslopes are designed to (1) ensure overall slope stability, (2) provide sufficient protection against rockfall events, and (3) provide adequate right-of-way for highway function (Hoek and Bray, 1981). Typical rockslope design involves multiple steps, beginning with (1) site investigation and rock mass characterization, (2) slope layout, stability analysis, and rockfall mitigation, and (3) construction and monitoring. Criteria used in each of these steps is specific to site geology, climatic conditions, and project requirements.

As with most projects, site investigation is often a first step in evaluating project constraints and challenges. Inspection of a rockslope provides information about potential groundwater conditions, rock mass quality, and geologic site constraints. More advanced site investigation may include drilling and sampling of geologic materials, surface measurement of rock mass properties (e.g., Schmidt hammer measurements), structural mapping, and in more recent years, creation of high-resolution digital terrain models (Abellan et al., 2014). Characterization of rock mass enables determination of rock strength parameters relevant to slope stability analyses (Eberhardt, 2003) as well as insight towards structural controls on various rockfall mechanisms (Hoek and Brown, 2019; Barton and Choubey, 1977). Based on stability analyses, evaluation of rockslope structural kinematics and project requirements, design parameters such as the slope angle, slope height, reinforcement and mitigation measures (if necessary) are determined (Hoek and Bray, 1981). Finally, rockslope construction (e.g., excavation and grading) is performed to meet right-of-way and stability specifications. During construction, inspection and monitoring are often performed to ensure safety and appropriate implementation of design elements.

2.4 ROCKSLOPE INSPECTION PROCEDURES AND TOOLS

2.4.1 Rockfall Hazard Rating and Analysis Systems

Rockfall hazard rating systems (Table 2-1) have been in use for many decades and help transportation agencies quantify the risk of potential rockfalls to prioritize the mitigation and stabilization of rockslopes along highways. They have been an important part of a geotechnical asset management framework (e.g., Anderson et al., 2022) for meeting performance goals in managing slopes. The rating systems provide detailed rules based on different geological criteria in order to determine the site score. Although not a perfect system, these rating systems have been valuable for prioritization and serve as an important step towards development of more robust methods. Several limitations to these systems are important to recognize in their implementation, particularly rockfall hazard rating systems:

- Require significant time, effort, and cost to inventory the vast amount of rockslopes that can impact highways.

- Tend to be qualitative and subjective. They are ultimately based on judgement of a trained professional tasked with assessing very large areas with limited resources. As a result, the assessment may vary between different personnel completing the task which can bias the prioritization results.

- Lack detail. Typically, sections several hundreds of meters in length are assessed and provided with a single score despite the substantial amount of variability of rockslope instability throughout a given rockslope. These methods are too coarse in order to adequately understand the morphological processes behind rockslope evolution.

Table 2.1: Summary of different rockfall hazard rating systems (modified from Olsen et al., 2020).

Rating system	Design Intent	Description	Modifications	Factors
The Rockfall Hazard Rating System-RHRS (Qualitative)	Designed to aid transportation agencies to identify and rank hazardous rockslopes for decisions regarding funding allocation.	Created by Pierson (1984) and refined by Pierson (1992). Contains six main features: (1) a uniform method for slope inventory, (2) a preliminary rating of all slopes, (3) a detailed rating of all hazardous slopes, (4), a preliminary design and cost estimate for the most problematic sections, (5) project identification and development, and (6) annual review and update. Provides a standardized approach for DOTs to rate rock slopes by assigning higher weights to more critical items that likely governs stability. The preliminary rating stage groups all known rockslopes into three categories (high, moderate and low) based on the estimated potential for rock on roadway and historical rockfall activity. This grouping improves the efficiency of the detailed ratings at a statewide scale as those that scored high for both criteria will be first to be evaluated with the detailed system. The detailed rating system includes 10 categories, with each category containing four possible scores that increase exponentially from 3 to 81 (Table A-1) to quickly isolate rockslopes with significant rockfall hazard.	Many DOTs (e.g., Alaska DOT, Huang et al. 2009) have adapted the RHRS by adding, modifying, or removing parameters according to their specific needs and geologic settings. For example, the factors considered within the RHRS can be divided into risk (possibility of loss), and hazard (the possibility of something occurring that may or may not result in loss). The initial versions of the RHRS considered hazard and risk together, but later versions considered the hazard and risk separately (ODOT, 2001) by dividing the rockfall history into annual maintenance frequency and accident history (Table A-2). Average traffic levels were also added as a category for computation of rockfall risk.	**Primary:** Geologic character, climate, history, road shape, slope morphology (12 total)

Rating system	Design Intent	Description	Modifications	Factors
Italian Modified System- IMS (Semi-Quantitative)	Adapted from the RHRS to reduce subjectivity.	Introduced by Budetta et al. (2004) as an adaptation of the RHRS. The name of IMS was proposed by Li et al. (2009). The current version of the IMS is shown in Table A.4	• The categories "climate and water circulation" and "geologic characteristics" from the RHRS (1993) were removed and replaced with the categories "Annual rainfall and freezing periods" and "Slope mass rating (SMR)," respectively. • This modification enables the quantitative ranking of climate conditions by using the defined values used in the IMS version. • The SMR category (Table A.3) is adapted from the slope mass rating (Romana, 1985, 1988, 1991). • The "ditch effectiveness" category was updated as a quantitative parameter and a new category "block size" was added	**Primary:** Road shape, climate, previous rockfall volume/size, slope, ditch effectiveness (11 total)
The Rockslope Deterioration Assessment-RDA (Semi-Quantitative)	The Rockslope Deterioration Assessment (RDA) was designed to examine the shallow weathering processes of rock slopes (Nicolson 2004).	This system has three stages: classification, rock mass type and remediation. Four main factors and nine adjustment factors can be added for special circumstances such as earthquake failure. Many of these are determined through plots based on field data. The RDA focuses on the progressive breakdown of rock slopes by considering erosional processes. Most categories can be measured but are often estimated due to safety concerns. There is also some	N/A	**4 Primary Factors:** Fracture spacing, fracture aperture, rock strength, rock weathering grade +9 adjustment factors.

Rating system	Design Intent	Description	Modifications	Factors
		flexibility in the system to fit the assessment needs. Unfortunately, this system is not designed for inventory purposes across large areas, limiting its effectiveness to be implemented by transportation agencies.		
Other (Semi-Quantitative)	Evans & Hungr (1993) introduced a simplified approach for rockslope assessment based on the shadow angle.	The shadow is defined as the area where boulders fallen from the slope settle beyond the talus pile. The shadow angle is defined as the angle between a horizontal line drawn at the top of the talus slope and the furthest boulder fallen from the rockslope. This suggests that infrastructure within this angle is at risk of damage from potential rockfall to occur on that rockslope. They found the minimum shadow angle to be 27.5º in SW British Columbia from observations at 16 sites.	N/A	Shadow angle (1 total)

2.4.2 Remote Sensing Tools

Remote sensing technologies continue to evolve as well as be utilized in new applications, particularly for geohazard assessments. Remote sensing technologies such as lidar provide many benefits (Bouali et al., 2017) for rockslope assessments and monitoring (Table 2-2) to support many applications. A variety of remote sensing technologies are regularly used for rock slope assessments, including: terrestrial lidar, mobile lidar, unmanned aircraft systems (UAS) structure from motion (SfM) multi-view stereopsis (MVS), and ground-based radar (Table 2-3). Scaioni (2015) provides a detailed discussion of less common technologies including terrestrial, geophysical, aerial, and satellite techniques.

The spatial and temporal resolution now offered by remote sensing techniques is critical in the ability of engineers and scientists to monitor and analyze geomorphological change to a higher degree than ever before through the creation of highly detailed 3D terrain models that can capture geomorphic processes (Table 2-4). Current mobile or terrestrial scan systems georeferenced with GNSS can collect millions of points per second at accuracies (Root Mean Square (RMS)) on the order of 3-10 cm at spatial resolutions of 5-10 cm on the target surface. SfM/MVS photogrammetric methods can provide similar results. In addition to detailed geometric information, most systems concurrently photograph the scene, providing a video log as well as assigning RGB color values to each scan point. Intensity information (i.e., the strength of the signal degradation) captured with each pulse can provide additional information about the type of reflecting material (e.g., geology, vegetation cover, etc.) when analyzed with appropriate radiometric calibration processes (Kashani et al., 2015).

Morphological parameters such as slope, curvature, and surface roughness can be computed from the geometric information within point clouds using a variety of methods (Table 2-5). Compared to limited field measurements at a few discrete points, these parameters can also be derived at multiple scales across the entire slope to a higher accuracy and resolution. With any of these parameters, it is important to calculate them at the appropriate scale(s) of the processes they represent. For example, a slope value computed on a 0.1 m window of the rock slope will represent a localized feature and be very different compared with a slope value computed across a 5 m window representing an overall trend of the surface.

Table 2.2: Summary of benefits and limitations of remote sensing for rockslope assessments (adapted from Bouali et al., 2017 to be applicable to broader remote sensing tools beyond lidar).

Benefits	Limitations
• Ability to collect data over inaccessible and hard to reach terrain. • Coverage several orders of magnitude larger than manual mapping methods • Enables continuous monitoring of rockslopes over a period of time so both long- and short-term change can be detected. • Field based manual methods can easily be supplemented if not replaced, with remote sensing allowing extra detail and accuracy to be captured. • Large historic libraries of datasets showing the evolution of sites can be created for monitoring as well as measure the effect of remediation techniques. Examples of these will be covered in the data inventory section. • Non-invasive and does not affect the structural integrity of rockslopes.	• "Shadow zones" may result from collecting data on rough complex topography common in hazardous rockslopes resulting in data gaps that cannot accurately be filled. Olsen et al. (2015) developed a thin plate spline technique to effectively interpolate gaps. • May not be cost-efficient if used incorrectly. Routinely acquiring cm level resolution covering all rockslopes in a large state would not be economical or feasible. Mobile lidar can be utilized to cover a large portion of the highway network annually. • Noise inducing factors such as dust, water vapor and wet surfaces can create errors, reducing the use of remote sensing in certain conditions. Lidar can penetrate these to some degree. UAS require low wind conditions to be operated. • Some data collection and analysis techniques require training and often have a steep learning curve.

Table 2.3: Summary of capabilities, limitations, and example applications of common remote sensing technologies for rockslope assessment (modified from Olsen et al., 2020).

Technology	Capabilities	Limitations	Example Studies and Applications
Terrestrial Lidar	• Provides safety, accuracy, access, and analysis speed compared to ground-based techniques (Kemeny and Turner, 2008). • Because of the look direction, TLS can capture significantly improved data on steep cliffs that are difficult to obtain when using airborne systems (Young et al., 2010). • Lidar technology continues to increase in speed, precision, and resolution capabilities.	• Still challenges and safety issues arising from setting up a stationary TLS instrument next to a busy transportation corridor (Miller et al. 2008). • Abellan et al. (2014) discussed potential issues with surveying rockslopes with TLS as well as provides requirements to track and reduce these errors.	• Telling et al. (2017) provides a detailed summary of the role of lidar in earth science investigations • Abellan et al. (2014) provides a detailed review of TLS use for rock slope instability assessment. • Jaboyedoff (2012) summarizes many applications of TLS for rockslope assessment, including rock face imaging, quantifying discontinuity orientations, trajectory modeling, monitoring of surface displacements, detection of pre-failure displacements, and quantification of rockfall activity (volumes). • Kemeny et al. (2006) report on many uses for evaluating the geotechnical conditions of unstable slopes, including rock mass characterization, surficial slope stability, rockfall analyses, and displacement monitoring. • Olsen et al. (2009, 2011) provide an efficient, robust methodology to acquire TLS (stop and go) of long coastal cliff sections as well as perform a detailed parametric analysis to determine scan acquisition parameters such as optimal scan spacing, distance from the cliff, and resolution settings.
Mobile Lidar	• Enable rapid, continuous data collection along highway corridors to support a wide range of applications.	• Limited view of the cliff given limited options for scanning geometry close to cliff from highway. Particularly the upper	• For a detailed discussion of mobile lidar technology and its role in transportation applications, please refer to NCHRP Report 748: “Guidelines for the use of mobile lidar in transportation applications” (Olsen et al., 2013)

Technology	Capabilities	Limitations	Example Studies and Applications
	• Highly advantageous from a safety perspective to survey rockfalls in rockcuts, which are typically located at narrow locations of the highway with limited shoulders since those are the locations that require rock cuts. • Allows for safe, controlled surveys to be conducted without the requiring closure of the road, which can put strain on nearby roads as well as cause a hindrance to users.	portions cannot be captured unless the cliff is relatively short (e.g., Eddyville) but struggled on taller cliffs (e.g., Rowena). • Lower resolution than terrestrial lidar. • Sometimes requires slower speeds or multiple passes to acquire usable data (Olsen et al., 2020).	and the accompanying e-learning website, http://learnmobilelidar.com. • Lato et al. (2009), used mobile lidar to conduct analysis on rockfalls along rail corridors in Ontario, Canada. Using early mobile lidar technology, point densities of 50-500pts/m^2 were achieved, enabling measurements such as slope angle & geometry, ditch height & width, and surface curvature to be determined. Lato et al. found that mobile lidar was advantageous compared to static TLS with respect to efficiency and safety. • Metzger et al. (2014) demonstrate the use of mobile lidar in a risk framework to support geotechnical asset management.
Uncrewed Aircraft Systems (UAS) Structure from Motion (SfM)/ Multiview Stereopsis (MVS) Photogrammetry	• Enable efficient data acquisition in areas that are otherwise inaccessible due to hostile or hazardous terrain (e.g., Lato et al., 2015). • These systems are gaining popularity in transportation applications (O'Neil-Dunne and Estabrook, 2019) given increased safety and decreased costs for various tasks.	• Impacted heavily by lighting conditions and surface texture (Eltner et al., 2016, Bemis et al., 2014). • Requires additional ground control points (Eltner et al., 2016, O'Banion et al., 2018). • The precision of SfM data can deteriorate near the outcrop edges and over-smoothing rounds off	• Eltner et al. (2016) summarize a variety of geohazard and geomorphological investigations • Repeat surveys from UAS platforms can quantify landslide displacements of large, slow-moving landslides (Niethammer et al., 2012; Fernández et al., 2015; Fernández et al., 2017; Lucieer et al., 2014; Turner et al., 2015, James et al., 2017). • Mapping landslide features such as scarps and deposits for small areas from the UAS imagery (e.g., Al-Rawabdeh et al., 2016). • Greenwood et al. (2016) utilized UAS to map rock masses and slides in Nepal after the 2015 earthquake event.

Technology	Capabilities	Limitations	Example Studies and Applications
	• UAS SfM provides reasonable consistency with TLS in determining morphological parameters such as slope, roughness, and the Rockfall Activity Index (O'Banion et al., 2018). • Tends to have less data gaps compared with TLS and MLS given the improved vantage point on the upper sections of the slope. (O'Banion et al., 2018).	sharp rock edges within the outcrop (Wilkinson et al., 2016). • An "elaborate" data acquisition and processing approach is often required to achieve results similar to TLS (Wilkinson et al., 2016). • Over smoothing, multiple surfaces, and surface drifting can occur with UAS SfM/MVS data. Supplementing UAS imagery with handheld ground-based imagery for rock slopes provided improved results (O'Banion et al., 2018)	• Rockfall hazard analysis (e.g., Manousakis et al., 2016, Cunningham et al. 2016, O'Banion et al. 2018) • SfM-based digital outcrop acquisition has been successfully performed by various studies (e.g., James and Robson, 2012; Bemis et al., 2014; Lato et al., 2015; Wilkinson et al., 2016).
Ground-based Radar	• Compared with lidar, radar has improved accuracy (mm-level within line-of-sight vs cm-level) for change detection.	• Ordinarily the sensor must be semi-permanently placed at a stable location with a clear view of the slope, which can be difficult along narrow	• Detailed review of the application of ground-based radar for slope monitoring can be found in Mitri and Vannes (2014) and Rosenblad et al. (2015). Notably Rosenblad et al. (2015) focuses on the usage of the technology in transportation applications.

Technology	Capabilities	Limitations	Example Studies and Applications
	• High temporal resolution and used as an early warning system • Can detect slow movements/small changes (mm-cm level).	highway corridors through canyons. • Lower resolution (m to dm) compared to lidar (cm to dm) and SfM/MVS (cm to dm)	• Permanently mounted systems can continuously Monitor slopes and can even provide early warning in mining applications (Carla et al. 2017) or transportation (Miller et al., 2013). • Collection of repeat data using ground-based interferometric radar has been utilized to develop slope failure prediction equations by continually evaluating rockfall activity leading up to the eventual slope failure (Carla et al., 2017; Kothari and Momayez, 2018). • Provide data to support forensic analysis (Carla et al., 2018) and determine threshold movements for detection based on boulder size. • Caduff et al. (2014) detected and quantified slow (mm-cm) displacement in rockfaces.

Table 2.4: Summary of common point cloud processing tasks for rockslope analysis (modified from content in Olsen et al., 2020).

Task	Method/ References	Procedure	Comments
Discontinuity Detection	Best Fit Plane (Sturzenegger & Stead, 2009)[1]	• Manually sub selects an area of the point cloud known to be part of the plane, • A best fit plane is automatically fitted based on the relative position of those points	(+) Potentially most accurate in complex locations where as planes are often mistakenly misidentified as joint or other planes. (-) most time intensive (Abellan et al., 2012).
Discontinuity Detection	TIN (Kemeny et al., 2006).[1]	• Generate a TIN • Calculate the normal vector for each triangle • Use the normal vectors as "poles" to the various discontinuity planes.	(*) The three primary control variables of the resulting normal vector are the maximum angle between triangular points, density of triangles and the minimum patch size

[1] Battulwar et al. (2021) and Daghigh et al. (2022) provide detailed reviews of techniques and tools for discontinuity detection from point clouds. Discontinuity features present in rockslopes, such as faults, joints, foliation and bedding planes can have a large effect on the failure mechanisms of rockslopes. Thus, by successfully extracting these features, important parameters affecting rockslope stability can be understood. Dip and strike can be extracted from "near-planar" features in lidar data to produce stereoplots to analyze slope stability. To extract planar surface orientation, three methods are commonly used (Abellan et al., 2012).
While using lidar is widely considered more accurate for discontinuity extraction due to reduction in human bias and georeferencing error, several biases still exist (Abellan et al., 2010):

- "Terzaghi bias" from the large perceived spacing between discontinuities due to their orientation compared to the rockslope face (Terzaghi, 1965).
- "Persistence bias" from the erosion and truncation of smaller discontinuities (Sturzenegger & Stead, 2009).

The "observation scale effect," which is a function of the distance of the rockslope from the scan positions, results in smaller discontinuities being difficult to recognize in distant areas (Sturzenegger & Stead, 2009).

Task	Method/ References	Procedure	Comments
		• Determine planar regions by consistencies in normal. • Compute an average normal vector for the plane.	(*) This approach has been integrated into the SplitFX software.
Discontinuity Detection	Segmentation (Jaboyedoff et al., 2007; Abellan et al., 2010).[1]	• Segment the point cloud based on similar normal vectors • Calculate local planar strike and dip values using eigenvalue analysis of the local segmented covariance matrix • Color points by orientation to identify points with similar orientation values • Generate stereonets showing the common strike a dip direction of these features.	
Block size and volume computation	Planar reconstruction (Gigli et al., 2014)[2]	• Create 3D models depicting the shape and volume of unstable blocks • Geomechanical analysis was used where the points defining the blocks were extracted • Least squares fitting planes were created to define the block's dimensions.	This technique results in the realization of the position and magnitude of the blocks along the highway, highlighting the sections most at risk

[2] Unstable blocks on rock slopes often result in large failures that can cause severe damage to infrastructure given the forces and momentum associate with the large mass.

Task	Method/ References	Procedure	Comments
		• Volume of the blocks calculated from these planes.	
Block size and volume computation	Volumetric analysis (Mavrouli et al., 2015).[2]	• Calculate the size distribution of an unstable rock mass • Calculate the distribution of in situ blocks on the slope face. • Calculate the volume of the blocks using the intersection of the different joint sets on the rock slope	
Magnitude-frequency relationships and rockfall detection	DB scan clustering (Tonini and Abellan, 2014; Carrea et al., 2015)[3]	• Generate clusters based on a K-nearest neighbors algorithm. • Clutter removal • Semi-automatic approach to calculate volumes of each rockfall cluster • Generate magnitude–frequency relationships.	
Magnitude-frequency relationships and rockfall detection	Connected components Clustering (Olsen et al., 2015)[3]	• Interpolate holes with a thin plate spline • Compute change grids. • Isolate individual failure clusters (*i.e.*, rockfall events) on the rock slope utilize a connected components algorithm on the change model to isolate individual rockfalls.	This streamlined approach to analyze time series point clouds is the basis for Rambo. They also investigate the resulting differences in magnitude frequency curves based on the differences in modelling resolution as well as

[3] Multi-temporal TLS datasets from rockfall monitoring are utilized to establish magnitude–frequency relationships to show the frequency distribution of large to small volumes of material release for rock slopes (D'Amato et al., 2015; Olsen et al., 2013; Barlow et al., 2012; Santana et al., 2012; Rosser et al., 2005; Lee and Jones., 2004). Such distributions provide important information needed to support landslide hazard and risk assessment (Santana et al., 2012; Lee and Jones., 2004).

Task	Method/ References	Procedure	Comments
		• Quantify volumes of each cluster from change grids • Generate magnitude–frequency relationships from those clusters.	whether or not holes (data gaps) are interpolated.
Magnitude-frequency relationships and rockfall detection	Evolution Modeling (Whadcoat, 2017)[3]	• Numerical modelling to predict the evolution of rockslopes over a period of time • The model used a discontinuous approach allowing for failure simulation along discontinuities. • Used a Lattice spring model, where the rock is represented as conglomeration of nodes joined together by nonlinear springs. • These springs represent the properties of the rock mass including density, elasticity and the tensile strength. • The distance between the nodes represents the resolution of the model and the approach allows for simulation of brittle fracture.	• Similar to many topographic features, rockslopes evolve over time in an attempt to reach a state of equilibrium. • The mechanisms and rates of evolution of rockslopes are important to understand impacts on infrastructure. • Assumed that previous failures influence future failures. • Rockfall events cluster in both space and time, with rockfall scars tending to grow outwards and upward.
Susceptibility Analysis	Slope Angle[4]	• Calculated the susceptibility of the sources based on the normalized cumulative distribution function, which is calculated using the mean angle of the steep slope distribution.	

[4] Matasci et al. (2015, 2017), developed a rockfall susceptibility index for several types of failure mechanisms based on the local rockslope orientation of the joints.

Task	Method/ References	Procedure	Comments
Susceptibility Analysis	Joint and Failure Mode Analysis[4]	• Joint orientations are identified (Jaboyedoff et al. 2007) • Joint spacing was calculated by finding the normal vector of the average joint plane and projecting this through subsequent joint planes to measure the spacing. • Unstable slope areas were then found by looking at the intersections between joint sets and the rockface. • Susceptible locations were identified based on failure modes: ○ *Planar failure* – Occurs where the dip direction of a given point on the rockface at the intersection with a joint falls between the tolerance of the dip direction of the joint and the slope angle of the rockface exceeds the slope angle of the joint. ○ *Wedge failure* – Occurs where two joint sets intersect, forming a linear feature of weakness. If the plunge of this line is exceeded by the slope of the rockface and the dip direction of a point on the rockface at the intersection falls within the tolerance of the trend of the line then is deemed likely to occur. ○ *Toppling failure* – Occurs with the same definitions as planar failure when the joint set has a "negative	• Exfoliation fractures which are slope parallel and generally hard to identify, were captured by the planar and toppling failure identification methods (Matasci et al., 2017).

Task	Method/ References	Procedure	Comments
		dip" (joint set dipping into the rockface).	

Table 2.5: Summary of morphological parameters (modified from content in Olsen et al., 2020).

Morphological Parameter	Description	Calculation Method	Comments
Slope	Local orientation for the rockslope in relation to the Z (elevation)-axis,	$Slope = \tan^{-1}\left(\sqrt{\left(\frac{d_z}{d_x}\right)^2 + \left(\frac{d_z}{d_y}\right)^2}\right)$ d_x, d_y, and d_z are the differences in X, Y, and Z coordinates between two points or cells.	Can be determined for each point where the slope is the average slope between that point and a defined number/distance of other points around it. By calculating slope, features such as overhangs can be mapped providing critical information regarding rockfall hazard (Dunham et al., 2017).
Curvature	Curvature describes the amount a surface varies from a flat plane. This can be used to describe the morphology of the surface independent to any predefined axis giving an indicator on the nature of the surface.	$\boldsymbol{Curv} = \frac{\boldsymbol{x'y''} - \boldsymbol{y'x''}}{(\boldsymbol{x'^2} + \boldsymbol{y'^2})^{\frac{3}{2}}}$ x and y refer to local points on a 2D plane fit to local points around a center point	Overhangs or protrusions provide higher curvature in profile and plan view, respectively. Higher levels of curvature on the surface can lead to increased rockfall activity.
Roughness	Surface roughness provides the deviation from a planar surface for a given area in the direction of the plane normal. Surface roughness within a window can be calculated using the either standard deviation of the elevation from a given plane or slope. This can provide an indication of the stability of the slope as well as give an estimation of the bounce and velocity of falling rocks (Wang, 2010).	$\boldsymbol{R} = \sqrt{\frac{\sum_{i=1}^{N}(\boldsymbol{E_i} - \bar{\boldsymbol{E}})^2}{\boldsymbol{N-1}}}$ where E_i is the distance offset from a plane for sample i within a window of evaluation corresponding to the spatial scale of interest, $\bar{E}$ is the average offset from the plane within the window, and N is the number of samples within the window.	A variety of techniques exist to compute surface roughness from a TIN or DEM. Berti et al. (2013) examined a variety of techniques and found that simple techniques performed similarly to more complex techniques provided that they de-trend the surface (i.e., account for the overall surface trend). Rougher surfaces can indicate weathering, fracturing, and other indicators of rockfall activity.

2.4.3 Magnitude-Frequency Relationships

Magnitude-frequency relationships provide a quantifiable metric to compare rockfall risk between sites. Tebbens et al. (2020) provides a thorough review of magnitude-frequency relationships and modeling approaches for landslides and rockfalls. Several variants of these relationships are used in practice including size-frequency distributions, cumulative frequency, noncumulative frequency, probability density, and frequency density distributions depending on how data are normalized and processed. To compute these relationships, individual failures of mapped landslides (or rockfalls) are binned based on volume to obtain a count for each bin. Many curves show a rollover portion (Clauset et a. 2009) at small volumes due to insufficient spatial and temporal resolution and accuracy that prevent those events from being reliably quantified (Olsen et al. 2015). A power-law regression line is then fit to the remaining data providing a scaling parameter and an exponent to define the frequency with which large and small blocks of rock fall at a site. The higher the scaling parameter in a magnitude frequency relationship, the more active the site.

2.4.4 Rockfall Activity Index (RAI)

The RAI (Rockfall Activity Index) is a quantitative method of rockfall hazard assessment developed by Dunham et al. (2017) in response to recognized limitations in conventional rockfall hazard rating systems. As described in Section 2.4.1, those systems tend to be qualitative and subjective, rely on visual inspection, and produce coarse spatial resolution outputs that are ill-suited to characterizing the localized morphological processes governing rockslope evolution. Capitalizing on advances in terrestrial lidar technology that allow rock slopes to be imaged at centimeter-scale resolution from a safe standoff distance, Dunham et al. (2017) developed the RAI as a point cloud-derived, morphology-based approach capable of objectively and repeatedly assessing rockfall hazard across slopes of virtually any size. The RAI was subsequently updated and refined through several years of additional data collection and analysis from rockslopes in Alaska, conducted through PacTrans-funded research (Markus et al., 2023). In prior ODOT research (SPR-809), the RAI was further modified to function with coarser point cloud data (e.g., MLS data) at approximately 0.1 m resolution (Olsen et al., 2020).

2.4.4.1 Morphological Classification

The RAI is based on morphological analysis of high-resolution three-dimensional point cloud data. The first step in the method consists of classifying the rock slope surface into one of seven distinct morphological classes, each of which is associated with characteristic mass-wasting processes and unique rates of activity. The classification scheme (Figure 2-1) uses two primary morphological parameters derived from the point cloud: local slope angle and surface roughness computed at two spatial scales (35 cm and 85 cm window sizes, denoted R_{35} and R_{85}, respectively). Roughness is calculated as the standard deviation of slope within each window, a simple yet reliable approach for characterizing surface texture at multiple scales (Dunham et al., 2017).

The seven classes are defined as follows (Table 2-6). *Widely to moderately spaced discontinuous rock* (Dw) and *closely spaced discontinuous rock* (Dc) represent intact blocks separated by joints with spacings of approximately 30 cm or greater and 10–20

cm, respectively, while *fragmented discontinuous rock* (Df) captures joint spacings of less than approximately 10 cm. Together, these three discontinuous rock classes encompass the range of blocky rockslope morphologies that dominate mass wasting through block release. *Intact rock* (I) represents areas with few or relatively minor discontinuities, which tend to degrade through shallow surface erosion and raveling rather than discrete block failures. Two *overhanging rock* classes are distinguished based on inclination geometry: *cantilevered overhang* (Oc), whose lower face is inclined at 120° or greater from horizontal, and *shallow overhang* (Os), inclined between 90° and 120°. Overhangs typically form through differential erosion between rock units and are among the most hazardous morphological features on a slope due to their potential for sudden, large-volume tensile failure. Finally, *talus* (T) identifies zones of accumulated mass-wasting debris typically located near the slope toe or on benches, which fail primarily through shallow, planar raveling processes.

The classification algorithm proceeds as a logic tree (Figure 2-1). Slope values exceeding 90° first identify overhanging rock, which is further subdivided by inclination into Oc or Os. Among non-overhanging areas, fine-grained roughness (R_{35}) is then used to separate relatively smooth surfaces (R_{35} < 6°)—which are assigned to either T or I based on slope angle relative to the angle of repose—from rougher areas that are classified into the discontinuous rock categories based on the magnitude of both R_{35} and R_{85}. The original talus slope angle threshold was established at 35°, reflecting the typical angle of repose of coarse rock debris (Dunham et al., 2017).

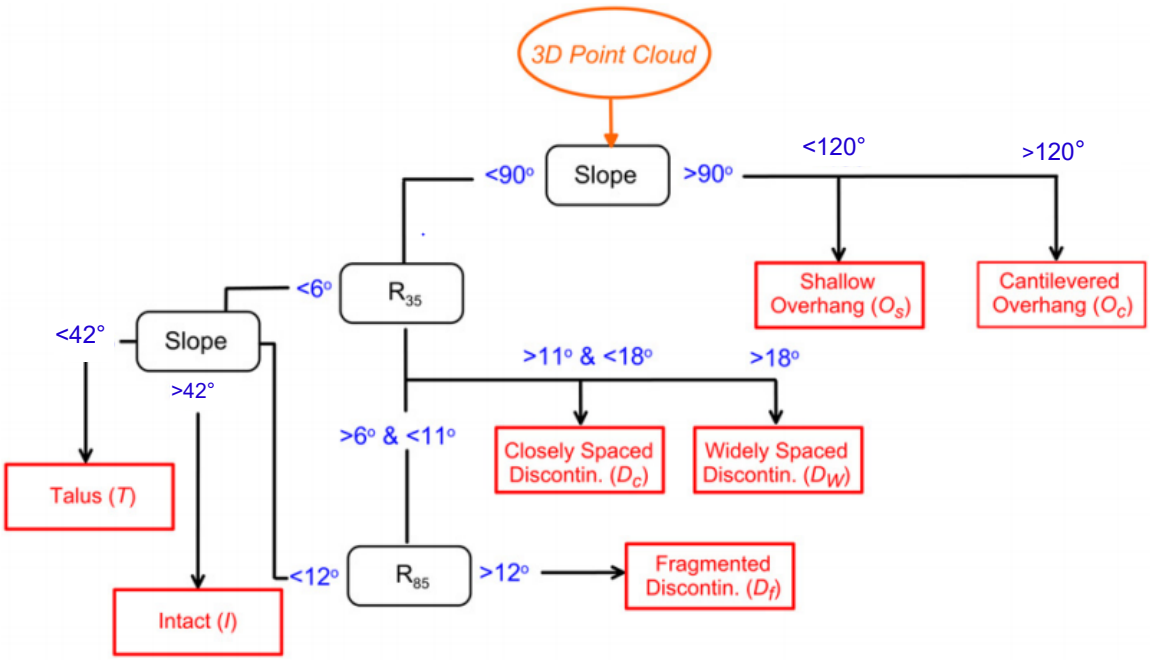

Figure 2.1: Classification scheme utilized for the RAI (Rockfall Activity Index) modified from Dunham et al. (2017) and Markus et al. (2023).

2.4.4.2 RAI Computation

Following morphological classification, the RAI is computed for each 1-m length segment of the slope as the estimated annual cumulative delivery of kinetic energy (kJ) to the base of the slope. For each cell within a given segment, kinetic energy is estimated as the product of the cell's representative failure mass—determined from an assumed failure depth and rock specific gravity—and the square of the free-fall velocity calculated from the vertical height above the slope base. These per-cell energy values are then scaled by an *instability rate* (r), which represents the fraction of cells within a given morphological class expected to fail in a given year, and summed across all cells within each 1-m segment. Rock overhangs consistently exhibit the highest instability rates due to their susceptibility to sudden tensile failure and their comparatively large associated failure volumes; talus and intact rock exhibit the lowest rates (Dunham et al., 2017). The RAI thus integrates slope morphology, release height, failure volume, and activity rate into a single quantitative metric that can be mapped along the full length of a transportation corridor to identify high-hazard zones and inform mitigation prioritization.

2.4.4.3 Validation and Field Assessment

Dunham et al. (2017) applied the RAI method at two study sites along the Glenn Highway (Alaska State Route 1) in southcentral Alaska, a region characterized by steep road cuts in sedimentary rock, extreme freeze-thaw cycling, and a well-documented history of rockfall maintenance activity. Qualitative comparison of morphological classifications with field observations at these sites and approximately 15 additional road cut sections across Alaska demonstrated that the automated classification routine reliably distinguished the principal morphological units and correctly inferred the dominant mass-wasting processes active on each slope. The RAI source mapping and 1-m segment profiles effectively identified localized high-hazard zones, including areas of concentrated cantilevered overhang, that aligned with observed maintenance records and visible rockfall scars. The authors acknowledged that the most significant source of uncertainty in the RAI computation is the instability rate *r*, which is sensitive to site-specific geology, climate, and weathering conditions; however, parametric analyses indicated that the RAI is relatively insensitive to modest variations in *r* because kinetic energy is predominantly governed by release height and failure mass, both of which are more directly constrained by the point cloud data.

2.4.4.4 Recent Refinement of RAI Parameters

Recognizing that the preliminary instability rates and failure depths in Dunham et al. (2017) were based on only one year of change detection data at two Alaskan sites, Markus et al. (2023) significantly expanded the empirical foundation of the RAI through the development of a comprehensive lidar-based rockfall inventory. Using TLS surveys collected at four sites along the Glenn Highway between 2012 and 2017, Markus et al. (2023) catalogued 4,381 individual rockfall events over a five-year period at sites spanning a range of geologic settings, including carbonaceous mudstone, gabbro sills, and interlayered mudstone-sandstone formations of the Chickaloon Formation. Each

event was assigned a volume derived from change detection analysis, and a predominant RAI class based on the classification of the failed cells.

Analysis of the resulting inventory demonstrated that cumulative magnitude-frequency distributions follow power-law relationships across several orders of magnitude, consistent with observations from other lidar-based rockfall inventories (e.g., Barlow et al., 2012; Hartmeyer et al., 2020). The power-law parameters—the activity parameter (β) and the scaling parameter (α)—varied appreciably among the four sites, reflecting the influence of site-specific geology, structural controls, and groundwater conditions on rockfall activity. Significant temporal variation in these parameters was also observed from year to year at each site, likely driven by interannual variability in precipitation and freeze-thaw cycling. Importantly, Markus et al. (2023) demonstrated that magnitude-frequency distributions and their associated power-law parameters also vary systematically among the seven RAI classes, confirming that the RAI morphological framework effectively discriminates areas of the slope with distinct erosion and mass-wasting behavior. Talus areas, for example, exhibited high activity parameters and low scaling parameters—consistent with frequent, relatively large planar adjustments driven by the progressive loading of debris from higher on the slope—while intact rock showed the opposite pattern, reflecting infrequent, small-scale erosive failures.

Using the five-year inventory, Markus et al. (2023) calculated revised average annual failure rates and average failure depths for each RAI class, weighted by site area to account for the substantial differences in slope size among the four study sites. The revised parameter values, which supersede the preliminary estimates of Dunham et al. (2017) and are incorporated into the *Rambo* software as default values, are summarized in Table 2-6. Notably, the revised instability rates for the overhang classes (Oc and Os) are considerably lower than the original preliminary values, reflecting the more robust empirical basis of the updated estimates. Conversely, the revised failure depths are generally greater across all classes, particularly for the discontinuous rock and overhang categories, with important implications for hazard computations at sites where large individual failure masses are expected.

Markus et al. (2023) also identified that the original talus slope angle threshold of 35° (used to distinguish talus from intact rock in the classification algorithm) systematically misclassified portions of the talus areas at the Alaska study sites, where measured talus angles frequently exceeded 40° and in some locations approached 45°. This steepening relative to natural talus slopes reported in the literature is likely attributable to periodic undercutting of the slope toe during highway maintenance operations, which over-steepens the talus accumulation. To address this, Markus et al. (2023) recommended either raising the default talus slope threshold to 42° or, preferably, implementing a variable, site-adjustable threshold within the *Rambo* software interface. The 42° default has since been incorporated into *Rambo* as the standard classification parameter (Figure 2-1).

Ultimately, the Dunham et al. (2017) and Markus et al. (2023) studies established the RAI as an empirically grounded and calibrated framework for quantitative rockfall hazard assessment. The RAI serves as a quantitative metric that can be utilized for

prioritizing and evaluating maintenance and mitigation efforts. It provides a promising basis for characterizing the morphological effects of slope mitigation activities such as scaling.

Table 2.6: Updated and original activity rates and assumed failure depths for each RAI classification, table modified from Markus, 2018.

RAI Classification	Description	Original Instability rate (Dunham et al, 2017)	Updated instability rate (Markus, 2023)	Original Assumed Depth (m) (Dunham et al, 2017)	Updated Assumed Depth (m) (Markus, 2023)
Unclassified (U)	Locations with sparse data where morphological parameters cannot be determined accurately	0.001	0.0326	0.025	0.1452
Talus (T)	Slope failure derived fragmented rock material that accumulates at the base of a rock slope.	0.000	0.129	0.025	0.1240
Intact (I)	Rock mass with no/very little discontinuity features	0.001	0.0234	0.05	0.1704
Fragmented discontinuous rock (D_f)	Intact blocks within rockslope separated by discontinuities spaced 10cm or less	0.0018	0.0306	0.1	0.1724
Closely spaced discontinuous (D_c)	Discontinuity features spaced between 10-20 cm.	0.0034	0.0334	0.2	0.1702
Widely to moderately spaced discontinuous rock (D_w)	Discontinuity features spaced 30 cm or greater.	0.0071	0.0295	0.3	0.2169
Cantilevered Overhang (O_c)	Overhanging rock with ground facing side inclined 120º or less.	0.0198	0.0228	0.5	0.2125
Steep Overhang (O_s)	Overhanging rock with ground facing side inclined 120º or more.	0.0197	0.0362	0.75	0.2316

2.4.5 Rambo

Rambo (Rockfall Activity Morphological Bigdata Optimizer) is a powerful software tool developed by the research team through several PacTrans and ODOT research projects (e.g., SPR-809) to efficiently perform detailed morphological analysis of rockslopes with high resolution point cloud data (e.g., lidar, structure from motion, multi-view stereo). The software has a GUI to simplify the selection of processing parameters and performs batch processing of multiple epochs of data simultaneously. This software is currently being maintained by EZDataMD LLC, a tech transfer company spun out of OSU. A summary of key capabilities of the software is provided in Table 2-7. Prior to running *Rambo*, the point clouds for each epoch should be cropped to the cliff section of interest. Long sections with substantial plan curvature should be divided into smaller sections for best results.

The main output of the software is a processed point cloud with many attributes (e.g., slope, roughness, curvature, aspect, RAI classification, change, etc.) provided as extra bytes in a LAS/LAZ or csv file output. The software also provides summary and detailed results in tabular format in a series of supporting csv files for more advanced analyses.

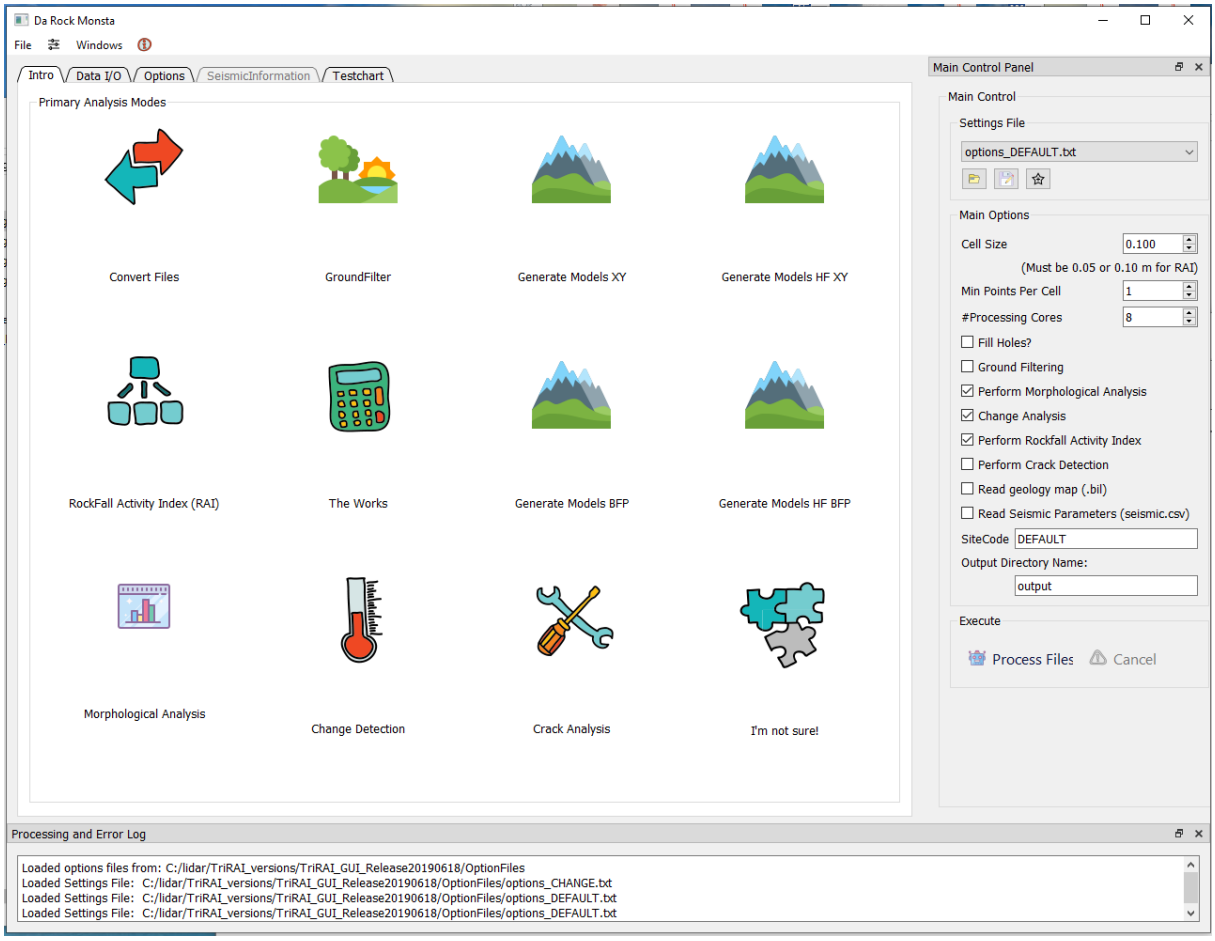

Figure 2.2: Graphical User Interface of *Rambo*.

Table 2.7. Summary of features available in Rambo to analyze point clouds of rockslopes (modified from Olsen et al., 2022).

Feature	Description	Image
Ground Filtering	*Rambo* can implement a ground filter that is flexible to operate on steep rock slopes. The filter operates in the best fit plane of the data such that steep features of the cliff are preserved. It also operates progressively across several window sizes and performs statistical analyses to remove vegetation points while still preserving distinct features on the rock slope surface. While ground filtering can be implemented in the same run as the RAI or change analysis, it is ordinarily recommended to perform separate ground-filtering runs to ensure the parameters are selected appropriately.	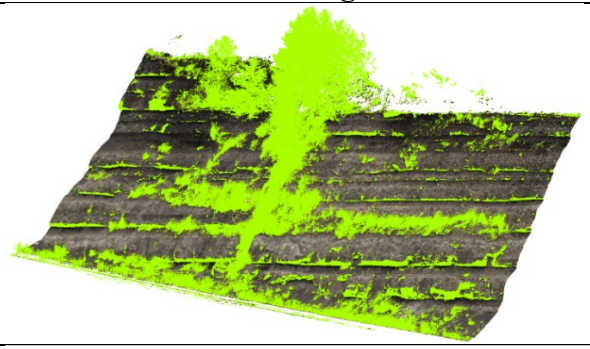
Smoothing/ Modeling	A key feature of *Rambo* is the ability to analyze rock slopes in the best fit plane rather than the XY plane or a vertical plane. This enables the efficiency of a planar analysis combined with a higher resolution analysis on the slope. *Rambo*, however, can also be run in the XY plane when appropriate. Users can also constrain the analysis to the best fit plane of the first dataset (and likewise the same indexing structure) when performing change analyses for consistency. The user can also specify the plane and indexing structure, when desired. Rambo produces triangulated surface models which are output as an .obj file with normals and supporting files for RGB texture mapping (mtl, .png).	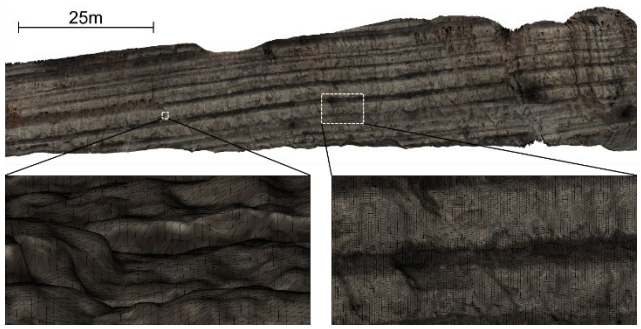
Hole Filling	*Rambo* can interpolate across data gaps/holes with a thin plate spline using the approach outlined in Olsen et al. (2015). The thin plate spline helps provide a more natural look to the interpolation compared with other common methods. Users can constrain the size of holes to be filled and limit the hole filling to areas with relatively dense data for the interpolation to avoid poor interpolation in areas of sparse data. A regularization parameter also determines how precisely the thin plate spline will match the input data points used to compute the spline.	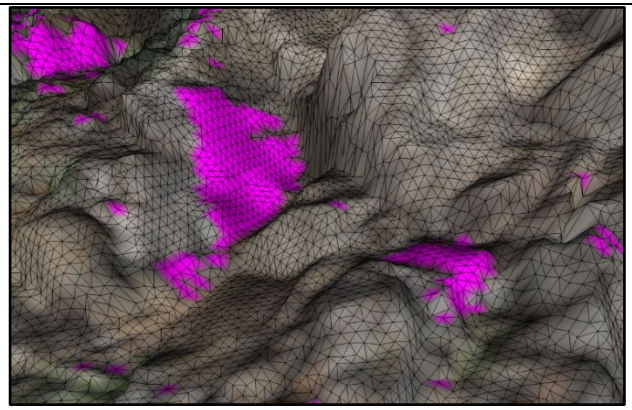

Feature	Description	Image
Morphological Analysis	*Rambo* can compute a wide range of morphological parameters and metrics across the slope face for each slope (including relative elevation, slope, roughness, aspect, curvature, and bending energy). These parameters are computed across several spatial scales, based on the user selection. *Rambo* can then generate a set of output files that can be plotted as histograms of these morphological parameters for each dataset. The figure shows example slope values (in degrees) computed for window sizes of (a) 3x3 (0.3x0.3m), (b) 11 x 11 (1.1 x 1.1 m), and (c) 21 x 21 (2.1m x 2.1m) for the May 3, 2011 survey of Redcliffs Southwest in the Port Hills, Canterbury, New Zealand.	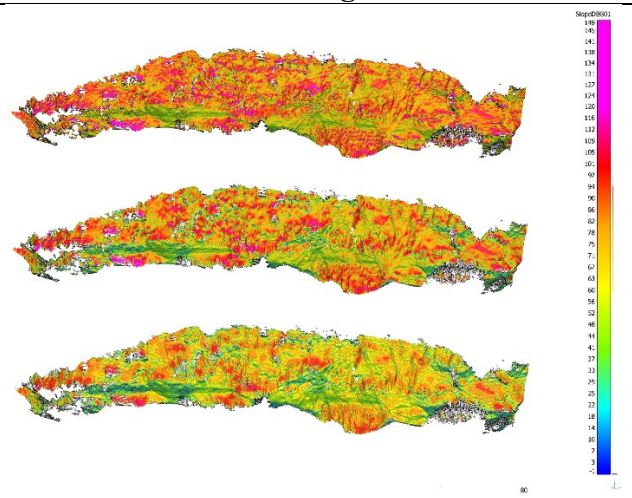
Rockfall Activity Index	*Rambo* implements the rockfall activity index (RAI) analysis by performing the classification and computing the RAI score as defined in Dunham et al. (2016) with updated parameters from Markus (2018). *Rambo* also provides additional output files with summary statistics based on the RAI classification. The default RAI values can be edited in the GUI, if desired, to adapt to local parameters.	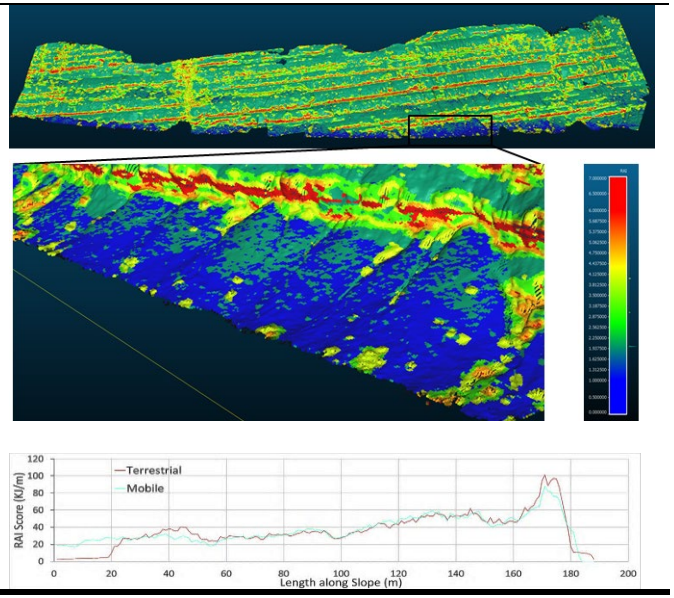

Feature	Description	Image

Change Analysis	*Rambo* implements several functions for change analysis in either the XY plane or best fit plane with a fixed indexing scheme between all epochs.
	
	• At the basic level, *Rambo* performs change detection and analysis for each cell and each set of epochs by determining the orthogonal distances relative to the analysis plane between both epochs. (i.e., in an analysis in the XY plane, it computes the difference in elevation between each epoch).
	• *Rambo* then identifies both areas of erosion and accretion across the surface. For this classification (and subsequent analyses), a significant change threshold is implemented to minimize false positives resulting from georeferencing error.
	• *Rambo* identifies individual rockfall clusters and outputs the associated volume of each cluster using the approach detailed in Olsen et al. 2015, which implements a connected components algorithm on the change grid. *Rambo* then tags these with the predominant RAI classification.
	• *Rambo* performs an analysis of the prior failure history for each cell by determining how many times that cell has failed with each prior epoch. (note that all epochs need to be processed together).
	• *Rambo* also analyses failed neighbors to each cell to determine spatial relationships and clusters of failure activity with time. These are presented in two metrics.
	  ○ First, the percent neighbor failed (one change epoch) is the number of neighboring grid cells, within a given range of grid cells (window) from 1 to n around the given the cell, which have changed (failed) in the previous change model, divided by the total number of grid cells that could have changed within the given window.
	  ○ Second, the failure rate is computed as the number of neighboring grid cells, within a given range of grid cells (window) from 0 (the given grid cell) to 10 around the given the cell, which have changed (failed) in previous change models (ALL change model epochs prior to this one), divided by the total number of cells that could have changed (within the given window and for all change model epochs), divided by the number
		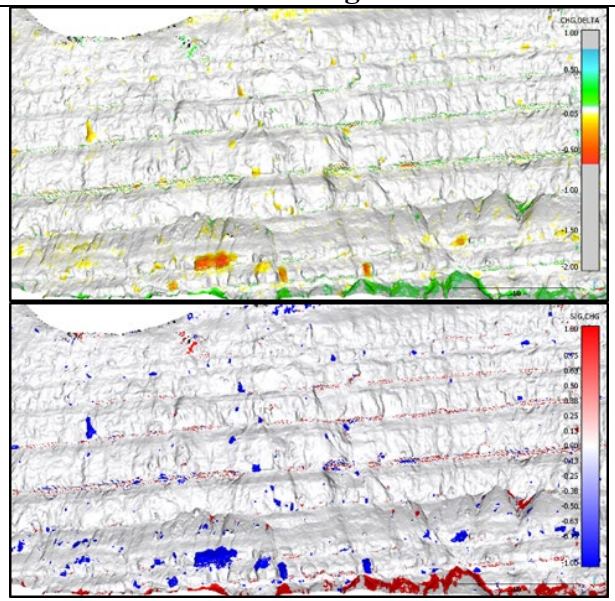

Feature	Description	Image
	of change models. Note that when a cell has failed multiple times, each failure is included in the summation. • Automatically generates tabular data (csv files) for plotting magnitude frequency curves that can be plotted in MS Excel. • Outputs a csv file summarizing the overall volumetric change for each epoch. • Point cloud outputs can be visualized using the CloudCompare software to quickly toggle between layers.	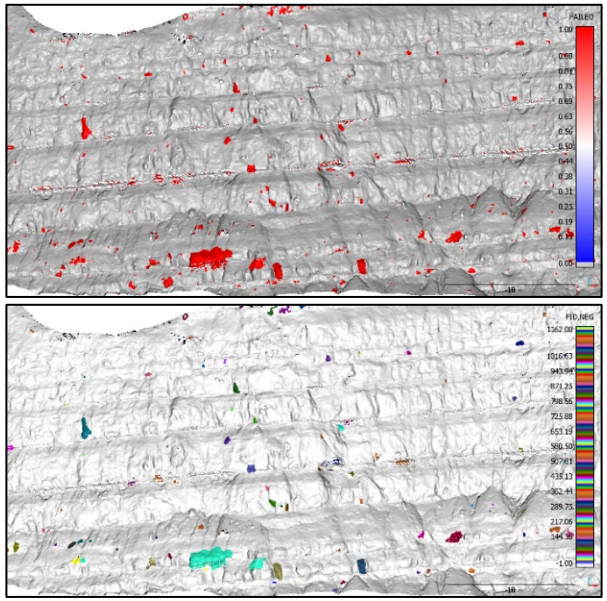 ***Example change analysis outputs coloured by field of change (m), significant change (m), failed blocks and failed clusters (from top to bottom).***
Seismic Analysis	*Rambo* can read in PGA (Peak Ground Acceleration) values so that seismic forcing can be considered between epochs. This file also can contain precipitation (mean and max annual precipitation). This file is useful to tag these forcing attributes with the morphological and other analysis factors in subsequent statistical analyses such as logistic regression. Within the GUI, this file, when available, can be viewed in a tabular form. This file is also used to provide labels/names to each epoch to improve the readability of output files.	N/A

2.5 ROCKFALL MODELING

There are a variety of tools developed to evaluate rockfall runout modeling, focusing on modeling initiation, trajectory, and impact. Trajectory models tend to be statistically-based, physically-based, or a hybrid of both (Li and Han, 2015). These approaches are often two-dimensional (2D), but three-dimensional (3D) approaches are also available. The rockfall mass can be treated as a rigid or an elastic-plastic lumped mass. The probabilistic elements owe to the uncertainties of source location and initial kinematics, of rockfall shape and properties, and of rockfall response during impact (fracture, restitution). There are a variety of tools that perform these analyses, but herein we focus on the most commonly-applied tools in the United States at the time of this project: RAMMS and RocFall. Other GIS and DEM approaches exist. The results are highly sensitive to the resolution of the DEM utilized in the analysis (Kakavas et al., 2023) as low resolution DEMs wash out surface roughness which can alter bounce patterns, damping, and trajectories. Kakavas et al. (2023) recommend DEMs with resolutions at the sub-decimeter level for the analysis; however, they obtained generally reliable results with DEMs with resolutions < 5 m with high accuracy.

2.5.1 RAMMS (Rockfall Analysis and Monitoring in Engineering and Mining Services)

RAMMS (Rockfall Analysis and Monitoring in Engineering and Mining Services) is a software package used to simulate and model rockfall trajectory in 3D using a physics-based approach to model the behavior of rockfall events in terms of the initial rockfall parameters (such as rock mass size and velocity), site topography, and the properties of the site, such as its hardness, roughness, and slope angle (Leine et al., 2014). RAMMS allows users to assess the potential impact of rockfall events, both in the form of velocity and runout location. The program can also be used to evaluate the effectiveness of existing rockfall protection measures, such as rockfall barriers or rigid rockfall mitigation systems.

2.5.2 RocFall

RocFall (Stevens, 1998) is a software package developed by RocScience, Inc. for modeling and simulating rockfalls in 2D and 3D. It uses a physics-based approach with statistical distributions of properties to calculate the motion and impact of rock masses as they fall, slide, and bounce down a given rockslope. The software considers various factors that affect rockfall behavior, such as slope angle, rock mass properties, and environmental conditions. The user provides rockslope geometry, and then defines the rock mass properties, such as size, shape, density, and strength, thereafter, simulating the motion of rock masses as they fall. The simulation takes into account the gravitational force acting on the rock masses, as well as the friction, impact, and rebound forces that occur during the fall. The software calculates the velocity, displacement, and impact energy of the rock masses at each step of the simulation. The results of the simulation can be visualized in 3D and can be used to assess the hazard potential of rockfall events and to evaluate different rockfall mitigation measures.

2.5.3 GIS-based tools

Many GIS-based approaches have been developed to model rockfall in GIS. These approaches have the benefit of scaling to analyze a large area with computational efficiency as well as integrate a variety of data sources. However, a key limitation is that they do not often incorporate the rigorous physics and geotechnics that RAMMS and RocFall incorporate. Here are some examples of GIS tools:

- Rockfall Analyst GIS Extension (Lan et al., 2007, 2010) focused on identifying locations potentially requiring stabilization. This extension consists of two key components to analyze DEMs derived from airborne lidar:
    - Rockfall trajectory simulation, which estimates the bouncing height of falling rocks and the associated kinetic energy
    - Rockfall distribution modelling to identify locations of sharp topographic change by evaluating differences between the original 1m resolution DEM with a smoothed 5m DEM.
- Heckmann et al. (2012) also used GIS to quantify rockfall hazards, including:
    - Computing rockfall volumes during an event by comparison of the pre-failure airborne lidar derived DEM and a post failure TLS derived DEM.
    - Trajectory modeling using an algorithm that considered: a slope threshold (the local slope gradient above which the direction of the steepest slope is chosen), a divergence factor (the chance of the block diverging from the steepest slope path) and a persistence factor (a block continues in a certain direction if its previous slope was considerably larger than current slope).
- Abellan et al. (2010) studied the evolution of rockslopes in Catalonia, Spain with the following techniques:
    - To detect change they used a similar method to Rabatel et al. (2008) by extracting areas where a rockfall had occurred from the point cloud and subsequently using a local reference frame to compute the volume of each rockfall event.
    - Predictions of future rockfalls were made using the pre-failure deformation by calculating rockslope creep. Rockslope creep has been correlated with mass movement events (Maruyama & Kozima, 1994), often triggered by external factors such as freeze thaw or seismic events) of individual parts of the rockslope.

2.5.4 Modelling mitigation techniques using lidar derived surfaces

In addition to supporting slope stability analyses, the high-resolution digital surface representation provided by lidar are also useful to support the planning and design of the rockfall mitigation techniques discussed in Section 2.6 following the techniques described in Section 2.5.1 to 2.5.3. Lidar supports many applications of those stages including:

- Providing estimates of the estimated size and trajectory of falling rocks to inform the design of mitigation techniques such as rock fences, attenuator systems, catch ditches and embankments.

- Conducting a full "trajectory analysis" of potential rockfall prior to construction of embankments to estimate flying/bouncing height, velocity, spatial distribution and block mass. Lambert & Bourrier (2013) performed simulations using lidar DEMs and found that embankments were successful in reducing the passing frequency by several orders of magnitude. They also noted limitations in resolution when using airborne lidar-derived DEMs. Similarly, Agliardi et al., (2009) used back analysis from lidar DEMs to assess the potential reduction in damages and financial losses during a rockfall event in 2004. They determined that a provisional embankment would lower damage costs from €7 million to €43,000 and long-term protection embankments would lower damages to less than €1,000.

2.6 MITIGATION TECHNIQUES

Rockfall mitigation is often performed on a case-by-case basis for rockslopes and frequently consists of a combination of mitigation techniques. Sites for mitigation can be identified through geotechnical asset management programs such as the Unstable Slopes program at ODOT. Other times sites are selected for mitigation given road closures or other safety hazards resulting from the site. Conventional rockfall mitigation includes various methods, both preventative and active, including but not limited to (1) barriers and nets, (2) scaling and evacuation of rockfall-prone debris, (3) mechanical reinforcement of rockslopes, (4) monitoring, risk assessment, and warning systems, and (5) avoidance.

It is essential to identify a mitigation strategy that will both economically and safely reduce rockfall risk. Rockslopes from 45º to vertical are often considered for mitigation, but gentler rockslopes may also need mitigation if geologic structure (e.g., bedding, fracture patterns) predisposes the slope to failure. In general, blasting and benching are considered and evaluated if they can achieve a goal of 90% retention of rock in the catchment area with a goal of 99% for free failing rocks (ODOT, 2003). If this cannot be achieved with blasting and benching, then other costlier techniques such as rock bolts and nets can be implemented to increase the retention of falling rocks. This section provides a general overview of these systems and their relevant applications for rockfall mitigation, which are summarized in Table 2-8.

Table 2.8: Summary of the advantages and disadvantages of mitigation methods that can be used to reduce rockfall hazard (Modified from Olsen et al., 2020)

Category	Technique	Description	Advantages	Disadvantages
Slope Modifications	**Scaling**	Removal of dangerous loose or overhanging blocks by hand tools up to small explosives.	-Removes dangerous blocks. -If done correctly minimizes other mitigation methods required.	-Requires constant action and road closures. -expensive and potentially dangerous -requires detail survey to identify features for removal.
Slope Modifications	**Benches**	Horizontal features excavated into rockslope at least 4m thick.	-Reduce erosion rates. -intercept rockfall -Provide maintenance access.	-Requires massive excavation. -not suitable for weak or seeping rock layers.
Slope Modifications	**Blasting**	Blasting is mainly used in the highway construction phase to design the morphology of the rockslope including the gradient.	-Allows for altering of rockslope gradient -Required during the construction phase in many areas to widen road.	-Requires large closures and clean-up. -Potential environmental impacts. -Can cause vibration damage to nearby infrastructure.
Physical Barriers	**Catch Ditches**	Ditches constructed adjacent to rockslopes to catch and stop falling rocks.	-Simple to construct. -Can be implemented along with other methods.	-Not guaranteed to prevent bouncing rocks. -Require constant cleaning and removal.
Physical Barriers	**Attenuator Systems**	A hybrid of rock fences and rock curtains designed specifically for rocks falling from the upper rock slope	-Reduces energy of falling rocks. -By guiding rocks into catch ditches maintenance is substantially easier.	- Should not be used to prevent large blocks. -Require careful thought and design to ensure fallen rocks are fully captured.
Physical Barriers	**Rock Nets, curtains & fences**	Nets or meshes made from steel cable are used to secure block and	-Simple to construct with low maintenance needs.	-Limitations in block size they prevent. -Unsightly, potential negative effects on wildlife.

Category	Technique	Description	Advantages	Disadvantages
		prevent rocks from reaching the highway.	-Work well in conjunction with other methods such as catch ditches or rock bolts.	
Physical Barriers	**Impact walls**	Protective wall barrier consisting of stacked baskets of rocks (gabion) or concrete blocks	-Quick to construct -Permeable (gabion) -Tolerate movement from rock impact	-Often poor aesthetics -Require significant space to construct -Can be costly (concrete)
Rockslope Reinforcement	**Shotcrete**	A cement type material that can be used to fill fractures and provide cohesion between blocks increasing stability.	-Fast and easy to apply. -Reduces water access to rock potentially reducing weathering.	-Requires repetition every few years. -Unlikely to prevent extremely unstable blocks from failure. -Generally poor performance in wet climates
Rockslope Reinforcement	**Rock anchors, bolts & dowels**	Steel rods installed into the rockslope in order to improve stability.	-Can stabilize large blocks in an efficient manner. -Scan be used locally to stabilize individual problem parts of the rockslope.	-Require in depth knowledge of rockslope. -Requires minimum rock strength requirement.

2.6.1 Slope Modifications

2.6.1.1 Rock Scaling

Rock scaling involves removing loose or unstable rock and debris from the face of a rockslope as to prevent it from falling at times where the public may be exposed to the hazard. This technique is often time-consuming, dangerous, and expensive. It requires extensive expertise as it requires identifying the most weakened and precarious rocks (Duffy, 2018). On highly active rockslopes, scaling may need to be repeated every few years (Highland & Bobrowsky, 2008).

Removal may be performed manually (with protected climbers suspended with ropes using handheld equipment to pry away loose debris) or with specialized equipment (cranes, excavators modified to remove debris on lower portions of the rockslope). The techniques used for scaling depend on several factors, such as the size and location of the unstable rockslope materials, accessibility, and safety. Manual removal typically involves physically dislodging debris using hand tools, such as picks, crowbars, etc. These techniques are usually most effective in locations where potential rockfall debris is small and difficult-to-access (Laimer et al., 2022). Removal of rockfall using specialized equipment often involves use of cranes, bulldozers and primarily excavators with sufficient boom length, where the shovel can be used to scrape loose debris from the slope face. These techniques are most effective for large debris that is accessible in the lower reaches of a rockslope. Of course, dislodged debris may pose a hazard for equipment operators downslope.

2.6.1.2 Rock Slope Scaling Practice and Contracting

The current state of practice for rock slope scaling adjacent to highways is documented in NCHRP Synthesis 555, which gathered data from 42 state departments of transportation (DOTs) and two federal offices. Of these, 24 agencies (termed "scaling states") performed sufficient scaling work to respond to the full questionnaire and provide detailed insights into their program administration and design practices. Follow-up interviews with six DOTs (California, Colorado, Idaho, New Hampshire, Ohio, and Tennessee) provided additional depth on program administration, design practices, and long-term performance tracking.

The synthesis identified that most scaling projects are initiated either through programmed project selection processes (approximately 37%) or as emergency responses following rockfall events (approximately 34%). A minority are performed as routine maintenance or as components of broader highway preservation work. Nearly 75% of scaling work is contracted to specialty scalers meeting minimum qualification requirements, with low-bid-only selection practiced in only one state.

With respect to design estimation, nearly all scaling states begin design efforts through roadside visual review, supplemented by maintenance input and, increasingly, remote sensing technologies such as terrestrial lidar scanning and UAV-based photogrammetry (used by approximately 42% of scaling states at the time of the survey). Despite these

tools, scaling states rely heavily on expert judgment for estimating both debris quantities and scaler production rates. Nearly half of respondents indicated that production rates are too variable to specify, while those who did provide estimates generally considered 50–200 square feet per individual scaler hour to be reasonable for general scaling under standard conditions. No standardized national guidelines exist for estimating scaling volumes or production rates, representing a clear gap in the state of practice.

For payment, 67% of scaling states use hours as the unit of measure — either crew hours or individual scaler hours — with volume of removed material used in a minority of cases. Separate bid items for hand scaling versus heavy equipment-assisted scaling are employed by approximately half of scaling states. Temporary roadway and rockfall protection measures vary considerably among agencies, with standard concrete barriers being the most commonly used, though moveable rockfall barriers were identified as the most effective system when used as part of a comprehensive protection approach.

The synthesis also examined scaled slope performance and long-term record-keeping practices. Literature reviewed as part of the synthesis suggests that scaling effectiveness, in the absence of additional mitigation measures, typically spans 2 to 15 years depending on geology, climate, and rock quality — though these durations are based largely on professional experience rather than systematic data analysis. Approximately one-third of scaling states maintain records of post-scaling rockfall activity through maintenance management systems or similar tracking tools, while the remainder rely on informal knowledge retention. Several DOTs, including Tennessee, were beginning to use pre- and post-scaling lidar surveys to measure removed volumes and evaluate slope performance, signaling an emerging trend toward more rigorous, data-driven assessment of scaling efficacy.

The synthesis concludes by identifying several priority research needs: developing data-driven tools to supplement experience-based estimation approaches; preparing scaling frameworks and best-practice guidance; creating decision support tools for slope selection and prioritization; and establishing a national scaling database linking production rates, rock quality metrics, and slope condition data. These gaps are directly relevant to the objectives of SPR864, which seeks to develop quantitative methods for evaluating rockslope improvement outcomes using remote sensing data.

2.6.1.3 Blasting

Blasting is often used in conjunction with both scaling techniques as it (1) breaks larger debris into smaller blocks that can be removed manually, and/or (2) facilitates easier removal of weakened rock mass. All of these techniques can be dangerous and consequently require trained professionals using appropriate practices (Duffy, 2018). The scaling and removal of debris through blasting may, in some instances, cause or even amplify ensuing rockfall hazards as a result of the blast waves propagating through the rock. Blasting is a common approach utilized during highway construction given its efficiency (ODOT, 2001).

2.6.1.4 Benches

Benches (Highland & Bobrowsky, 2008) are horizontal features excavated into the rockslope to (1) reduce erosion rates and tensional forces in the surface rock), (2) intercept rockfall from above reducing kinetic energy, and (3) provide maintenance access (ODOT, 2016). Slopes with benches can be constructed at a steeper angle due to the interception of rockfalls; however, vertical slopes still should be avoided as overhangs and tension cracks can occur. Benches are not suitable for weak rock layers, water seeps or fractured layers to ensure structural integrity. Proper drainage should be installed where necessary.

2.6.2 Physical Barriers

Physical barriers, such as rockfall fences, walls/gabion barriers, netting and rockslope mesh, or catchment systems, all of which are installed to prevent rockfalls from reaching vulnerable downslope locations, such as right-of-way. These systems are typically installed downslope of particularly active rockslope locations and are intended to break the energy of rockfalls, either retaining debris or reducing their mobility and kinetic energy during transport.

2.6.2.1 Catchment Ditches

The most common form of these mitigation systems is rockfall catchment ditches, which provide a relatively soft, low-elevation area aside right-of-way that intercept and retain rockfall debris (Pierson and Chassie, 2001). This system prevents further mobility of rockfall, ensuring that debris does not enter adjacent roadway. To prevent bouncing, catch ditches should be constructed with loose unconsolidated soil that absorbs the energy of falling blocks to prevent bouncing (Highland & Bobrowsky, 2008).

The width and depth of rockfall catchment ditches are often designed based on the activity and geometry (e.g., height and slope) of adjacent rockslopes. For example, larger, steeper rockslopes (or rockslopes with significant rockfall activity) often require deep and wide ditches for sustained function (Badger and Lowell, 1992) due to the increased kinetic energy of falling rocks. Inclined rockslopes require a wider catch ditch due to the lateral movement of failing rocks. Similar to catchment ditches are rockslope benches, which are often applied to large rockslopes with sufficient access, where gentle or insloped benches are placed along the rockslope face as intermediate barriers to prevent modest rockfall from continuing downslope. Catchment ditches require maintenance, often in the form of debris removal, to ensure continued function and efficacy (Shakoor and Admassu, 2010). These systems also require extensive right-of-way, which is not always possible in steep and mountainous terrain or where property boundaries are a limitation.

2.6.2.2 Barriers

Engineered rockfall barriers intercept and deflect rockfall from entering roadways and tend to be either “flexible” or “rigid” systems, classified based on their function and material properties (Volkwein, 2005). Rockfall barriers, typically installed on a rockslope

or at its base, typically consist of a wall or fence made of steel, concrete, and/or other materials that can withstand the force of falling rocks (De Miranda et al., 2015).

Flexible systems tend to consist of elastic elements, such as steel mesh, curtains, or nets that may translate the kinetic energy of rockfalls into elastic, potential energy that deflects or redirects the rockfall trajectory away from vulnerable locations (Hearn et al., 1995, Buzzi et al., 2015). These systems are widely used in locations with limited space as they effectively enhance the depth of catchment systems and can be installed with relative ease. Challenges with these systems include limitations to rockfall sizes that can be deflected, frequent maintenance, and to some level, limited mechanistic design procedures for their application (Hearn et al., 1995). For example, metal cable can anchor large blocks to the slope, while nets or meshes prevent small ($<0.75 m^3$) rocks from failing (Highland & Bobrowsky, 2008). Wire meshes can be implemented in conjunction with rock bolts to securely constrain blocks from failing. Attenuator systems (ODOT, 2016) provide a hybrid solution combining rockfall fences and curtains to guide falling rocks from the upper portions of the slope into a catch ditch.

Rigid rockfall barriers tend to include walls made of reinforced concrete or other gravity wall systems (e.g., jersey barriers, block walls). They function similarly to flexible systems but require more robust and stringent installation practices (e.g., construction access, transport of significant quantities of materials). Rigid barriers have the advantage of being able to resist larger rockfalls and prolonged service, although these systems also require frequent maintenance and inspection (Mentani et al., 2016). Some systems, such as gabion walls, serve as hybrid systems that are more flexible than concrete systems, but less so than rockfall fences (Ma et al., 2020).

In some instances, overhead barriers such as rockfall shelters are constructed in narrow and steep areas where overhead rockfall is persistent and other rockfall mitigation techniques are largely infeasible. These shelters are commonly constructed of reinforced concrete or tunneled through existing rock (Calvetti and Di Prisco, 2012).

2.6.3 Rockslope Reinforcement

When site access allows, the face of a rockslope can be reinforced to increase both its local superficial stability (i.e., against small rockfalls) and overall stability (i.e., preventing wedge failures, rock avalanches, etc.). A combination of techniques may be used for rockslope reinforcement based on a rockslope's specific geologic, hydrologic, climatic, and geometric conditions.

The most common techniques for rockslope reinforcement often include a combination of rock bolts (Li and Stillborg, 1999) and rock mesh/netting (Li 2010). Rock bolts are engineered steel rod elements that anchor weak or loose rock to more competent, less weathered rock mass within the rockslope. These bolts are often grouted to ensure tensile capacity and may be further tensioned to enhance stability (Li and Stillborg, 1999). Rockbolts tend to be used to support surficial rock. Anchors are used for large blocks. In some cases, rock dowels are used without applying tension on installation (Highland & Bobrowsky, 2008). Use of rock bolts often requires appropriate characterization of rockslope structure and strength to ensure it mitigates weaknesses

stemming from fractures, joints, and discontinuities; however, they can be applied to stabilize debris of modest sizes (Bobet and Einstein, 2011). Rockslope mesh or netting is a broader rockslope reinforcement technique as it can span a large area of rock face. Often anchored in locations with sufficient rock mass strength, mesh is primarily effective in stabilizing smaller debris in areas with extensive discontinuities and weathering.

Other surficial stabilization techniques for rockslopes include sprayed concrete (shotcrete) and in some instances, vegetation. Shotcrete provides modest stability against small fragments of rockfall debris after curing by providing a superficial cemented layer (Heltzen, 1979). Shotcrete can also reduce weathering and exposure to the elements, decrease dry ravel, provide resistance to erosion, fill in cracks and other features that allow water to penetrate the slope, and provide a superficial layer of cementation to fractured rockslopes to increase stability. However, shotcrete is rarely used alone (i.e., it is often used with mesh to provide internal tensile strength, Stille et al., 1989) and may have problems in locations that are excessively wet (i.e., poor standup, enhanced weathering) or cold (freeze-thaw causes cracking, weakening). Vegetation may be used to stabilize small debris on rockslopes (e.g., soil) where the slope angles are sufficiently gentle. Vegetation can also serve as a barrier that breaks the energy of rockfalls (Masuya et al., 2009; Dorren and Berger, 2006). However, vegetation can also amplify rockfall hazards - for example, shrubby or woody vegetation can increase rockfall activity through root growth in cracks or through cyclic loading during wind events (i.e., "windrocking"). Surficial rockfall stabilization is largely ineffective under long-term conditions when used in isolation of other mitigation techniques; however, the application of shotcrete is a relatively quick process compared to other approaches such as scaling (Highland & Bobrowsky, 2008).

Drainage may be used to assuage rockslope instability, and to a lesser level, reduce rockfall frequency. Drainage in rockslopes may consist of horizontal drains, weep holes for surficial structures (e.g., in shotcrete) and earth retaining structures (retaining walls), trenches, interceptor drains and surface drainage channels in rockslope benches for removal of surface water. Drainage techniques are often used in conjunction with other mitigation measures to add redundancy to stabilizing and reinforcing systems (Hoek and Bray, 1981).

2.6.4 Seismic mitigation strategies and design guidelines

Findings from investigations following the Canterbury earthquake sequence provided substantial insight into the performance of mitigation techniques during and following seismic events, which have been integrated into:

- *Rockfall: Design considerations for passive protection structures* (Green et al., 2016), which consists of (1) detailed instructions for information gathering and site assessments to guide the design process, (2) guidance on the applicability and appropriate usage of maintenance and mitigation techniques, (3), descriptions of potential modeling approaches, and (4) worked examples as a reference to aid with implementation.

- *Port Hills Rockfalls: Rockfall Mitigation Design Strategy* (Richards, 2012), which provides design strategies to consider seismic effects on mitigation strategies in a risk-based framework.

2.7 ROCKFALL MONITORING AND WARNING SYSTEMS

Rockfall monitoring can serve as a means of mitigating the impact and risk from rockfalls before or shortly after they occur (Abellan et al., 2011). In both scenarios, continuous monitoring and interpretation is necessary. After rockfalls occur, monitoring systems reduce the risk of injury or impact to the traveling public through detecting rockfalls and consequently enabling decisions about appropriate actions (e.g., alarms, road closure, Feng et al., 2021). These systems can be active or passive, the former typically consisting of remote sensing techniques like terrestrial radar or lidar, the latter consisting of cable, vibration or mesh alarms that respond to impact. Remotely-sensed techniques require housing a system on site and having algorithms to continuously process or interpret change (Fanos and Pradhan, 2018; Volkwein et al., 2011). While complex, various commercial remotely sensed systems enable such monitoring and warning after events, although they are expensive and site-specific. Either system can allow for quick responses from emergency personnel to prevent further damage or injury. Alternatively, with sufficient, continuous monitoring, precursors of large rockfall events may enable predictive alarms for emergency actions such as road closure. Such systems can be based on environmental variables (e.g., precipitation), in-situ sensors (e.g., crackmeters), or remotely sensed data (e.g., change from terrestrial radar or lidar).

As an example, Williams et al. (2018) installed a TLS system to acquire hourly scans of a rockslope over a ten-month period to evaluate the frequency and magnitude of rockfalls. This study provides several important insights on monitoring, including:

1. 98% of the rockfall events had a volume less than $0.1 m^3$ compared to previous estimates of 67% from scans spaced further apart in time.

2. Rockfalls, in general, occurred 3 orders of magnitude more frequently than previously estimated using longer interval scans.

3. The more frequent survey interval led to higher cumulative error when estimating the net change over a long period of time.

4. Rockfall scars were found to be spatially continuous by examining the spatial relationship between failures and their relation to subsequent failures captured in this rich dataset.

2.8 OTHER DATASETS

High resolution datasets capturing effects of rockslope improvements are very limited as much of this work is completed and assessed qualitatively without rigorous QA or QC programs. The research team has identified potential datasets that may be utilized in this SPR864, which will be described in this section.

2.8.1 Oregon Sites

For SPR809, the research team collected high resolution lidar data at five sites in Oregon in Fall 2017 and Summer 2018. Some additional scans have been completed at select sites. ODOT's

wizards at Engineering Automation have completed biannual surveys statewide for the last decade. Some of these data can be leveraged at these rockslopes and others in the state to help compensate for the limitations described above. Datasets collected at each site are shown in Table 2-9. Examples of change analysis completed for Eddyville, OR using the Rambo software are shown in Figure 2-3.

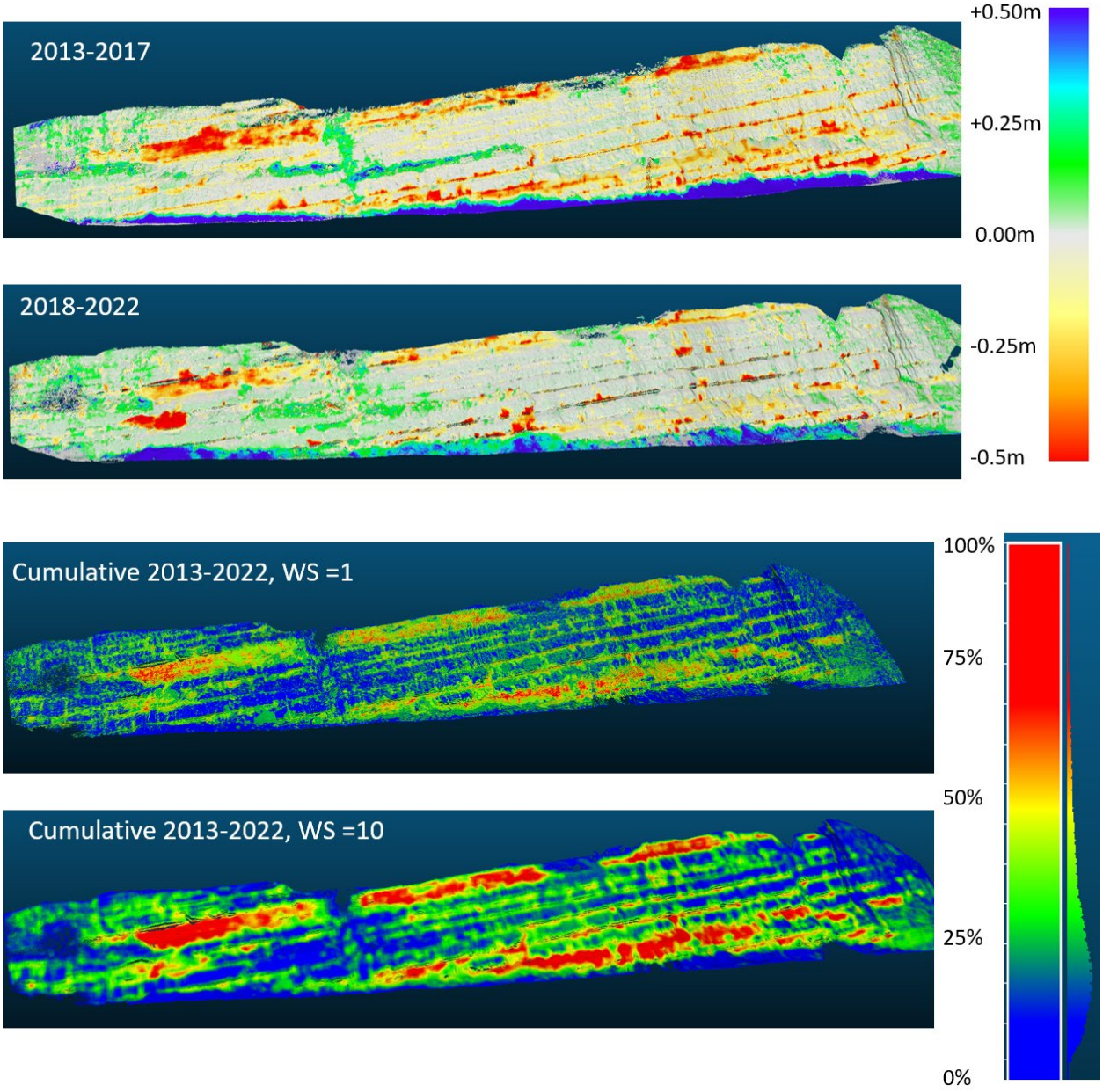

Figure 2.3: Example change analyses for Eddyville, OR from 2013-2022. The top shows the magnitude of change between 2013-2017 and 2018-2022 while the bottom shows the failure rate between 2013-2022 for window sizes of 1 and 10 pixels, highlighting the hotspots on the cliff.

Table 2.9: Summary of MLS and TLS acquisition for each site (expanded from Olsen et al., 2020).

Site	ODOT Region	# of MLS passes	# of TLS scans	Additional Surveys	Notes on applicability and feasibility for SPR864
Canyon Mt	3	5 passes - 3 NB, 2 SB	4	08/2022 (PacTrans)	No mitigation work has been done.
Hogg Rock	2	3 passes - 1 WB, 2 EB	8	N/A	Site is difficult to access logistically and requires a lane closure to perform laser scanning.
Pioneer Mt Eddyville	2	5 passes - 2 WB, 3 EB	5	01/2013, 05, 2013, 08/2022 (PacTrans)	Site is easy to access and captured well in terrestrial laser scans. This slope was blasted in approximately 2010 as part of the new highway alignment project. No data exist prior to the blasting or immediately after. The site can potentially provide data on activity rates over time. Vegetation has significantly increased at site, which limits the area that can be reliably captured with laser scanning
Rowena	4	5 passes - 3 WB, 2 EB	13	N/A	Site is difficult to access logistically and requires coordination with the railroad for a safe location to set up.
Yellow Jacket	3	3 passes - 2 WB, 1 EB	11	08/2022 (PacTrans)	Some scaling work was completed at this site after the SPR809 scans were completed.

2.8.2 New Zealand

GNS Science and other entities in New Zealand have been actively collecting data following major earthquake events. Many of these datasets were utilized on SPR809. Data collections have followed two major events.

- Canterbury Earthquake Sequence (2010/2011). Detailed terrestrial lidar scans have been collected in the Port Hills for the Red Cliffs, Peacock's Gallup, and Wakefield sites. Peacock's Gallup underwent major slope modifications in 2018. Post-earthquake scans conducted by GNS spanned 2011 to 2016. An additional dataset was collected in December 2019 and Fall 2024.

- Kaikoura Earthquake (2016). GNS Science, through their Endeavour program has collected ~10 airborne lidar surveys slopes on Highway 1 where mitigations such as sluicing were conducted. (Sluicing is a technique of dropping substantial amounts of sea water on the rock slope from buckets attached to a helicopter. Note that a challenge with airborne lidar is that data can be limited on steep slopes. Detailed flight logs were captured and can potentially be used to identify the sluiced areas.

2.9 SUMMARY

This literature review has provided the following insights:

1. Rockslope mitigation evaluation is frequently subjective in nature and there are no formal metrics defined. However, there are potential metrics from other work in rockslope assessment that can be applied to evaluate the effectiveness of rockslope mitigation. Improved objectivity would enable enhanced asset management.

2. There are a variety of mitigation techniques for rockfall and combination of techniques is commonly used. In the most critical cases, expensive, proactive mitigation techniques such as scaling may be employed, but method efficacy is largely unquantified.

3. Remote sensing data collected with sufficient temporal frequency, particularly terrestrial or mobile lidar, enables evaluation of change and consequently estimates of rockfall magnitudes and frequencies. This data serves as a basis for estimating potential rockfall hazard and demands for mitigation and maintenance.

4. Direct improvements to the slope are observed such as a decrease in overhanging material, increase in intact rock, decrease in RAI scores or other hazard metrics, and decrease in roughness are observed from preliminary analysis of datasets capturing improved slopes. It is still unclear how long those effects remain following mitigation efforts.

5. While this project is fortunate to have additional datasets to leverage, several challenges exist in those datasets, including:

a. Irregular temporal coverage.

b. Limited baseline datasets prior to mitigation at many sites.

c. Difficulty in tracking down what mitigation work was done and where it was performed specifically. Some information has to be estimated from coarse field notes and observations in point cloud data.

3.0 DATA COLLECTION PROTOCOLS AND SITE CHARACTERIZATION

3.1 OVERVIEW

Several sites that underwent scaling in Oregon were utilized for monitoring (Table 3-1). For visualization, several web-based point cloud viewers have been created for select sites:

- RUMBLE PIT: https://research.engr.oregonstate.edu/lidar/pointcloud/rockfall/RUMBLEPIT/
- Green Spring, OR66 MP13: https://research.engr.oregonstate.edu/lidar/pointcloud/rockfall/OR66MP13/
- Siskiyou Pass, I-5 MP4: https://research.engr.oregonstate.edu/lidar/pointcloud/rockfall/I5SISK/
- Yellow Jacket, HWY 138 MP13: https://research.engr.oregonstate.edu/geomatics/projects/rockfall/spr-809/digital-appendix/yellow-jacket/

3.2 TYPICAL WORKFLOW

The following represents a typical workflow for the repeat surveys at each site. However, the workflow is adapted based on the site conditions as well as issues encountered at the site. Note that earlier surveys prior to the surveys conducted for SPR864 at the sites may have followed different field protocols or used different equipment.

- Perform on site safety briefing and set up survey crew signs. Follow safety protocols outlined in Section 4.5.4.
- Set up GNSS base station on 2 m fixed height pole. Secure legs with rocks or sandbags if windy.
- Set up pivot checkerboard targets on red poles with tripod supports (target height 1.428 m) over GCPs. If a 2 m pole is used, the target height is 2.120 m.
- Securely place clipboard targets at visible locations on the base of the slope. Distribute approximately every 20 m.
- Set up the scanners and securely attach the GNSS mounts to the scanner. Verify the mount is secure, stable, and not tilted or loose.

- Start scanning the site with the Leica P50 and/or Leica RTC360. The P50 must be precisely leveled. With the RTC360, use the level bubble as a guide to get it approximately level, but do not spend more than about 30 seconds leveling it for each position. Regularly ensure that the GNSS unit is securely attached to the scanner (e.g., not rotating off). Also verify that the tripod legs are securely locked in place and embedded in the ground to ensure a stable setup. Settings should be verified for each individual site. Typical settings are:

    - Leica P50 – 270 m range, 0.015 m @50 m resolution. 360-degree field of view, vertical cutoff 65 degrees. Photographic images enabled. Be sure to adjust exposure and other camera settings based on lighting conditions. At sites with busy traffic, double scans may be necessary.

    - Leica RTC360- Medium resolution (165 m range), Vis system enabled, no double scan, images enabled. Be sure that the High Accuracy Tilt compensator is enabled.

- Obtain GNSS data (ORGN+ raw data logging at 1 second increments) during the scan. (Do not start the observation until the scanner is set up and stable).

- During scanning move the pole mounted checkerboard targets to other control points, as necessary so they remain at reasonable distances relative to scanner. Note that the field crew needs to be careful to not let this activity slow down the scanning process. Not every GCP needs be occupied, and targets do not need to be seen in every scan.

- Acquire measurements with the total station. This can often be done simultaneously with the scanning process for efficiency. The following strategy should be used:

    - Enter temperature, pressure, and humidity for EDM corrections.

    - Use 0.0, 0.0, 0.0 for the total station location coordinates and 0.0 m for the height offset.

    - Verify the prism offset height. It is recommended to use the 6.6 ft height on the prism pole which is 2.0117 m. Use the Leica 360-degree prism with the threads on top.

    - Setup over GCPs with the bipod. Use averaging mode with 10 measurements. Perform both direct and reverse.

    - Carefully sight in on targets and obtain coordinates in reflectorless mode. For these use single measurements and obtain direct and reverse measurements. Verify that the sighting is correct between the direct and reverse measurements.

    - Repeat a few measurements on select targets or GCPs to verify the setup remained stable.

- When time permits, capture additional static GNSS observations on control points (approximately 20 minutes).

- Obtaining scans with GNSS coordinates is the most critical activity. The total station and additional GNSS work is important but a lower priority if field conditions do not permit that work.

Table 3.1. Monitoring frequency for sites for rockfall activity in Oregon/Washington.

Site	High-way	MP	ODOT Region	OCRS Zone	MLS datasets	Purpose	TLS surveys	Comments	Approximate Scan Time	#TLS Scans	Scanning notes
Siskiyou Pass	I-5	4-4.5	3	Siskiyou	2018, 2023	Scaling quantification Post-monitoring	6/1/2023 (pre scaling) 10/2023 (post scaling) 6/2024, 11/2024, 10/2025	Scaling in Summer 2023.	½ day	~13	P50 360 scan: GNSS
Green Spring	OR66	13-14	3	Siskiyou	2018, 2020	Scaling quantification Post-monitoring	5/31/2023 (pre scaling) 10/2023 (post scaling), 6/2024, 11/2024, 10/2025	Scaling in Summer 2023.	½ day	~35	RTC360 (high) GNSS only. Ideal to get one P50 at each end for QC.
Yellow-jacket	US HWY 138	10-11	3	Cottage Grove - Canyonville	2017 2018 2020	Baseline rates Scaling quantification Post-monitoring	11/7/2017, 10/2/2018,(pre-scaling) 08/2022 (post scaling) 10/2023, 11/2024, 10/2025	2017 and 2018 data from SPR809. Scaling work was completed after the SPR809 scans were completed.	½ day	11 (P50) 15 (RTC360)	RTC360 GCPs, targets, TS15 GNSS
Eddyville	US HWY 20	16 – 25	2	Oregon Coast	2017 2018 2020 2023	Can potentially provide data on activity rates over time after blasting.	01/2013, 05/2013, 12/8/2017, 9/10/2018, 2018, 08/2022, 10/2023, 11/2024,	See note 1 below.	½ day, day trip	~10 RTC360 or 5 P50	RTC360 GCPs, targets, TS15, GNSS

Site	High-way	MP	ODOT Region	OCRS Zone	MLS datasets	Purpose	TLS surveys	Comments	Approximate Scan Time	#TLS Scans	Scanning notes
							11/2025				
Rowena	I-84	74-76	4	Columbia River East	TBD 2017 2018	Baseline Rates. Comparison to SR14 MP73	11/7/2017, 10/2/2018	Site is difficult to access logistically and requires coordination with the railroad.	N/A	13	N/A
SR14 MP73	SR-14 (WA)	73-73.5	N/A		No MLS data	Scaling quantification Monitoring	2/2022 (Pre-scaling) 8/2022 (Post-scaling) 10/2023, 11/2024 10/2025	Similar geology to Oregon side of the Gorge.	½ day- 1 day. Overnight.	30RTC360 or 20 P50	GCPs, targets, GNSS
Canyon Mountain	I-5	95-98	3	Cottage Grove - Canyonville	2017 2018 2020 2023	Baseline rates	12/6/2017, 8/3/2018	No mitigation work has been done. Lower priority.	N/A	4	N/A

1. This slope was blasted sometime around 2010 as part of the new highway alignment project. No data exist prior to the blasting or immediately after. Vegetation has significantly increased at site, which limits the area that can be reliably captured with laser scanning.

3.3 SISKIYOU PASS

3.3.1 Site Geology

The geology of the Siskiyou Pass area has been described in detail by Bestland (1987), and the following description is largely drawn from that work. The geology of the broader region has been mapped by Sherrod and Smith (2000). The Siskiyou Pass area exposes rocks belonging to the base of the Tertiary volcanic sequence of the Western Cascade Range in southern Oregon. The dominant stratigraphic unit at the site is the Oligocene Colestin Formation, a sequence of nonmarine volcaniclastic and pyroclastic deposits and lava flows. The formation was deposited in an alluvial apron setting adjacent to volcanic centers situated to the east along the Oligocene Cascade arc, and its members reflect repeated episodes of volcanism separated by periods of quiescence and weathering.

Near Siskiyou Pass, the Colestin Formation is subdivided into nine sub-members that collectively reach a maximum thickness of approximately 1,600 m. The lower sub-members of the formation are contained within a northeast-southwest-trending graben bounded to the north by the Siskiyou Summit fault, a major northeast-southwest-trending structure that offsets Cretaceous and Tertiary rock outcrop patterns by as much as 15 km and brings the Colestin Formation into contact with basement rocks of the Klamath Mountains Province.

The lowermost member of the Colestin Formation (member Tcc; See Sherrod and Smith, 2000) consists of a poorly consolidated, poorly sorted basal fluvial conglomerate resting with angular discordance on the Cretaceous Hornbrook Formation, overlain by a matrix-supported volcanic breccia interpreted as a lahar. Overlying this is a substantial pyroclastic flow sequence, the tuff of Chocolate Falls (member Tcft), which reaches up to 250 m in thickness and consists predominantly of welded crystal and pumice tuff with plagioclase crystals and yellow pumice lapilli. Basaltic and andesitic lava flows of member Tclb, consisting largely of plagioclase and pyroxene-phyric basaltic andesites, are interbedded with and overlie the tuff of Chocolate Falls, capping ridges and forming dip slopes in the upper Cottonwood Valley area.

The upper part of the Colestin Formation, well exposed in roadcuts along Interstate 5 and Highway 99, comprises several members recording distinct depositional episodes. Member Tcl consists of volcaniclastic units, including a basal white pumice lapilli tuff, overlying tuffaceous sandstones and siltstones, bedded epiclastic sandstones, and an unconsolidated andesitic boulder breccia capped by a prominently developed lateritic paleosol. Member Tcs, consisting of volcanic epiclastic sandstones, conglomerates, and lahars of andesitic and basaltic composition, is also well exposed in roadcuts along Interstate 5 and Highway 99 at Siskiyou Pass. Many matrix-supported lahar units within this member grade upward into clast-supported, discontinuously bedded, pebbly conglomerates and granular sandstones interpreted as flood flow deposits, representing a flow regime intermediate between laharic debris flow and normal fluvial transport. A distinctive white crystal tuff (member Tct), up to 10 m thick, is sandwiched within the volcaniclastic deposits of member Tcs. The uppermost Colestin member (Tcts) consists of approximately 250 m of tuffaceous sandstones, siltstones, and intercalated vitric and pumiceous tuffs, and includes a lacustrine sequence exposed along Beacon Rock.

The Colestin Formation is overlain by the Roxy Formation, which consists predominantly of basalts and andesites forming prominent dip slopes and cliff-forming ridges around Pilot Rock. The contact between the two formations is recognized at the base of the prominent cliff-forming Roxy basaltic lava flows overlying the white tuffs of member Tcts, a boundary placed at a stratigraphically higher position than that mapped by other researchers. Numerous landslides originate at the contact between the tuffaceous sandstones of member Tcts and the overlying Roxy basalts. Quaternary landslide deposits are present in the area and are mapped as such by Sherrod and Smith (2000).

3.3.2 Data Collection

The Siskiyou Pass site underwent scaling in July/August 2023. The survey work at Siskiyou Pass consists of approximately 11 TLS scans (Figure 3-1) with the Leica ScanStation P50 & Leica GS14 GNSS mounted above the scanner (Figure 3-2). For safety reasons, scans were completed on the hillslope above I-5 so that the field crews were not in proximity to traffic. Additionally, no targets are utilized at this site given there are no safe locations to set them near the rockslope. At each location a medium resolution 360° scan (Resolution Setting = 6.3mm@10m ~2 min) without images is completed followed by focused ~180° scans at higher resolution on cliff with photographic images (0.02 m at 100 m sampling ~12 min). Most scans are completed with 270 m range for the EDM setting; however, at a few locations in the center with a wide viewpoint of the site a 570 m range 360-degree scan (6.3 mm at 10 m) was captured instead. For the 11/2024 survey, only 8 scan positions could be completed due to wet, foggy weather preventing access to the southern portion. While most of that section of cliff was visible from the other scans, there are still some data gaps that were filled in from the southern scans, which provided a different perspective looking northward. The GNSS base was set up on a utility box (Figure 3-3 and Figure 3-4) in a parking area with access to the slopes. The OCRS Siskiyou Pass Zone was used for the coordinate system. Appendix B provides more details on the survey plans.

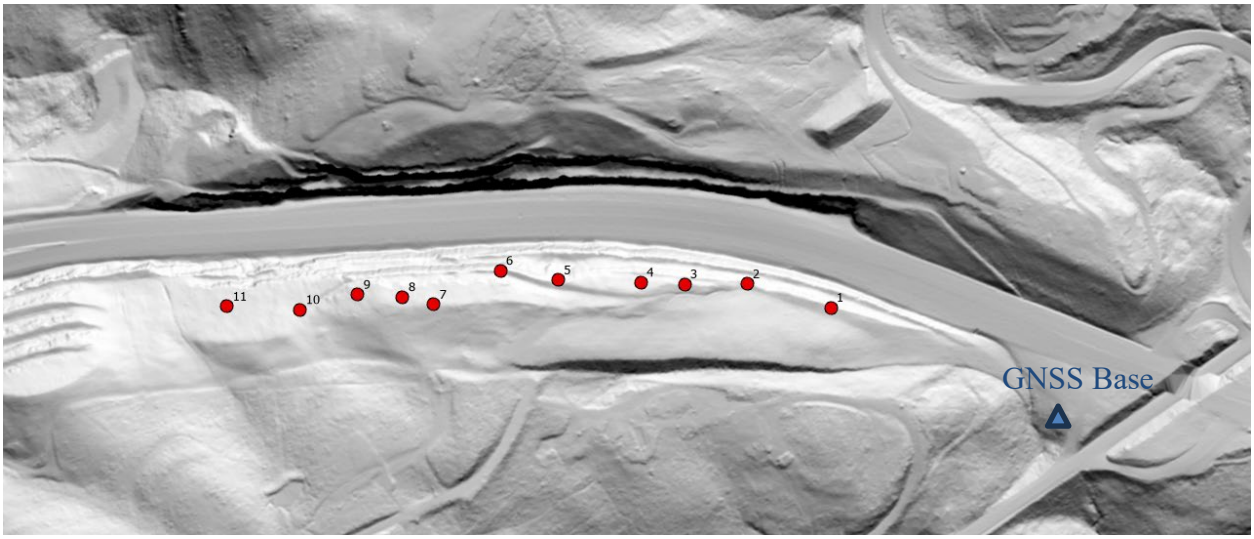

Figure 3.1: Site plan of the Siskiyou Pass showing position of the GNSS base and the TLS locations.



Figure 3.2: Example TLS setup at the Siskiyou Pass field site.



Figure 3.3: GNSS Base Station setup at the Siskiyou Pass field site.



Figure 3.4: Close-up of the GNSS base setup location.

3.4 GREEN SPRING, OR66

The Green Spring site, located near MP13 on OR66 was also scaled during the August 2023 timeframe. Data at the Green Spring site was collected with the Leica RTC 360. Scans were spaced approximately 25 m apart behind the guardrail and in pullouts (Figure 3-5). Some locations require careful coordination as there is limited working space behind the guardrail. Scans were completed with the high tilt accuracy enabled as well as at high resolution. Periodic medium resolution scans were conducted at a few of the scan locations to provide longer range in addition to the high-resolution scan from that location. In areas of dense vegetation, only medium resolution scans were performed.

Approximately 36 scans are required for this site. A custom GNSS mount (Figure 3-6) was used at this site (offset of 0.090 m for the 3D printed prototype in May 2023 and 0.1125 m of the aluminum mount with quick release in future surveys). This site has insufficient safe working space to set targets or control points. The GNSS base station was set up in the gravel lot to the west of the site in front of the "eyes" graffiti (Figure 3-7). Later, an ODOT survey control monument was found at the site and used as the base station setup location. The OCRS Siskiyou Pass was used for the coordinate system. Appendix B provides more details on the survey plans.



Figure 3.5: Scan setup locations at the Green Spring field site (OR66 MP13.2).



Figure 3.6: Example RTC360 setup with the prototype custom GNSS mount.



Figure 3.7: Initial GNSS base station setup location.

3.5 YELLOW JACKET CREEK

The Yellow Jacket site contains one rockslope approximately 350 m long, between 30-60m high that was surveyed using MLS and TLS techniques (Figure 3-8). Heavy vegetation is used to constrain the eastward and westward extents of the survey. This site is located within the Cottage Grove – Canyonville OCRS which was used for GNSS acquisition and subsequent lidar projection. The GNSS base was set up over a stake with a 2m fixed height tripod pole and data was logged at a 1" interval. In some of the surveys, static GNSS data were obtained for GCPs.

Additionally, a total of five control points were surveyed at this site using a combined GNSS/total station network. A single total station setup was utilized due to the close proximity of the control points allowing all five to be surveyed from a single setup. GNSS antenna heights were 0.1125 m for the RTC 360 and 0.1175 for the P50. Scan targets were setup with the 1.3 m red poles\tripods on control points for relevant scans. (e.g., set up for CP01 02 and 05 at first and then move to CP03 and CP04 as the scanning progresses eastward farther from CP01 and CP05). Clipboard targets are placed along the cliff base. Prism & rod measurements were obtained on control points, (averaging mode with 10 direct, 10 reverse on each control point). Reflectorless measurements were obtained for most clipboard targets. In several surveys, one direct and one reverse measurement was obtained.

SPR809 (2017/2018) and PacTrans (2022) procedures: For the mobile lidar collection for this site, two passes were completed in the westbound lane and a single pass was completed in the eastbound lane between mileposts 10-11. As shown in Figure 3-8, a total of 11 terrestrial lidar scans were performed using the Leica P40 at a spacing of ~30-35 m apart.

SPR864 (2023+ procedures): Scan behind barrier, with RTC in medium resolution, spaced at about 15 m apart, so approximately 24 scans in total for site. On the east side where cliffs are taller, a few P50 scans were performed to capture higher portions of the slope. These can be obtained at the same time as the RTC scans. Appendix B provides more details on the survey plans.

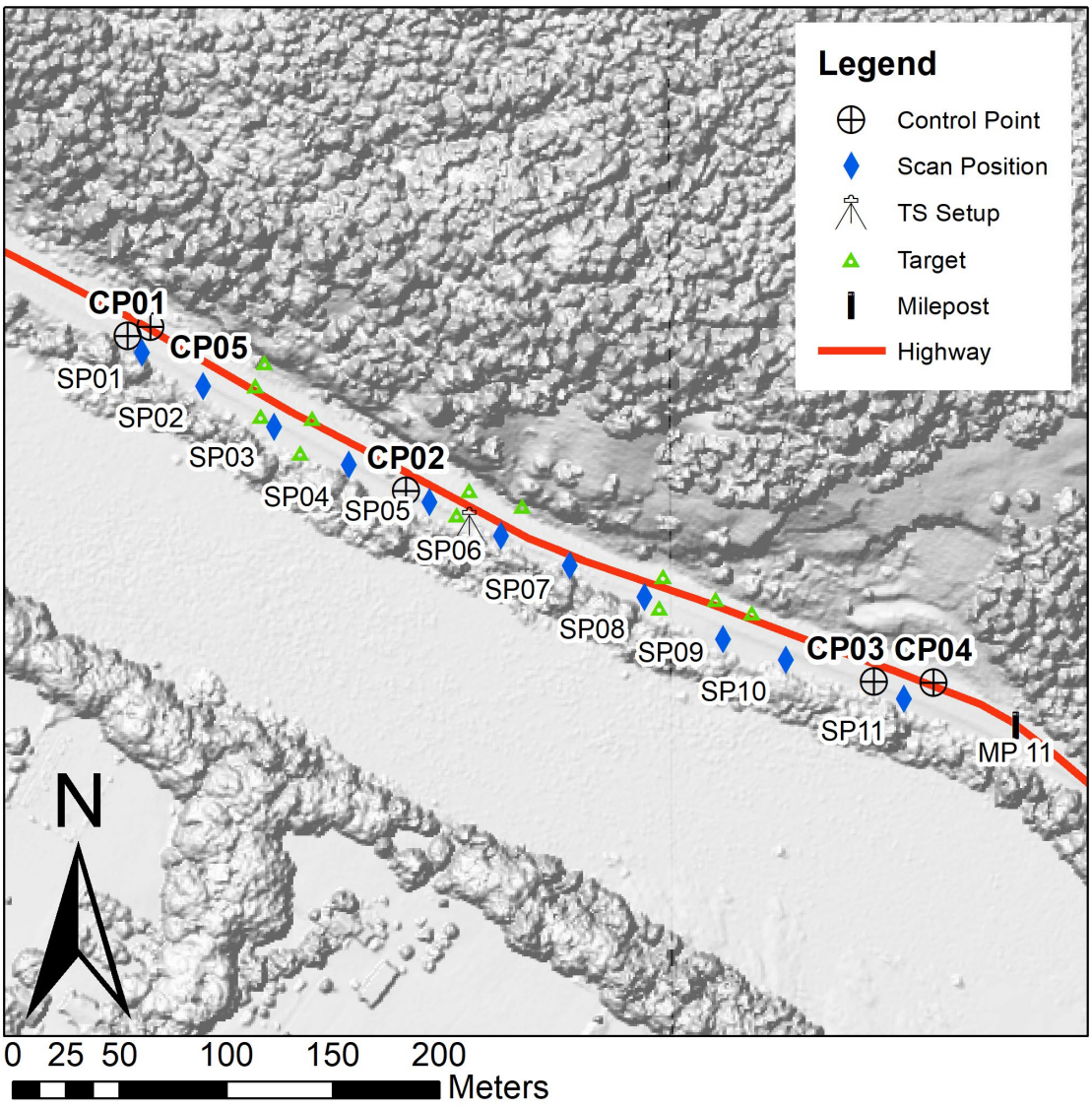

Figure 3.8: Site plan of Yellow Jacket showing position of control points, TLS scan positions, TS setups and targets.

3.6 EDDYVILLE

The rockslope furthest east on the older section of the highway US-20 (Figure 3-9 and Figure 3-10) was surveyed using TLS, UAS and mobile lidar. This site is located within the OCRS Oregon Coast zone which was used for GNSS acquisition and subsequent lidar projection at this site. One total station setup was adequate at this site due to the short and relatively straight nature of the road. Appendix B provides more details on the survey plans.

SPR809 (2017/2018) and PacTrans (2022) procedures: At the TLS/UAS rockslope, a total of 4 control points were surveyed using a combined GNSS/Total station network. Figure 3-10 shows the setup used for the terrestrial lidar rockslope as well as the location of the control points throughout the rest of the site. A total of 5 terrestrial lidar setups were completed using the Leica P40.

SPR864 procedures: For efficiency the RTC360 was used in future surveys and spaced closer (~20 m) resulting in about 20 scans. Place clipboard targets along the cliff base for scanning. You can also set up other targets on the tripods at random locations and move those. For those not set up on a control point, no need to precisely level, but they do need to be stable. Commence TLS scans at the rock slope at the East side prior to the split in the highway for Crystal Creek Loop through Eddyville. ~250m section from grass on opposite side of road. Obtain GNSS coordinates for each scan. Tag CP02, CP03, CP04 and the new control points with GPS- 5-minute occupations when possible.



Figure 3.9: Overview of site plan of Eddyville showing position of control points and TLS scan positions.

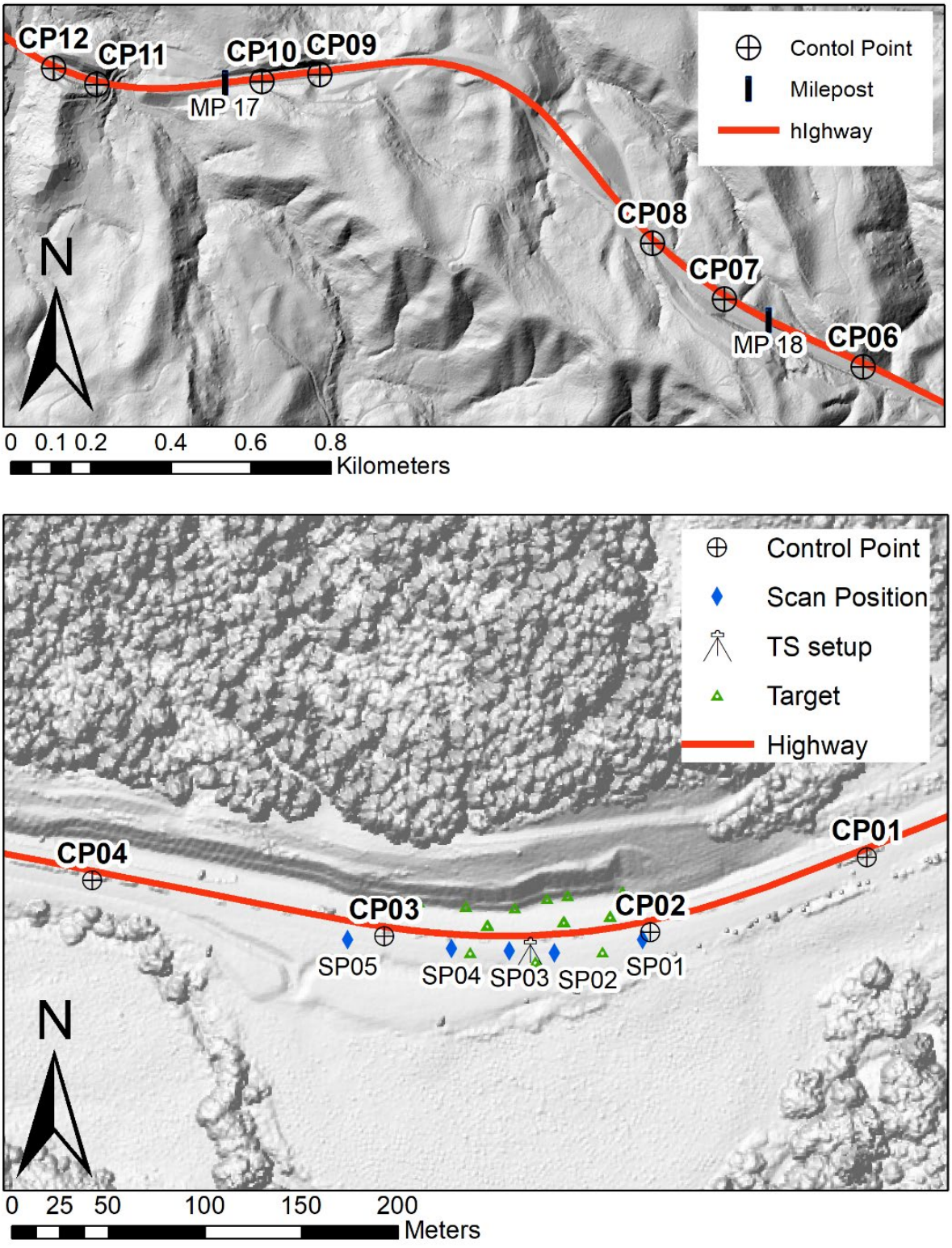

Figure 3.10: Site plan of Pioneer Mt Eddyville showing position of control points, TLS scan positions, TS setups and targets.

3.7 SR14 MP73, COLUMBIA RIVER GORGE, WASHINGTON

3.7.1 Site Geology

The geological characterization of the SR14 MP73 site draws primarily on a detailed geotechnical investigation conducted by Fish and Newman (2021) on behalf of the Washington State Department of Transportation (WSDOT). That investigation included geologic site reconnaissance and field mapping, test pit explorations, geophysical seismic refraction surveys, and three-dimensional point cloud acquisition using an unmanned aerial vehicle, providing a comprehensive basis for the site description presented here.

The SR14 MP73 site is located along the Washington side of the Columbia River Gorge in Klickitat County, within the South Cascades physiographic province. The slopes are cut into basalt flows of the Roza Member of the Wanapum Basalt, a middle Miocene unit of the Columbia River Basalt Group (Fish and Newman, 2021). The Roza Member at this location is composed of fine- to medium-grained basalt that is dark gray when fresh, weathering to light brown and yellowish gray on exposed surfaces. The formation was emplaced as low-viscosity flood basalt flows that moved through the ancestral Columbia River Gorge, and the resulting rock mass preserves the internal cooling structure characteristic of thick, laterally extensive lava flows of this type. At the project location, the basalt flows dip gently to the southeast and do not appear to be tilted or overturned, consistent with the broadly subhorizontal attitude of the Columbia River Basalt Group in this portion of the Gorge (Fish and Newman, 2021). The site is located near the southern margin of the active Yakima fold belt, and a series of northwest-southeast-trending faults with suspected Quaternary offset are present in the broader project vicinity, though the basalt flows exposed in the subject slopes do not display evidence of significant tectonic disruption at the outcrop scale.

The exposed rock mass at SR14 MP73 is defined by two principal structural domains reflecting the internal cooling architecture of the Roza Member flows: a lower colonnade and an upper entablature. The colonnade forms near-vertical bedrock cliffs in the lower portions of the slopes and is characterized by well-developed, regularly spaced columnar jointing produced by thermal contraction during cooling. Column dimensions vary along the exposure, ranging from approximately two to eight feet in width and five to fourteen feet in height, and the columns exhibit a predominantly hexagonal cross-section in plan view (Fish and Newman, 2021). The columnar joints range from closed and tight to open and dilated in aperture, and from smooth-planar to moderately rough-undulatory in surface texture. Many columns are further subdivided by subhorizontal cross-joints that produce prismatic column segments, and locally, gently to moderately inclined fractures of limited persistence cross-cut individual columns in orientations that are geometrically capable of facilitating sliding failure of overlying segments. A subordinate set of highly persistent subvertical fractures, distinct from the columnar cooling joints and generally smooth-planar to smooth-undulatory in character, is also present within the colonnade. The entablature, which crops out in the upper bedrock cliffs, exhibits a markedly different structural fabric. It is composed of smaller, pseudo-hexagonal columnar blocks in a chaotically jointed, randomly oriented arrangement with more closely spaced fractures than the colonnade below. Joints within the entablature are predominantly closed and tight. The contact between colonnade and entablature reflects the original thermal gradient within the cooling flow, with the

colonnade representing slow, organized cooling from the base and the entablature representing more rapid and irregular cooling in the flow interior.

Weathering at the site is variable and reflects both the mineralogical susceptibility of the basalt and the influence of preferential fluid pathways along joints and flow contacts. Fresh to slightly weathered rock predominates across most of the colonnade exposure, with individual blocks appearing gray-black on recently fractured surfaces. Moderate weathering is concentrated in discrete zones, particularly along the base of the entablature, where erosional overhangs and associated talus cones indicate that differential weathering of these zones has been an active process in slope denudation. The colonnade basalt weathers to light brown and yellowish gray on exposed faces, and the entablature in moderately weathered zones is notably lighter in color than the surrounding fresh rock. No active groundwater seepage was observed at the slope face during the geotechnical investigation, though maintenance records indicate that surface water is episodically present on the slope, suggesting that transient moisture infiltration along joints contributes to weathering and may play a role in the seasonal timing of rockfall, which is reported to occur predominantly during fall and winter months (Fish and Newman, 2021). Uniaxial compressive strength testing of intact basalt specimens from the site yielded values of 16,116 psi and 34,989 psi, reflecting the inherent variability in intact rock strength associated with differences in vesicularity, grain size, and degree of weathering across the flow (Fish and Newman, 2021). At the rock mass scale, the dominant control on mechanical behavior and rockfall potential is the discontinuity network rather than intact rock strength, with the colonnade joint geometry governing block detachment through the release of prismatic and columnar segments along pre-existing cooling fractures and subhorizontal cross-joints.

3.7.2 Data Collection

Several surveys have been completed at a site located in Southern Washington on SR14 near Milepost 73 (SR14MP73). Table B-5 summarizes the data collected. This site is across the Columbia River Gorge from the Rowena site and has similar geology. The first scan survey was completed on February 11, 2022 days before the scaling operations started. The second survey was completed in August 15, 2022. While there is some erosion signal present in the data, the bulk of the change is due to scaling operations, which removed approximately 2,800 m^3, affected a surface area of 5,600 m^2 (21%) of the slope. Baseline data to quantify rockfall activity rates before the improvements are not available; however, erosion rates estimated from the Rowena site in SPR809 can serve as an indicator of the "baseline level" for comparison. A limitation to this assumption is that the Rowena site faces northward and the SR14MP73 site faces southward, resulting in differences in sun exposure.

The pre scaling survey was completed with a Maptek I-Site Scanner. The 2022 post scaling survey used a Leica P50 scanner. The 2023 scans were collected with the Leica RTC 360. GNSS data and total station work was completed on control points at the site. For subsequent surveys, targets on poles should be mounted atop of control points and moved as the scans progress. Scans will be completed with RTC scans spaced 10-15 m apart. The length is approximately 700 m so it requires approximately 45 scans with the RTC (Figure 3-11).

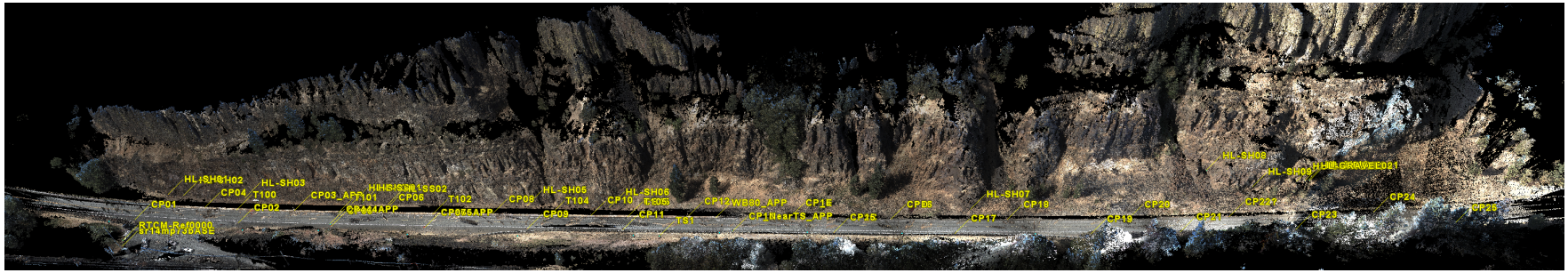

Figure 3.11: Control point plan of SR14 MP73.

4.0 RUMBLE PIT - ROCKSLOPE UNDERSTANDING OF MORPHOLOGICAL BEHAVIOUR AND LONG-TERM EVOLUTION- PLACE OF INSTABILITY AND TRANSFORMATION

A rockfall observatory site was established in order to monitor scaling effectiveness under controlled conditions. This site was called the Rumble Pit (Rockslope understanding of morphological behavior and long-term evolution- place of instability and transformation). Several quarries in the state were reviewed as candidates, and the site was selected based on:

1. Relevant geology- Predominately basalt sites were of interest. Sites were identified to have different predominate RAI classes.

2. Availability for safe access and use by the research team. ODOT owns the site.

3. Security of the site for safety of operations as well as ensure the site is undisturbed.

4. View/perspective of the site to ensure that data can be collected efficiently to observe activity rate and morphological changes on the site.

5. Cell phone/data signal to enable communication as well as data upload from an onsite weather station.

6. Proximity to research team at OSU so that frequent measurements can be obtained with minimal budget.

In consultation with ODOT, the research team explored several candidate sites. After field visits and deliberation, Iron Mountain Quarry, located in Newport Oregon was selected as the research site after approval was given by ODOT.

4.1 SITE GEOLOGY

The Rumble Pit site, located north of Newport in Lincoln County, Oregon, occupies the footprint of the Iron Mountain Quarry. The site and its geological setting have been described in prior literature, including an aggregate resources assessment by Wyttenberg et al. (2002), which identified the nearly 50-acre property as containing approximately 5,000,000 cubic yards of fine-grained basalt of very good quality. The present investigation draws upon that prior characterization as well as the foundational petrological and geochemical work of Snavely et al. (1973), whose study of Miocene tholeiitic basalts of coastal Oregon and Washington established the broader geological framework within which Iron Mountain is situated.

The site exposes the Cape Foulweather Basalt, a middle Miocene tholeiitic unit that Snavely et al. (1973) defined and mapped across a series of coastal vent complexes extending from Seal Rocks northward to Cape Falcon. Iron Mountain itself is described in that study as a small stock

of Cape Foulweather Basalt, representing a localized intrusive center in which magma rose through and solidified within the surrounding Astoria and Yaquina Formations approximately 2 km northeast of Yaquina Head. As mapped on the Geologic Map of the Yaquina and Toledo Quadrangles (Snavely et al., 1976; USGS Miscellaneous Investigations Series Map I-867), the intrusive rocks at the site are designated unit Ticf, representing the intrusive facies of the Cape Foulweather Basalt, which includes dikes, sills, and irregular intrusive bodies of the same composition as the associated extrusive rocks. The cross-section reproduced from that map (Figure 4-1) illustrates the structural relationship of the Iron Mountain stock to the surrounding sedimentary units, showing the Ticf body intruding upward through the Astoria Formation (Ta) and the Yaquina Formation (Tn), with the intrusion reaching elevations of approximately 2,000 feet above sea level at its exposed crest.

As a small stock, Iron Mountain represents a volcanic neck or plug in which the originally ascending magma did not breach the surface to produce extensive extrusive sequences but instead cooled and crystallized within the vent conduit. This geometry is reflected in the well-developed radiating columnar joints and vesicular margins noted at the site by Snavely et al. (1973), features that are characteristic of relatively rapid, near-surface cooling within a confined intrusive body. The discordant contact relationships with the enclosing sedimentary formations are consistent with forceful emplacement along a north-trending crustal fracture zone that Snavely et al. (1973) proposed as the primary structural control on Miocene coastal volcanism in this region.

The Cape Foulweather Basalt at Iron Mountain is petrographically distinguished from the other two Miocene coastal basalt units by the presence of ubiquitous but sparse large labradorite phenocrysts, approximately An55 in core composition, which are typically up to 2 cm in length and constitute less than one percent of the rock by volume. The groundmass consists of plagioclase, augite, pigeonite, olivine, opaque minerals, and basaltic glass. Chemically, the unit is characterized by lower SiO2 content and higher total iron, TiO2, and P2O5 relative to the older Depoe Bay Basalt, yielding a quartz-normative tholeiitic composition that is uniform across analyzed samples from the type locality and correlative outcrops along the coast (Snavely et al., 1973). Fresh surfaces of the basalt are dark gray to grayish black, weathering to medium gray or brownish gray; the rock is dense and aphanitic to fine-grained in texture.

The geological significance of the Cape Foulweather Basalt, and by extension of the Iron Mountain stock, lies in the consanguinity that Snavely et al. (1973) demonstrated between this coastal volcanic unit and the late-Yakima petrographic type of the Yakima Basalt erupted from fissure vents on the Columbia Plateau more than 500 km to the east. Despite the extraordinary separation between their source areas, the coastal and plateau units are virtually identical in stratigraphic position, chemical composition, and lead and strontium isotopic ratios, a correspondence that the authors interpreted as evidence for a regional mechanism of magma generation operating across a broad segment of the Pacific Northwest during the middle Miocene.

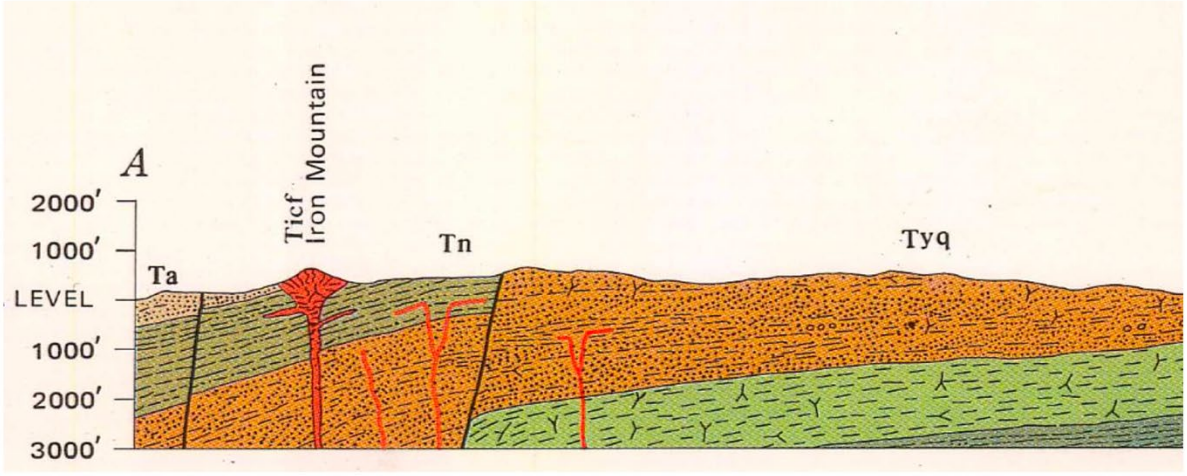

Ticf — Intrusive basalt — Dikes, sills, and irregular-shaped intrusive bodies; composed of slightly porphyritic, massive or columnar-jointed tholeiitic basalt, breccia, or peperite; related to Cape Foulweather Basalt on the basis of petrography and chemical composition (Snavely and others, 1973)

Ta — ASTORIA FORMATION (middle Miocene) — Thick- to thin-bedded, very fine to medium-grained, micaceous, carbonaceous, arkosic marine sandstone and sandy siltstone; commonly fossiliferous; contains calcareous ledges and concretions, dacitic tuff beds ½ to 4 m thick, and basaltic sandstone interbeds; sandstone and siltstone commonly show bioturbation; molluscan faunas are assigned to the Temblor Stage[1] of Weaver and others (1944) and foraminiferal assemblages are referred to the Saucesian Stage of Kleinpell (1938)

Tn — NYE MUDSTONE (lower Miocene) — Dark-olive-gray massive organic-rich marine mudstone and siltstone; contains sandy siltstone and very fine grained sandstone in upper and lower parts; dolomitic and calcareous concretions and lenticular beds up to ½ m thick occur locally; fish scales and Foraminifera abundant; north of Yaquina Bay contains thick interbeds of very fine grained micaceous carbonaceous arkosic sandstone; molluscan faunas are assigned to the upper part of the Blakeley Stage[1] of Weaver and others (1944) and foraminiferal assemblages are assigned to the Saucesian Stage

Tyq — YAQUINA FORMATION (upper Oligocene and lower Miocene) — Thick- to thin-bedded sandstone, glauconitic sandstone, conglomerate, and tuffaceous siltstone of deltaic origin; locally contains thin coal and ash beds; sandstone is fine to coarse grained, fossiliferous, and commonly crossbedded, foreset bedded, and has scour-and-fill structures; conglomerate and sandstone contain abundant clasts of pumice and dacitic volcanic rocks; contains molluscan faunas referred to the upper Blakeley Stage[1] of Weaver and others (1944) and foraminiferal assemblages of the Zemorrian and lower Saucesian Stages of Kleinpell (1938)

Figure 4.1. Geologic cross-section showing the Iron Mountain stock (i.e., the current "Rumble Pit" site; unit Ticf, intrusive Cape Foulweather Basalt) intruding through the Astoria Formation (Ta) and the Yaquina Formation (Tn) in the vicinity of the Rumble Pit site, Lincoln County, Oregon. Cross-section A–A' reproduced from Snavely et al. (1976), Geologic Map of the Yaquina and Toledo Quadrangles, Lincoln County, Oregon, USGS Miscellaneous Investigations Series Map I-867. (Not to scale).

4.2 Rock Mass Characterization

The exposed rock mass at the Rumble Pit site exhibits characteristics consistent with a near-surface intrusive stock, reflecting the thermal and structural complexity expected at a former volcanic vent center. Field observations across the quarry reveal a dark gray to black, dense, fine-grained basalt that is generally of good to very good quality, with the high-strength properties typical of the Cape Foulweather Basalt at this locality.

The dominant structural feature governing rock mass behavior at the site is the jointing architecture inherited from the cooling history of the stock. Discontinuity character varies spatially across the quarry face, with closely spaced, steeply dipping to sub-vertical joints producing a platy to columnar fabric in some portions of the exposure, and a radiating, fan-like joint pattern in others. The latter geometry is interpreted as reflecting a convex cooling front at a flow lobe margin, where joints rotated to maintain perpendicularity to a curved isotherm during solidification. Other portions of the face transition to a blockier, more widely jointed fabric, differing markedly from the tightly spaced columnar zones.

This spatial variability in discontinuity structure has direct implications for rockfall source characterization across the site. Toppling and columnar detachment are the dominant anticipated failure modes where sub-vertical joints prevail, while wedge and planar sliding mechanisms become kinematically more probable where joints rotate to moderate dip angles intersecting the free face. The heterogeneity of the rock mass underscores the need for spatially resolved hazard characterization rather than a uniform treatment of the exposure.

4.3 PREPARATORY WORK

In the last half of September 2023, the research team cleared vegetation and obstructions at the base of site as well as a yellowjacket wasp nest (Figure 4-2). A Hobo weather station was installed to capture local meteorological data including temperature, pressure, dew point and rainfall at the site (Figure 4-3). These same systems are being used on the ODOT debris flows project. Lastly, desired locations for scaling were identified.



Figure 4.2. Examples of vegetation obstructions to be cleared at the site.



Figure 4.3. Weather station installed at the site.

4.4 BASELINE SURVEY (9/29/2023)

In conjunction with the baseline survey, the research team will prepare the site for repeat monitoring (Figure 3-5), including:

- Install ground control points at the site (initial survey only). Stamp reference mark on top of GCPs. GCPs 0 and 3 will be brass cap monuments while the other GCPs will be orange cap nails.

- Put wood stakes with flagging at scanning and total station locations so that approximately the same location is occupied each survey so that scans have a similar viewpoint throughout the monitoring period. Use different colors of flagging for each equipment type.

The team will then obtain baseline scans at the positions indicated in Figure 3-5. They will also obtain total station measurements on targets to help improve the relative accuracy between scans. Several additional people from the team will be present to be trained on the workflow for the site to ensure a variety of people are available for the site to ensure consistent data collection procedures are followed throughout the process.

4.5 SURVEYS

A total of 21 surveys were completed at the Rumble Pit site (Table 4-1). Generally, the survey plan was followed; however, some deviations were made, primarily due to field conditions.

Table 4.1. Summary of data acquisition at the Rumble Pit site.

Date	Time (days)	Additional data collection	Notes
9/29/2023	-42	GNSS data at scan origins.	Baseline survey. GNSS data collected at each scan origin.
11/9/2023	-1	—	Rainy weather. Some loss of laser scan data on cliffs due to wet surface. Starting with this survey, the scanning plan was adapted. To improve coverage, the P50 resolution was increased and a long range scan was performed. Additionally, a prism mounted to the scanner to provide higher relative accuracy positioning compared with GNSS.
11/10/2023	0	Gigapan, GNSS baselines	Immediate post scaling scan.
11/11/2023	1	UAS	Missing high resolution P50 scan.
11/13/2023	3	—	—
11/15/2023	5	—	—
11/17/2023	7	—	—
11/24/2023	14	UAS	—
12/1/2023	21	—	—
12/8/2023	28	—	—
12/21/2023	41	—	—
1/19/2024	70	—	Windy. P50 scans could not be completed with level compensator. Checkerboard targets were not used.
2/16/2024	98	—	Windy. P50 scans could not be completed with level compensator. Checkerboard targets were not used.
3/14/2024	125	—	—
4/30/2024	172	—	No reverse shots were obtained on scan positions. Started adding an additional RTC scan to improve loop closure. (Applies to most later surveys).
6/1/2024	204	—	Second P50 scan was not completed.
8/6/2024	270	UAS	—
11/19/2024	375	—	—

Date	Time (days)	Additional data collection	Notes
3/8/2025	484	—	Potential calibration issue with the RTC360 leading to 3-4 cm offsets. An additional local registration was completed to the extracted scans on the cliff sections for this epoch to minimize the bias.
7/2/2025	600	—	Similar calibration issue to 3/8/2025
11/11/2025	732	—	—

4.5.1 General Survey Plan

Typically, the fieldwork will follow the same procedures and settings to improve change detection results with consistent datasets (e.g., resolution, coverage, etc.). However, in some cases additional work will be performed during certain surveys to help verify that the GCPs are stable and as an additional check on the results. The field work will consist of the following key steps:

- During the baseline survey, wood stakes with flagging were placed at the site to identify the locations of the total station (orange), Leica P50 scanner (green), Leica RTC360 scans (pink, Figure 4-8), and GCPS (yellow).

- Setup ~4 swivel targets on poles over GCPs 1,3,5, and 7. The offset for the red poles is **1.428 m.** If a 2m fixed height pole is used, then the offset will be **2.120 m.**

- Place ~22 clipboard targets around the scene (distributed uniformly).

- GNSS baseline surveys (Figure 4-4).

    - Setup GNSS receivers on GCPs 1, 2, 3, 5, 6, and 7 and log raw data for 4 hours. *(Initial, 1 year, and final survey only)*. If not all units are available, then split to do GCPs 1,2,4, and 6. Then swap and set up over 1,3,5 and 7.

- When using GNSS to obtain the scanner origin, set up the GNSS base station on GCP 1 and ensure it is logging raw data.

- First set up and start the *Leica P50* scanner (Figure 4-5) with a full 360-degree horizontal field of view, vertical cutoff of 45 degrees, 120m range, and a resolution of 0.005 m @50 m. Use HDR imaging for the photographs. Set it to perform a double scan. (Approximately 45 minutes of scanning and imagery). Ensure the scanner is leveled and the level compensator is enabled. Two methods can be used for obtaining the position of the scanner. Option 1 is the preferred method as it is higher accuracy and reduces the equipment and batteries required on site.

    - *Option 1:* Obtain 5 direct and 5 reverse readings on the 360-degree (GRZ122) prism above the P50 scan. The offset for a GRZ122 prism mounted to the scanner with adapters GAD110 & the Leica prism stud adapter is **0.2847 m.** Wait until you have the P50 set up and leveled before putting the prism in the mount so that it is stable.

    - *Option 2:* Obtain GNSS observations (ORGN with raw data logging) for the entire duration of the survey (ideally 2 hours). The offset for Leica GAD110 for the P50 is **0.1175 m.**

- After the first P50 scan completes (~1 hr), perform a second 360 scan at 570 m range, 6.1 mm @10 m resolution, no images with the P50. (Approximately 7 minutes). It should take just shy of 7 minutes. Note that this second scan can't be started until the RTC360 is completed as the prism cannot be in the field of view of the scanner.

- Conduct *RTC scans* being careful to avoid blocking the scanner. Two methods can be used for obtaining the scanner position while scanning. Option 1 is the preferred method as it is higher accuracy and reduces the equipment and batteries required on site.

    - *Option 1:* Obtain 5 direct and 5 reverse readings on the 360-degree prism above the RTC scan. The offset of the custom mount used by the geomatics lab for the RTC360 in conjunction with the Leica GAD112 stud and the 4.0 cm quick release adapter is **0.2317 m.**

    - Option 2: Obtain ~3-minute GNSS observations (ORGN with raw data logging) for each scan and utilize the high accuracy tilt compensator. (12 scans total). The offset for the custom mount used by the geomatics lab for the RTC360 in conjunction with a 4.0 cm quick release is **0.1125 m**.

- Obtain total station (Figure 4-5) measurements on targets and GCPs (Figure 4-6 and Figure 4-7). One crew member can do much of this while the other operates the scanner.

    - Backsight to GCP05 as 180°00'00" using the set orientation mode. This will approximately align the data with North.

    - At each GCP obtain 5 direct and 5 reverse readings using a circular prism. Use a bipod to keep the prism stable. Use the prism height of **6.6 ft (2.0117 m).**

    - Obtain 5 direct and 5 reverse readings on each B&W swivel target (4) in reflectorless, averaged mode.

    - For each clipboard target, obtain 5 direct and 5 reverse readings in reflectorless single measurement mode.

- If performing Option 1 (prism on scanners), for the total station, focus on the shots on the RTC prism while that is underway so that process can be completed efficiently. In between you can shoot in the swivel targets on the control points and do some circular prism shots on the other control points. Then when that is done, perform a sweep of the reflectorless shots on the clipboard targets. Then shoot in GCPs 1,3,5,7 with the circular prism after the scanning is all done as a final check.

- For surveys that include UAS flights:

    - Place photogrammetric targets on the GCPs. Use rocks to weigh down sides.

    - Perform UAS flights with the DJI Mavic 3E RTK Enterprise.

        - Perform the automated gridded Smart Oblique flight mission (200ft AGL) shown in Figure 4-9 and Appendix B.

            - Ensure Shutter priority is set to around 1/1000

            - Uses 30-degree oblique image angle

- ♦ Perform the manual or waypoint mission close-up oblique image flights.

- Obtain GigaPan images of rockslope sections. *(Post scaling only)*

- Carefully pack up all gear and leave site.

Note: Each trip should be timed to occur during reasonable weather conditions (e.g., light showers, clear skies, etc.) with a window of a few hours. If absolutely necessary in cases where there are only small windows in which the field work can be completed due to heavy rainfall during the time critical surveys in the weeks after the scaling, then some settings can be adapted so that the most critical data are prioritized. This includes modifying the P50 collection plan to not perform double scans and reducing the resolution to 0.015 m @50 m instead of 0.005 m @ 50 m. For the monthly and quarterly surveys, simply adjust the surveys to occur on a day with clearer conditions where there are large blocks of time with clear weather within a week of the scheduled date.

A UAS survey will be conducted at regular intervals during some of the surveys and will be conducted using the DJI Mavic 3E RTK Enterprise sUAS equipped with a 4/3 CMOS Wide Camera using the inbuilt shutter priority settings. Each mission consists of a gridded "optimized oblique" flight that dynamically gathers oblique photos in each cardinal direction and NADIR that adequately covers the designated flight area. Another oblique flight that is flown at a lower altitude will also be conducted for each UAS survey, and the associated coordinates orientation for the photos will be recorded and used as a repeatable flight path for each following survey. GSD for the Gridded Smart Oblique flights was around 1.64 cm/pixel.



Figure 4.4. GNSS Base Station setup over GCP#1.



Figure 4.5. Leica P50 setup with GNSS mount and total station setup.



Figure 4.6. Example GCP#4 and stake for identification.



Figure 4.7. Left: close-up of GCP#4 and Right: Closeup of GCP#5 with prism pole centered in the divet.



Figure 4.8. Stake to indicate the location of RTC Scan #10.



Figure 4.9. Gridded Smart Oblique flight plan of the Rumble Pit showing key parameters. More details and screenshots of the flight plan can be seen in Appendix B.

4.5.2 Scaling

Scaling occurred November 10, 2023. The approximate scaling extents are shown in Figure 3-20. Two ~15 m sections (Sections A & C shown in Figures 3-20 to 3-23) were able to be scaled during one day of operations. In another section, specific rocks were loosened from the slope in order to track changes in the surrounding rock (Section B). Scaling followed ODOT's scaling standard specification and procedures. An engineering geologist from ODOT was on site during the scaling to monitor and direct the operation.

4.5.3 Repeat monitoring plans

The research team followed the field monitoring plan (Figure 4-14, Table 4-1) to collect frequent scans after the scaling and then decrease the frequency with time. This plan consisted of capturing scans every other day for the first week after scaling, once every week for a month after scaling, then every month for the first 6 months after scaling and then taper to every 3 months until the end of the monitoring period (November 2025).



Figure 4.10. Scaling extents and control sections at the RUMBLE PIT

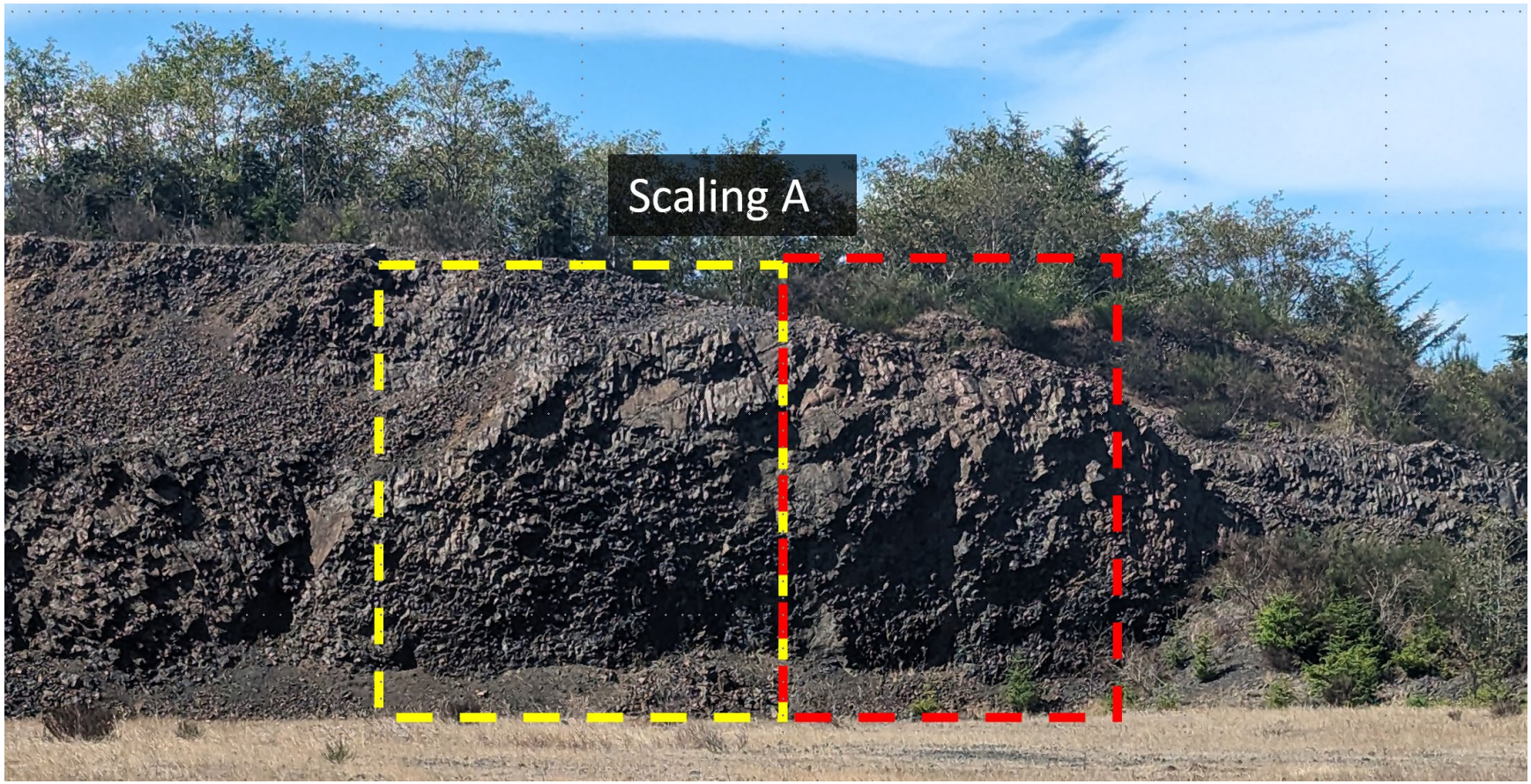

Figure 4.11. Scaling extents and control sections of section A at the RUMBLE PIT

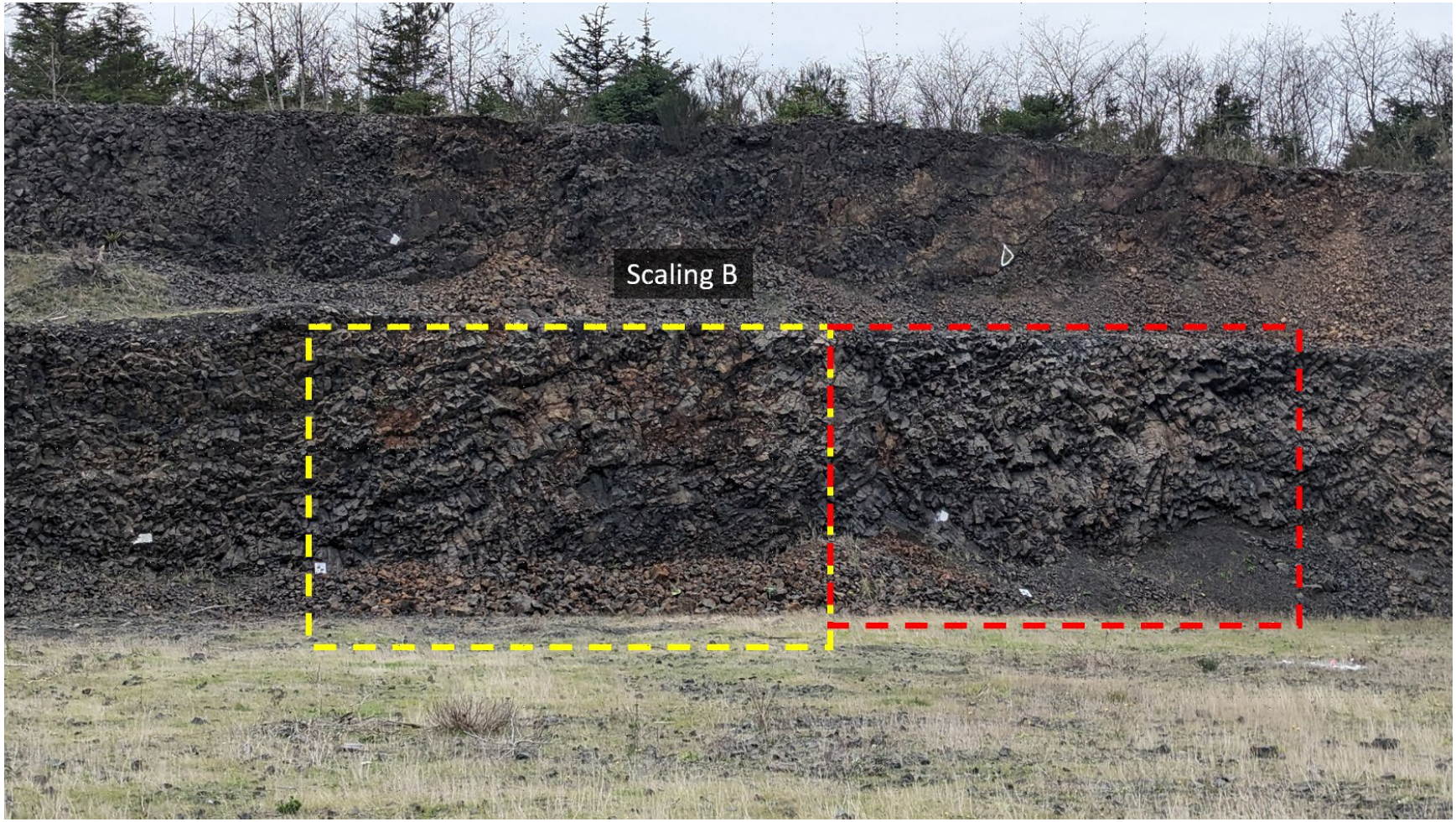

Figure 4.12. Scaling extents and control sections of section B at the RUMBLE PIT

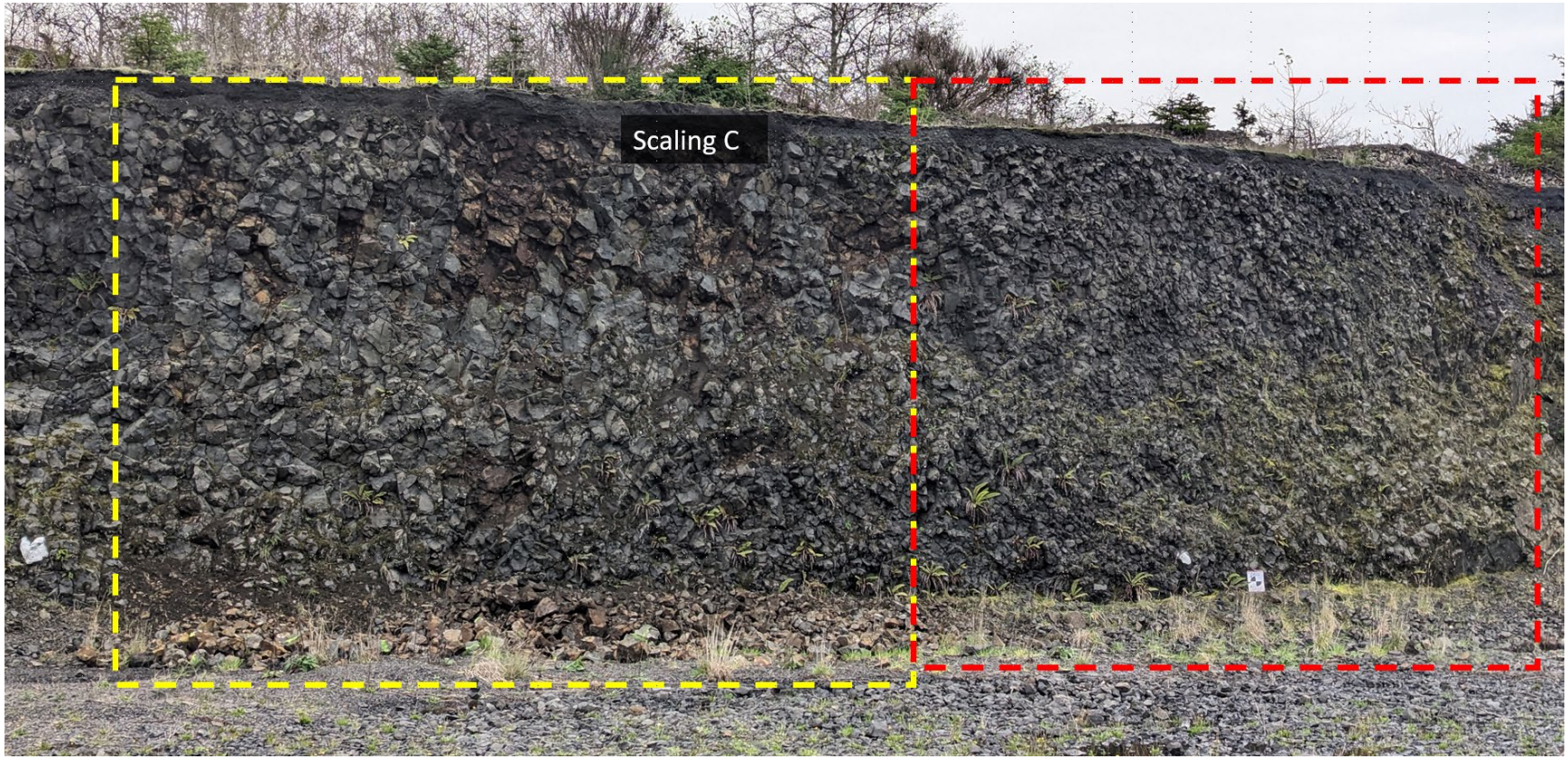

Figure 4.13. Scaling extents and control sections of section C at the RUMBLE PIT

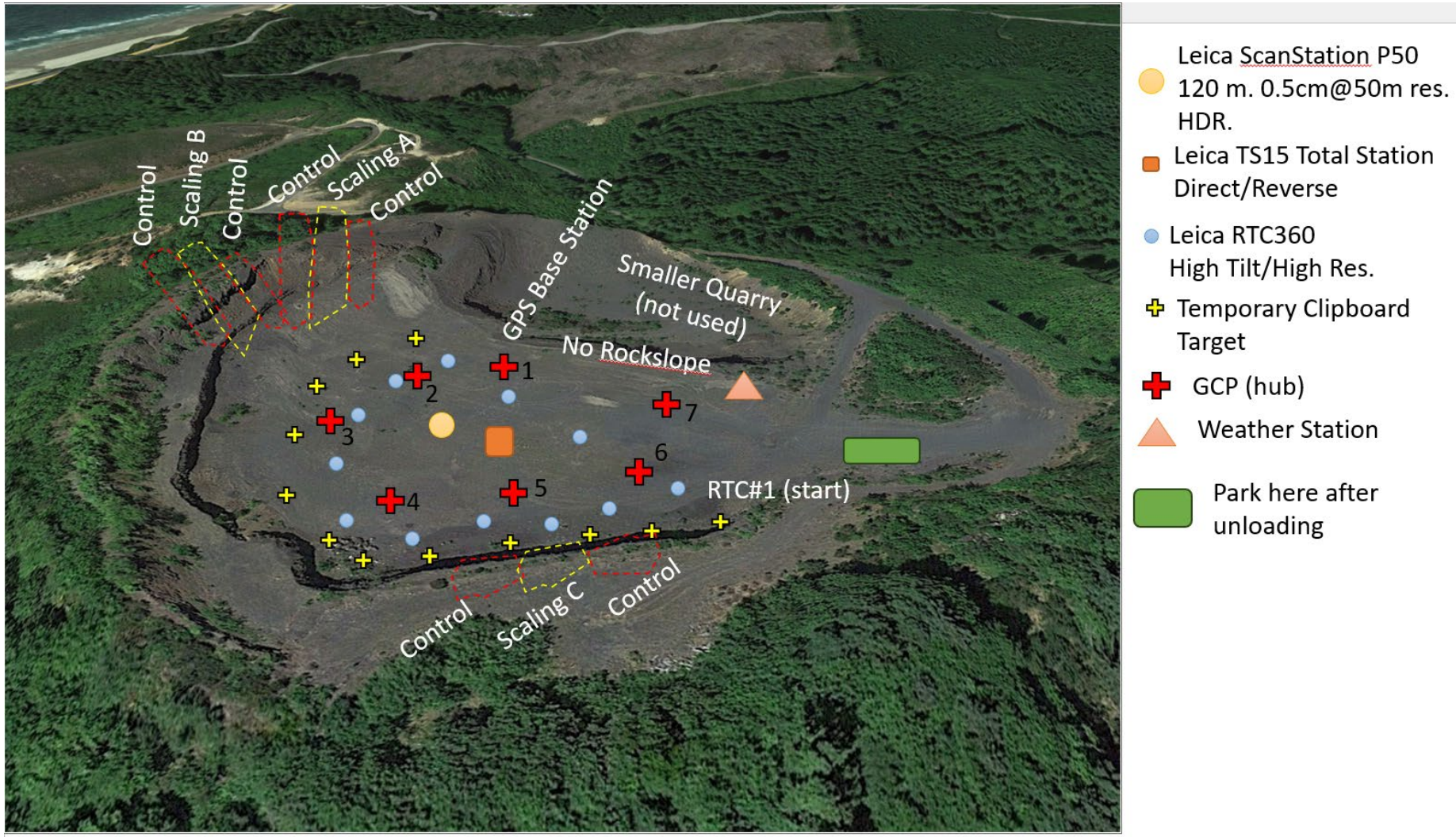

Figure 4.14. Typical monitoring survey plan at the RUMBLE PIT

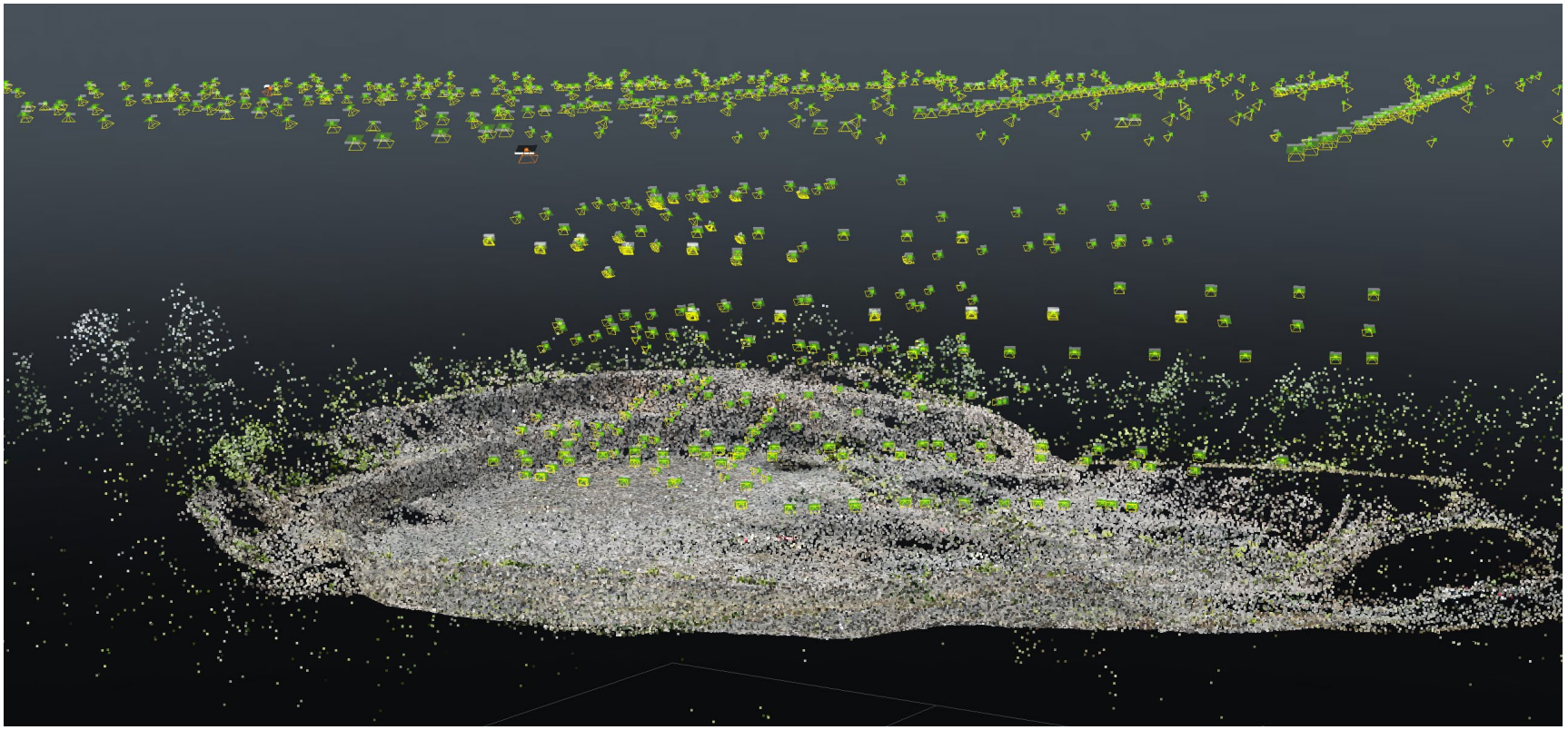

Figure 4.15. Example sparse point cloud rendering from first UAS survey depicting camera pose positions from the gridded optimized oblique flight path and additional manually collected photos.

4.5.4 Safety Plan

The following safety protocols will be employed during fieldwork to ensure safety during data acquisition activities:

4.5.4.1 Before Field work

- Appropriate personnel in ODOT and OSU are notified prior to conducting field activities (Table 4-2). An email should be sent out at least 3 days prior to conducting the field work including the persons listed below.

Table 4.2. Project contact list.

Contact	Entity	Role	Email	Phone	Relevant Sites
Michael Olsen	OSU	PI	Michael.olsen@oregonstate.edu	P: 541-737-9327 C: 801-244-4836	ALL
Ben Leshchinsky	OSU	Co-PI	Ben.Leshchinsky@oregonstate.edu		ALL
Kira Glover-Cutter	ODOT	Research Coordinator	Kira.M.GLOVER-CUTTER@odot.oregon.gov	971-701-0051	ALL
Curran Mohney	ODOT	Research Champion	Curran.E.MOHNEY@odot.oregon.gov	(503) 986-3490	ALL
Sarah Hunt	ODOT	Region 2 Geologist	sarah.hunt@odot.oregon.gov	503-302-7231	RUMBLE PIT
Jon Barnard	ODOT	TMM Ona Beach	Jon.BARNARD@odot.oregon.gov	541 380-7800	RUMBLE PIT
Jill Dekoekkoek Bruce (Bob) Harshman Randy Camp	ODOT	Region 3 Geologist	Jill.DeKoekkoek@odot.oregon.gov Bruce.HARSHMAN@odot.oregon.gov Randy.CAMP@odot.oregon.gov	541-452-1359	Siskiyou, Green Spring, and Yellowjacket
Michael Fairchield	ODOT	Maintenance	Michael.J.FAIRCHILD@odot.oregon.gov	-	Yellowjacket
Guy Mamac	ODOT	Maintenance	Guy.A.MAMAC@odot.oregon.gov	541-757-4112	Eddyville

- Each field team member must complete basic safety training prior to departing for a given trip. Safety training sessions are organized with PI Michael Olsen and include road survey safety utilizing the ODOT Geometronics safety manual.

- For the RUMBLE PIT, ensure that the field crew has the key to the gate locks.

- For the RUMBLE PIT, Review the site management plan.
- For the SR14 MP73 site in Washington, no notification is necessary.

4.5.4.2 AT SITE (Each visit)

- Prior to departure, review that the field crew has all equipment listed on the checklist.
- Ensure that you have a first aid kit (included in all motor pool vehicles), ample water, snacks, sunscreen, and other items.
- Send a text or email to Michael Olsen and Ben Leshchinsky.
- For the RUMBLE PIT, lock both gates after passing through.
- The field crew should consist of at least 2 people present on site. Both should generally work in close proximity but have a walkie talkie radio for communication if they are separated.
- Safety briefings are conducted at arrival of site prior to beginning work to identify, discuss, and mitigate all potential risks. Should an unanticipated safety risk be present at the site, contact the PIs.
- At the RUMBLE PIT, high-visibility clothes should be worn (e.g., bright orange shirt). At other field sites adjacent to roadways, ANSI II safety vests should be worn at all times.
- Rugged boots should be worn while performing field activities.
- Hard Hats should be worn when working while at the site to protect from falling debris.
- Consult the ODOT Geometronics safety manual for further suggestions regarding safe operation.
- Should any rock harvesting activities be in progress at the site, DO NOT PROCEED WITH FIELD WORK. Notify the PIs and appropriate ODOT personnel.
- Notify ODOT of any concerns at the site (e.g., unauthorized persons present at site). In an emergency, call 911 and then notify the PIs.
- Any UAS work will require a Part 107 licensed pilot as well as follow the Part 107 regulations.
- RUMBLE PIT special considerations

- Potential site restrictions may occur from Jan 1- June 30th due to the potential for Eagle nesting near the site. ODOT staff is currently looking into whether a permit is necessary for these low impact activities.

- Be sensitive of birds and other animals

Additional instructions for field sites other than the RUMBLE PIT where field crews will be in closer proximity to the highway. These include:

- "Survey Crew Ahead" signs should be placed approximately 200-300 feet in front of the far extents of the survey area.

- Orange flashers should be placed on top of vehicles parked on the side of the road at the survey site to ensure road users are aware of the vehicle and surveyors presence.

- Cones and lane closures should be coordinated with ODOT team members if surveying activities are to take place on the road. This is unlikely to be necessary for this project.

- Road crossings should be minimized as much as possible and a spotter should be utilized when doing so.

- Surveying should take place with each team member advancing in the opposite direction of traffic. A spotter should be utilized when turning individual back on traffic.

- Work as far back in the shoulder as possible to reduce proximity to traffic.

4.5.4.3 UPON COMPLETION

- Ensure both gates are locked (RUMBLE PIT only).

- Send notification to Michael Olsen and Ben Leshchinsky that work has concluded and you are leaving the site.

- Discuss any safety concerns noted and report those.

4.5.5 Documentation required for each site.

For each field trip the following items were brought for reference:

- Copy of this safety and fieldwork plan as well as the checklist in Appendix C.

- SPR864 fieldbook for recording notes from all sites in the project.

- Printout of Google drive document containing OCRS zones used for each site's GNSS control

- Printout of site plans described in this research methodology document.
- ODOT team phone numbers.
- .kmz files of control points and scan positions should be loaded on a smartphone to aid in rapid recovery of these points.

5.0 DATA PROCESSING PROTOCOLS

The data processing procedures were adapted from those developed for SPR807, SPR809, and previous research for PacTrans. The main data processing is completed in PointReg software available through EZDataMD, LLC, a technology transfer company from Oregon State University. It is recommended to carefully review the PointReg User Manual to understand how the data needs to be structured, file naming conventions, and the appropriate input and output files. Note that this workflow need not be followed in order. For example, the preliminary scan registration can be completed before the GNSS data has been processed rather than wait for the precise ephemeris to be available. Alternatively, the registration can use initial coordinates for the GNSS and then be updated when the precise ephemeris is available. However, if done in a different sequence, one needs to verify that the key processing procedures have been implemented.

A running log of processing should be kept for each site that tracks information such as:

- Issues encountered with data (e.g., a scan that has poor leveling or other distortion due to an unstable setup).
- Inconsistent numbering.
- Incorrect antenna heights.
- Deviations from the processing procedures and rationale.

5.1 PROJECT SETUP

- Set a directory on the shared drive for each survey campaign at each site using the naming convention and file structure used by the OSU geomatics research lab.
- Create a working directory on your local drive to process lidar data before backing it up to the folder created above. Each site should have its own subfolder.
- Create a subfolder for PointReg processing in each site folder. Note that all epochs/surveys will be processed together in a multi-epoch adjustment in PointReg. For Leica Infinity and Cyclone processing; however, each epoch should be stored in the appropriate subfolder corresponding to that survey.
- Create a second subfolder for the *Rambo* processing results.

5.2 GNSS PROCESSING

5.2.1 Setup procedure for workstation

- Install Leica Infinity through software center.
- Download and load Geoid 18, Geoid 12B & OCRS zones (ODOT website) into Leica Infinity.
- Select the appropriate OCRS Zone and Geoid for each site as described in Table 3-1. Data should be referenced to NAD83(2011) Epoch 2010.00.

5.2.2 Processing

- Wait 14-16 days to allow for the precise ephemeris to be available prior to processing the GNSS data.
- Upload m00 files from the GNSS base station/s (longest observation) to the NGS OPUS. Alternatively load the m00 files into Infinity and export each baseline to a RINEX file and upload to OPUS; however, it is preferred to use the m00 files directly.
- Create a new Leica Infinity project and store it in the GNSS folder in the processed folder in the project folder on the shared drive.
- Import the precise ephemeris for the duration of the survey into Leica Infinity.
- Assign the base points as “control points” and copy the NAD83 2011 (epoch 2010) coordinates from OPUS into the “Geodetic coordinates” section.
- Ensure “NGS absolute” is selected for antenna calibration.
- Change the ephemeris type to “Precise”.
- Verify that all antenna heights are correct.
- In the GNSS timeline window, identify the control points as reference stations and shorter observations as rovers then select the “process” icon.
- Assess the ambiguities and residuals of each position to ensure adequate results.
- Once satisfactory select “store”.
- Export the coordinates as a comma delimited ASCII TXT file (PROJNAME_GNSS.csv) in the form:
    - ID, Easting, Northing, Ortho Height, CSF, SD Easting, SD Northing, SD Ortho Height.

5.3 TOTAL STATION PROCESSING

- Part 1. Leica Infinity:
    - Create a new infinity project for each total station position in the appropriate location in the project folder.
    - Verify the prism heights and types used.
    - Verify that the names of the points are consistent. Ensure each overlapping TS/GNSS position have identical names.
    - Export the data as a csv/txt file on the total station in format X,Y,Z,PID with a name to indicate the epoch of the survey and total station (e.g., 1090 where 10 is the survey epoch number and 90 is an ID assigned to the total station position). Save in the PointReg_Targets folder. Make sure that the PID for the total station origin (0,0,0, PID) matches the PID in the main csv file. (e.g., 1090).
- Part 2. Leica Cyclone:
    - Create a new Cyclone database in the project folder on your local hard drive. Double check the registration and precision settings.
    - Import the exported GNSS and total station coordinates. Be sure to select TargetID instead of PointName for the PID.
    - Create a registration. Add both scan worlds. Ensure they are toggled level. Set the GNSS data to be the home scanworld. Auto-add constraints. Run the registration.
    - Verify that residuals are reasonable (few cm) and that all expected GCPs are used as constraints. Resolve any naming convention or outlier issues.
    - Export the resulting data as a csv/txt file in the format X,Y,Z, PID. This file is not used later but can be used as a check.
    - Save the diagnostics file as a text file. Extract the total station position and rotation information from the diagnostics file (e.g., Translation X, Y, Z, and rotation Z).

5.4 PRELIMINARY SCAN REGISTRATION

- Import scans into the same cyclone database used for the total station processing. This can take tens of minutes to several hours to complete. Do not use smart align. Be sure auto target extraction is selected.
- For each scan position, carefully identify and extract all targets that are visible and have satisfactory resolution. If the target ID is known, enter the name. If not, give it a unique name (e.g., T1001_01 where 1001 is the ScanID and 01 is a unique number to that target.

The next would be 02, etc.). Enter the appropriate target heights for targets set up over control points. Label the vertex at 0,0,0 with the appropriate scanID (e.g., 1001).

- Export the targets for each scan position as a txt file in the format X, Y, Z, TargetHeight, TargetID to the targets folder in the PointReg folder for the site.

- Create a new registration in cyclone. Add scanworlds to the registration (recommended to do this in chunks of 10 scans). Perform a visual alignment for the scans. Each scan should be linked at least one other scan that can be linked through the chain back to the home scanworld.

- Auto add constraints to add the target constraints. Disable any targets that may not be a correct match (e.g., CP100 is matched to CP103).

- After completing each chunk, run the registration. Verify the constraint residuals are satisfactory (typically < 0.01 m). If so, select all of the scans and view interim results to ensure the data are consistent. If not, identify where the problems are at and resolve.

- When the registration has been verified, export all scans as separate E57 files with color and intensity. Normals are not necessary.

- Export the diagnostics as a text file. Run the ExtractCycloneParameters.exe to extract the key information.

- Drag and drop the E57 files into the EZE57_to_LocalLaz.exe from EZPC by EZDdataMD LLC. This process can take some time.

- Move all laz files to the \PointReg\scans folder.

- Rename the LAZ files to follow the PointReg convention: (PROJNAME_SCANID_BSID_LID.laz).

    - For the SCANID, it is recommended to have the first two digits represent the survey # and the last two the scan number. For example, for the first survey epoch, use 10, and for the first scan use 01. So that scan would be 1001. For the second survey epoch, the first scan would be 1101, etc.

    - For BSID, use the date of the survey (e.g., 20231023)

    - For LID, use “L” to indicate level and then a code to identify the GNSS processing approach or survey device (e.g., LORGN, LPPK, LRTK, LMLS, LUAS, LTS, LPRISM, LRESECT).

5.5 MOBILE LIDAR

ODOT Geometronics has collected mobile lidar data (multiple passes per site) for each site for two survey epochs for SPR809. Premark (Control) targets were placed at each site to improve the georeferencing quality of the MLS data resulting in improved consistency between passes

within a survey as well as between surveys. These adjustments were applied by ODOT Geometronics prior to providing the research team with an ASPRS LAS 1.2 file of the georeferenced point cloud.

Each LAZ file should be split such that the data from each profiler and each pass are in a separate file. The LAZ files for the mobile lidar data are run through the LAS_Reader_BPD.exe program provided with PointReg. In this program, the centroid for each mobile lidar pass is computed. The data are then offset by that centroid. This essentially simulates a scan origin.

The resulting "local" LAZ files should be copied to the PointReg\scans folder and renamed following the PointReg convention outlined in the previous section).

If GCPs were present and extracted in the mobile lidar data, they can be added to a target file for the associated pass. (This should be the value from the point cloud NOT the GCP coordinate value). However, the centroid XYZ coordinates for that pass should be subtracted so that they are in "local" coordinates.

5.6 UNMANNED AIRCRAFT SYSTEM DATA

The UAS photogrammetric data are processed in Bentley Context Capture software:

- Process the GNSS trajectory using Leica Infinity as described in https://globalsurvey.co.nz/surveying-gis-news/dji-drone-gnss-post-processing-now-available-in-leica-infinity/
- Import control point coordinates as a csv file and the photos into Bentley ContextCapture.
- Import post processed photo poses to overwrite original photo poses
- Reference & tag control points in the images.
- Run aerotriangulation of photos and control points for a sparse point cloud alignment
- Create an orthophoto at 2 cm resolution.
- Create a dense point cloud and export as a laz file in the appropriate coordinate system. (Use EZProj for any coordinate system conversions). Export in tiles approximately 100 m x 100 m.

The tiled dense point clouds (and targets) can then be used in the PointReg Adjustment following the same procedures as the mobile lidar data exports.

5.7 MULTI-EPOCH, MULTI-SCAN, MULTI-SENSOR LEAST SQUARES ADJUSTMENT

5.7.1 CSV file setup

Using the PointReg template as a guide, create a PROJNAME.csv file that has the core scan georeferencing and naming information. Ultimately, all survey epochs should be combined in one file. However, it is sometimes easier to work on a temporary file for each epoch and then copy the information into the main file after everything is set up.

5.7.1.1 Leica P50/RTC360 scans

- For X,Y,Z,roll,pitch, and yaw, copy the values from the _scnparams.csv file created during the E57 to local Laz conversion. Note that roll and pitch should normally be 0.0 unless there is a leveling issue with the scan.

- Copy in the information from the PROJNAME_GNSS.csv file to the CSF (combined scale factor), GX,GY,GZ, GH, GSDX,GSDY, and GSDZ columns. (GH is the antenna height – See Section 3.2.3).

- Verify that the XYZ and GX,GY,GZ values are similar (e.g., within a cm or so).

- For WSFXY and WSFZ use 1.0 for ORGN\RTK data. Use a value between 100 for PPK. For scans that did not have a GPS coordinate or have a poor GPS coordinate, use WSFXY = WSFZ = 10000.

- For GPSCORR, set to 0 for Leica P50 scans. For RTC scans set to 0 for initial processing. (A correction process to correct the scans for out of level setups will be implemented later in the process).

- For ADJUST, enter 1 for all scans.

- Fill in the SCANID, BSID, LID to match your scan names.

5.7.1.2 Total Station

- Add the total station transformation information as another entry to the csv file. Use WSFXY = WSFZ = 10000 for the total station.

5.7.1.3 Mobile lidar and UAS SFM/MVS data

- Add the mobile lidar/UAS XYZ translation information as another entry to the csv file from the csv file. Those values should be used for both XYZ and GX, GY, GZ. Roll, pitch, and yaw should be 0.0. GH should be 0.0. Use 1.0 for the CSF. Use WSFXY = WSFZ = 10000. Other values can be the same as those recommended in the previous section.

5.7.1.4 GNSS control points GCPs).

- Extract the GCP coordinates from PROJNAME_GNSS.csv and save as PROJNAME_cntrl.csv in the same folder as PROJNAME.csv. Each point ID should start with CP.

5.7.2 Adjustment

- Run the Cloud to Cloud pairwise matching in PointReg. (Note this process can take a long time given the number of matches required, so run it in the background, overnight, and/or over a weekend). After it has run a few pairs, check the results to make sure they are reasonable. Resolve any issues (e.g., misnaming, coordinate errors, etc.).

- Perform target checks using the tools in PointReg to help identify misnamed targets, missing targets, and issues with target heights. Correct those and iterate.

- Run the PointReg least-squares adjustment. Use the _ADJOBS file to identify issues (indicated by "!").

- Adjust the weighting and re-run the adjustment as necessary until outliers are removed and the registration is satisfactory.

- Apply the registration to the laz files to create the _reg.laz files for each scan.

- Perform basic QA/QC of the results to ensure the data overlap and are consistent.

5.7.3 Adjustment Results

This section provides the detailed results of the adjustment for each site. Note that for all sites, a single adjustment was completed including all epochs of data at the site to improve the quality of the registration. Table 5-1 summarizes the factors analyzed in the adjustment. Descriptive statistics include: Mean, median, standard deviation (Std. Dev.), minimum (min), maximum (max), root mean square (RMS) error, and the number of observations (N) for each factor.

Table 5-1 also presents target values for each category. There are several considerations in interpreting the adjustment results and error metrics. First, the total stations used in this project have a horizontal measurement accuracy of 1" (1-s) and 3 mm +3 ppm when measuring to a circular prism. However, additional error will accumulate when manually sighting and using reflectorless measurements to the checkerboard target centers. The Leica P50 has a per-point angular accuracy of 8" (1- σ) and ranging accuracy of 1.2 + 10 ppm. The Leica RTC360 has a per-point angular accuracy of 18" (1-σ) and ranging accuracy of 1.0 + 10 ppm. However, numerous other factors such as leveling quality, ranging accuracy, beam divergence, and more will affect the overall accuracy of the point coordinates as well as the ability to extract the target centers. GNSS measurements have a nominal accuracy of 0.01 m horizontally and 0.02 m vertically. However, GNSS measurements can vary substantially based on obstructions, multi-path effects, and observation duration. Research such as Allahyari et al. (2018) showed more

typical GNSS accuracies to be 0.02 m horizontally and 0.05 m vertically for RTK and PPK GNSS data in field conditions.

Weightings of each category and observation can be done in the adjustment such that the error is distributed properly across the observations and the adjustment does not overfit to one observation type at the expense of another. Hence, multiple iterations of the adjustments were performed with different weights in order to balance the errors across the observations to be consistent with the expected errors.

Lastly, it is important to note that these errors are associated with the determination of the scan registration parameters (translation XYZ and rotation Z) and coordinates of the control points and targets. Hence, while they do indirectly provide an indication of the overall scan quality, the actual uncertainty will vary throughout a scan and differ for each point in the point cloud.

Table 5.1. Summary of quality control metrics from the registration.

Factor and Units	Description	Target RMS
CC Hor Angle (“)	Measure of how well the rotational (Horizontal-Hor) angular component in each cloud to cloud (CC) pairwise match matches the overall adjusted value.	< 120”
Target Hor Angle (“)	Measure of how well the measured horizontal angle measured in each scan or total station setup matches the overall adjusted value. This includes both total station and scan targets.	< 60”
CC Hor Dist (m)	Measure of how well the horizontal distance computed between the scan origins in each cloud to cloud (CC) pairwise match matches the overall adjusted value.	<0.01 m
Target Hor Dist (m)	Measure of how well the horizontal distance measured to each target from the scan or total station setup matches the overall adjusted value. This includes both total station and scan targets.	<0.01 m
CC Elev. (m)	Measure of how well the elevation difference computed between the scan origins in each cloud to cloud (CC) pairwise match matches the overall adjusted value.	<0.01 m
Target Elev. (m)	Measure of how well the elevation difference measured to each target from the scan or total station setup matches the overall adjusted value. This includes both total station and scan targets.	<0.01 m
SP GNSS X (m)	Measure of how well the observed GNSS X, Y, or Z coordinate for the scan origin matches the overall adjusted value for the scan origin X, Y, or Z coordinate.	<0.01 m
SP GNSS Y (m)		<0.01 m
SP GNSS Z (m)		<0.02 m
CP GNSS X (m)	Measure of how well the observed GNSS X, Y, or Z coordinate for each control point matches the overall adjusted value for the X, Y, or Z coordinate.	<0.01 m
CP GNSS Y (m)		<0.01 m
CP GNSS Z (m)		<0.02 m
GNSS BL X (m)	Measure of how well the observed GNSS baseline vector X, Y, Z distances between control points match the overall adjusted value for the distances in X, Y, or Z.	<0.01 m
GNSS BL Y (m)		<0.01 m
GNSS BL Z (m)		<0.02 m

5.7.3.1 Rumble Pit

For the Rumble Pit, all observation types were used in the adjustment. The dataset had over 300 scans from the 21 surveys. Note that in addition to targets shot in reflectorlessly with the total station and extracted from the scans, prism-based measurements were acquired on control points as well as for the scan locations. These observations all are included in the "Target" results. Only the first survey at the Rumble Pit utilized a GNSS receiver mounted above the scanner. The Control Point results were based on several hours of GNSS observations on six of the control points post-processed in NGS OPUS-S. The GNSS baselines were computed from that same survey.

Table 5.2. Registration QC metrics for the Rumble Pit site.

Observation Type	Mean	Median	Std. Dev.	Min	Max	RMS	N
CC Hor Angle (")	-0.5	-0.1	38.4	-313.1	626.2	38.4	35129
Target Hor Angle (")	-1.4	-0.5	17.5	-127.9	95.9	17.6	2233
CC Hor Dist (m)	0.0014	0.0006	0.0073	-0.0266	0.0384	0.0074	38562
Target Hor Dist (m)	-0.0007	-0.0007	0.0039	-0.0307	0.0163	0.0039	2233
CC Elevation (m)	0.0008	0.0006	0.0074	-0.0508	0.0580	0.0075	38562
Target Elevation (m)	-0.0010	-0.0005	0.0070	-0.0323	0.0314	0.0071	2233
SP GNSS X (m)	-0.0050	-0.0057	0.0037	-0.0116	0.0007	0.0062	14
SP GNSS Y (m)	0.0003	-0.0009	0.0043	-0.0038	0.0096	0.0042	14
SP GNSS Z (m)	-0.0008	0.0014	0.0087	-0.0188	0.0139	0.0085	14
CP GNSS X (m)	-0.0022	-0.0017	0.0049	-0.0108	0.0031	0.0050	6
CP GNSS Y (m)	-0.0061	-0.0060	0.0054	-0.0136	-0.0005	0.0078	6
CP GNSS Z (m)	-0.0003	0.0008	0.0093	-0.0156	0.0133	0.0085	6
GNSS BL X (m)	0.0088	0.0072	0.0024	0.0069	0.0118	0.0090	5
GNSS BL Y (m)	0.0235	0.0234	0.0069	0.0166	0.0325	0.0243*	5
GNSS BL Z (m)	0.0059	0.0054	0.0017	0.0045	0.0089	0.0061	5

** Although the GNSS baseline vector RMS value is larger than the desired 0.01 m in Y, this result has minimal impact on the overall registration accuracy of the survey. Each control point was observed multiple times with the total station and several were observed with scan targets throughout the many surveys at the site. Hence, the baseline vector has little influence on the overall final coordinates of the control points given the many other observations.*

5.7.3.2 Siskiyou Pass

In Siskiyou Pass, GNSS observations were acquired for the scan origins. No targets or control points were used due to safety constraints to set up and establish those. Table 5-3 summarizes the registration statistics. All values were within the desired range.

Table 5.3. Summary of registration QC metrics for Siskiyou Pass.

Observation Type	Mean	Median	Std. Dev.	Min	Max	RMS	N
CC Hor Angle (“)	-1.2	0.1	20.2	-266.0	90.3	20.2	704
CC Hor Dist (m)	0.0006	0.0004	0.0042	-0.0124	0.0179	0.0042	765
CC Elevation (m)	-0.0004	-0.0004	0.0031	-0.0110	0.0118	0.0032	765
SP GNSS X (m)	-0.0021	-0.0019	0.0062	-0.0151	0.0179	0.0065	54
SP GNSS Y (m)	0.0026	0.0007	0.0050	-0.0121	0.0144	0.0056	54
SP GNSS Z (m)	0.0031	0.0032	0.0106	-0.0322	0.0234	0.0109	54

5.7.3.3 Green Spring

In Green Spring, GNSS observations were acquired for the scan origins. No targets or control points were used due to safety constraints. Table 5-4 summarizes the registration quality statistics. All RMS values were within the desired range. There were some locations with poorer registration quality, but those occurred where scans were spaced further apart in areas of dense vegetation. These areas were not needed for the analysis. Data were primarily collected in those areas to provide continuity.

Table 5.4. Summary of registration QC metrics for the Green Spring site.

Observation Type	Mean	Median	Std. Dev.	Min	Max	RMS	N
CC Hor Angle (“)	0.2	-0.6	47.7	-344.9	247.3	47.7	1447
CC Hor Dist (m)	0.0043	0.0024	0.0084	-0.0150	0.0524	0.0094	1614
CC Elevation (m)	0.0001	0.0001	0.0072	-0.0398	0.0389	0.0072	1614
SP GNSS X (m)	-0.0018	-0.0014	0.0092	-0.0439	0.0266	0.0093	188
SP GNSS Y (m)	-0.0007	-0.0013	0.0131	-0.0511	0.0357	0.0130	188
SP GNSS Z (m)	-0.0016	-0.0003	0.0172	-0.0440	0.0359	0.0172	188

5.7.3.4 Yellow Jacket

For Yellow Jacket, a combination of targets, control points, and GNSS were used. Table 5-5 summarizes the registration quality, with residuals falling within the expected range.

Table 5.5. Summary of registration QC metrics from the Yellow Jacket site.

Observation Type	Mean	Median	Std. Dev.	Min	Max	RMS	N
CC Hor Angle (“)	-0.3	-1.7	101.9	-884.1	774.4	101.9	2634
Target Hor Angle (“)	0.0	0.3	6.3	-24.6	22.3	6.3	195
CC Hor Dist (m)	0.0055	0.0030	0.0130	-0.0548	0.0825	0.0141	2723
Target Hor Dist (m)	-0.0004	-0.0003	0.0047	-0.0151	0.0204	0.0047	195
CC Elevation (m)	-0.0012	-0.0009	0.0109	-0.0714	0.0337	0.0109	2723
Target Elevation (m)	0.0000	-0.0002	0.0067	-0.0268	0.0247	0.0067	195
SP GNSS X (m)	0.0027	0.0022	0.0094	-0.0235	0.0338	0.0097	96
SP GNSS Y (m)	0.0008	-0.0002	0.0146	-0.0397	0.0381	0.0145	96
SP GNSS Z (m)	-0.0089	-0.0075	0.0220	-0.0512	0.0397	0.0236	96
CP GNSS X (m)	-0.0026	-0.0006	0.0088	-0.0156	0.0079	0.0083	5
CP GNSS Y (m)	-0.0005	-0.0008	0.0046	-0.0073	0.0043	0.0041	5
CP GNSS Z (m)	-0.0157	-0.0163	0.0064	-0.0240	-0.0064	0.0167	5

1.1.1.1 Eddyville

For Eddyville, a combination of targets, control points, and GNSS were used. Table 5-6 summarizes the registration quality, with residuals falling within the expected range.

Table 5.6. Summary of registration QC metrics for the Eddyville Site.

Observation Type	Mean	Median	Std. Dev.	Min	Max	RMS	N
CC Hor Angle (“)	-4.3	-2.1	50.2	-282.0	255.7	50.4	1127
Target Hor Angle (“)	0.1	0.1	4.9	-19.6	16.6	4.9	144
CC Hor Dist (m)	0.0033	0.0013	0.0091	-0.0207	0.0426	0.0097	1183
Target Hor Dist (m)	0.0000	0.0002	0.0031	-0.0080	0.0104	0.0031	144
CC Elevation (m)	-0.0008	-0.0007	0.0094	-0.0416	0.0361	0.0094	1183
Target Elevation (m)	0.0000	0.0002	0.0042	-0.0181	0.0113	0.0041	144
SP GNSS X (m)	0.0026	0.0020	0.0067	-0.0106	0.0208	0.0072	91
SP GNSS Y (m)	0.0012	0.0000	0.0074	-0.0152	0.0193	0.0075	91
SP GNSS Z (m)	-0.0081	-0.0048	0.0171	-0.0524	0.0291	0.0188	91
CP GNSS X (m)	-0.0017	-0.0014	0.0079	-0.0131	0.0074	0.0077	11
CP GNSS Y (m)	-0.0013	-0.0031	0.0092	-0.0172	0.0157	0.0089	11
CP GNSS Z (m)	0.0048	0.0114	0.0245	-0.0401	0.0310	0.0238	11

5.7.3.5 SR14MP73

At site SR14MP73 a combination of GNSS, control points, and targets were used. The results at site SR14MP73 were higher compared with other sites. While a few results exceed the desired RMS values in Table 5-7, they are close to the desired value.

Table 5.7. Summary of registration QC metrics for Site SR14MP73.

Observation Type	Mean	Median	Std. Dev.	Min	Max	RMS	N
CC Hor Angle (“)	-10.4	-9.4	115.5	-717.2	1042.3	115.9	1962
Target Hor Angle (“)	-0.2	0.3	20.2	-89.7	94.7	20.1	264
CC Hor Dist (m)	0.0051	0.0041	0.0109	-0.0292	0.0536	0.0121	2067
Target Hor Dist (m)	-0.0016	-0.0006	0.0078	-0.0301	0.0225	0.0080	264
CC Elevation (m)	-0.0012	-0.0012	0.0080	-0.0661	0.0428	0.0080	2067
Target Elevation (m)	0.0000	-0.0005	0.0114	-0.0392	0.0339	0.0114	264
SP GNSS X (m)	-0.0007	0.0002	0.0111	-0.0361	0.0230	0.0111	144
SP GNSS Y (m)	0.0006	0.0015	0.0129	-0.0376	0.0320	0.0129	144
SP GNSS Z (m)	-0.0009	-0.0013	0.0194	-0.0647	0.0332	0.0193	144
CP GNSS X (m)	-0.0051	-0.0043	0.0107	-0.0222	0.0229	0.0117	25
CP GNSS Y (m)	-0.0001	0.0006	0.0078	-0.0126	0.0155	0.0076	25
CP GNSS Z (m)	0.0177	0.0183	0.0075	0.0005	0.0315	0.0192	25

5.8 MODELING AND ANALYSIS PROTOCOLS

The registered data are then analyzed in *Rambo*. The workflow is documented in detail in *Rambo*, so only key steps or deviations will be briefly summarized herein

5.8.1.1 Data Cropping

- A polygon is created for each rockslope site as a reference for the processing. The same polygon is used across multiple epochs to keep the analysis extents the same.

- The EZVox DataCropping tool is used to efficiently crop each scan in batch. This tool keeps points inside and within a threshold distance of the best fit plane of a polygon.

5.8.1.2 Vegetation Removal

- Using Leica Cyclone\Cloud Compare\Maptek I-Site or another point cloud viewing software, clip out unwanted parts of the point cloud (road, trees etc.) to expose the rockslope that are still remaining after the cropping procedure.

- Clip the major vegetation from the rockslope manually removing the larger pieces. Smaller pieces can be removed later using automated procedures to save time.

- Utilize the ground filter in *Rambo* for refinement, as necessary.
- After validation, export the bare rockslope point clouds as a .laz.
- Use EZPC to merge all laz files for each epoch into a single laz file. Rename that file following the convention YYYYMMDD_SITE.laz so that the datasets will named in alphabetical/chronological order.

5.8.1.3 Rambo General Surface Modelling generalized workflow

- Run the GUI in Rambo to set the options. Select "the works." This should perform the morphological analysis, RAI analysis, and change analysis simultaneously. Determine if hole filling is appropriate and the appropriate cell size (e.g., 0.05 or 0.10m) for the analysis.
- Drag and drop the merged laz files for all epochs into the data i/o tab. Note the mobile lidar, UAS lidar and terrestrial lidar may need to be analyzed differently.
- Import the resulting files into Cloud Compare, Maptek Point Studio or similar point cloud viewing program for additional visualization and analysis.

5.9 SUMMARY OF PRODUCTS CREATED

For each site, the following products were produced:

- Raw data from survey devices backed up for each epoch.
- Control points based on the Total Station & GNSS data.
- Georeferenced point clouds from TLS, MLS and UAS acquired data.
- Cleaned .laz files of the rockslope for each epoch.
- Clean .obj surface models of the rockslopes for each epoch.
- Filtered .laz files with RAI classification and scores as well as morphological analysis of the rockslopes stored as extra bytes for each epoch.
- Change analysis of rockslopes between survey epochs
- Rockfall Trajectory Analysis results

For the RUMBLEPIT, orthophotos were also generated for key epochs based on the UAS photogrammetric data.

5.10 ROCKFALL SITE VIEWER

An interactive Rockfall Site Viewer (Figure 5-1) was developed as part of the SPR 864 project to provide a centralized, web-based interface for exploring the primary rockfall sites evaluated during the research. The viewer brings together site location information, geologic and topographic data, lidar-derived terrain products, and links to detailed three-dimensional point-cloud datasets. It is intended to provide ODOT personnel, researchers, and other users with an accessible means of reviewing the study sites and examining the spatial datasets used to evaluate rockfall activity and the effectiveness of rock slope mitigation. It can be accessed at the following link: https://experience.arcgis.com/experience/ee89babf04584b939567888d751ea426.

The Rockfall Site Viewer is implemented using the ArcGIS Experience Builder platform and contains an interactive map showing the primary sites investigated during SPR 864. Site-specific bookmarks allow users to quickly navigate to each of the core study locations without manually searching for or zooming to the site. At each location, users can examine the surrounding terrain and geologic setting using available geologic mapping and lidar-derived hillshade imagery. These datasets provide important context for interpreting observed rockfall activity, including the relationship between slope morphology, geologic materials, and areas of localized instability.

In addition to the map-based information, the Rockfall Site Viewer serves as a portal to detailed interactive three-dimensional point-cloud viewers developed for the project (Figure 5-2). Links associated with the study sites allow users to open Potree-based viewers containing the processed point clouds from the different survey epochs collected during the project. The Potree environment allows users to freely rotate, zoom, and navigate through the three-dimensional rock slope data, providing substantially more detail than can be conveyed through conventional maps or static figures. Where multiple surveys were completed at a site, users can examine the slope over the monitoring period and evaluate spatial patterns of rockfall activity and morphological change.

The point clouds available through these viewers are outputs from the Rambo software. Rather than displaying only the original lidar geometry or intensity information, the processed point clouds contain a series of derived morphological and change-detection attributes that can be interactively visualized. Users can change the displayed point-cloud attribute to examine parameters such as slope, surface roughness, curvature, detected change, and RAI classification. Viewing these attributes directly on the three-dimensional slope makes it possible to identify spatial relationships that may be difficult to interpret using two-dimensional maps or summary statistics alone. For example, users can compare areas of high rockfall activity with localized changes in slope geometry, roughness, or curvature and examine how those characteristics vary across different portions of a rock cut or through time.

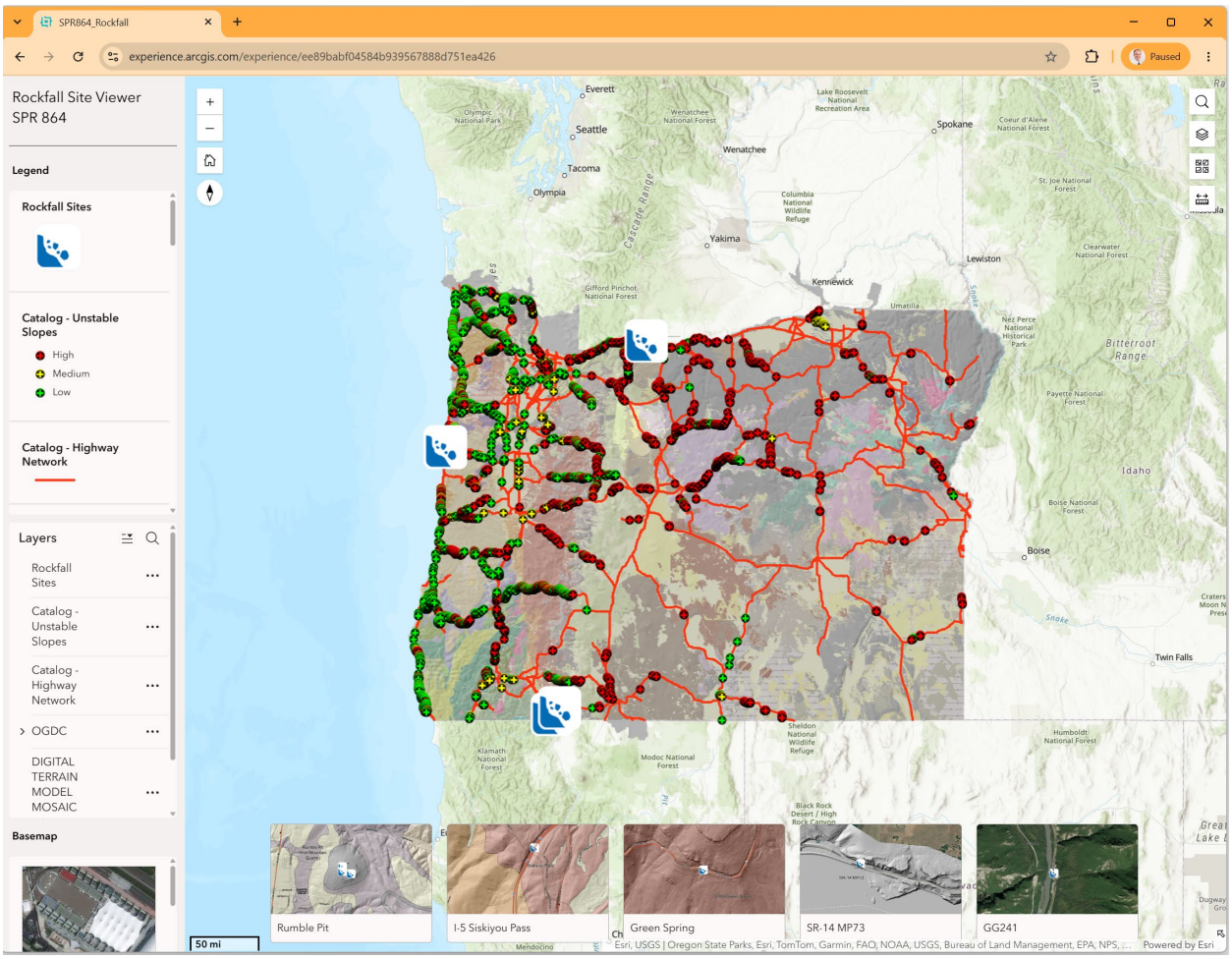

Figure 5.1. Main interface of the SPR864 Rockfall Site Viewer, showing the location so the sites, geology, and unstable slopes.

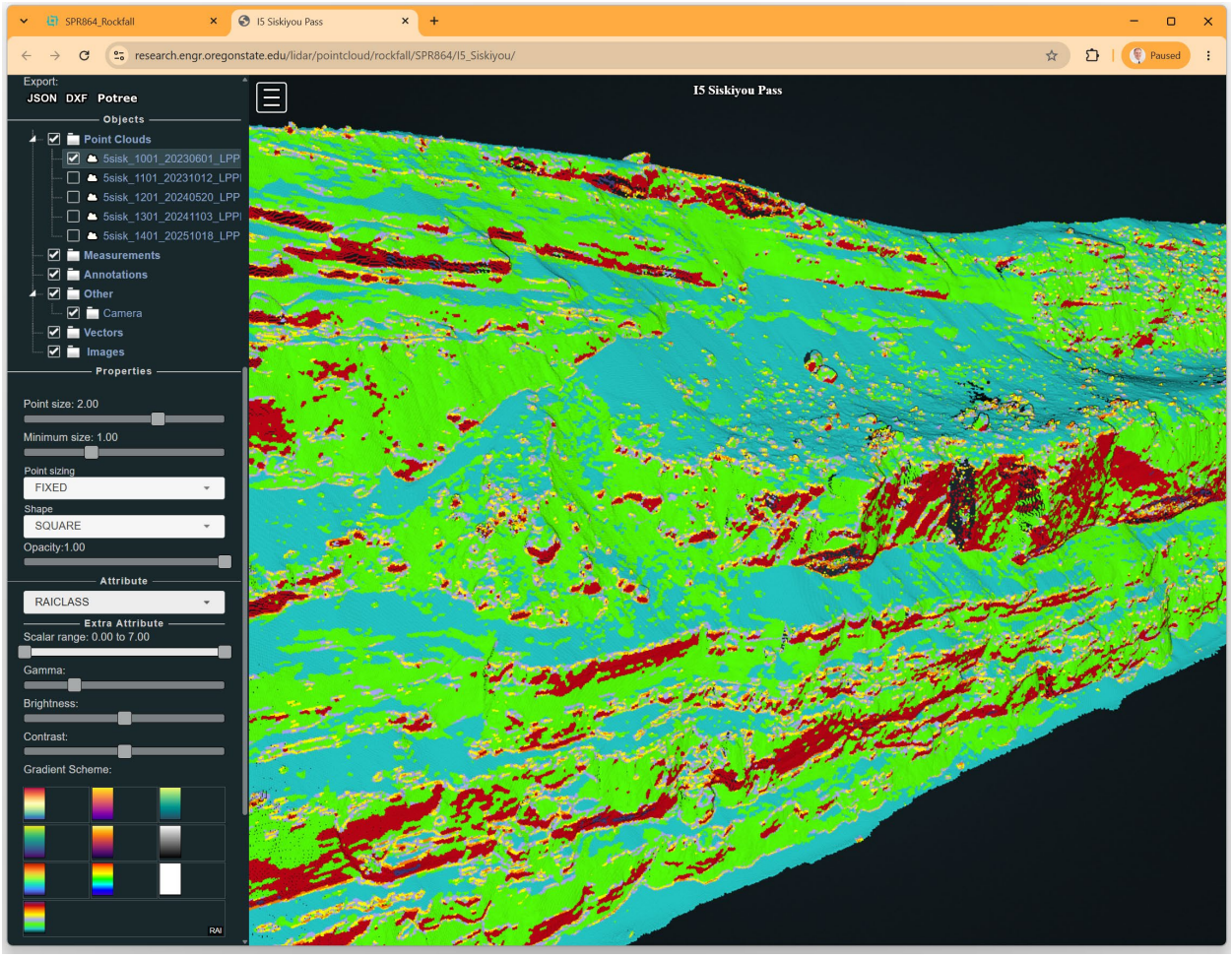

Figure 5.2. Example potree viewer for the I-5 Siskiyou dataset.

6.0 ANALYSIS METRICS

Several metrics can be extracted from the Rockfall Activity Index (RAI) morphological analysis and hazard scores. The RAI enables a detailed assessment of slope morphology and geological characteristics linked to significant improvements. As noted earlier in this report, rockfall hazards are evaluated in a two-step procedure in the RAI system (Dunham et al., 2017): first, morphological indices are used to classify mass wasting processes acting on a slope; next, these classifications are used with classification-specific instability or "activity" rates to map rockfall hazards across the slope face.

The metrics were developed to provide insight into the following questions:

- Before any mitigation, what was the morphological character of the rockslope (e.g., highly discontinuous, with significant overhangs, relatively intact, etc.)? How spatially heterogeneous (i.e., different RAI slope classes in close proximity) or homogeneous (i.e., dominated by a limited number of RAI slope classes) is the rockslope? What are the "baseline" (i.e., pre-mitigation) rockfall activity rates for the RAI classes present?

- Where was the scaling done, and did it change the rockslope? Specifically, how did mitigation affect the distribution of RAI morphological classes, if at all? How did the activity rates change, and how does this vary with time following a mitigation activity?

- How does mitigation change the character of the rockfall? That is, how do the (volume) magnitude-frequency (M-F) relationships change, if at all? (Here, note that the vertical position of M-F power law fit curves scale with overall rockfall activity, and steeper M-F curves imply that smaller events govern rockfall activity, and vice versa).

To help answer these questions, three categories of metrics were employed: global, morphological classification, and slope performance metrics. These metrics were applied both to the Rumble Pit controlled field site, where extensive pre-mitigation baseline scans were obtained prior to a well-documented scaling operation, and the Oregon /Washington sites, where pre- and post-mitigation scans enable an independent evaluation of scaling effectiveness. Together, these sites span a range of initial slope conditions, mitigation intensities, and monitoring durations, providing a basis for generalizing findings about mitigation performance. A separate rockfall trajectory analysis, described in Section 6.0, complements the RAI-based metrics by evaluating the runout behavior and energy delivery of individual rockfall events sourced from the lidar-derived terrain models.

6.1 GLOBAL METRICS

Global metrics provide summary-level characterizations of rockslope behavior that can be compared across pre- and post-mitigation epochs and, where appropriate, across sites. They are

particularly well-suited to communicating the overall efficacy of mitigation efforts in terms that are directly relevant to asset management and maintenance planning.

6.1.1 RAI Site Score

The RAI score is the estimated annual kinetic energy that rockfall produces along discrete 1-m length segments, or "bins," of the slope face. For a given site, the per-bin RAI scores can be summed to determine an overall RAI score for the entire site. Because the RAI score integrates both morphology (through the classification scheme) and kinematics (through the free-fall height and failure mass computation), it captures not only changes in the types of material present on the slope surface but also the spatial redistribution of hazardous material following mitigation. For example, scaling that removes overhanging rock near the top of a tall slope produces a disproportionately large reduction in the RAI site score relative to the same volume of material removed from the slope base, owing to the height-squared dependence of kinetic energy on release elevation. The RAI site score thus provides a physically meaningful, size-normalized measure of mitigation effectiveness.

Interpretation of changes in the RAI site score must account for several sources of complexity. First, post-mitigation scans may capture a larger portion of the slope face than pre-mitigation scans, for example because scaling removes vegetation, talus, or other obstructions that previously limited scan coverage. An increase in total classifiable slope area will tend to increase the summed RAI score independent of any change in slope activity, and comparisons must therefore be normalized appropriately. Second, scaling operations at highly active sites may temporarily increase apparent activity rates in the period immediately following mitigation, as newly exposed surfaces adjust to changed stress conditions before stabilizing. The temporal evolution of the RAI site score across successive post-mitigation monitoring epochs is therefore as informative as the immediate post-mitigation comparison.

6.1.2 Per-Class Instability Rates and Failure Depths

In addition to the overall RAI site score, changes in the per-class instability rates (r) and average failure depths (D) provide finer-grained insight into how mitigation alters the mass-wasting behavior of individual morphological units. The instability rate represents the fraction of cells within a given morphological class expected to fail during a given year; the average failure depth represents the mean depth of material removed per failed cell. Together, these parameters govern the per-cell contribution to the RAI computation (Dunham et al., 2017) and determine how the overall hazard is distributed across the seven RAI classes.

Markus et al. (2023) demonstrated, using a five-year inventory of 4,381 rockfall events at four Alaskan sites, that r and D vary substantially both among RAI classes and across time at a given site. The revised default values from that study (Table 2-6) serve as an empirical reference against which site-specific pre- and post-mitigation values can be compared. A post-mitigation reduction in r for overhang classes (Oc, Os), for example, would indicate that scaling successfully removed the most kinematically unstable surface material, while a corresponding increase in the proportion of the slope classified as intact rock (I), which carries the lowest default instability rate, would provide corroborating morphological evidence of improvement. Temporal trends in r and D across successive post-mitigation monitoring epochs further allow

assessment of whether mitigation effects are sustained or whether rates return toward baseline levels over time.

6.1.3 Magnitude-Frequency Relationships

Magnitude-frequency (M-F) relationships provide a quantitative, scale-independent characterization of the statistical distribution of rockfall event sizes at a site and serve as a key metric for evaluating whether scaling altered the overall rate or size distribution of rockfall events. As described in Section 2.4.3, rockfall event volumes at a site have been widely shown to follow a negative power-law scaling relationship (e.g., Barlow et al., 2012; Markus et al., 2023), expressed in non-cumulative form as:

$$f(V) = \beta V^{-\alpha} \tag{6-1}$$

where $f(V)$ is the non-cumulative frequency of events of volume V, β is the activity parameter, and α is the scaling parameter. Markus et al. (2023) demonstrated that both parameters vary significantly among RAI classes, among sites, and from year to year at the same site, confirming their sensitivity to both site-specific geologic and hydrologic conditions and to temporal forcing by weather and climate.

In the context of mitigation assessment, changes in β and α between pre- and post-mitigation epochs carry distinct physical interpretations. A reduction in β indicates an overall decrease in rockfall activity frequency, that is, fewer events per unit slope area per year at all volume scales, which is the expected signature of effective scaling. A change in α describes a shift in the relative proportion of large to small events: a steeper post-mitigation α (higher value) indicates that smaller events dominate more strongly following mitigation, consistent with the removal of large, structurally unstable blocks; a shallower α suggests that large events continue to govern the hazard, potentially indicating that the scaling did not adequately address the primary failure mechanisms at the site.

Comparison of pre- and post-mitigation M-F curves also provides a means of assessing whether the character of rockfall activity, not just its rate, has changed following mitigation. If scaling preferentially removes overhanging rock and widely spaced discontinuous material, the post-mitigation M-F distribution would be expected to shift toward smaller event volumes and steeper power-law slopes, as the residual slope surface becomes dominated by more finely fragmented or intact material with lower per-event failure volumes. Conversely, if scaling destabilizes adjacent material or introduces new large failure surfaces, the post-mitigation M-F curve might shift upward or flatten, signaling an increase in hazard rather than a net reduction.

M-F relationships were computed using the connected-components clustering approach implemented in *Rambo* (Olsen et al., 2015; 2020), following the methodology described in Markus et al. (2023) and the change analysis framework detailed in Section 6.0. Power-law parameters were fit to the linear portions of the cumulative M-F distributions on log-log axes, with a low-end roll-off applied at event volumes below the detection threshold associated with the 0.05 m significant change threshold used in the change detection analysis.

6.2 MORPHOLOGICAL CLASSIFICATION / ROCK SLOPE SURFACE ASSESSMENT

Morphological classification metrics evaluate changes in the distribution of RAI classes across the slope face between pre- and post-mitigation epochs. Because each RAI class is associated with characteristic mass-wasting processes and distinct instability rates (Dunham et al., 2017; Markus et al., 2023), shifts in the areal proportion of the slope occupied by each class provide direct evidence of how mitigation has altered the physical character of the slope surface. These metrics are expressed both in absolute terms (square meters) and as a proportion of the total classifiable slope face area, to account for any changes in the extent of the scanned area between epochs. The following morphological variables were evaluated:

- **Reduction in overhang area (Oc and Os):** Cantilevered and shallow overhangs represent the highest-risk morphological features on a typical transportation corridor rock slope. They exhibit comparatively large failure volumes, are susceptible to sudden tensile failure, and produce the highest kinetic energy delivery to the road surface per unit of failed area (Dunham et al., 2017) because they are typically located high on the slope face. A measurable post-mitigation reduction in the areal extent of Oc and Os therefore represents one of the most direct and consequential indicators of successful scaling. Changes in overhang area are assessed both globally across the entire site and locally along individual 1-m bins to identify whether improvements are spatially concentrated or broadly distributed across the slope face.

- **Increase in intact rock (I) area:** The intact rock class carries the lowest default instability rate among the non-talus classes and is associated with gradual surface erosion and raveling rather than discrete block failure (Dunham et al., 2017). An increase in the proportion of the slope surface classified as intact following scaling is consistent with the removal of overlying discontinuous or overhanging material to expose more competent, less fractured rock beneath. This metric serves as a complementary indicator of surface improvement that is independent of the overhang metrics.

- **Transition from fragmented discontinuous (Df) to widely spaced discontinuous (Dw) rock:** Within the three discontinuous rock sub-classes, Df carries the highest activity rate and represents the most highly fractured, near-failure surface material. A post-mitigation shift toward Dw, which has wider joint spacing and lower default activity rates, indicates that scaling has reduced surface fragmentation, either by removing the most highly fractured material or by exposing fresher, more competent rock beneath. This metric is particularly relevant at sites characterized by interbedded lithologies where differential weathering preferentially generates fragmented surface material over time.

- **Change in talus area and distribution:** Following scaling, an increase in talus accumulation at the slope toe or on catch benches is expected, as dislodged material accumulates as debris. The temporal evolution of talus area in subsequent monitoring epochs, specifically whether talus continues to grow or stabilizes, provides important information about the durability of the mitigation effect. As noted by Markus et al. (2023), talus at road cut sites may also be influenced by highway maintenance activities that periodically remove

material from the slope toe, and this dynamic should be considered when interpreting post-mitigation talus metrics.

6.3 SLOPE PERFORMANCE

Slope performance metrics capture the observable, practical consequences of rockfall activity for infrastructure maintenance and safety, complementing the morphological and statistical metrics described above.

- **Volume of talus accumulating on benches and at the slope toe:** The volumetric rate of debris accumulation at the base of the slope and on any intercepting benches provides a direct measure of the ongoing material flux from the slope surface. A post-mitigation reduction in the accumulation rate can be assessed by comparing debris volumes computed from successive change detection epochs. This reduction indicates that the slope is producing less rockfall material per unit time, consistent with a reduction in overall slope activity. This metric is also directly relevant to ODOT's maintenance planning, as it can be translated into an estimate of the frequency and cost of debris removal operations required to maintain the functional capacity of the catch ditch.

- **Spatial distribution of rockfall debris as a function of distance from the slope toe:** The spatial extent of rockfall deposit distribution provides information about the kinetic energy of individual events and the effectiveness of existing catchment features. Large, energetic events that deposit material far from the slope toe represent a greater threat to the travel lane than small, low-energy events that arrest within the catch ditch. A post-mitigation reduction in the maximum runout distance of deposited material, or a concentration of deposits closer to the slope toe, would indicate both a reduction in event magnitude and a decrease in the kinetic energy of individual failures. This metric is evaluated in conjunction with the rockfall trajectory analysis described in the following section, which provides a physics-based framework for estimating runout distance and energy delivery from lidar-derived source zones.

6.4 ROCKSLOPE IMPROVEMENT PERFORMANCE PREDICTION

Beyond characterizing observed pre- and post-mitigation slope behavior, this research also explored how improvement techniques such as scaling may augment stored potential energy (E, Joules) in the rockslope from the modification process itself, and how that energy is subsequently released through natural rockfall in the period following mitigation. Consideration of this energy rate and comparison between scaled and unscaled rockslopes, which is associated with rockfall volume (V, m^3), enables evaluation of how scaling may affect the rates and frequency patterns of rockfall hazard and associated risk. For example, these comparisons can be used to determine how intermittent, episodic, or regular rockfall is following mitigation; that is, whether scaling produces a concentrated burst of rockfall activity over a short period before stabilizing, or whether it results in less frequent but less predictable activity over a longer period.

As a quantitative measure to perform this assessment, we used volume-frequency relationships that describe the frequency ($F(V)$, m^{-3}) of rockfall volumes to characterize (1) removal of blocks from scaling, (2), natural rockfall frequency in unscaled rockslopes, and (3) subsequent rockfall

volumes following scaling or natural failure, all of which are defined using a power-law with coefficients (α, β) as:

$$\boldsymbol{F(V) = \alpha V^{\beta}}$$

(6-2)

By evaluating rockfall volumes that source from within or adjacent to the boundaries of scaled or naturally failed blocks of known volumes, we can associate how removal of a rockfall volume V_s may result in a specific, scaled distribution of subsequent rockfall of volume (V_{s-f}). We can compare these frequencies to similar evacuated rockfall following natural rockfall events (V_{n-f}) to compare whether statistically significant differences exist.

These three-dimensional initial failure magnitude-post-failure magnitude-frequency relationships (i.e., using bins of original rockfall, natural or scaled, to develop a magnitude-frequency relationship of subsequent rockfall volumes) was explored for various morphologies, such as those associated with source elevation, local slope, curvature, climate forcing (freeze/thaw, temperature) and/or RAI classes. This enables association of potential energy of initial and associated subsequent rockfall as a means of constraining rockfall hazard associated with scaling and natural rockfall. The rockfall following natural or scaled failure was also evaluated in time-dependent form as a rate ($R(V)$, m^3/day), defined using similar scaling relationships as:

$$\boldsymbol{F(R(V)) = \alpha R(V)^{\beta}}$$

(6-3)

These rates will enable understanding of how more protracted rates of different rockfall volumes from natural forcing *and subsequent evacuation of associated rockfall* differ from the timescales associated with scaling. Again, these data were parsed based on various measured climatic data and rockslope morphology. Equations 5-1 and 5-2 can leverage the associated potential energy in either energy-frequency relationships or as a time-dependent relationship (i.e., similar to Equation 5-2) to evaluate the time-dependent rockfall hazard associated with scaling and natural rockfall.

7.0 ROCKFALL TRAJECTORY ANALYSIS

The rockfall trajectory analysis consists of two primary procedures. The first procedure performs a change analysis based on the DEMs produced by the *Rambo* software. The second then performs physics trajectory analysis to determine where rocks will land when released from the slope. This section describes the fundamental mathematics and physics implemented for the trajectory analysis.

7.1 CHANGE ANALYSIS

For a given rockfall analysis, we use a DEM derived from terrestrial laser scanning to serve as potential rockfall sources and a possible surface for collision, represented as a psuedogrid with pixel dimensions of dx. The given DEM is rotated in space based on the best-fit plane for differencing, represented laterally with dimensions in the x, y and z space, with differences in z used to establish change between epochs ($\Delta z_{t/t-1}$), where change between epoch $t-1$ and t are defined as:

$$\mathbf{z}\Delta z_{t/t-1} = z_{t-1} - z_t \tag{7-1}$$

For this change, negative values represent erosion and positive values represent accretion stemming from rockfall or deposition, respectively. We consider erosion alone for analysis of rockfall source zones. Owing to measurement accuracy, we consider erosion less than a significant change, Δz_{sig}, to be zero. To consider discrete rockfall source zones, we use a Connected Components analysis to catalog and index individual rockfalls (i) and their volumes (V_i), where the summation of volumes for specific cell indices within a given cluster represents its volume.

For a given epoch interval of Δt, the rockfall activity rate (L^3/T) can be determined through division of equation (Eq. 7-1) by the Δt for all observed rockfall erosion, or for erosion binned by rockfall volumes. This enables comparison of change over time.

For each epoch, the frequency of volumes or rates can be considered. The frequency is often represented with a power law (Williams et al., 2019; Graber and Santi, 2022) in the form of:

$$f = aV^b \tag{7-2}$$

where f is the frequency (frequency, normalized probability, or frequency rate), a and b are scaling coefficients, and V is rockfall volume. These relationships present a means of comparing the dominance of various rockfall sizes or when not normalized, the relative increase or decrease in rockfall rates versus size for various epochs. There may be a sensitivity to epoch interval for

these relationships, but they tend to be insensitive beyond several month intervals (Williams et al. 2019).

7.2 ROCKFALL TRAJECTORY MODEL METHODOLOGY

A 3D rockfall trajectory model and associated algorithms for impact, sliding, bouncing, and computation of energy are described herein. Each rockfall is initially considered as a cube with side length d and density ρ. The mass of a rockfall (m_0) will govern its potential energy (PE), kinetic energy (KE), and depending on modelling choices, the restitution associated with momentum. The overall mass (m_0) of a given rockfall is defined as:

$$\boldsymbol{m_0 = \rho \mathrm{d}^3}$$

(7-3)

As real rockfalls are of irregular shapes and volumes and simulated rockfalls may be of any volume, we make a simplifying assumption that rockfalls are spherical in shape. To do this, we calculate an equivalent spherical radius, defined as:

$$\boldsymbol{r_{eq} = \left(\frac{\mathrm{d}^3 \cdot 3/4}{\pi} \right)^{1/3}}$$

(7-4)

As the best fit plane used for differencing rockfalls does not represent the real orientation of a rockslope in space, the rockslope is transformed to determine the vector that represents "down", which is used to define gravitational acceleration (a_g) in the x, y and z space as g_x, g_y, and g_z, respectively. The orientation of gravity is thus defined according to the unit vector that reflects "true vertical" as:

$$\boldsymbol{a_g = 9.81 \left(g_x, g_y, g_z \right)}$$

(7-5)

For a given timestep dt, the location (x_r, y_r, z_r), velocity (v_x, v_y, v_z), and acceleration (a_x, a_y, a_z) of a given rockfall is explicitly updated based on its current location (x_{ro}, y_{ro}, z_{ro}), velocity (v_{xo}, v_{yo}, v_{zo}), and acceleration (a_{xo}, a_{yo}, a_{zo}) where:

$$\boldsymbol{v_x = v_{xo} + 0.5(a_{xo} + a_x)dt}$$

(7-6a)

$$\boldsymbol{v_y = v_{yo} + 0.5\left(a_{yo} + a_y\right)dt}$$

(7-6b)

$$\boldsymbol{v_z = v_{zo} + 0.5(a_{zo} + a_z)dt}$$

(7-6c)

$$\boldsymbol{x_r = x_{ro} + 0.5(v_{xo} + v_x)dt}$$

(7-6d)

$$\boldsymbol{y_r = y_{ro} + 0.5\left(v_{yo} + v_y\right)dt}$$

(7-6e)

$$\boldsymbol{z_r = z_{ro} + 0.5(v_{zo} + v_z)dt}$$

(7-6f)

In absence of accelerations other than gravity, equations Eq. 7-6a to Eq. 7-6c simplify to the form of $v = v_o + gdt$. However, if chosen, seismic accelerations or other impulse loads could be considered in theory. For simplicity, we do not consider rotational velocities in this analysis as they are difficult to constrain and often play a smaller role than translational velocities in the overall trajectory of small to medium rockfalls.

In an analysis, numerous rockfall will impact terrain, and accurately characterizing the timing and the geometry of the impacted surface is necessary to modeling the response trajectory of the projectile. An impact detection algorithm was developed, where the direct distance between a rockfall and the interpolated rockslope surface with respect to the best-fit plane, Δz, is considered for each rockfall during each time step, defined as:

$$\boldsymbol{\Delta z(t) = z(t) - z_{surf}(x, y)}$$

(7-7)

where z_{surf} is the interpolated rockslope surface at the rockfall coordinates x and y for a given time t. The impact algorithm is triggered when $\Delta z \leq 0$, suggesting contact or penetration with the surface. Similar rockfall algorithms are employed in other trajectory analyses (Stevens, 1998). When using sufficiently small timesteps (e.g. 1ms in this analysis), the penetration depth of the rockfall is generally minor.

When impact is detected, the velocity before impact has to be decomposed to a rebound velocity that is a function of the normal vector at the rockslope surface and the restitution model considered. In vector form (shown in bold), velocity (presented in equations Eq. 7-6a to Eq. 7-6c) is decomposed into components normal and tangential to the impacted surface, defined as:

$$\boldsymbol{v_n = (v \cdot n)\, n}$$

(7-8)

$$\boldsymbol{v_t = v - v_n}$$

(7-9)

The updated normal and tangential velocities are thereafter scaled by a normal coefficient of restitution (e_n) and tangential coefficient of restitution (e_t), respectively. These coefficients depend on numerous factors, such as rock type, rock fracturing, weathering, shape of rockfall, and other factors, but range between zero and unity, where zero represents full loss of kinetic energy following and unity represents complete preservation of kinetic energy following impact. In the presented analysis, we consider restitution as a function of velocity and rockfall volume (i.e. momentum) modified from the approach proposed by Gischig et al. (2015). For momentum-dependent restitution, we define normal and tangential restitution as:

$$\boldsymbol{e_n = \frac{R_n}{dV_n^2 + R_n}}$$

(7-10)

$$\boldsymbol{e_t = \frac{R_t}{\mathrm{d}V_t^2 + R_t}}$$

(7-11)

where R_n and R_t are reference hyperbolic coefficients for deformation energy values when restitution is 0.5. For scalar restitution, R_n and R_t represent normal and tangential restitution, respectively. Normal and tangential velocities ($\boldsymbol{v_n'}$ and $\boldsymbol{v_t'}$, respectively) after applying restitution are considered as:

$$\boldsymbol{v_n' = -e_n\, v_n}$$

(7-12a)

$$\boldsymbol{v_t' = e_t\, v_t}$$

(7-12b)

$$\boldsymbol{v' = v_n' + v_t'}$$

(7-12c)

Sliding can be considered when normal impact velocity is small (i.e. less than a predefined $v_{slide,min}$) and the rockslope surface slope angle (θ) exceeds the surface friction angle (ϕ), defined as:

$$\boldsymbol{v_n < v_{slide,min}}$$

(7-13a)

$$\phi < \theta < 90^{\circ}$$

(7-13b)

where sliding acceleration occurs in the maximum downslope tangential direction t_2, defined as and added to equations (7-9) and (7-6):

$$\Delta v_t = 9.81\,(\sin\theta - \cos\theta \tan\phi)\,\Delta t\, t_2$$

(7-14)

During each timestep, the potential energy with respect to the lowest elevation of the model (or any arbitrary datum), kinematic energy, and total energy can be calculated as:

$$KE = \frac{1}{2} m|v|^2$$

(7-15a)

$$PE = mgz$$

(7-15b)

$$E = KE + PE$$

(7-15c)

The analysis is performed for a preallotted amount of time selected by the user (e.g. 5 seconds) that is considered sufficient to allow all rockfalls to find their final resting location. Taller rockslopes may require more time, while shorter rockslopes require less simulation time. The given approach can be applied to observed rockfall sources and volumes or applied to each potential location on the rockslope as a source with given volume. These approaches allow consideration of observed rockfall hazard and potential rockfall hazard for a given rockslope morphology, respectively.

1.1TRAJECTORY ANALYSIS AND VISUALIZATION TOOL

A prototype app, Rockit (Rockfall impact and trajectory), was developed to implement and test the methodology presented in this chapter as well as visualize the results. Two complementary desktop applications were created: the ROCKIT Analyzer and the ROCKIT Visualizer. Together, these tools execute the workflow for identifying observed rockfall events from multi-temporal terrain data, simulating their potential trajectories, summarizing trajectory characteristics, and interactively reviewing and communicating the resulting spatio-temporal information produced. A demonstration video was also produced to show how to execute the tool.

7.2.1 ROCKIT Analyzer

The ROCKIT Analyzer (Figure 7-1) executes the primary computational workflow. The tool uses repeat digital elevation models (DEMs) from Rambo and associated terrain information to identify areas of topographic change associated with rockfall activity. Individual rockfall events are delineated as spatially connected clusters, and event-level attributes such as location, area, estimated volume, slope, roughness, and temporal occurrence are calculated. These data can subsequently be used to evaluate rockfall rates, magnitude-frequency relationships, and changes in activity through time.

A key component of the Analyzer is the physics-based rockfall trajectory simulation. Trajectories can be modeled for specified rock sizes as well as for individual observed rockfall events. For observed events, the estimated event volume is used to determine rock mass and an equivalent rock size, while the mapped source area provides the initial release location. The trajectory model then evaluates rock motion over the three-dimensional terrain surface using parameters describing gravity, terrain orientation, restitution, friction, and rock properties. The resulting trajectory histories include three-dimensional position, kinetic energy, potential energy, total energy, lateral reach, and fall height.

The Analyzer is designed to process multiple survey epochs and, where desired, multiple analysis models or sites in batch. A graphical user interface allows key analysis parameters and input datasets to be specified without editing the underlying Python code. During processing, a dedicated progress window displays command-line-style output so that users can follow individual stages of the analysis, including event processing, trajectory simulations, and epoch-by-epoch progress. A notification is provided when processing is successfully completed, while error information is retained in the progress window to facilitate troubleshooting. Analysis outputs are stored in Python pkl files that preserve the calculated event, terrain, and trajectory information for subsequent visualization and additional analysis.

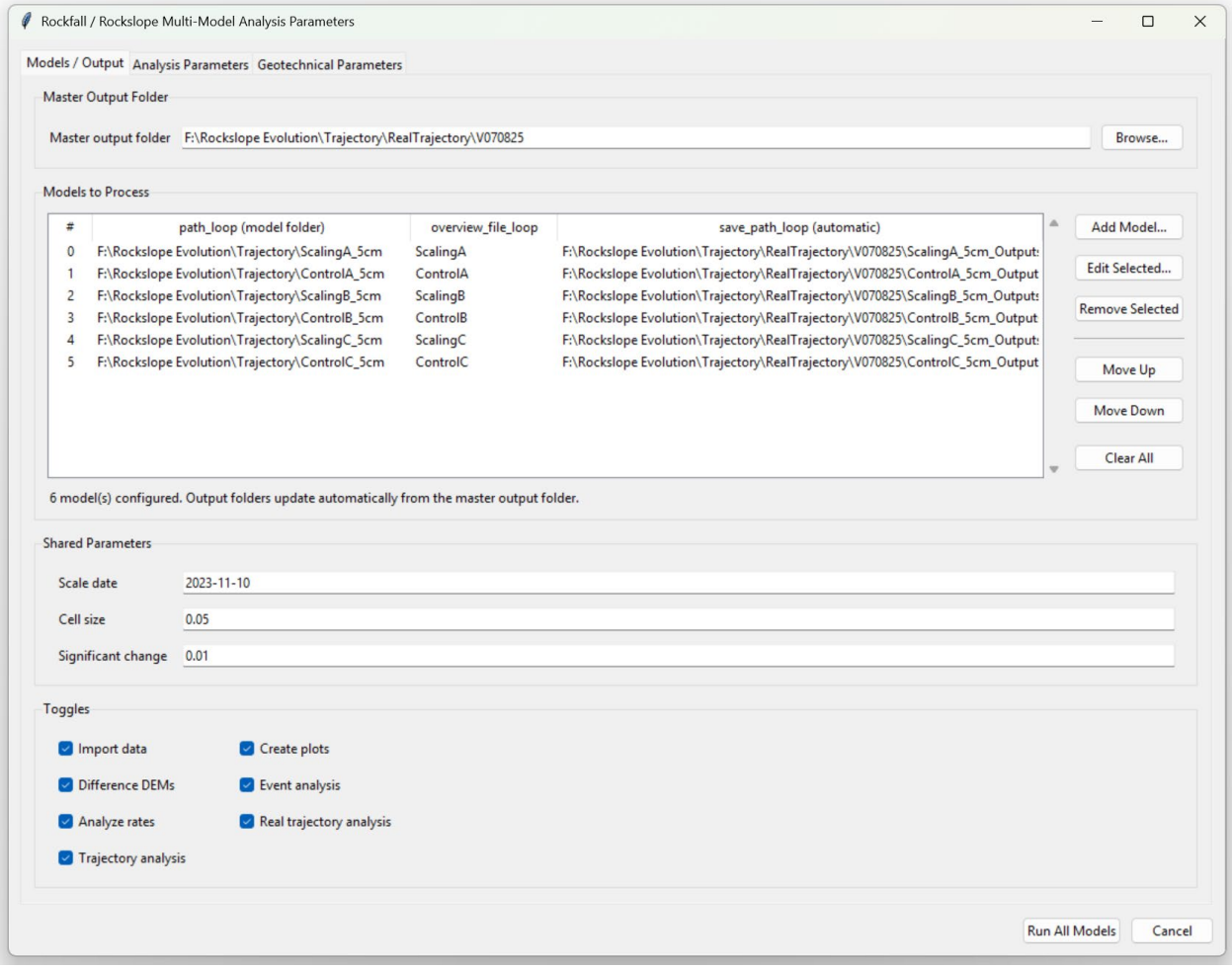

Figure 7.1. Main GUI of the Rockit analyzer tool

7.2.2 ROCKIT Visualizer

The ROCKIT Visualizer (Figure 7-2) provides an interactive environment for reviewing the trajectory results generated by the Analyzer. The application displays the DEM as a three-dimensional terrain surface and can overlay the complete trajectory of each modeled rockfall event, including its starting and ending positions. Users can rotate, pan, and zoom the display, switch between perspective and orthographic projections, specify a Z-axis viewing rotation, or quickly set the display to a north-oriented plan view. The DEM, trajectory lines, and start/end points can each be displayed or hidden as needed.

Trajectory results can be colored using several approaches. Features may be colored sequentially by trajectory index, by lateral reach, or by the maximum kinetic energy calculated for each trajectory. Kinetic-energy coloring uses a logarithmic color distribution to better represent the wide range of energies commonly associated with rockfall events, while the displayed color scale retains the actual kinetic-energy values for interpretation. Users can also specify the range of survey epochs to include in the visualization, allowing selected time periods to be examined independently.

In addition to interactive review, the Visualizer provides tools for producing presentation and reporting products. The current view can be exported as a high-resolution screenshot, and animated AVI files can be generated using the user-selected view orientation, projection, epoch range, color mode, and display settings. During animation, individual rocks move along their calculated trajectories while the corresponding trajectory lines progressively grow with time, providing an intuitive representation of rockfall movement across the terrain.

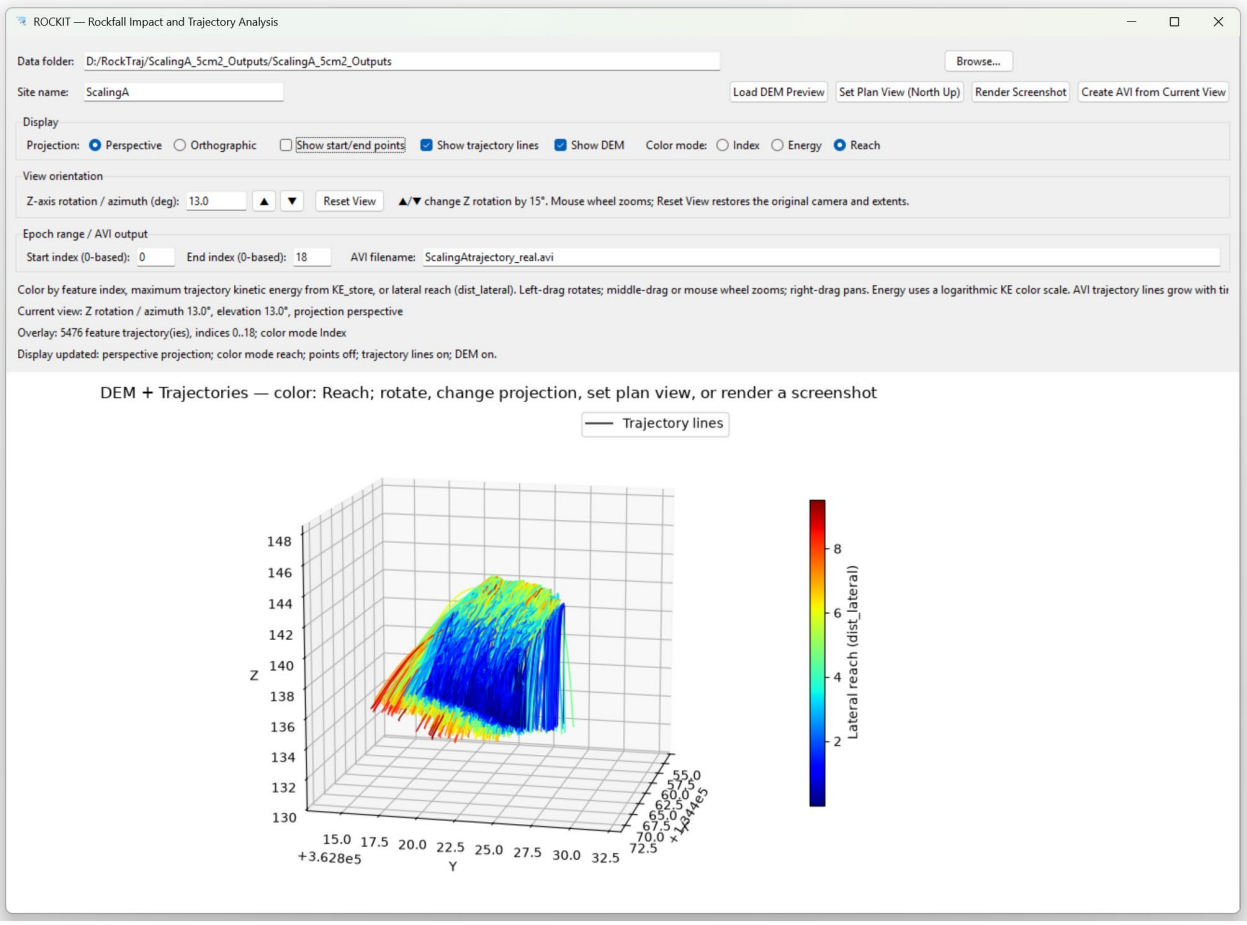

Figure 7.2. Main GUI of the Rockit visualizer tool

8.0 RUMBLE PIT ANALYSIS

This section presents comparative results for each of the three Rumble Pit scaling sites (A, B, and C) described in Section 4.0. Each scaling site was paired with an adjacent control site that was not subject to mitigation, enabling direct comparison of post-scaling slope behavior against background rockfall activity under equivalent environmental forcing conditions. The analysis applies the metrics defined in Section 6.0 and the trajectory modeling methods described in Section 7.0, and consists of the following components:

- RAI analysis. Comparison of the change in percent area of the slope across each RAI class between the scaling site and its paired control site, referenced to the scaling operation performed on 11/10/2023. The 9/29/2023 survey was used as the pre-scaling reference epoch due to data loss on the 11/9/2023 survey associated with rainfall. Results are also presented as time-series plots of the percent area occupied by each RAI class for each monitoring epoch, enabling assessment of both the immediate post-scaling morphological response and any subsequent temporal evolution.

- Rates and Volumes. Time-series plots of cumulative erosion, expressed as a normalized ratio of volume to surface area, comparing the scaled and control rockslopes across all monitoring epochs.

- Volume Frequency Analyses. Plots comparing power-law magnitude-frequency relationships, normalized by rockslope area and monitoring duration, for the scaled and control rockslopes. These relationships enable assessment of whether scaling altered the overall rate or size distribution of rockfall events.

- Trajectory Analyses. This analysis is subdivided into two sections:

    - Retrospective Trajectory Analysis (RTA): Plots showing the spatial distribution of rockfall deposits at the base of the cliff, together with exceedance probability curves for normalized travel distance and kinetic energy.

    - Probabilistic Trajectory Analysis (PTA): Plots of modeled rockfall trajectories, travel distances, and heat maps of impact locations across the slope face under pre- and post-scaling conditions.

8.1 SCALING SITE A

8.1.1 Scaling procedures

Figure 8-1 presents photographs of Scaling Site A at the Rumble Pit prior to the scaling operation. The exposed rock mass is a dark gray to black mafic volcanic unit consistent with the Siletz River Volcanics (wells et al. 2014) that characterize the Oregon Coast Range. The slope face displays a blocky to tabular rock mass fabric defined by at least two prominent joint sets: a steeply dipping to sub-vertical set that produces columnar to platy block geometry, and a second

set at moderate to shallow angle that intersects the first to define slab dimensions. Zones of reddish-brown to orange oxidation staining are visible, particularly in the upper-central portion of the face, indicating iron oxide weathering along preferential fluid pathways. A weathering gradient is apparent from the crest downward, with the upper zone near the vegetation line exhibiting more advanced disaggregation. The overall rock mass quality appears to range from poor to fair, consistent with the highly fractured and weathered character typical of this quarry exposure.



(a)



(b)



(c)

Figure 8-1. Scaling Site A (a) before (September 29, 2023), (b) during (November 10, 2023), and (c) after (November 10, 2023) scaling operations. A scaler standing on the slope provides scale.

Workers performed manual hand scaling on the upper half of the slope over a period of several hours. The operation relied on metal bars and pry tools to dislodge loose material, targeting both visibly precarious blocks and material that could be removed with modest effort, an approach consistent with the general hand scaling practice documented by Beckstrand et al. (2020), in which scalers work systematically across the slope face to remove unstable surface debris without extensive pre-selection of specific targets.

8.1.2 RAI Analysis

The RAI analysis for scaling site A (Figure 8-2 and Figure 8-3) reveals a moderate morphological response to the scaling operation. Intact rock area increased by approximately 2% and shallow overhang area decreased by a corresponding margin, while the remaining RAI classes showed comparatively small changes. The paired control site exhibited minimal class redistribution across all epochs, confirming that the observed shifts at the scaling site are attributable to the mitigation rather than to background environmental forcing. The time-series plot of RAI class percentages (Figure 8-3) demonstrates that the class distribution remained largely stable following the initial post-scaling redistribution, with no clear trend of reversion toward pre-mitigation morphology over the two-year post-scaling monitoring period.

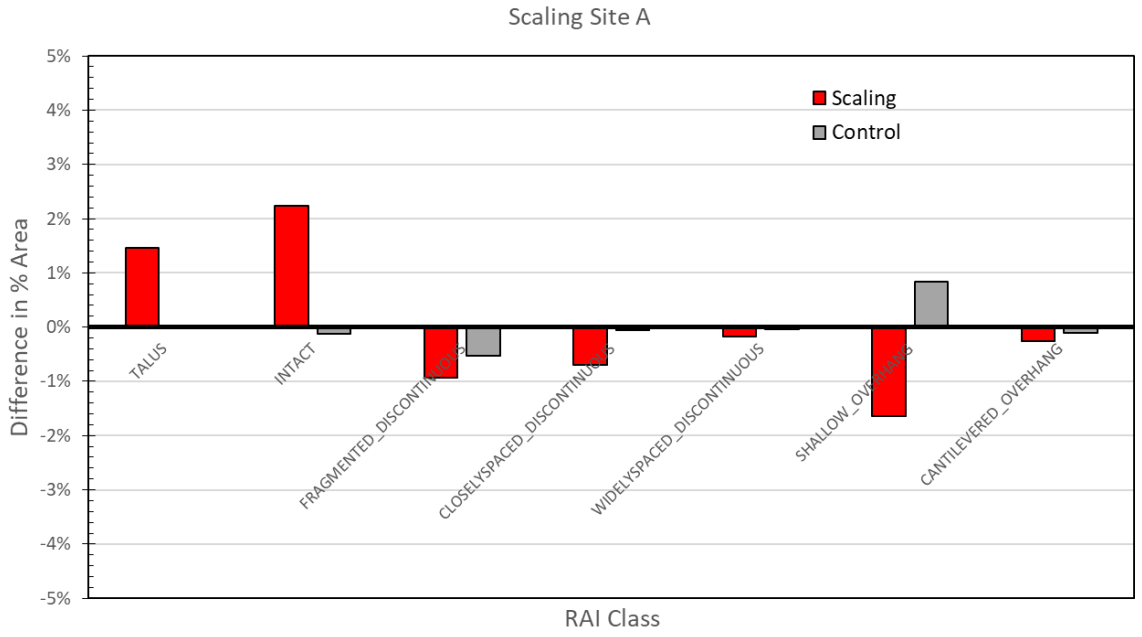

Figure 8.2. Changes in RAI classification resulting from the scaling operation for Scaling Site A and Control Site A. (11/10/2023 vs 9/29/2023).

The intact rock increase and shallow overhang decrease observed in Figure 8-2are directionally consistent with the removal of kinematically unstable surface material, representing the expected morphological signature of effective scaling as described in Section 6.2. The modest magnitude of these changes is consistent with a scaling operation that was limited to the upper half of the slope and conducted over a period of several hours using metal bars.

Figure 8-2 presents a bar chart comparing the difference in percent area for each RAI class between the scaled and control rockslopes at Site A. The scaling site (red bars) shows the characteristic morphological signature of effective scaling: intact rock increased by approximately 2%, while fragmented discontinuous and shallow overhang both decreased by roughly 1–2%. Talus shows a very modest increase, consistent with debris generation from the scaling process. The closely spaced discontinuous and widely spaced discontinuous classes show small decreases. The control site (gray bars) shows minimal changes across all RAI classes, with no class changing by more than approximately 1%, and notably, the shallow overhang class at the control site shows a slight increase—the opposite direction from the scaled site. This contrast between the scaled and control responses provides evidence that the RAI changes at the scaling site are attributable to the scaling operation rather than to ambient environmental processes occurring during the same period. The magnitude of the intact rock increase at Site A (approximately 2%) is modest compared to the larger-scale operations at SR14 MP73 (approximately 6.7%) or GG241, possibly reflecting the limited, hand-tool nature of the Rumble Pit scaling.

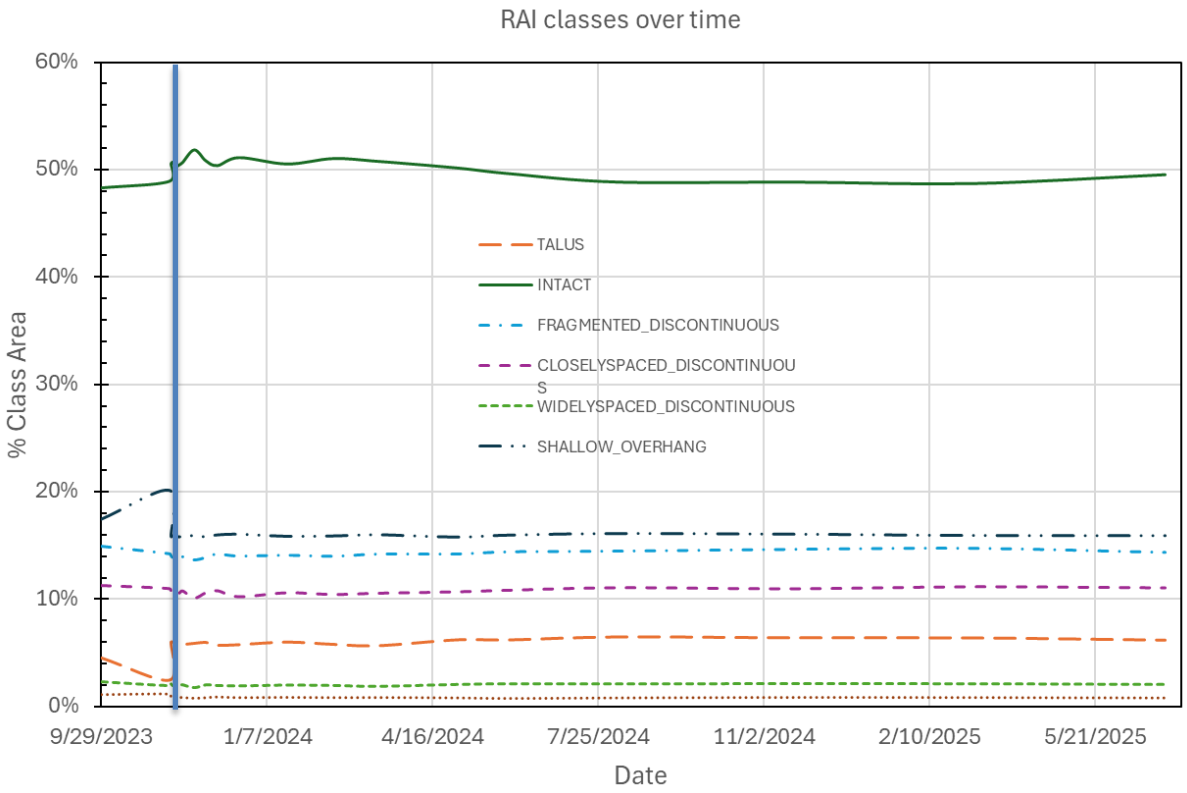

Figure 8.3. Changes in RAI classification percent areas over time for scaling Site A. The blue vertical line represents the date of scaling (11/10/2023)

Figure 8-3 shows the temporal evolution of RAI class proportions at Scaling Site A from September 2023 through approximately November 2025. The intact class dominates throughout, maintaining a level near 50–55% with a slight upward step at the time of scaling and then remaining relatively stable. It remained above the prescale levels for the monitoring period. The fragmented discontinuous class (approximately 15–20%) shows a brief perturbation near the time of scaling before stabilizing. The closely spaced discontinuous and widely spaced discontinuous classes each occupy approximately 5–10% and show modest fluctuations. The shallow overhang class declines slightly at the time of scaling and remains at the lower level. Cantilevered overhang remains near zero throughout. The overall stability of the RAI class proportions following scaling is notable: unlike the larger-scale sites in Chapters 9 and 10, where gradual post-scaling recovery is evident over months to years, Site A shows very little temporal evolution in its class distribution over the approximately 18-month monitoring period.

8.1.3 Rates and Volumes

8.1.3.1 Activity Rates

Figure 8-4 presents the daily activity rate at Scaling Site A compared with Control Site A in two panels. Panel (a) shows the full time series, including the pre-scaling baseline period. The scaling site (solid line) exhibits a sharp spike in activity rate at the time of scaling (day 0), reaching approximately 0.40–0.45. This elevated initial rate reflects the disturbance associated with the scaling operation and the subsequent adjustment of the "fresh" or newly exposed slope surface. Following the spike, activity rates at the scaling site decline rapidly and converge with the control site (dashed line) within approximately 100–200 days. The control site shows its own activity rate peak of approximately 0.20–0.25 during the same period, indicating that ambient conditions (likely the onset of the wet winter season in coastal Oregon) also elevated activity rates on unscaled slopes. Panel (b) focuses on the post-scaling period and fits logarithmic regression functions to both the scaling and control site data. The scaling site regression ($R^2 = 0.34$) shows a steeper initial decline than the control site regression ($R^2 = 0.15$), but the two curves converge by approximately 200–300 days after scaling. The similar logarithmic decay coefficients (−0.012 for both) suggest that the underlying rate of activity decline is governed by the same environmental processes at both rockslopes, while the initial offset reflects the additional disturbance from scaling.

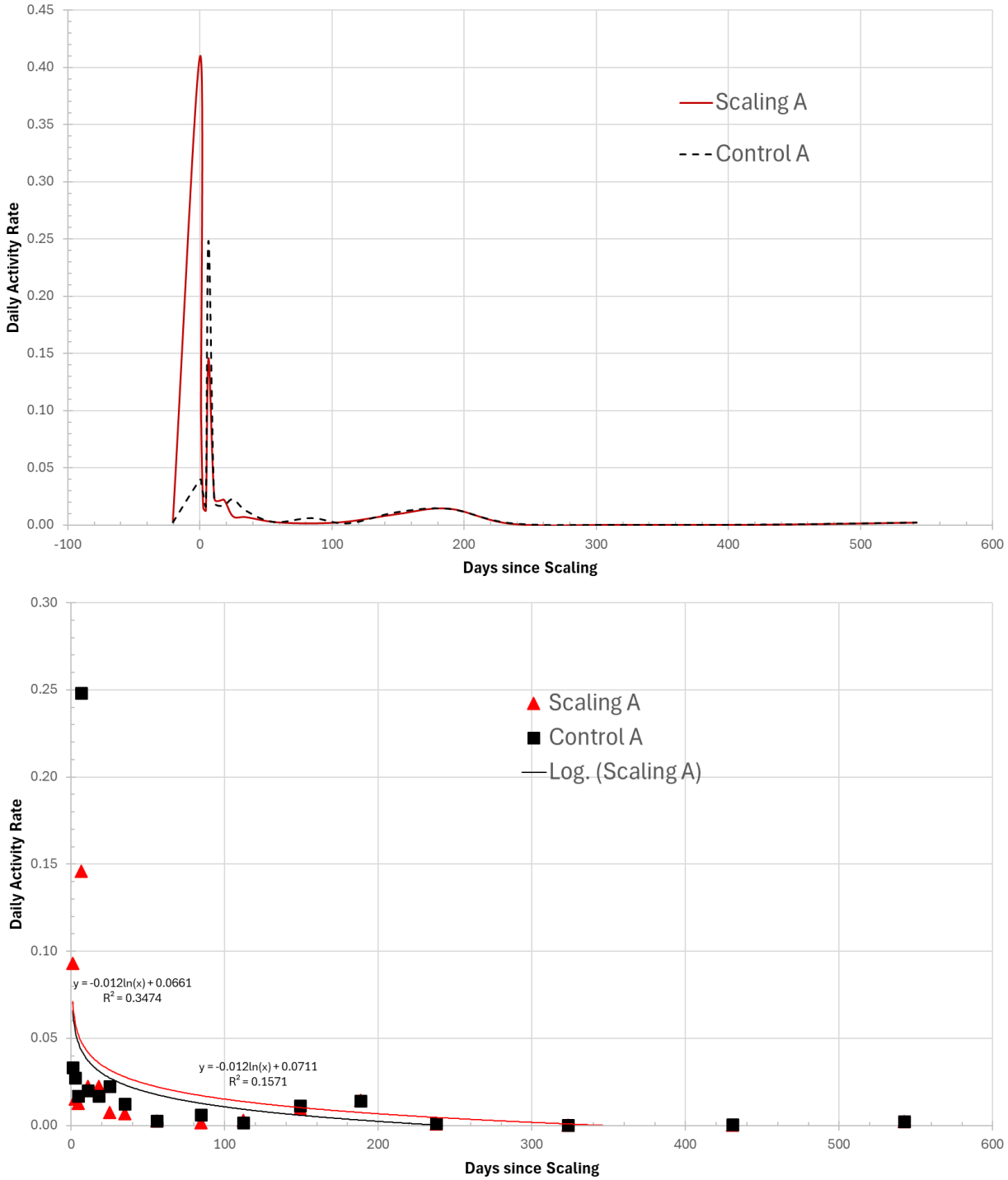

Figure 8.4. Changes in activity rates over time for scaling Site A compared with control site. (a) including baseline activity rates and (b) after scaling with regression functions.

8.1.3.2 Cumulative erosion volume

Cumulative erosion volume provides a means of quantifying how rockfall activity varies over time, particularly in relation to a scaling operation. For each rockslope, total erosion

volume is computed as a time integration of rockfall rate and normalized by rockslope surface area. When binned by rockfall size, these relationships illustrate the relative contribution of different event sizes to total volume change over time. Comparison of a scaled rockslope with a paired control rockslope sharing similar morphology, geology, and environmental forcing conditions allows differences in erosion volume to be attributed to the influence of scaling rather than to site-to-site variability.

Figure 8-5 presents three panels of cumulative rockfall erosion (area-normalized volume) for various size bins at both the scaled and control rockslopes at site A. The top panel shows the cumulative normalized erosion for the control rockslope, partitioned by volume bin. Larger rockfalls ($V > 0.01$ m³) constitute the majority of total erosion volume, with their contribution occurring in discrete step-like increments reflecting the sporadic nature of large events. Smaller rockfalls ($10^{-3} > V > 10^{-4}$ m³) contribute a more steady, continuous accumulation, and constitute a substantial proportion of total volume change, reflecting their comparatively higher frequency.

The central panel of Figure 8-5 shows the same analysis for the scaled rockslope, where the overall magnitude of cumulative erosion is visibly smaller than the control, particularly in the months immediately following scaling. The rates of volume change at the two slopes converged at approximately five months post-scaling. The largest rockfall bins show notably less step-like accumulation at the scaled slope, suggesting that scaling removed material that would otherwise have contributed to large discrete events.

The bottom panel of Figure 8-5 shows the ratio of scaled to control cumulative volume over time. This ratio is consistently below 1.0, confirming that the scaled rockslope accumulated less total erosion than the control throughout the monitoring period. The ratio is lowest in the first several months following scaling and gradually approaches 1.0 by approximately five months, suggesting that the differential benefit of scaling attenuates over time. The control rockslope experienced several larger rockfall events that the scaled rockslope did not, which may reflect either the removal of precarious blocks by scaling or inherent structural differences between the adjacent slopes. The largest changes and associated noise occur immediately following scaling. This initial variability may reflect rapid evacuation of material disturbed by the scaling operation or differencing errors introduced during shorter monitoring epochs.

The control rockslope experienced notably larger individual rockfall events during the observation period. Whether this reflects inherent structural differences between the two slopes or the effect of scaling in removing relatively large, unstable blocks is not possible to determine from the available data. The results at site A indicate that scaling produced a modest reduction in rockfall volume and frequency for a period of approximately five months following the operation.

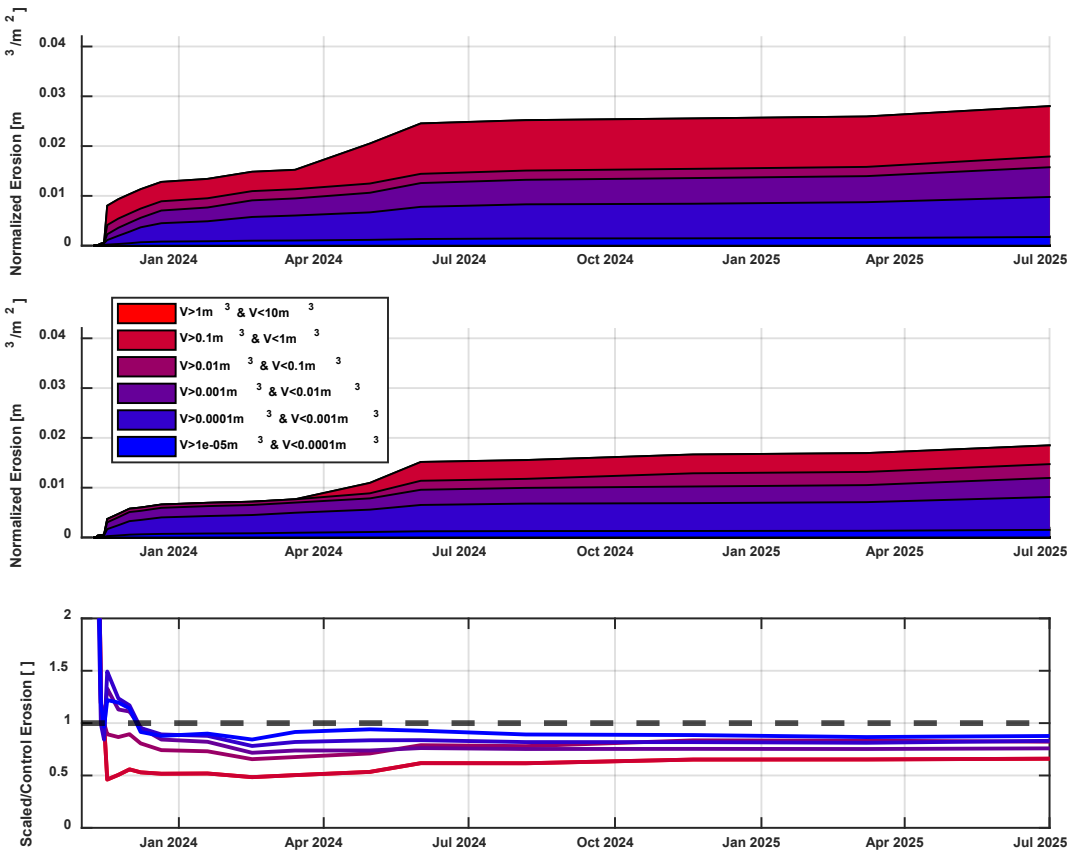

Figure 8.5. Cumulative normalized erosion for Control Rockslope A (top), Scaled Rockslope A (center), and ratio of scaled to control (bottom).

8.1.4 Volume-Frequencies

Magnitude-frequency relationships provide a means of characterizing rockfall hazard, and as described in Section 6.0, serve as an input to the trajectory modeling. Figure 8-6 compares volume-frequency relationships normalized by rockslope area and monitoring duration for the scaled and control rockslopes at site A for the first six months following scaling and for the period thereafter.

Figure 8.6 displays the magnitude-frequency relationships for Site A on log-log axes, comparing the scaled (green) and control (black) rockslopes for the six-month period following scaling. Both curves follow the characteristic inverse power-law relationship between volume and failure rate. The scaled rockslope curve lies below the control curve for larger rockfall volumes (approximately > 10^{-3} m^3), indicating a decreased frequency of larger rockfall events following scaling. At the smallest volumes, the scaled curve lies slightly above the control, suggesting a modest increase in the frequency of small rockfall. This pattern—reduced large rockfall frequency with slightly elevated small rockfall frequency—is consistent with the preferential

removal of larger, precarious blocks during scaling, which may expose fresh surfaces that subsequently generate smaller detachments. The crossover point at approximately 10^{-3} m³ marks the volume threshold above which scaling appears to reduce rockfall frequency at this site.

In the first six months following scaling, the scaled slope shows a decrease in the frequency of larger rockfall events ($V > 10^{-3}$ m³) relative to the control slope, accompanied by a modest increase in the frequency of smaller events. This shift in the size distribution is consistent with the removal of larger, unstable blocks during the scaling operation. However, consistent with the activity rate and cumulative volume results described in Sections 8.1.3.1 and 8.1.3.2, the volume-frequency relationships at site A show a return toward baseline conditions after approximately six months, after which the distributions for the scaled and control slopes are largely similar.

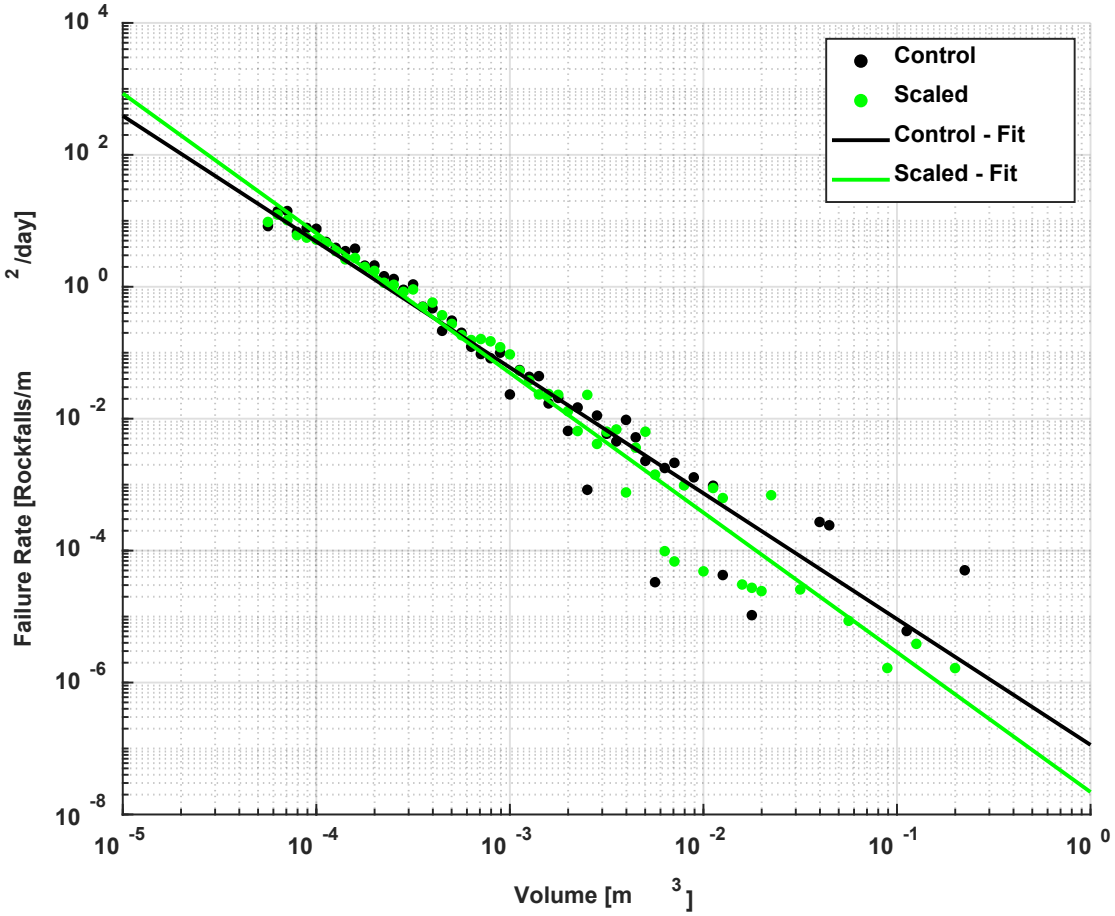

Figure 8.6. Volume-frequency relationships for both scaled (green) and control (black) rockslopes for the six months following scaling at Site A.

8.1.5 Trajectory Analysis

To characterize rockfall hazard for the control and scaled rockslopes at Site A, a set of parallel trajectory analyses were performed. First, a probabilistic trajectory analysis (PTA) was performed, which consisted of calculating trajectories from every possible source location on the

rockslope for a suite of volumes, ranging from 10^{-5} m^3 to 1 m^3. Restitution values were assumed to be that of medium hardness rock and momentum-based restitution (i.e. "lumped mass") was considered. Thus, the possible energy and travel path of rockfalls could be considered for various rockfall sizes without knowing possible rockfall sources *a priori*. The second analysis, termed a retrospective trajectory analysis (RTA), was performed using the volumes of observed rockfalls during each epoch and their associated source areas, calculated as the centroid of the cluster that was detected to fail. The PTA, along with volume-frequency relationships, serves as a means of characterizing probabilistic rockfall hazard based on purely rockslope morphology and the range of rockfall volumes considered. That is, the RTA serves as a semi-empirical basis for evaluating inferred rockfall energy and travel reach from actual, detected rockfall sources, while the PTA serves to evaluate the potential mobility and energy of potential rockfalls from any source on a rockslope, scaling volumes based on observed volume-frequency relationships. These analyses serve to compare changes in rockfall hazard indices stemming from scaling *and* a tool to consider rockslope locations that are particularly problematic in terms of rockfall mobility and energy.

8.1.5.1 Retrospective Trajectory Analysis (RTA)

Figure 8-7 presents the RTA results for Site A in two panels. The top panel shows rockfall source locations for a single epoch, with sphere sizes proportional to rockfall volume (not to scale). Sources are distributed relatively uniformly across the slope face, with the exception of the smoother, more intact massive rock outcrops on the control slope, which produce fewer rockfalls. The color coding by volume reveals that rockfall sizes vary considerably, with both small and large events sourcing from various portions of the face. The bottom panel shows the ending locations of all simulated rockfall trajectories across all epochs, color-coded by volume. Rockfalls originating from higher elevations tend to travel farther from the slope face, consistent with their greater potential energy. The spatial distribution of ending locations shows that most rockfalls arrest within a short distance of the slope base, but a subset of events—particularly those originating from upper portions of the slope or from above sub-vertical facies—reach distances well beyond the immediate toe. The elevation range at Site A spans approximately 132–144 m, providing a moderate height differential for trajectory development.

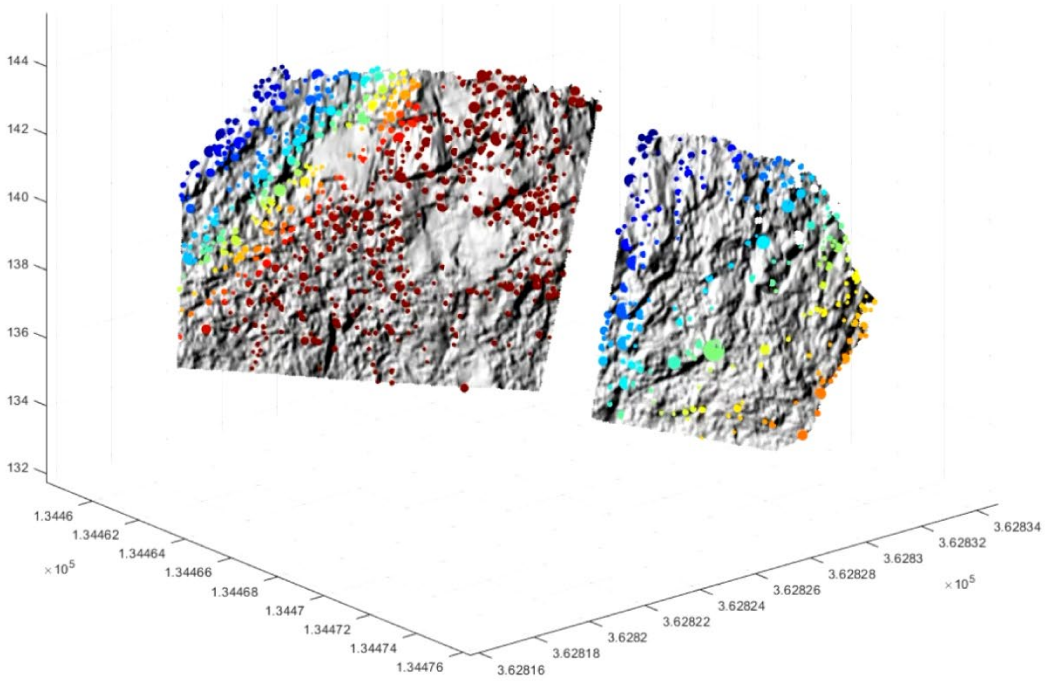

(a)

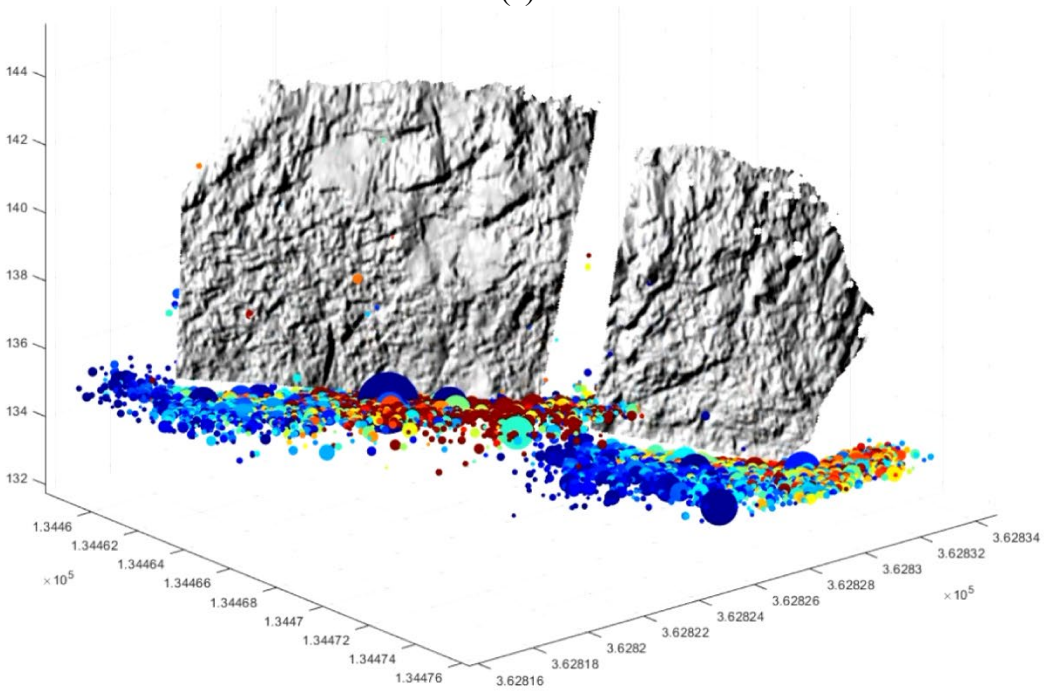

(b)

Figure 8.7. Rockfall sources (top) and ending rockfall locations (bottom) for Site A for all epochs.

As shown in Figure 8-7, the RTA demonstrates that rockfall sizes vary considerably for the rockslopes at Site A, while the distribution of rockfall sources is somewhat uniform. The exception to the latter statement is relative scarcity of rockfalls in the smooth, more intact massive rock outcrops on the Control slope. As expected, rockfalls that are higher in elevation have more potential to travel away from the slope owing to impacts with slope facies below. While difficult to discern directly from the visualization below, rockfalls that overhang or exist above slope facies that are subvertical have a tendency to increase rockfall trajectories. There is no clear trend for relationships between rockfall volume and travel reach.

However, these analyses demonstrate the associated starting and ending locations inferred from actual rockfall sources at the site, as well as associated kinetic energy upon final impact (assumed to be when velocity nears zero or the lowest elevation in the DEM). This enables a connection of lidar change detection and potential for rockfalls to impact downslope infrastructure.

Figure 8-8 presents four panels characterizing trajectory behavior at Site A. Figure 8-8 (a) shows the probability of exceedance (POE) of the reach length to drop height ratio (L/H) for pre-scaling conditions on the scaled rockslope (red), the mean for the control rockslope (green), and individual post-scaling epochs (gray) with their mean (black). For all epochs and both rockslopes at Site A, only between 20 and 40% of rockfalls exceed a lateral travel distance greater than half the source height. However, there is a heavy tail of rockfalls that exceed 75% and 100% of source height (between 5-10% and between 1-5%, respectively). This suggests that while most rockfalls do not travel far laterally from their original location, there is a small but sizeable proportion that does. Knowing this distribution of travel lengths provides a semi-empirical means of sizing rockfall retention structures based on a probability of exceedance. It also enables a means of quantifying the role of scaling on rockfall mitigation.

Figure 8-8 (b) shows the change in POE for the scaled rockslope relative to both the control (green) and the pre-scaling condition (red). There is a clear decrease in the POE for the post-scaling period, with the most pronounced reductions occurring at L/H ratios between 0.5 and 1.0, suggesting that scaling reduced the probability of rockfalls traveling moderate to long distances. The reduction relative to pre-scaling conditions (red) is particularly notable, reaching decreases of 0.2–0.4 in POE at certain L/H values. The substantial decreases in POE for rockfalls for travel length to source height ratios between 0.5 and 1 for both comparisons suggests a potential benefit of scaling, especially when done strategically for rockfalls at higher elevations on a slope (i.e. with higher absolute travel distance).

Figure 8-8 (c) shows the POE for kinetic energy at the lowest elevation, where the post-scaling mean (black) lies below both the pre-scaling (red) and control (green) curves, indicating reduced kinetic energy after scaling. This suggests that the decreased likelihood of exceeding certain ratios of travel distance to reach height appears to have affected modest levels of energy release (e.g. larger rockfalls sourcing from lower elevations or smaller rockfalls sourcing from higher elevations).

Figure 8-8 (d) confirms this with negative changes in POE for both comparisons, with the reduction versus pre-scaling conditions being somewhat more pronounced than the reduction versus the control. This lowered release of energy suggests that scaling may also decrease the potential hazard associated with direct rockfall impacts, quantified as kinetic energy.

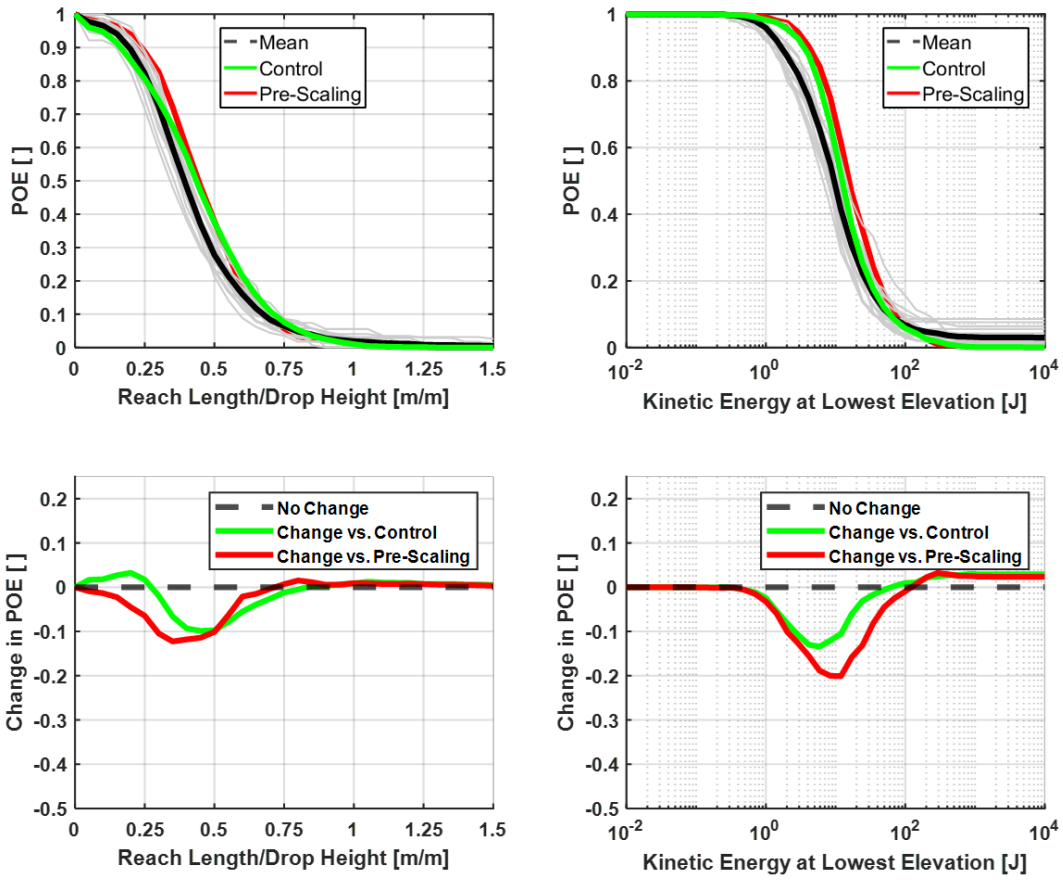

Figure 8.8. Probability of exceedance plots for Site A for POE vs (a) the ratio of reach length to drop height and (b) kinetic energy at the lowest elevation and the change in POE vs (c) the ratio of reach length to drop height and (d) kinetic energy at the lowest elevation. Green represents the control and red represents the pre-scaling.

8.1.5.2 Probabilistic Trajectory Analysis (PTA)

An alternative means of considering rockfall hazard is that any location on the rockslope can source a rockfall of any arbitrary size. While agnostic to the observed rates or geologic structure of a rockslope, this analysis determines potential problematic rockfall trajectories without a need for continued observation.

Figure 8-9 presents the probabilistic trajectory analysis results for Site A in four panels. Panels (a) and (b) show the starting and ending locations for all analyzed rockfalls at the scaled and control rockslopes, respectively, with color coding by trajectory endpoint.

Panels (c) and (d) show the full trajectory paths for the scaled and control rockslopes, respectively, with color coding indicating trajectory characteristics. The trajectory paths reveal the complex interaction between rockfall and slope morphology: blocks bounce, slide, and roll along the face, with their final positions determined by the sequence of impacts and the local geometry encountered. Both scaled and control slopes show that the upper portions of the face generate the most mobile trajectories, consistent with the greater available potential energy.

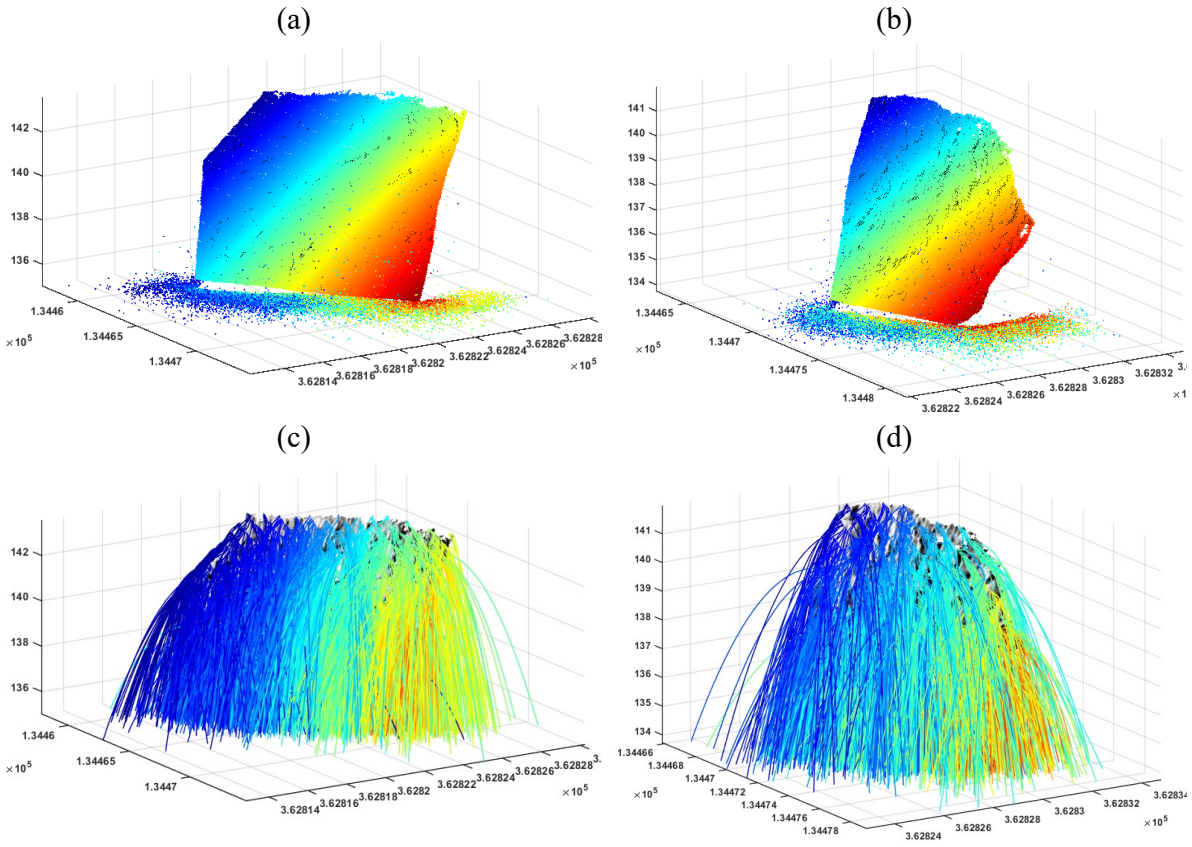

Figure 8.9. PTA results showing starting/ending locations and trajectories for Scaled and Control Rockslope A (four panels).

Notably, most trajectories terminate near the base of the slope, but events originating from higher elevations show sufficient potential energy to travel farther. However, in some instances, rocks may travel further than expected as demonstrated in for Scaled Rockslope A. Rockfalls with notable travel distance are observed on much of the upper part of the slope, but pockets of anomalously higher travel distance exist on the right and left hand sides of the rockslope face. The rockfalls on the left hand side stem from a modest overhand that impact the rockslope below with high energy of a freefall, resulting in more mobility. A small "knob" of rock exists midslope and to the right of the rockslope face, which also results in notable impact and sliding velocities away from the

slope, resulting more rockfall reach away from the slope. Figure 8-9b shows that these upper rockfall sources have significant kinetic energy on impact. Considering every rockfall source zone on the slope face also enables filtering of particularly problematic rockfall zones, such as rockfall with significant kinetic energy and travel distance, where an example of source zones with energy greater than five KJ and travel distance greater than five meters is shown and is generally concentrated on the upper rockslope, although not completely (Figure 8-9c). As expected, most rockfalls end up close to the base of the rockslope owing to limited energy and a direct path to deposition below.

Figure 8-10 presents four detailed views of the PTA results for Scaled Rockslope A. Panel (a) shows the spatial distribution of rockfall travel distance across the slope face, with warmer colors indicating greater travel distance. Rockfalls from the upper slope generally show the greatest travel distances, but localized pockets of anomalously high travel distance appear on both the right and left flanks of the face. The left-hand pocket stems from a modest overhang that launches blocks into freefall, producing high-energy impacts on the slope below and correspondingly greater mobility. A small rock knob at mid-slope on the right side similarly produces elevated impact velocities and longer reach. Panel (b) shows the kinetic energy distribution, confirming that these same upper-slope source zones generate the highest-energy impacts. Panel (c) presents a filtered view showing only source zones where both kinetic energy exceeds 5 kJ and travel distance exceeds 5 m, effectively identifying the most hazardous rockfall sources on the slope. These high-hazard zones are concentrated on the upper rockslope but are not exclusively confined there, indicating that some mid-slope sources also produce consequential trajectories. Panel (d) shows a heatmap of rockfall impact locations, with the highest impact density concentrated along the base of the slope directly below the face, confirming that most rockfalls deposit near the toe despite the tail of longer-reach events documented in the preceding panels.

The PTA approach enables consideration of observed rockfall volume-frequency relationships (Figure 8-11) and multiple trajectory analyses with different rockfall sizes to look at overall distribution of energy stemming from a rockslope and compare hazard before and after scaling. This is considered probabilistically by characterizing the probability of exceedance (PoE) of certain rockfall energy normalized to rockslope area and time (Figure 8-11). The top panel shows the probability of exceedance of normalized kinetic energy rate (J/m^2/year) for both the scaled (green) and control (black) rockslopes. The scaled curve is shifted to the left of the control curve, indicating that the scaled rockslope has a lower probability of exceeding any given energy rate threshold. The separation between curves is most pronounced at intermediate energy levels (approximately 10° to 10^2 J/m^2/year), which correspond to the moderate-sized rockfalls that experienced the greatest frequency reduction in the volume-frequency analysis. The volume-frequency relationships then demonstrate a notable downward shift in rockfalls greater than 10^{-3} m^3 (approximately 2 kgf in weight), shown in Figure 8-11. These rockfalls contain more kinetic energy than smaller rockfalls, and consequently, result in a notable decrease in the PoE for kinetic energy in scaled rockslopes versus the control rockslope for the limited period of monitoring (Figure 8-11). This response is likely rockslope specific and dependent on the size of rocks scaled and methods used to remove hazardous rockfall sources.

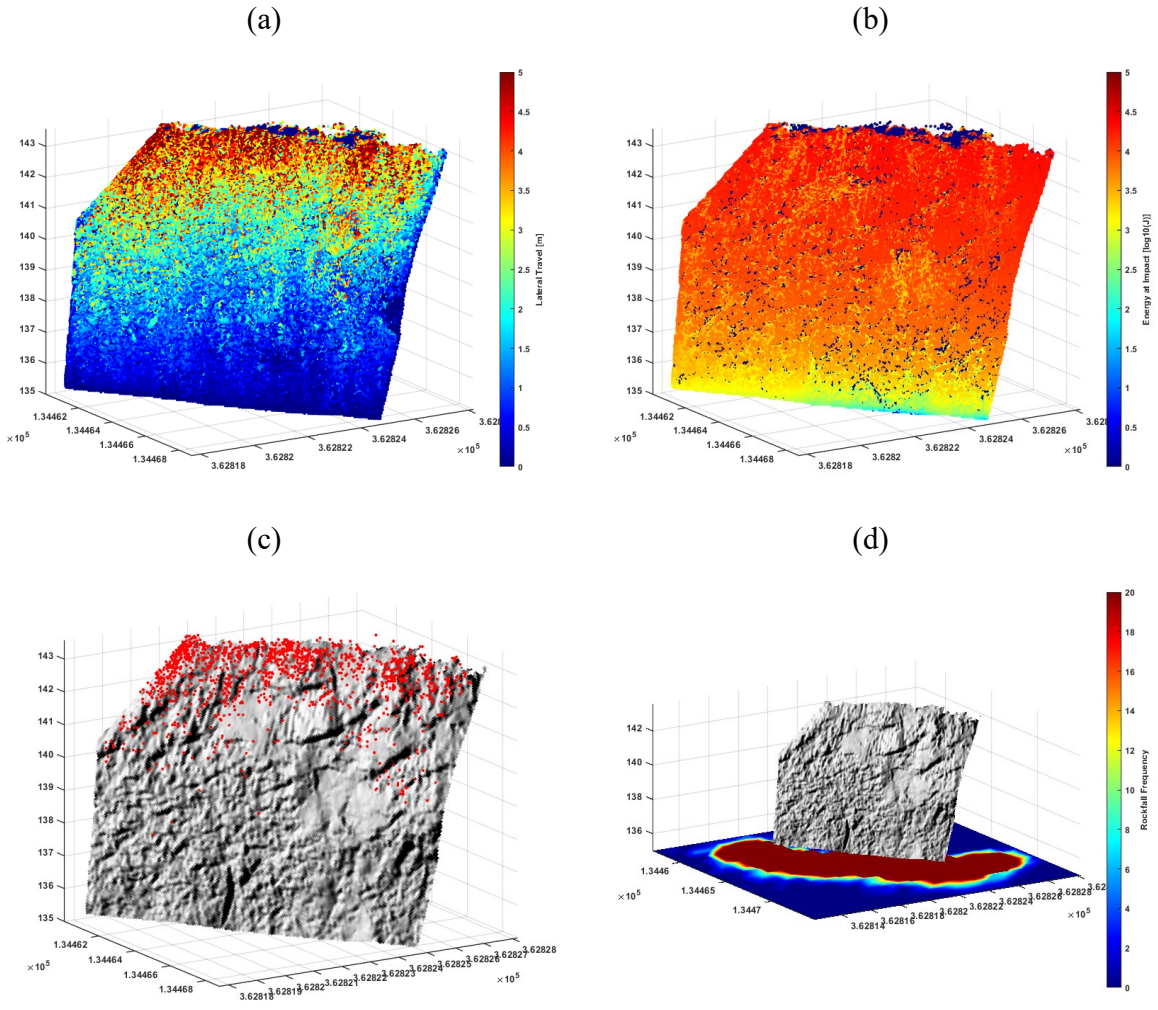

Figure 8.10. PTA results for Scaled Rockslope A: (a) travel distance, (b) kinetic energy, (c) filtered high-hazard sources, and (d) impact heatmap.

The bottom panel quantifies the reduction in POE, showing a peak reduction at intermediate energy levels before tapering at both the lowest and highest energies. This bell-shaped reduction profile is physically consistent: the smallest rockfalls carry too little energy for the frequency reduction to register in the energy domain, while the largest events are too rare for the limited monitoring period to resolve statistically. Hence the proposed concept does demonstrate a means of leveraging volume-frequency relationships and trajectory analyses to evaluate and compare rockfall hazard of a given rockslope probabilistically.

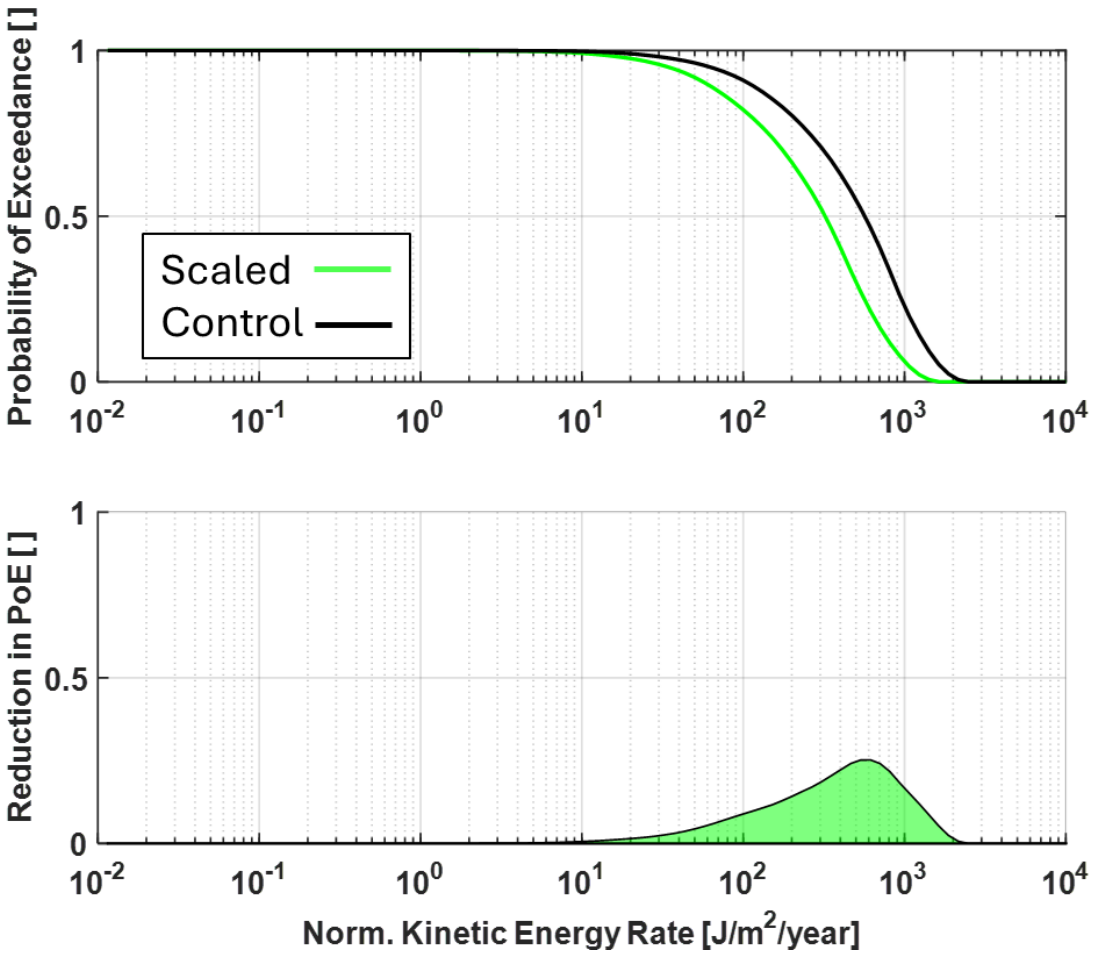

Figure 8.11. PTA-derived probability of exceedance of normalized kinetic energy rate for Site A (top) and reduction in POE (bottom).

8.2 SCALING SITE B

8.2.1 Scaling procedures

The scaling operation at site B differed from that performed at site A in its approach and spatial extent. Figure 8-12 shows the scaling operation in progress at Site B. Scalers are positioned on

the slope face among a mass of highly fragmented, angular basalt debris. The slope surface shows a mix of dark gray fresh basalt faces and lighter, weathered surfaces, indicating variable degrees of exposure to atmospheric processes. Unlike the more systematic, slope-wide approach at Site A, workers performed a targeted operation in which specific rocks were identified for removal prior to dislodgement. This targeted approach was applied across the full slope face rather than being confined to the upper portion, reflecting the distributed nature of the identifiable hazardous features at this site. As at site A, workers used metal bars and pry tools to dislodge material, and the operation was completed within a period of a few hours.



Figure 8.12. Scaling operation in progress at Scaling Site B.

A notable characteristic of the scaling operation at site B was the response of the surrounding rock mass to individual block removals. The photograph in Figure 8-12 illustrates the fragile, already-disaggregated character of the rock mass at this location: the visible material consists predominantly of small to moderate-sized angular fragments with limited intact rock mass continuity. The high degree of pre-existing fragmentation meant that the removal of targeted blocks caused adjacent material to dislodge as well, resulting in more extensive material removal than initially planned during the operation. This cascading response is consistent with the behavior described by Beckstrand et al. (2020) for scaling in closely fractured rock, where the removal of one block can reduce lateral support for neighboring material. As a consequence, the

total volume of material removed at site B was likely greater than what would have been predicted from the number of blocks originally identified for removal, and the scaling operation effectively disturbed a larger portion of the slope surface than the targeted approach would suggest. This combination of targeted block selection and material fragility distinguishes the site B operation from site A and is relevant to interpreting the RAI and volume-frequency results that follow. The scale of the slope and the size of the visible blocks are consistent with the volume-frequency data showing that small to medium-sized rockfalls dominate the erosion budget at this site.

8.2.2 RAI Analysis

The RAI analysis for scaling site B (Figure 8-13 and Figure 8-14) reveals a more pronounced morphological response to scaling than was observed at site A, which is consistent with the more extensive disturbance of the slope surface described in Section 8.2.1.

Figure 8-13 presents the RAI class difference bar chart for Site B. The scaling site (red bars) shows the most pronounced intact rock increase of the three Rumble Pit sites, with approximately a 4% gain—double the magnitude observed at Site A. Shallow overhang decreased by approximately 2%, while fragmented discontinuous and closely spaced discontinuous each decreased by approximately 1–2%. These changes are roughly twice the magnitude of the corresponding shifts observed at site A, despite the two operations being of similar duration and using the same tools. The larger morphological response at site B is likely attributable to the cascading removal of adjacent material that accompanied the targeted block extractions, which effectively disturbed a greater proportion of the slope surface than the number of originally identified targets would suggest.

The paired control site (gray bars) exhibited minimal redistribution across all RAI classes over the monitoring period, with no class exceeding approximately 1% in either direction. This minimal change confirms that the morphological shifts observed at the scaling site are attributable to the mitigation rather than to background environmental forcing or seasonal variability. The talus class shows a very modest increase at the scaling site, consistent with debris accumulation from the removed material. This distinction between the scaled and control sections is clearer at site B than at site A, where the smaller magnitude of changes made attribution somewhat less straightforward.

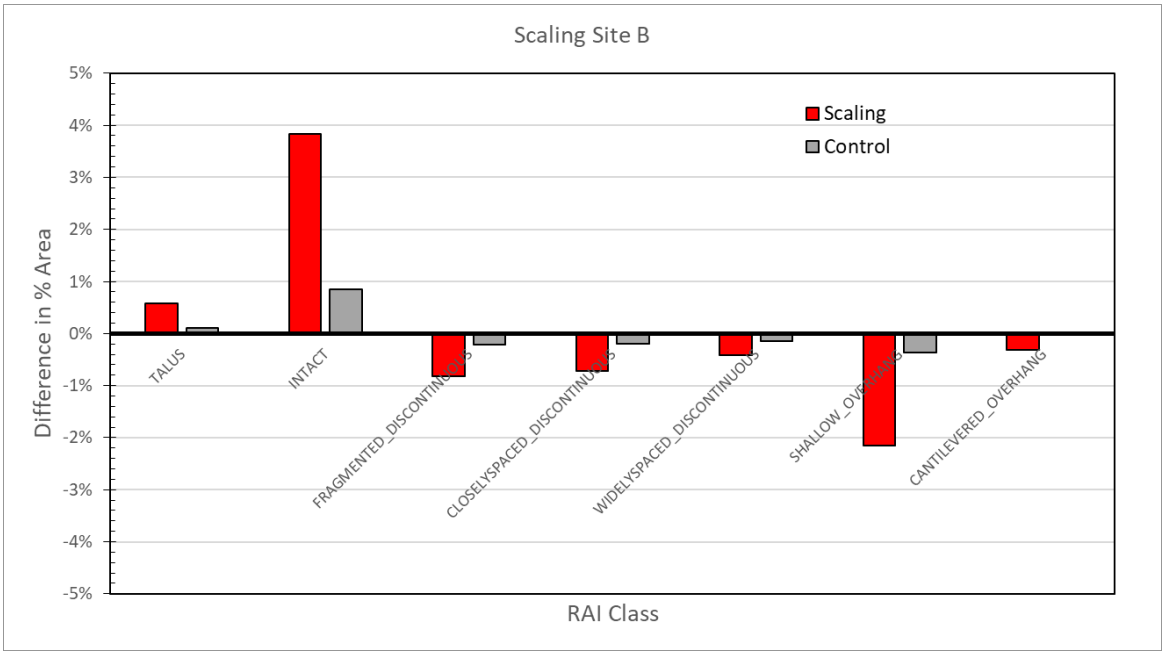

Figure 8.13. Changes in RAI classification resulting from the scaling operation for Scaling Site B and Control Site B (11/10/2023 vs 9/29/2023).

Figure 8-14 shows the temporal evolution of RAI class proportions at Scaling Site B from September 2023 through approximately May 2025. These time-series plots of RAI class percentages shows some variability in the percent area occupied by individual classes across monitoring epochs, though the overall distribution remained largely stable throughout the approximately 20-month monitoring period. Importantly, there is no clear trend of reversion toward pre-scaling class proportions, suggesting that the morphological improvements achieved by the scaling operation were sustained over the duration of observation. This temporal stability is consistent with the Section 6.2 expectation that a durable mitigation effect should manifest as sustained changes in class proportions rather than a transient perturbation followed by recovery toward baseline conditions.

For example, the intact class shows an upward step at the time of scaling, rising from approximately 35% to nearly 45%, and then continues to increase gradually over the monitoring period, reaching approximately 45–50% by mid-2025. This progressive increase in intact rock beyond the initial scaling-related step is a distinctive feature of Site B that is not as pronounced at Sites A or C and may reflect ongoing evacuation of loosened material from the fragmented rock mass or progressive stabilization of the scaled surface.

Other classes exhibit comparatively minor changes. The fragmented discontinuous class remains relatively stable at approximately 15–18% with some modest fluctuation. The closely spaced discontinuous class shows a brief perturbation near the time of scaling before stabilizing at approximately 10–15%. The shallow overhang class declines at the time of scaling and remains at the reduced level. Widely spaced discontinuous and cantilevered overhang maintain low, stable proportions throughout.

In terms of the Section 6.2 morphological metrics, the intact rock increase and shallow overhang reduction at site B represent the expected signature of effective scaling: the removal of kinematically unstable surface material has exposed more competent rock beneath and reduced the area of the slope face most susceptible to sudden, large-volume tensile failure. The 4% increase in intact rock is notable given that the operation was completed within a few hours using hand tools and reflects the efficiency of targeted block removal in a closely jointed rock mass where individual extractions produced broader surface modifications through the cascading mechanism described in Section 8.2.1.

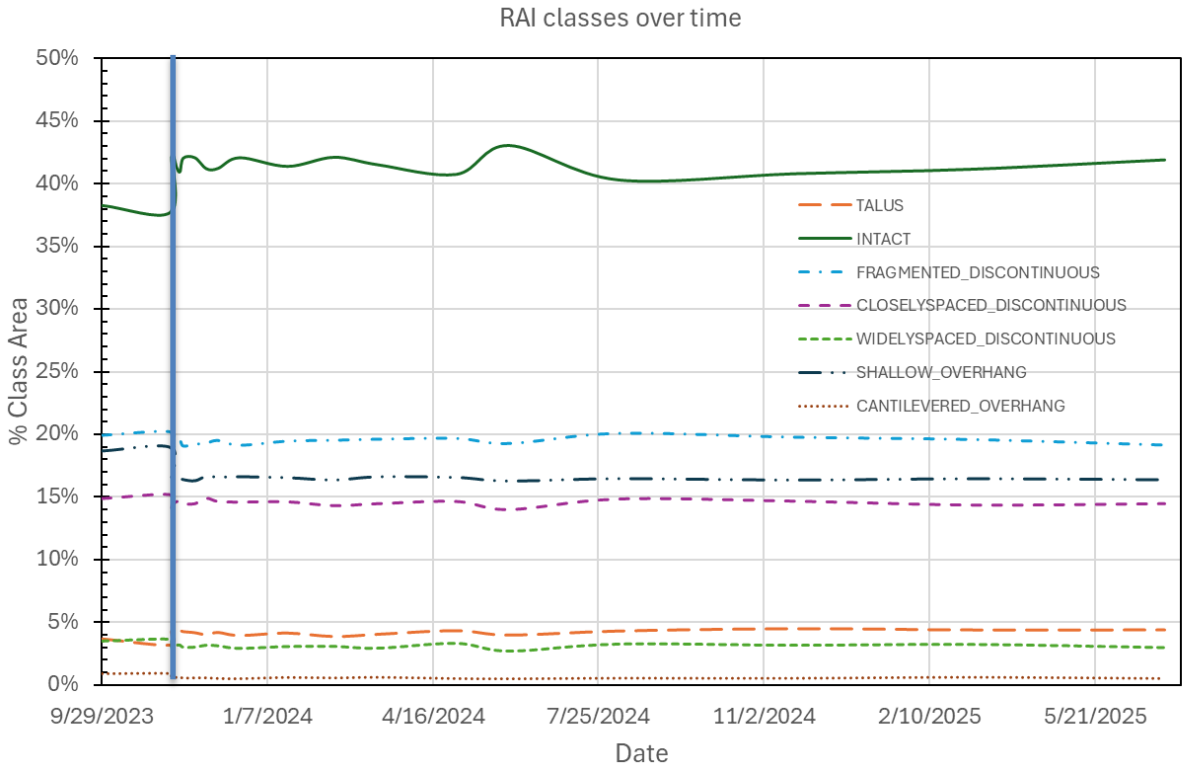

Figure 8.14. Changes in RAI classification percent areas over time for Scaling Site B. The blue vertical line represents the date of scaling (11/10/2023).

8.2.3 Rates and Volumes

Figure 8-15 shows the activity rate comparison for Site B in two panels. Panel (a) shows the full time series, where the scaling site (solid line) exhibits a sharp spike at scaling (day 0), reaching approximately 0.40, before declining rapidly. The control site (dashed line) shows a similar but slightly lower spike of approximately 0.20–0.25 during the same period, again reflecting the influence of seasonal environmental forcing (winter wet season) on both slopes. The two curves converge within approximately 100–200 days. Panel (b) fits logarithmic regressions to the post-scaling data. The scaling site regression ($R^2 = 0.41$) has a similar form to the control site regression ($R^2 = 0.20$). A notable feature is that the scaling site curve begins with a higher initial rate but declines to levels comparable to or slightly below the control within approximately 100–200 days, after which both sites show similarly low rates through the remainder of the

monitoring period. As with site A, the initial elevated rate at the scaling site reflects the post-disturbance adjustment period during which newly exposed surfaces shed loosened material immediately following mitigation.

Figure 8-16 presents the cumulative erosion analysis for Site B. The top panel shows that the control rockslope accumulates erosion volume across a range of size bins, with small to medium-sized rockfalls ($10^{-2} > V > 10^{-4}$ m³) dominating the total volume change—a different pattern than Site A, where large rockfalls dominated. This difference in the size distribution of contributing events reflects the character of the rock mass at site B, where the closely jointed and fragile material tends to produce more frequent, smaller failures rather than the less frequent but larger events characteristic of site A. The central panel shows the scaled rockslope, where cumulative erosion is visibly lower than the control for several months following scaling. The difference is most pronounced in the first five months, after which the rates of accumulation become more similar between the two slopes. The bottom panel shows the ratio of scaled to control cumulative volume, which is consistently below 1.0, confirming sustained lower erosion at the scaled slope. As at Site A, the ratio is lowest immediately after scaling and gradually approaches 1.0 over approximately five to six months.

The comparison of scaled and control rockslopes at site B reveals a pattern broadly consistent with that observed at site A. Cumulative volume change at the scaled rockslope was notably smaller than at the control slope for several months following scaling, after which the rates of volume change converged at approximately five to six months post-scaling. The ratio of scaled to control cumulative volume (Figure 8-16, bottom panel) confirms that the scaled rockslope consistently accumulated less total erosion volume over the monitoring period. As at site A, the largest changes and associated noise occur immediately following scaling, likely reflecting rapid evacuation of material disturbed by the operation or differencing errors introduced during shorter monitoring epochs.

The control rockslope at site B experienced notably larger individual rockfall events than the scaled rockslope during the observation period, consistent with the pattern observed at site A. As discussed in Section 8.1.3.2, whether this reflects inherent structural differences between the paired slopes or the effect of scaling in removing the largest unstable blocks cannot be resolved from the available data.

The cumulative volume results at site B indicate that scaling produced a reduction in erosion volume relative to the control for a period of approximately five to six months following the operation, after which the two slopes returned to comparable rates of activity. This temporal pattern is consistent with the results at site A and reinforces the finding that the effective period of scaling-induced volume reduction at the Rumble Pit is on the order of five to six months under the geologic and environmental conditions present at this site.

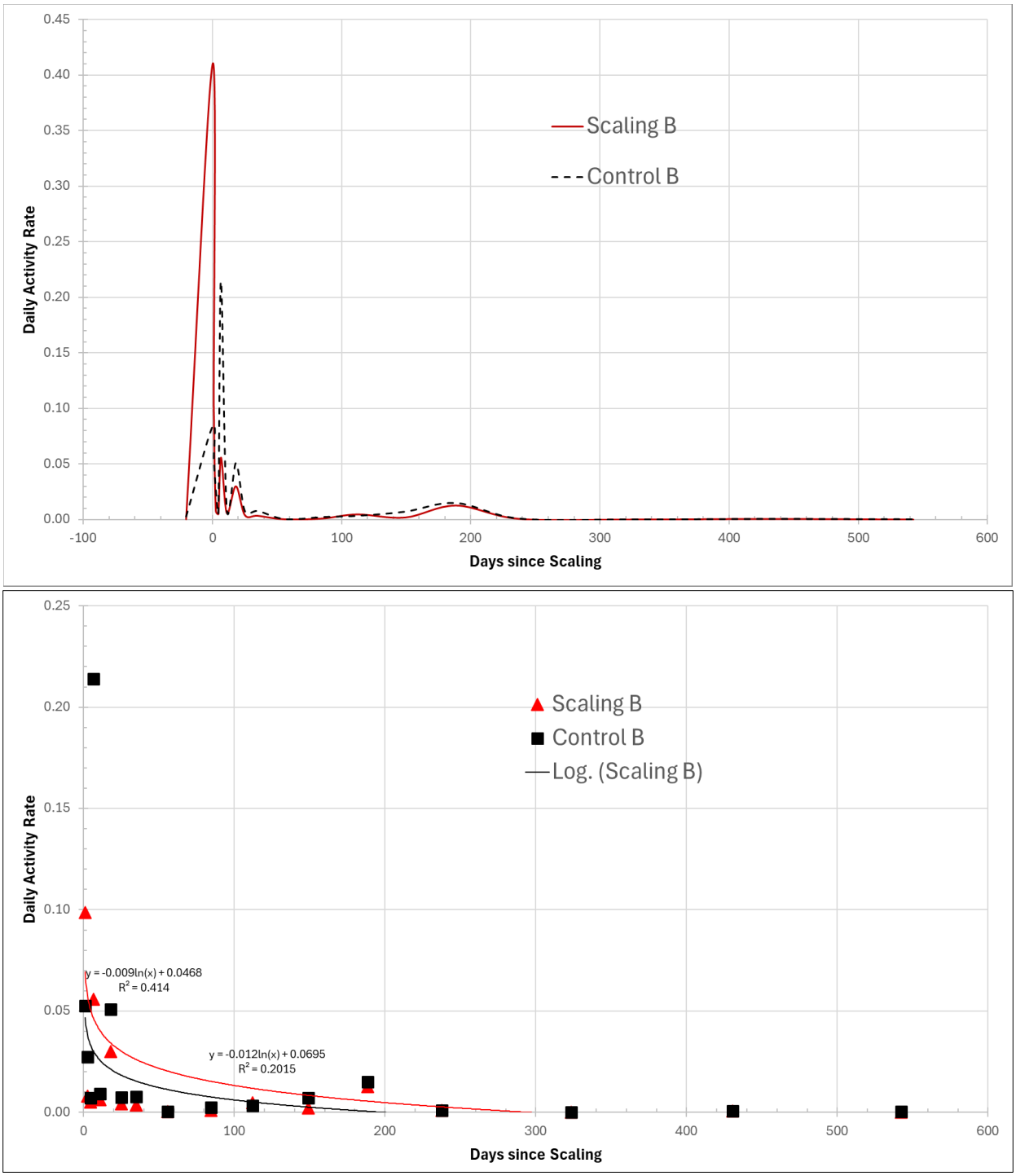

Figure 8.15. Changes in activity rates over time for Scaling Site B compared with control site B. (a) Including baseline activity rates and (b) after scaling with regression functions.

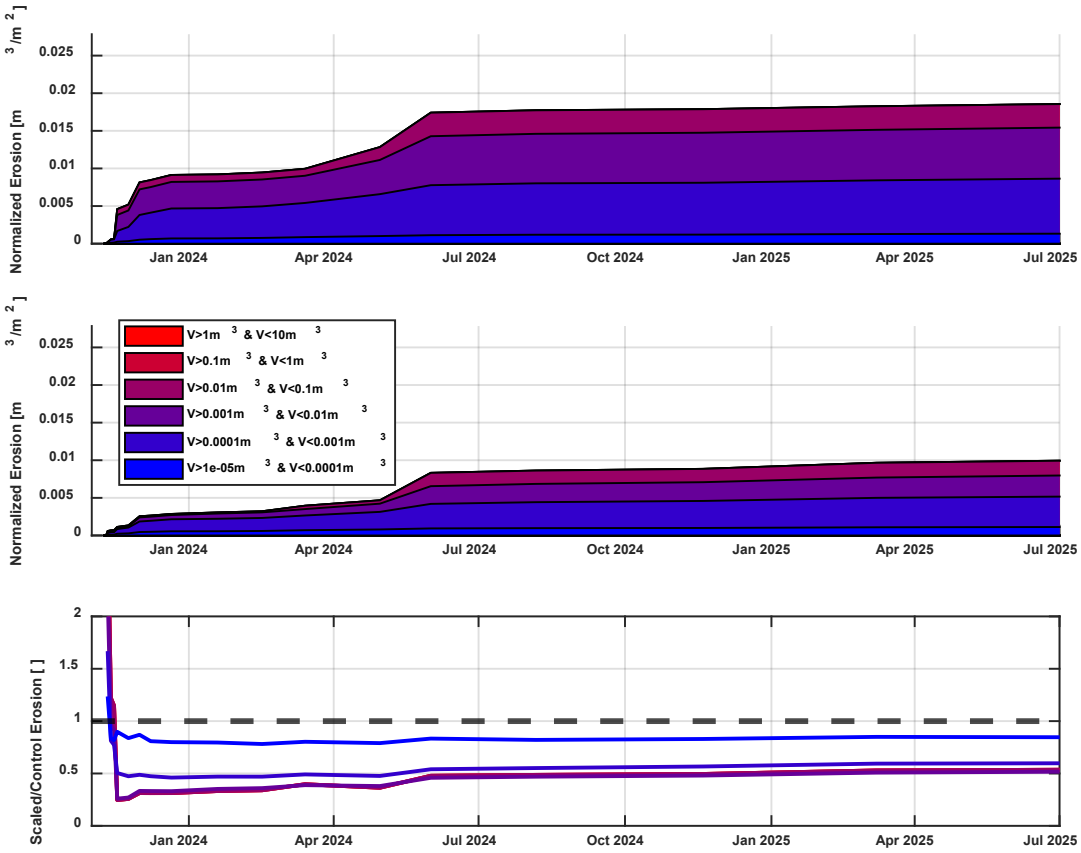

Figure 8.16. Cumulative normalized erosion for Control Rockslope B (top), Scaled Rockslope B (center), and ratio of scaled to control (bottom).

8.2.4 Volume-Frequencies

Figure 8-17 displays the volume-frequency relationships for Site B, normalized by rockslope area and monitoring duration, for the scaled and control rockslopes at site B for the first six months following scaling and for the period thereafter.

The volume-frequency comparison at site B produces the most pronounced mitigation signal among the three Rumble Pit sites. The scaled rockslope (green) lies notably below the control (black) across nearly the entire volume range, indicating a reduction in rockfall frequency for all sizes, not just larger events as observed in site A, where the post-scaling decrease was concentrated primarily in the larger size classes. The decrease at Site B is most pronounced for rockfalls larger than approximately 10^{-3} m³, but a measurable reduction extends to smaller volumes as well.

In the first six months following scaling, the scaled slope shows a decrease in the frequency of larger rockfall events ($V > 10^{-3}$ m³) relative to the control slope, as well as a decrease in the frequency of rockfall events across all size classes. In the framework of Section 6.1.3, this result

corresponds to a reduction in the activity parameter β across all event sizes, representing a more complete suppression of rockfall activity than was observed at site A.

The practical significance of this finding is that scaling at site B reduced both the more frequent hazard of smaller rockfall events that could directly impact passing motorists and the less frequent but more consequential hazard of larger events capable of depositing debris in the roadway. However, consistent with the activity rate and cumulative volume results presented in Section 7.2.3, the volume-frequency relationships at site B show a return toward baseline conditions after approximately six months, after which the distributions for the scaled and control slopes are largely similar.

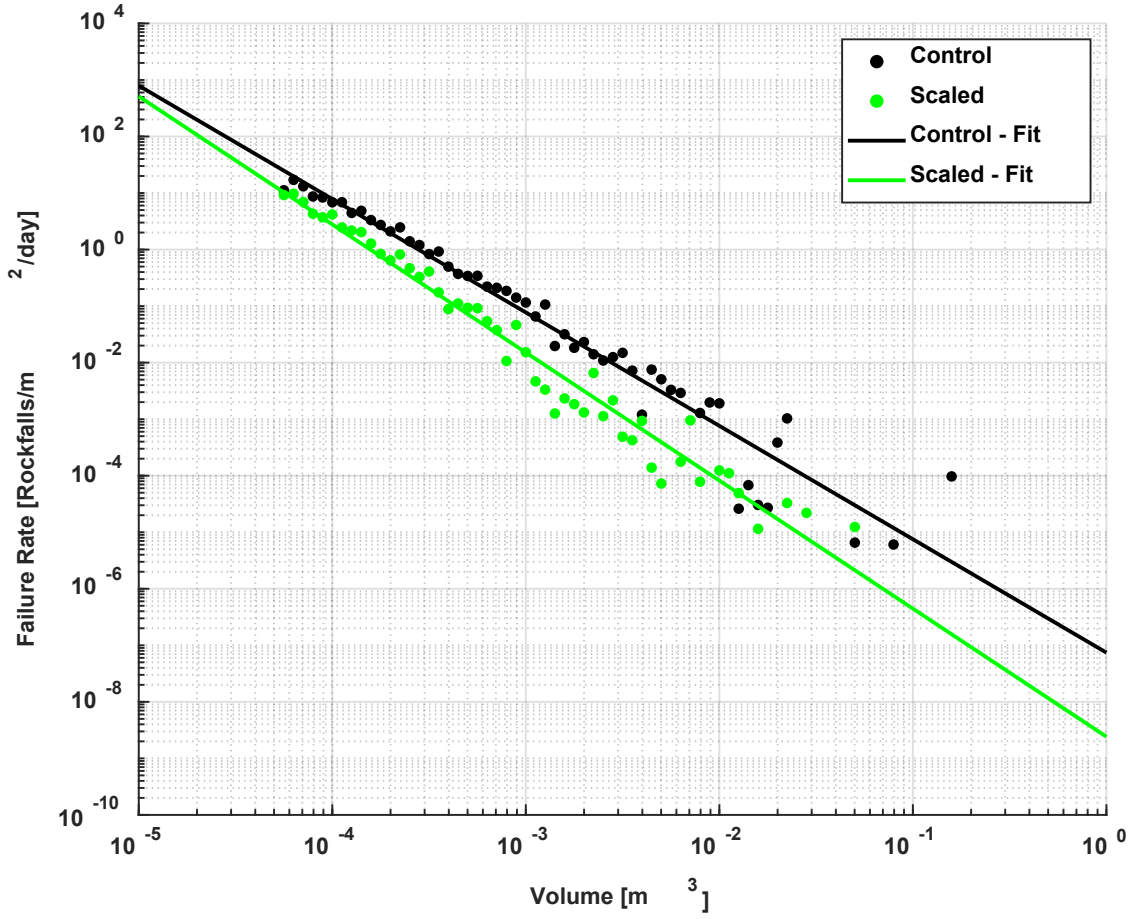

Figure 8.17. Volume-frequency relationships for both scaled (green) and control (black) rockslopes for the six months following scaling for Rockslope B.

8.2.5 Trajectory Analysis

To characterize rockfall hazard for the control and scaled rockslopes at Site B, a set of parallel trajectory analyses were performed. First, a probabilistic trajectory analysis (PTA) was performed, which consisted of calculating trajectories from every possible source location on the rockslope for a suite of volumes, ranging from 10^{-5} m^3 to 1 m^3. Restitution values were assumed to be that of medium hardness rock and momentum-based restitution (i.e. "lumped mass") was considered. The second analysis, the retrospective trajectory analysis (RTA), was performed using the volumes of observed rockfalls during each epoch and their associated source areas, calculated as the centroid of the cluster that was detected to fail. The PTA, along with volume-frequency relationships, serves as a means of characterizing probabilistic rockfall hazard based on purely rockslope morphology and the range of rockfall volumes considered. The PTA serves to evaluate the potential mobility and energy of potential rockfalls from any source on a rockslope, scaling volumes based on observed volume-frequency relationships.

8.2.5.1 Retrospective Trajectory Analysis (RTA)

Figure 8-18 presents the RTA results for Site B. The top panel shows rockfall source locations for a single epoch, with sphere sizes proportional to volume. The distribution of sources is broadly distributed across the slope face, with rockfall sizes varying considerably. The bottom panel shows ending locations for all trajectories across all epochs, color-coded by volume. Rockfalls from higher elevations (approximately 138–140 m) tend to travel farther from the slope, while lower-elevation sources deposit near the immediate base. The overhanging structure of portions of the Site B rockslope is reflected in the trajectory endpoints: rockfalls launched from overhangs above sub-vertical facies show enhanced mobility, depositing at distances notably greater than those from lower, more uniformly inclined portions of the face. The range of ending locations is somewhat wider than at Site A, consistent with the higher proportion of rockfalls exceeding 50% of source height documented in Figure 8-19. A few large, isolated events (visible as larger colored spheres at extended distances) indicate that Site B periodically produces high-mobility rockfall.

Figure 8-19 presents the four-panel trajectory analysis for Site B. Panel (a) shows that 40–70% of rockfalls at Site B exceed a lateral travel distance of half their source height—notably higher than the 20–40% at Site A—reflecting the more overhanging morphology of this rockslope. The heavy tail is also more pronounced, with 5–25% exceeding 75% of source height and approximately 1–4% exceeding 100%. Panel (b) shows that post-scaling conditions produce a decreased POE relative to both the control (green) and pre-scaling (red) conditions, with the greatest reductions concentrated at L/H ratios around 0.5 but extending through the 0.5–1.0 range. Panel (c) shows the kinetic energy POE, where the post-scaling mean (black) lies below both the pre-scaling (red) and control (green) curves across much of the energy range. Panel (d) confirms negative changes in POE for both comparisons, with reductions of approximately 0.1–0.2 at intermediate energy levels.

Similar to Rockslope A, the RTA demonstrates that rockfall sizes vary considerably for the rockslopes at Site B. Rockfalls that are higher in elevation have more potential to

travel away from the slope owing to impacts with slope facies below and some rocks show mobility owing to the roughened slope face. Again, overhanging rockfalls above slope facies that are subvertical have a tendency to increase rockfall reach.

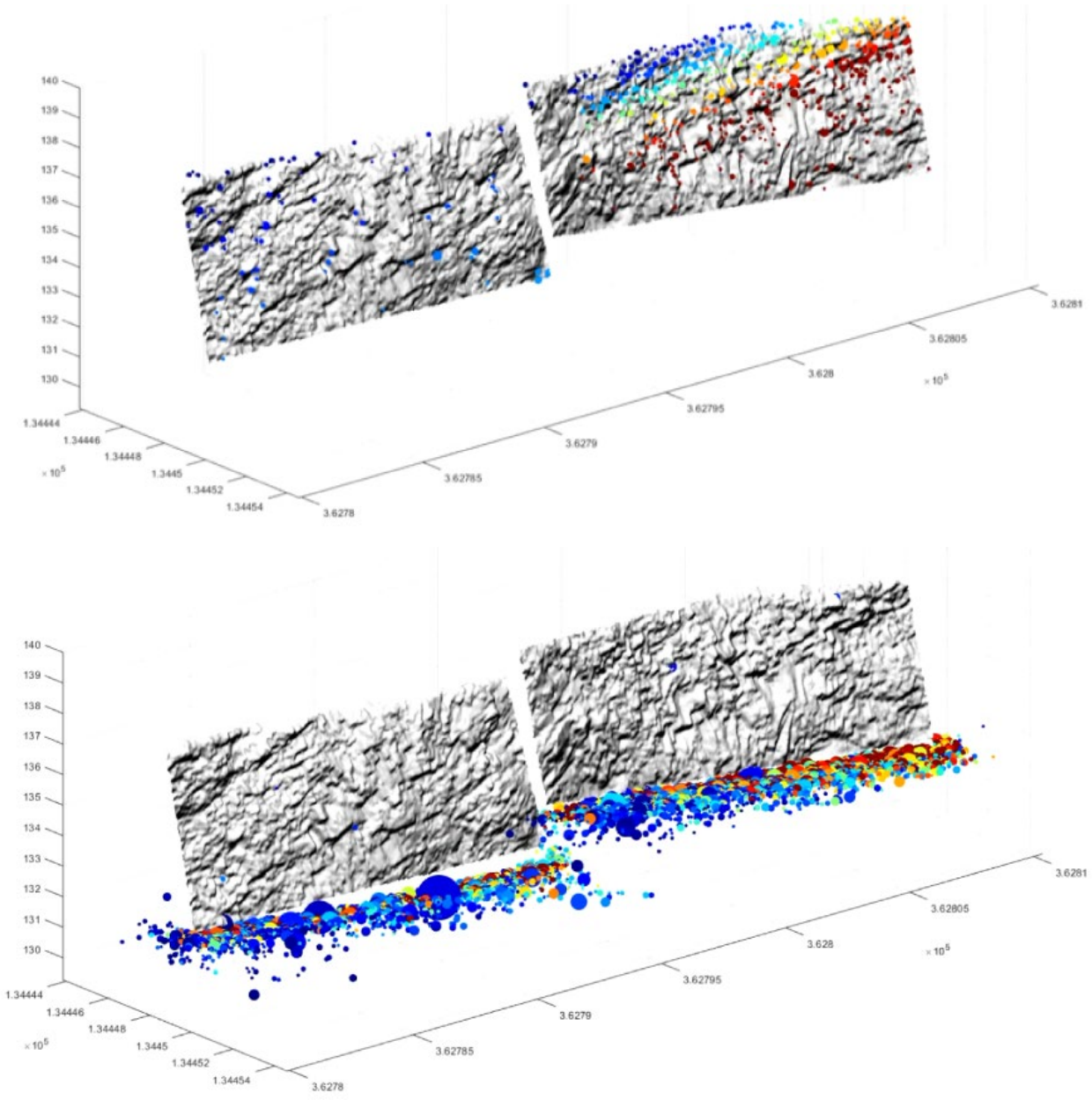

Figure 8.18. Rockfall sources (top) and ending rockfall locations (bottom) for Site B for all epochs.

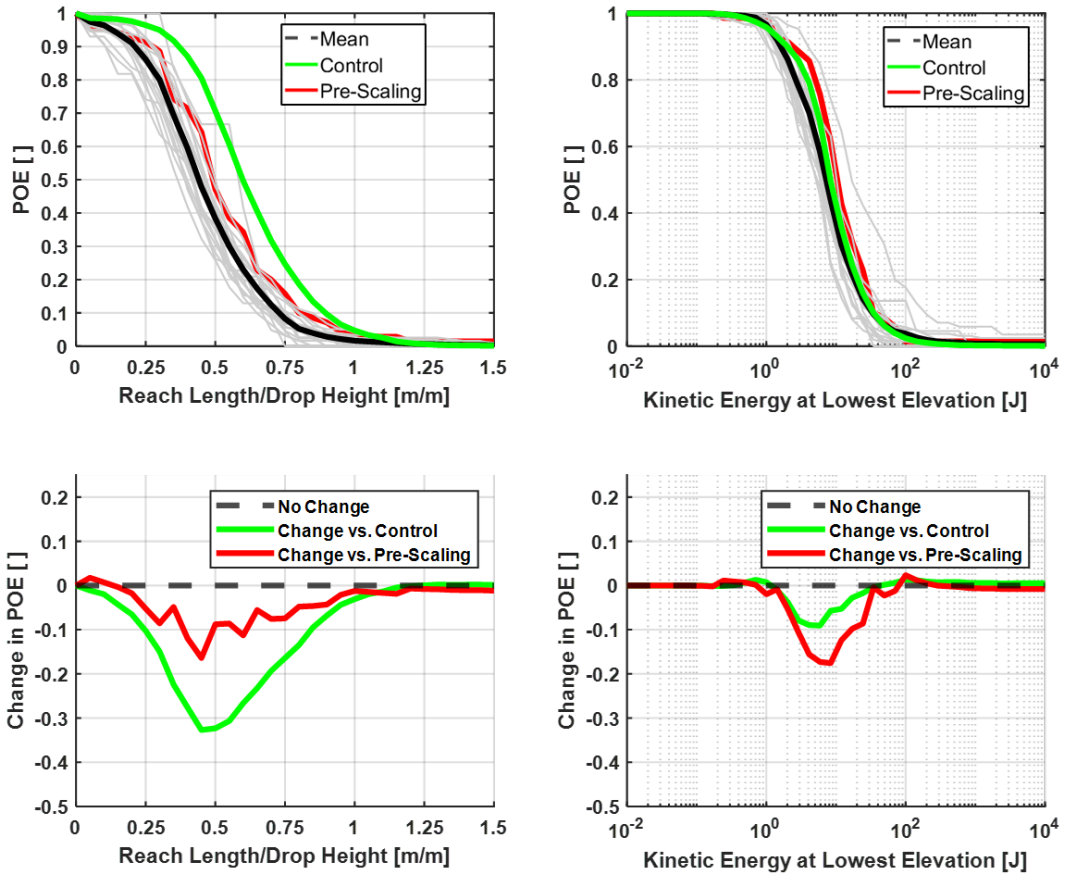

Figure 8.19. Probability of exceedance plots for Site B for POE vs (a) the ratio of reach length to drop height and (b) kinetic energy at the lowest elevation and the change in POE vs (c) the ratio of reach length to drop height and (d) kinetic energy at the lowest elevation. Green represents the control and red represents the pre-scaling.

These analyses demonstrate the associated starting and ending locations inferred from actual rockfall sources at the site, as well as associated kinetic energy upon final impact (assumed to be when velocity nears zero or the lowest elevation in the DEM). As shown in Figure 8-19(a), for all epochs and both rockslopes at Site B, only between 40 and 70% of rockfalls exceed a lateral travel distance greater than half the source height, which is notably higher than Rockslope A. There is a notably heavier tail of rockfalls that exceed 75% and 100% of source height (between 5-25% and approximately 1-4%, respectively) for Rockslope B. This suggests that a sizeable proportion of rockfalls demonstrate notable mobility, likely owing to the overhanging structure of this rockslope. Again, knowing this distribution of travel lengths provides a semi-empirical means of sizing rockfall retention structures based on a probability of exceedance – this rockslope may benefit from a wider catchment ditch in design.

This analysis again enables a means of quantifying the role of scaling on rockfall mitigation. For example, in Figure 8-19(b), there appears to be a decreased probability of

exceedance in rockfall reach for Scaled B after scaling in comparison to pre-scaling conditions and to Control B. Much of the decreased probability of exceedance occurs for rockfalls with a travel length to source height ratio of approximately 0.5, but there appears to be substantial decreases in potential for exceedance for rockfalls for travel length to source height ratios between 0.5 and 1 for both comparisons. Once again, at least for this rockslope and the several months following scaling, this observation suggests a potential benefit of scaling, especially when done strategically for rockfalls at higher elevations on a slope (i.e. with higher absolute travel distance).

For Site B, scaling appears to result in a modest, decreased likelihood to exceed certain levels of kinetic energy, as shown in Figure 8-19(c). This suggests that the decreased likelihood in exceeding certain ratios of travel distance to reach height appear to have affected modest levels of energy release for both pre-scaling conditions and versus the control rockslope as well (Figure 8-19d). This lowered release of energy suggests that scaling may also decrease the potential hazard associated with direct rockfall impacts, quantified as kinetic energy.

8.2.5.2 Probabilistic Trajectory Analysis (PTA)

The observed rockfall volume-frequency relationships for Rockslope B (Figure 8-20) and multiple trajectory analyses with different rockfall sizes are used to evaluate the overall distribution of energy stemming from a rockslope and compare hazard before and after scaling. The probability of exceedance (PoE) of certain rockfall energy normalized to rockslope area and time for Rockslope B are shown in Figure 8-20. The top panel shows the POE of normalized kinetic energy rate for the scaled (green) and control (black) rockslopes.

For Rockslope B, there is a large difference in the probability of exceedance for scaled conditions (in the few months following scaling) versus control conditions. Namely, the scaled PoE is shifted far to the left of the control rockslope, suggesting that the scaled rockslope is less likely to exceed energy releases from large rockfalls. The separation between curves is substantially larger than at Site A. The particular exaggerated shift for Rockslope B is sensible as the volume-frequency relationships demonstrate a notable downward shift for all rockfall sizes, shown in Figure 8-20. This pronounced separation reflects the broader frequency reduction documented in the magnitude-frequency analysis: whereas Site A showed frequency reductions primarily for larger events, Site B showed reductions across nearly all volume bins, amplifying the integrated energy-based hazard reduction.

Notably, for larger kinetic energies, there are notably larger energy releases in the control rockslope. The bottom panel shows the reduction in POE, which reaches approximately 65% at intermediate energy levels—the largest reduction among the three Rumble Pit sites. This peak reduction occurs in the range of normalized energy rates from approximately 10^{0} to 10^{2} J/m²/year, corresponding to the moderate-sized rockfalls that are both frequent enough to influence the statistics and large enough to carry meaningful kinetic energy. Again, this response is likely rockslope specific and dependent on the size of rocks scaled and methods used to remove hazardous rockfall sources, but the proposed

concept does demonstrate what appears to be a temporary reduction in rockfall hazard from scaling for Rockslope B.

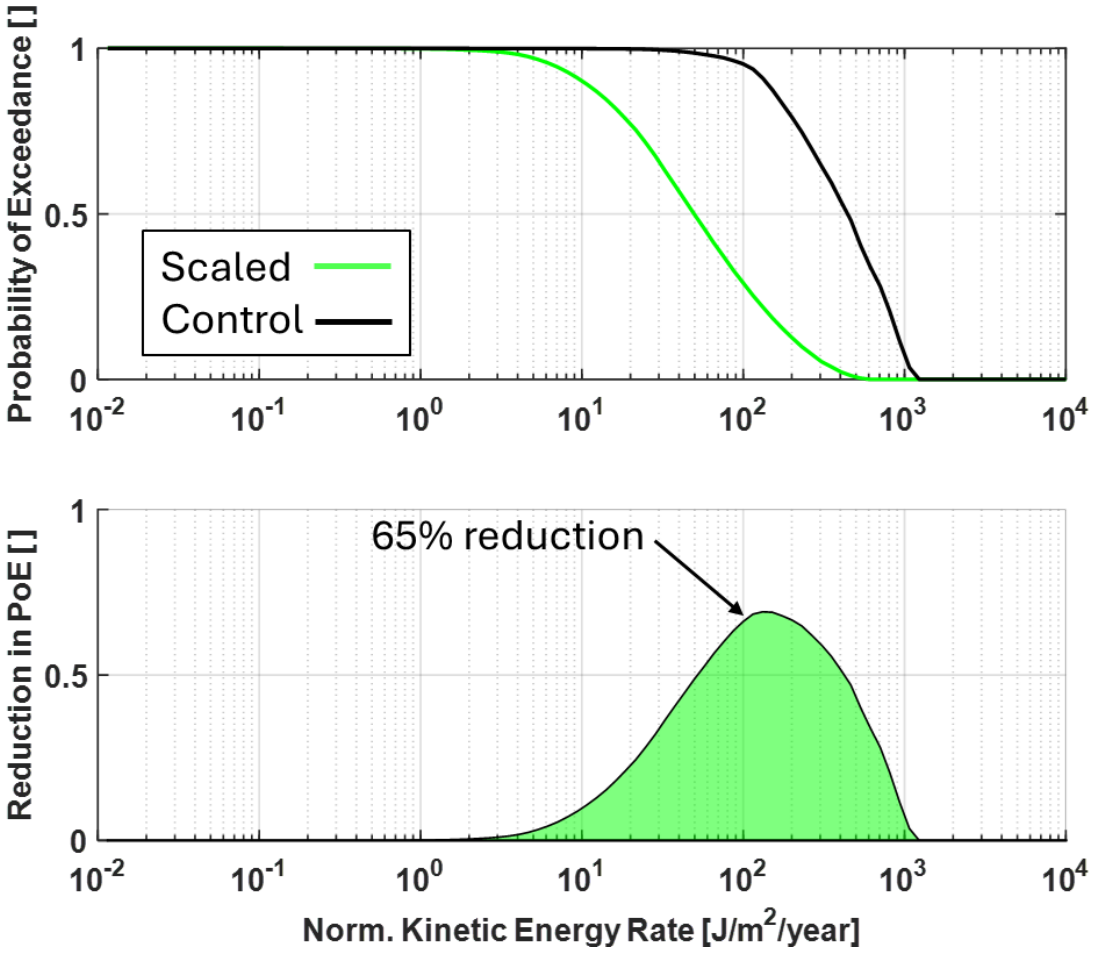

Figure 8.20. PTA-derived probability of exceedance of normalized kinetic energy rate for Site B (top) and reduction in POE (bottom).

8.3 SCALING SITE C

8.3.1 Scaling procedures

The scaling operation at site C was conducted in a manner similar to that described for site B in Section 8.2.1. Workers used metal bars and pry tools to target specific rocks identified for removal across the slope face, completing the operation within a period of several hours. As at site B, the removal of targeted blocks resulted in the dislodgement of adjacent material due to the closely jointed character of the rock mass.

8.3.2 RAI Analysis

The RAI analysis for scaling site C (Figure 8-21 and Figure 8-22) reveals a more limited morphological response to the scaling operation than was observed at either site A or site B. The pre- and post-scaling comparison shows a modest increase in intact rock area and a reduction in fragmented discontinuous area, though the magnitudes of these changes are smaller than those recorded at the other two scaling sites. Unlike sites A and B, where minimal differences were observed at the paired control sections, some of the class redistribution at site C is partially echoed at the control site, which complicates direct attribution of the observed changes to the scaling operation.

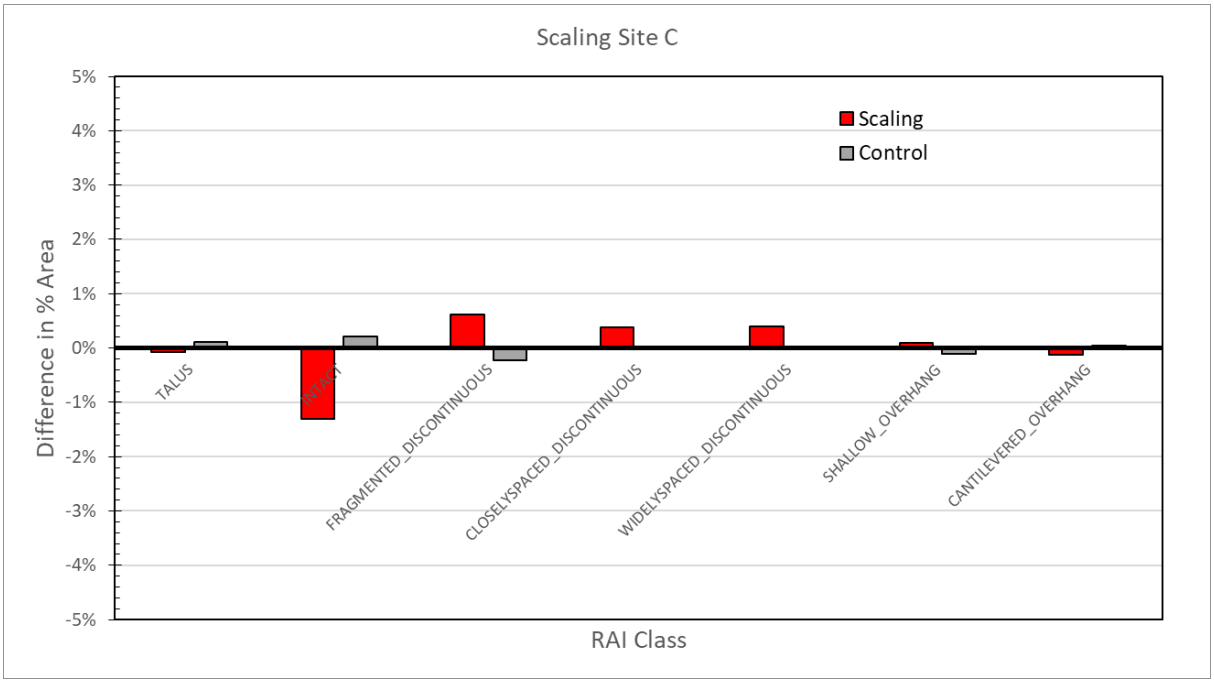

Figure 8.21. Changes in RAI classification resulting from the scaling operation for Scaling Site C and Control Site C (11/10/2023 vs 9/29/2023).

Figure 8-21 presents the RAI class difference bar chart for Site C, which shows a markedly different pattern from Sites A and B. The scaling site (red bars) shows a decrease in intact rock of approximately 1% rather than the increases observed at the other sites, along with modest increases in closely spaced discontinuous (approximately 1%) and widely spaced discontinuous (approximately 0.5–1%). The shallow overhang class shows a decrease of approximately 4%—the largest single-class change at any of the Rumble Pit sites—but this is accompanied by an increase in cantilevered overhang of approximately 1%. The control site (gray bars) shows some changes as well, including a small decrease in shallow overhang and a small increase in closely spaced discontinuous. The lack of an intact rock increase at the scaling site is a departure from the expected scaling signature and may reflect the structural character of the rock mass at Site C, which consists largely of disaggregated basalt columns. At such a slope, removing surface blocks does not expose a more intact underlying surface because the entire rock mass is already pervasively fragmented; instead, scaling may simply reveal additional discontinuous material beneath the removed blocks.

Figure 8-22 shows the temporal evolution of RAI class proportions at Scaling Site C from September 2023 through approximately May 2025. The time-series plot of RAI class percentages shows that the distribution of classes at site C remained relatively stable over the monitoring period, with the largest class proportions exhibiting limited variability across epochs.The intact class starts at approximately 30–35% and remains relatively stable or shows a very gradual decline over the monitoring period, without the upward step observed at Sites A and B. The shallow overhang class (approximately 30–35%) dominates the slope classification more than at the other sites, reflecting the columnar basalt geometry that produces persistent overhanging geometries. The fragmented discontinuous and closely spaced discontinuous classes each occupy approximately 10–15% and show modest fluctuations over time.

The overall picture is one of a slope whose RAI class distribution was not substantially altered by scaling and shows little temporal evolution in the monitoring period. The subdued morphological response at site C is consistent with the geologic character of this rockslope. The already disaggregated nature of the slope surface means that the removal of individual blocks does not fundamentally alter the overall surface morphology or expose significantly more competent rock beneath. In terms of the Section 6.2 metrics, site C represents a case in which the initial slope conditions constrain the potential for scaling to produce the morphological improvements observed at sites A and B.

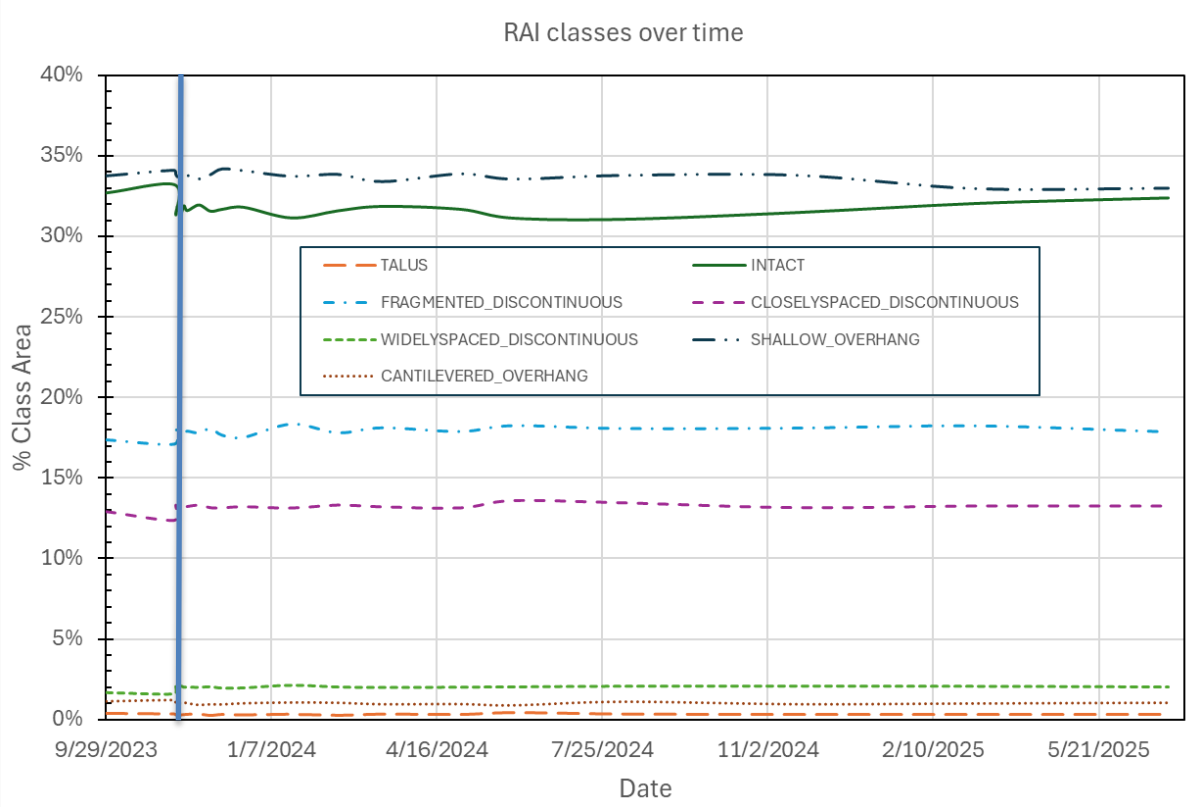

Figure 8.22. Changes in RAI classification percent areas over time for Scaling Site C. The blue vertical line represents the date of scaling (11/10/2023).

8.3.3 Rates and Volumes

Figure 8-23 presents the activity rate comparison for Site C. Panel (a) shows a sharp spike in activity at the scaling site (solid line) reaching approximately 0.30 at the time of scaling, which then declines rapidly. The control site (dashed line) shows a smaller but notable spike of approximately 0.05 at a slightly later time (approximately 100 days post-scaling), possibly reflecting seasonal environmental forcing. The two curves converge quickly, within approximately 100–150 days. Panel (b) fits logarithmic regressions: the scaling site ($R^2 = 0.38$) and the control site ($R^2 = 0.19$). A notable feature is that the control site shows a single elevated data point at approximately 350 days (a daily activity rate of approximately 0.15), substantially above the trend. This isolated spike at the control may reflect a discrete large rockfall event rather than a sustained change in activity. The scaling site decay coefficients are smaller in magnitude than at Sites A and B (−0.006 vs −0.012), suggesting a less pronounced post-disturbance signal, which is consistent with the more limited morphological change documented in the RAI analysis. Overall, the activity rate analysis at Site C shows less differentiation between the scaling and control conditions than at the other two sites, evidenced by the similarities in the regression parameters.

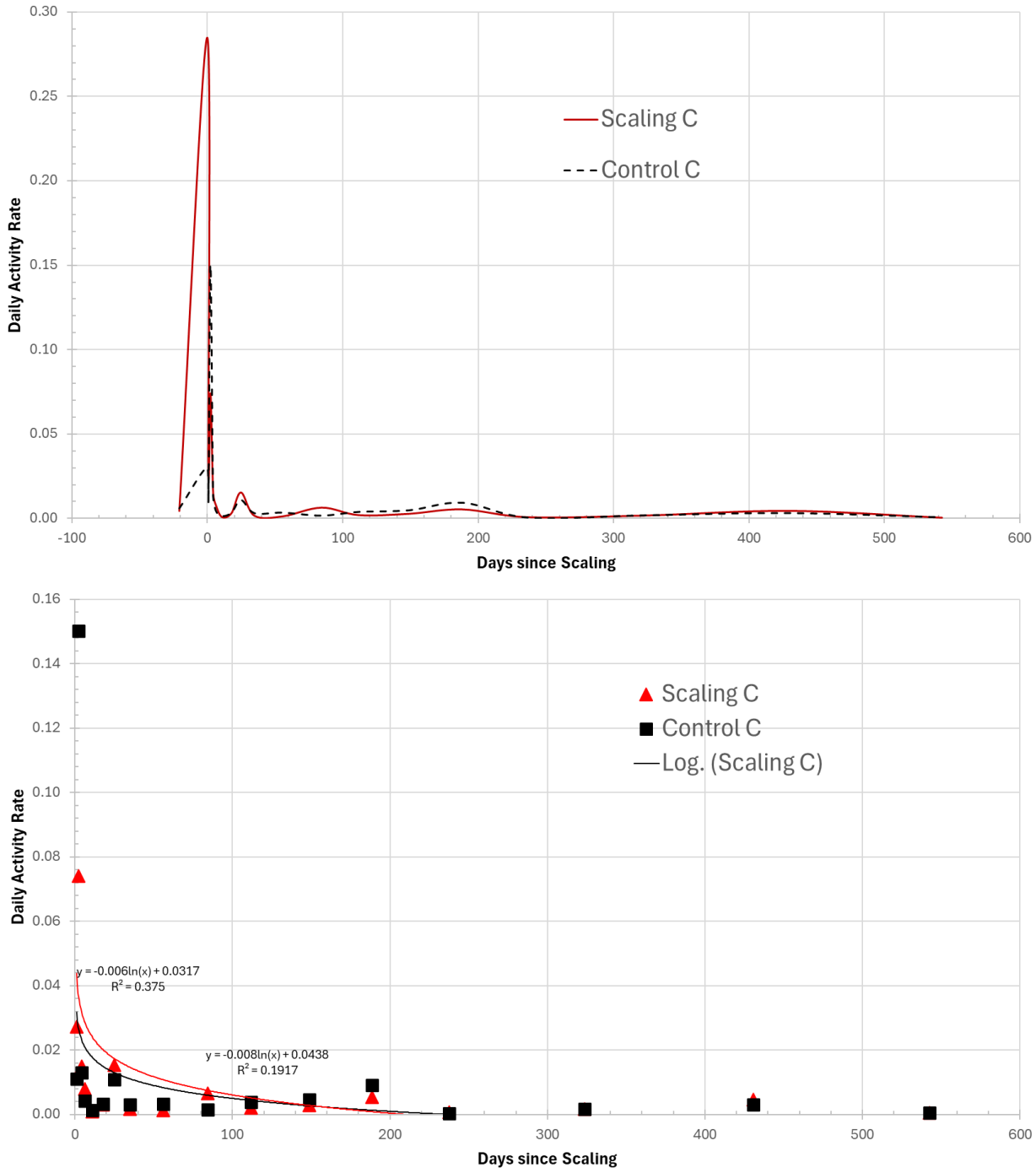

Figure 8.23. Changes in activity rates over time for Scaling Site C compared with control site C. (a) Including baseline activity rates and (b) after scaling with regression functions.

Figure 8-24 presents the cumulative erosion analysis for Site C for various size bins at both the scaled and control rockslopes. Site C shows the least differentiation between scaled and control conditions of the three Rumble Pit sites. The top panel (control) and central panel (scaled) show similar patterns of cumulative volume accumulation, with small to medium-sized rockfalls dominating the erosion budget at both slopes. As at site B, smaller and medium-sized rockfall events ($10^{-2} > V > 10^{-4}$ m³) account for a majority of total volume change at both the scaled and control rockslopes. Unlike sites A and B, the comparison of scaled and control rockslopes at site C reveals limited differences in cumulative erosion volume, with no period of visibly suppressed accumulation at the scaled slope following scaling. The two curves track each other closely from the outset.

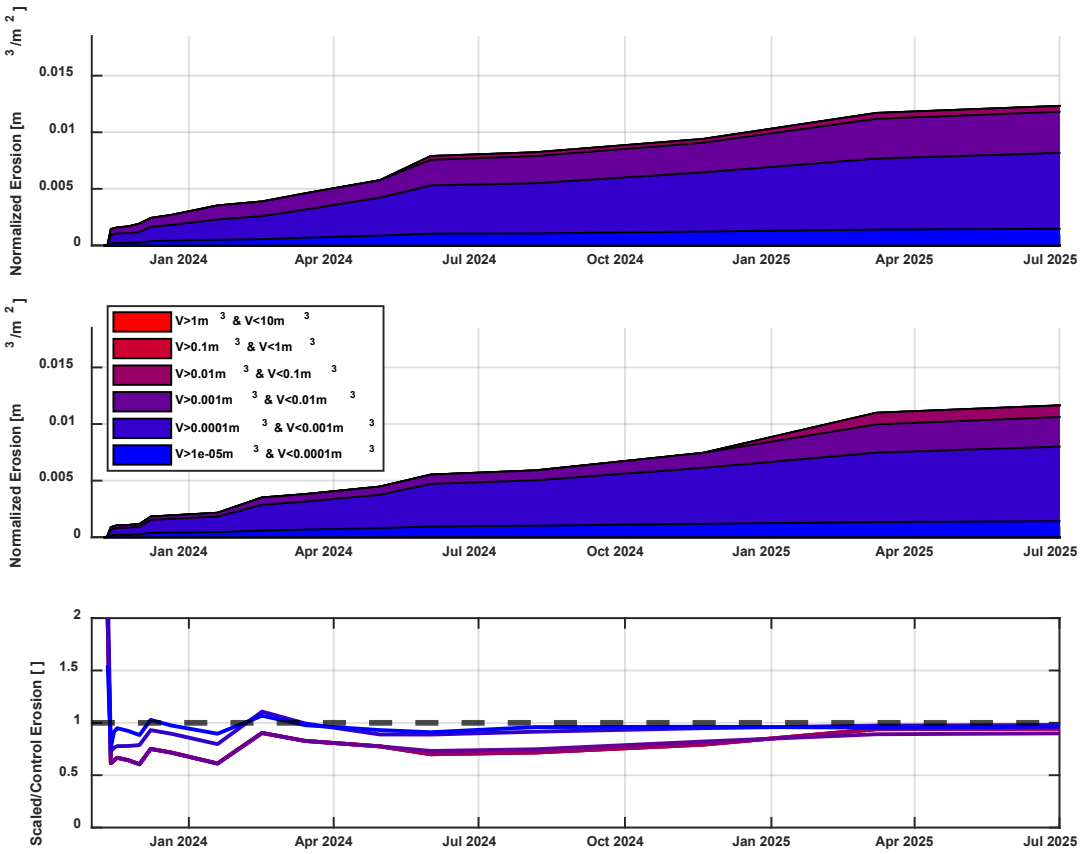

Figure 8.24. Cumulative normalized erosion for Control Rockslope C (top), Scaled Rockslope C (center), and ratio of scaled to control (bottom).

Cumulative volume change at the scaled and control rockslopes was broadly similar in the period following scaling, and the ratio of scaled to control cumulative volume (Figure 8-24, bottom panel) shows that while the scaled rockslope accumulated slightly less total erosion volume, the two slopes converged closely shortly after the scaling operation. As at the other sites, the largest changes and associated noise occur immediately following scaling, likely reflecting rapid evacuation of disturbed material or differencing errors during shorter monitoring epochs.

In the bottom panel, the ratio of scaled to control cumulative volume hovers near 1.0 throughout the monitoring period, only briefly dipping below 1.0 immediately after scaling before quickly returning. This near-unity ratio indicates that scaling did not produce a measurable reduction in cumulative erosion at Site C. The absence of a sustained difference in cumulative erosion volume between the scaled and control rockslopes at site C is consistent with the subdued morphological response observed in the RAI analysis. The already disaggregated, columnar basalt structure of the rock mass at this site limits the extent to which scaling can reduce overall rockfall rates or alter the size distribution of events.

These observations suggest that the effectiveness of scaling is not universal but depends on the rock mass structure and the extent of intervention: slopes where the rock mass is already pervasively fragmented may not benefit from conventional hand-tool scaling to the same degree as slopes with more intact rock and discrete precarious blocks.

8.3.4 Volume-Frequencies

Figure 8-25 presents the volume-frequency relationships normalized by rockslope area and monitoring duration for the scaled and control rockslopes at site C for the first six months following scaling and for the period thereafter. The scaled (green) and control (black) curves nearly overlap across the entire volume range. A very modest decrease in the frequency of larger rockfalls ($> 10^{-3}$ m³) is visible at the scaled slope, along with a slight increase in small rockfall frequency, but these differences are minor compared to the clear separations observed at Sites A and B. The near-congruence of the two curves confirms that scaling did not meaningfully alter the rockfall size-frequency distribution at this site.

In the framework of Section 6.1.3, the absence of a reduction in the activity parameter β or a steepening of the scaling parameter α indicates that the scaling operation did not alter either the frequency or the relative size distribution of rockfall events at site C in a detectable way. This finding is consistent with the limited morphological response documented in the RAI analysis and the absence of a sustained reduction in cumulative erosion volume described in Section 7.3.3, and together these independent lines of evidence support the conclusion that scaling did not produce a measurable improvement in rockfall hazard at this site.

Although the results at site C show limited evidence of mitigation effectiveness, the volume-frequency comparison is nonetheless informative. The close correspondence between the scaled and control slope distributions confirms that the magnitude-frequency framework is capable of detecting the absence of a mitigation effect as clearly as it detects its presence, supporting its value as a diagnostic tool within the Section 6.0 assessment framework.

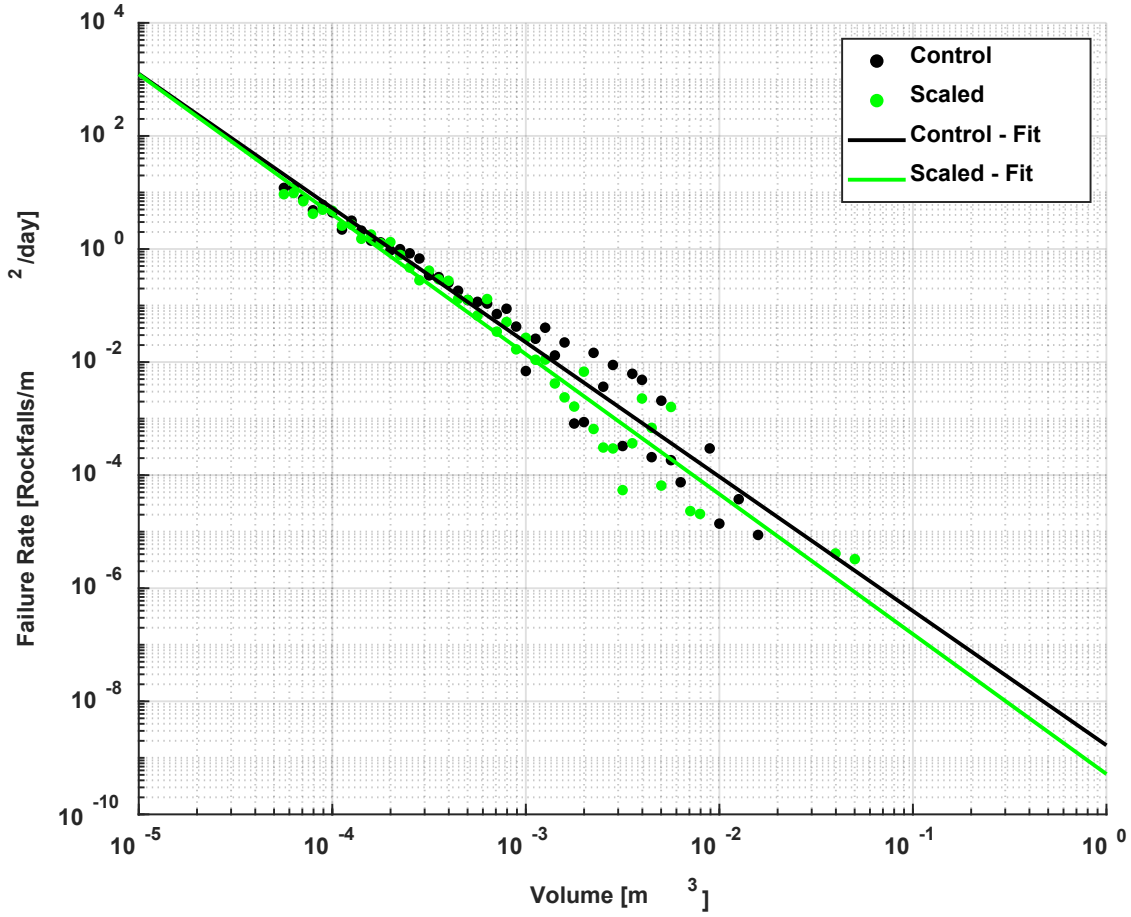

Figure 8.25. Volume-frequency relationships for both scaled (green) and control (black) rockslopes for the six months following scaling for Rockslope C.

8.3.5 Trajectory Analysis

As with the previous rockslopes, a set of parallel trajectory analyses were performed to characterize rockfall hazard for the control and scaled rockslopes at Site C. First, a probabilistic trajectory analysis (PTA) was performed, which consisted of calculating trajectories from every possible source location on the rockslope for a suite of volumes, ranging from 10^{-5} m^3 to 1 m^3. Restitution values were assumed to be that of medium hardness rock and momentum-based restitution (i.e. "lumped mass") was considered. The second analysis, the retrospective trajectory analysis (RTA), was performed using the volumes of observed rockfalls during each epoch and their associated source areas, calculated as the centroid of the cluster that was detected to fail. The PTA, along with volume-frequency relationships, serves as a means of characterizing probabilistic rockfall hazard based on purely rockslope morphology and the range of rockfall volumes considered. The PTA serves to evaluate the potential mobility and energy of potential rockfalls from any source on a rockslope, scaling volumes based on observed volume-frequency relationships.

8.3.5.1 Retrospective Trajectory Analysis (RTA)

Figure 8-26 presents the RTA results for Site C. The top panel shows that smaller-volume rockfall dominates the activity, with fewer large spheres compared to Sites A and B. Sources are distributed across the face, though the overall impression is of more uniformly small events reflecting the disaggregated, columnar rock mass. As with Rockslope B, Rockfalls that are higher in elevation have more potential to travel away from the slope owing to impacts with slope facies below. Again, overhanging rockfalls above slope facies that are subvertical have a tendency to increase rockfall reach.

The bottom panel shows ending locations color-coded by volume. The slope profile at Site C (elevations approximately 128–138 m) is somewhat lower than the other sites, and the distribution of ending locations is more concentrated near the slope base, with fewer long-reach outliers. The rockfall trajectories at this site appear to be less varied than at Sites A or B, consistent with a more uniform slope morphology and a narrower range of rockfall sizes.

Figure 8-27 presents the trajectory analysis for Site C. These analyses demonstrate the associated starting and ending locations inferred from actual rockfall sources at the site, as well as associated kinetic energy upon final impact (assumed to be when velocity nears zero or the lowest elevation in the DTM). As shown in Figure 8-27(a), for all epochs, rockfall from Control C tend to travel further (75% exceeding a lateral travel distance greater than half the source height), while rockfall from Scaled C show limited travel distance (only 30% exceed a lateral travel distance greater than half the source height).

For Scaled C, very few rockfalls exceed 100% of the height in terms of reach, both before and after scaling, whereas Control C demonstrates that 10% exceed the rockslope height in terms of reach – a notably higher proportion. The relatively small change in mobility before and after scaling on Scaled C suggests that scaling has little to do with the differences in rockfall trajectories between slopes; rather, it owes to differences in the slope morphology. While a limited size rockslope and limited timeframe of observation, it appears that the geometry of Control C enables more rockfall mobility, perhaps owing to the more concave facies on the lower part of the slope. Again, knowing this distribution of travel lengths provides a semi-empirical means of sizing rockfall retention structures based on a probability of exceedance – this rockslope may benefit from a wider catchment ditch in design.

Panel (b) shows that the change in POE for the scaled slope relative to both the control (green) and pre-scaling condition (red) is small—near zero across most L/H ratios—confirming that scaling did not meaningfully alter rockfall reach at this site. Panel (c) shows that the kinetic energy POE curves for the scaled slope before and after scaling are nearly superimposed, with the control curve offset upward reflecting its inherently higher mobility. Panel (d) confirms minimal change in energy POE.

Unlike previous RTA, the differences in rockfall mobility on the scaled slope C versus the control slope C appear to be a function of differences in slope geometry, not scaling. The similar trajectory and energy levels for Scaled C before and after scaling appear to

support this observation. For Site C, scaling does not appear to yield any appreciable, decreased likelihood to exceed certain levels of kinetic energy, as shown in Figure 8-27c). This observation is different than Rockslopes A and B, which demonstrated a change in rockfall mobility and energy for the 5-6 months following scaling.

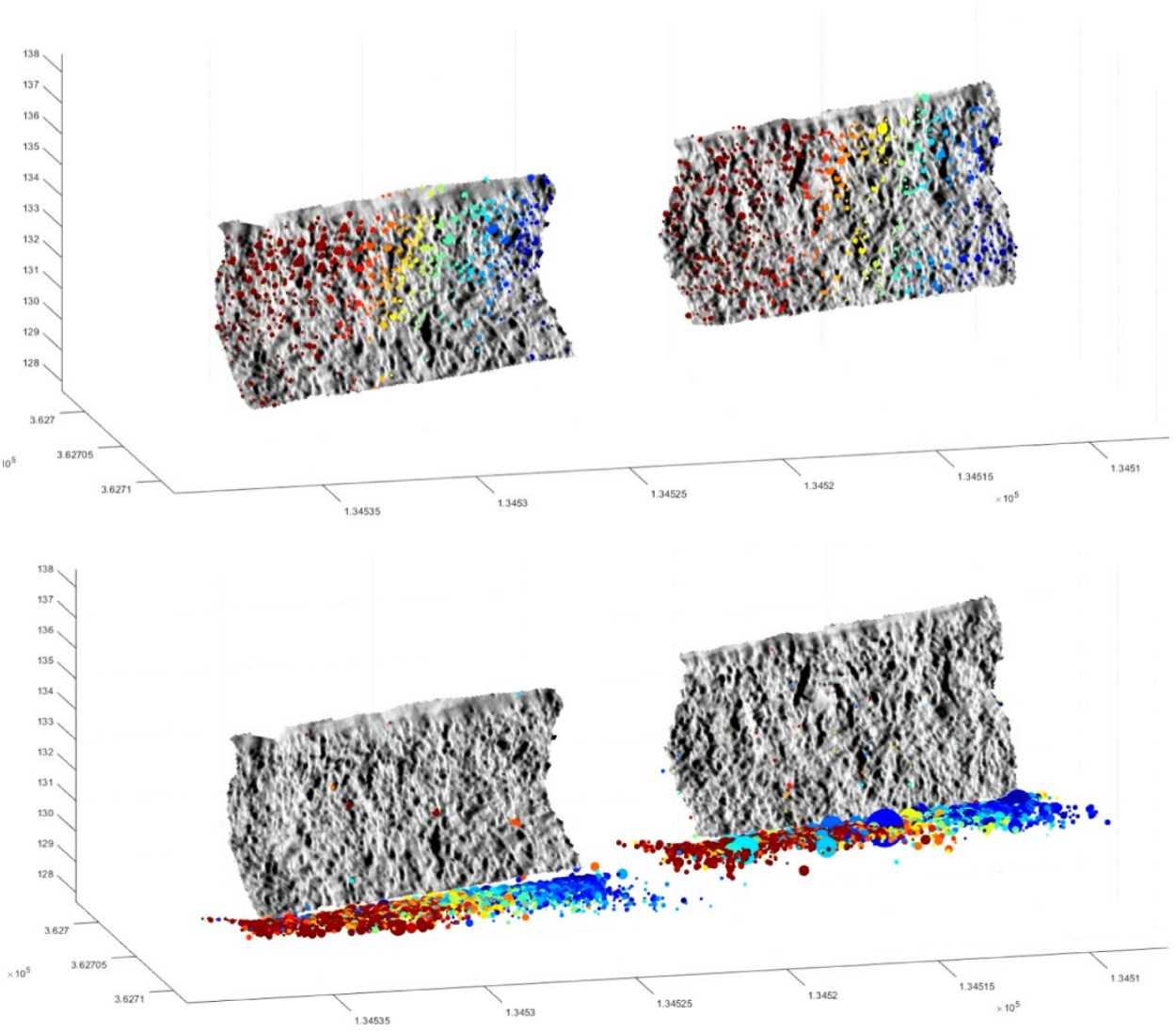

Figure 8.26. Rockfall sources (top) and ending rockfall locations (bottom) for Site C for all epochs.

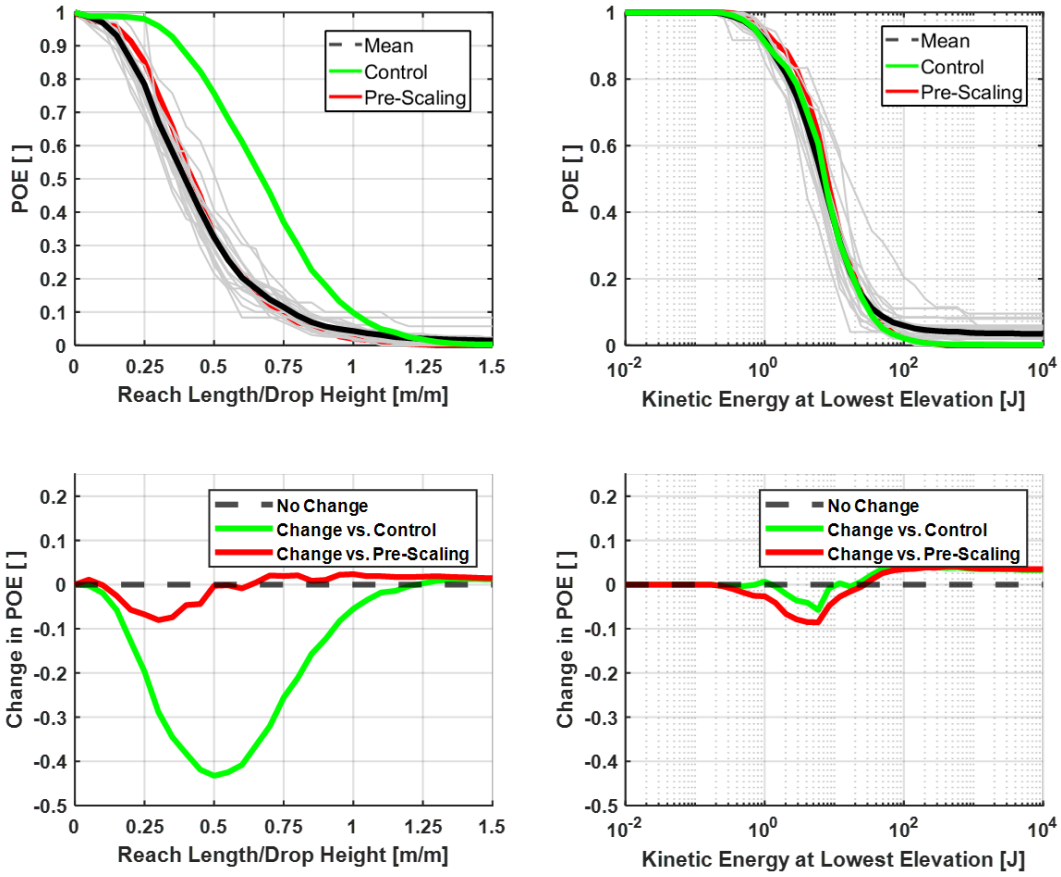

Figure 8.27. Probability of exceedance plots for Site C for POE vs (a) the ratio of reach length to drop height and (b) kinetic energy at the lowest elevation and the change in POE vs (c) the ratio of reach length to drop height and (d) kinetic energy at the lowest elevation. Green represents the control and red represents the pre-scaling.

8.3.5.2 Probabilistic Trajectory Analysis (PTA)

The observed rockfall volume-frequency relationships for Rockslope C (Figure 8-28) and multiple trajectory analyses with different rockfall sizes are used to evaluate the overall distribution of energy stemming from a rockslope and compare hazard before and after scaling. The probability of exceedance (PoE) of certain rockfall energy normalized to rockslope area and time for Rockslope C are shown in Figure 8-28. The top panel shows that the scaled (green) and control (black) POE curves nearly overlap, with only a negligible leftward shift of the scaled curve. This minimal shift for Rockslope C is sensible as the volume-frequency relationships are similar between rockslopes, shown in Figure 8-28. The bottom panel confirms minimal reduction in POE across the full range of normalized kinetic energy rates, with the reduction hovering near zero throughout. This stands in clear contrast to Sites A and B, where reductions of approximately 20–65% were observed at intermediate energy levels. Again, this response is likely rockslope specific and dependent on the size of rocks scaled and methods used to remove

hazardous rockfall sources, but for Rockslope C, scaling does not appear to diminish the potential energy release of rockfall in for this site.

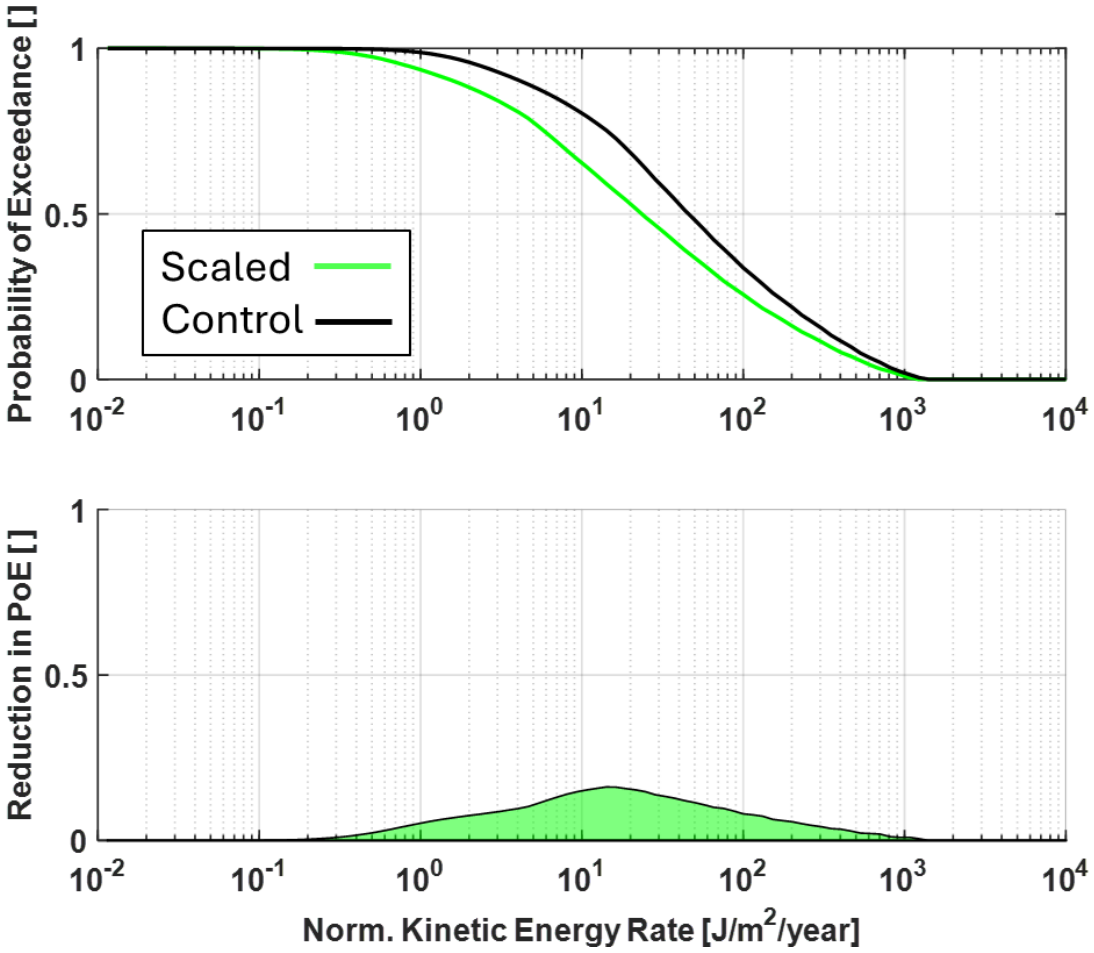

Figure 8.28. PTA-derived probability of exceedance of normalized kinetic energy rate for Site C (top) and reduction in POE (bottom).

9.0 OREGON SITE ANALYSIS

Chapter 9 extends the RAI-based evaluation framework developed and demonstrated at the Rumble Pit to operational highway rock slope sites: the I-5 Siskiyou Pass corridor in southern Oregon and the SR14 MP73 site along the Columbia River Gorge in Washington state. These sites differ from the controlled Rumble Pit experiment in several respects that bear directly on how the Section 6 metrics can be applied and interpreted.

At the Rumble Pit, the experimental design provided paired scaled and control rockslopes, multiple pre-scaling baseline surveys, and a well-documented scaling operation of known spatial extent and method. These are conditions that enabled full application of all Section 6 metrics and direct attribution of observed changes to the scaling treatment. The operational highway sites analyzed in this chapter lack one or more of these conditions. At Siskiyou Pass, terrestrial lidar monitoring commenced at the time of the scaling operation, precluding direct comparison of post-scaling conditions against a pre-scaling terrestrial baseline. At SR14 MP73, pre- and post-scaling terrestrial lidar surveys are available, enabling morphological classification and activity rate comparisons, but no paired control slope was established. At both sites, the scale of the slope face is substantially larger than any of the Rumble Pit study areas (i.e., A, B, or C).

Together, the sites span a range of geologic settings, slope scales, and mitigation intensities. The I-5 Siskiyou Pass site is a large, structurally complex rock cut along a major interstate corridor, where a substantial scaling operation was conducted and subsequently monitored with both mobile and terrestrial lidar. The SR14 MP73 site is a Columbia River Gorge basalt slope that underwent extensive scaling targeting a large, cantilevered overhang system, with pre- and post-scaling terrestrial surveys enabling direct morphological comparison. The analysis of each site follows the structure established in Chapter 8, progressing through RAI morphological classification, activity rates and cumulative erosion volumes, magnitude-frequency relationships, and trajectory analysis where the data and computational resources permit.

9.1 I-5 SISKIYOU PASS

9.1.1 RAI Analysis

The RAI morphological analysis at the I-5 Siskiyou Pass site documents a measurable response to the scaling operation across several morphological classes, though the absence of a pre-scaling terrestrial lidar baseline precludes interpretation to a comparison between the immediate post-scaling epoch and subsequent monitoring surveys. The slope gradient maps (Figure 9-1) illustrate the spatial character of this response: in the pre-scaling condition, extensive zones of steep to overhanging slope angle indicated by orange and red hues corresponding to gradients exceeding 60° and 90° respectively are distributed across multiple benches throughout the length of the cut. In the post-scaling condition, the areal extent of these steep zones is reduced, with a corresponding increase in areas classified at lower gradient angles, reflecting relaxation of the slope profile through material removal.

The RAI classification maps (Figure 9-2) document the associated morphological changes in greater spatial detail. In the pre-scaling condition (panel a), overhang material is distributed across the upper benches and along several locally steep zones throughout the site. Following scaling (panel b), the extent of overhang classification is reduced and the intact rock class occupies a larger proportion of the slope face, particularly along the benches where scaling was concentrated. These changes are quantified in Figure 9-3, which shows the net change in percent area by RAI class between the pre- and post-scaling surveys. Intact rock increased by several percent, consistent with the exposure of more competent material beneath the removed surface debris. Fragmented discontinuous rock decreased, representing the removal of the most highly fractured surface material — the morphological class carrying the highest default instability rate among the discontinuous sub-classes (Markus et al., 2023). The cantilevered and shallow overhang classes both show net reductions, providing direct evidence that the scaling operation addressed the highest-risk morphological features on the slope face as identified in Section 6.2.

Of particular note within the Figure 9-3 class change data is the reduction in fragmented discontinuous rock accompanied by a corresponding shift toward widely spaced discontinuous material. Under the Section 6.2 evaluation framework, this Df-to-Dw transition indicates a reduction in surface fragmentation, consistent either with the removal of the most highly comminuted surface material or with the exposure of fresher, more competent rock beneath. At a site such as Siskiyou Pass, where the slope geology includes structurally complex rock with multiple discontinuity sets, this shift in the discontinuous sub-class distribution represents a substantive improvement in surface character beyond what is captured by the overhang and intact rock metrics alone.

Figure 9-4 presents the temporal evolution of RAI class distributions across the full monitoring period, from June 2023 through August 2025. The talus class exhibits a pronounced and sustained increase over this period, growing from a modest initial proportion of the classified slope area to become one of the more prominent classes by the later monitoring epochs. Under the Section 6.2 framework, an initial increase in talus following scaling is expected, reflecting the accumulation of debris dislodged during the operation. However, the continued growth of the talus class across successive epochs — rather than stabilization or decline — warrants careful interpretation. Two mechanisms may contribute to this sustained talus increase: ongoing detachment of loosened material from freshly exposed slope surfaces as stress conditions adjust following the removal of overhanging rock, and the progressive expansion of the scan footprint as talus accumulation and changes in slope geometry reduce occlusion of previously shadowed areas. The relative contribution of these mechanisms cannot be resolved from the available data alone, but the distinction has practical significance: talus growth driven by ongoing rockfall represents a continued material flux from the slope, while talus growth driven by improved scan coverage is a measurement artifact that does not reflect a change in slope activity.

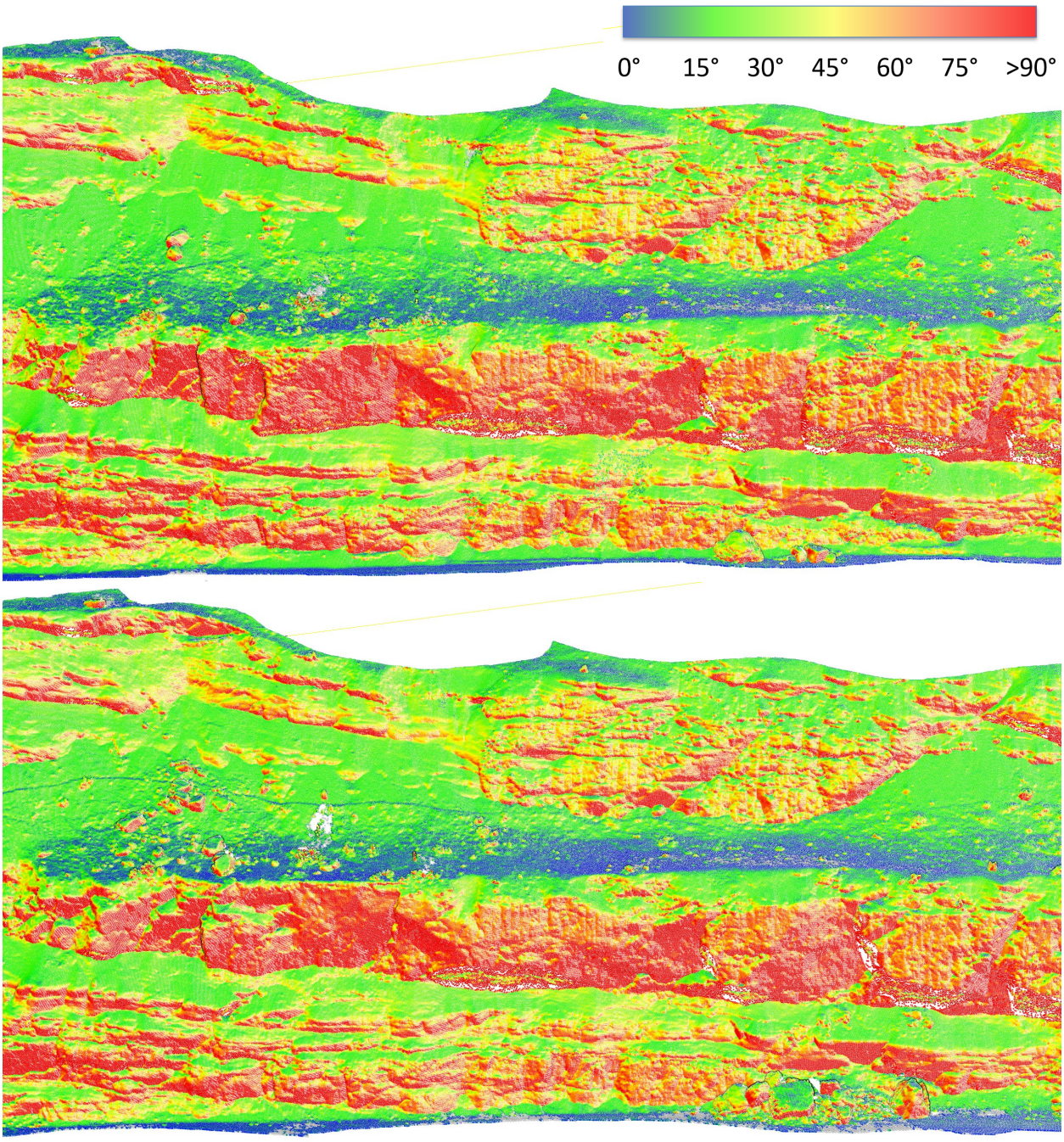

Figure 9.1. Changes in slope gradient resulting from the scaling operation for a portion of the I-5 Siskiyou Pass site. (6/1/2023 vs 10/12/2023).

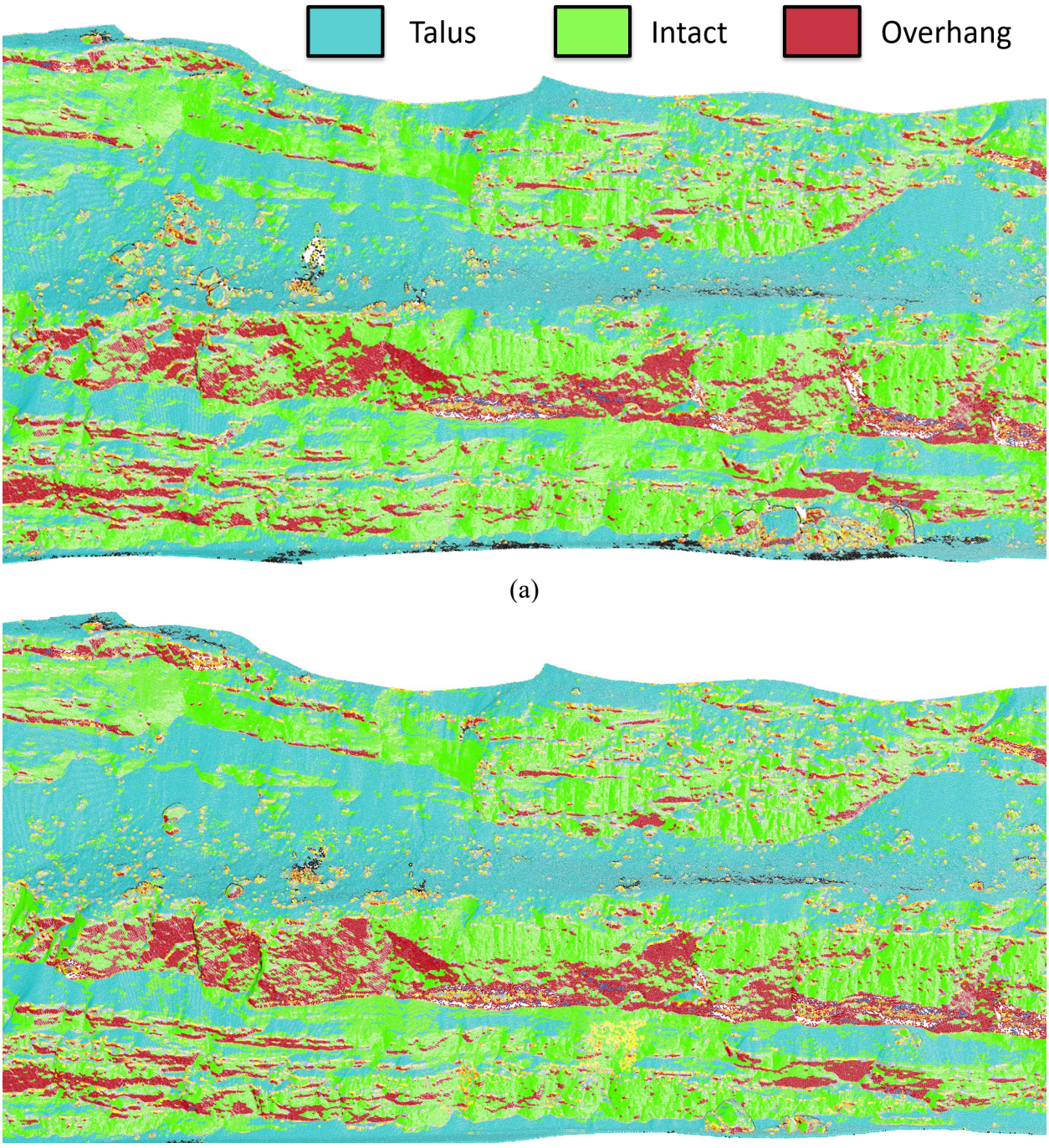

(a)

(b)

Figure 9.2. Changes in the RAI classification resulting from the scaling operation for a portion of the I-5 Siskiyou Pass site. (6/1/2023 vs 10/12/2023).

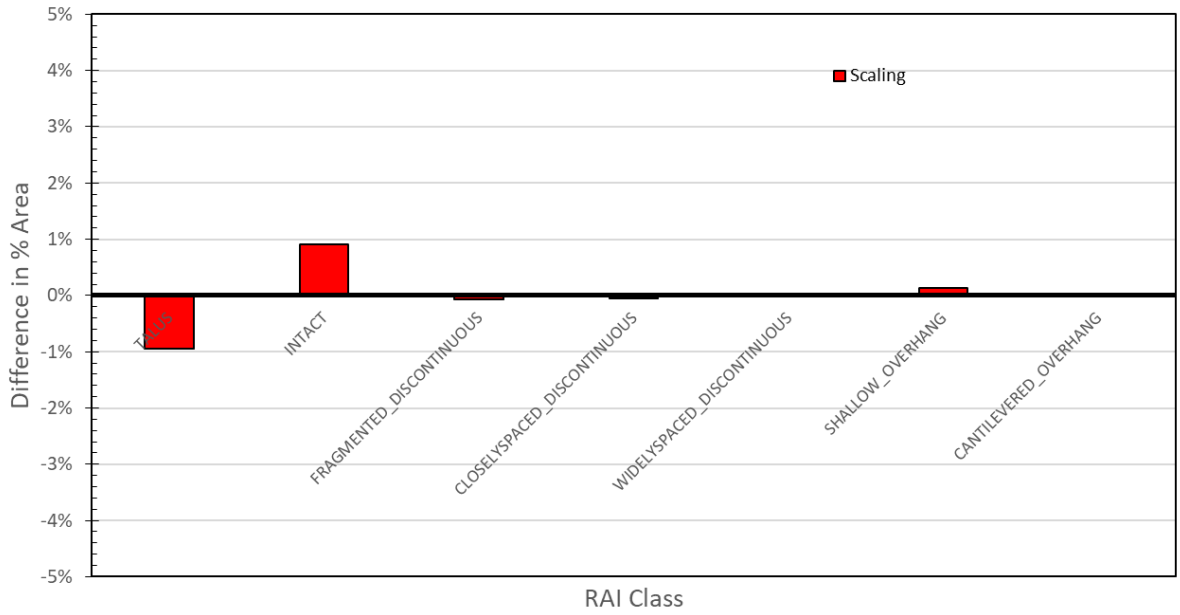

Figure 9.3. Changes in the distribution of RAI classes resulting from the scaling operation for a portion of the I-5 Siskiyou Pass site. (6/1/2023 vs 10/12/2023).

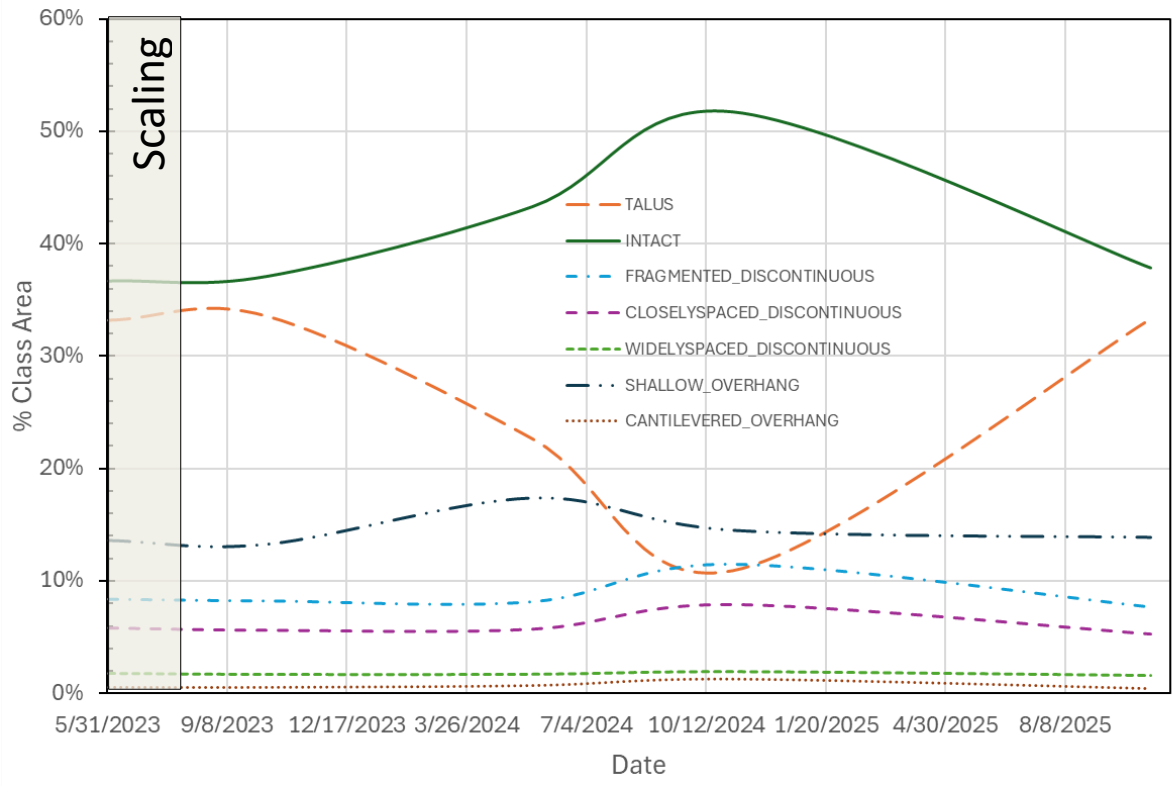

Figure 9.4. Changes in the RAI classification over time for the I-5 Siskiyou Pass site.

The intact rock class remains relatively stable across the post-scaling monitoring period following its initial increase, suggesting that the freshly exposed intact surfaces have not undergone rapid deterioration within the timeframe of the current monitoring record. The overhang classes likewise remain at reduced levels through the monitoring period, with no pronounced rebound toward pre-scaling proportions. Together, these temporal patterns are consistent with a scaling operation that produced durable morphological improvements within the observation window, though the absence of a pre-scaling terrestrial baseline prevents definitive quantification of the magnitude of improvement relative to the pre-treatment slope condition.

9.1.2 8.1.2 Rates and Volumes

Figure 9-5 presents the change detection results for the Siskiyou Pass site, showing the spatial distribution of surface change associated with the scaling operation. Areas of material loss, indicated by warm hues in the false-color change map, are concentrated along the upper benches and overhang zones, consistent with the targeted removal of precarious blocks during scaling. The spatial pattern of detected change confirms that the scaling operation was not uniformly distributed across the slope face but was concentrated at locations where overhanging and steeply inclined material was most accessible and most visibly precarious, a pattern consistent with the hand scaling approach described for this site.

A baseline rockfall activity rate of 0.128%/yr was established from mobile lidar data collected between 2013 and 2018, computed using a significant change threshold of 0.07 m to account for the higher positional uncertainty inherent in mobile lidar relative to the static terrestrial laser scanning used for post-scaling monitoring. This baseline rate provides the only pre-treatment activity reference available for the Siskiyou Pass site and serves as an approximate benchmark against which post-scaling rates can be compared. However, two sources of uncertainty limit the precision of this comparison. First, the detection threshold applied to the mobile lidar data (0.07 m) differs from the threshold applied to the terrestrial post-scaling surveys (0.05 m), meaning that the mobile baseline suppresses detection of smaller events that the terrestrial surveys would capture, introducing a systematic bias toward underestimating pre-scaling activity relative to post-scaling measurements. Second, the mobile lidar baseline spans a five-year period ending approximately five years before the scaling operation, during which time the slope may have evolved morphologically. These considerations do not invalidate the mobile baseline as a reference but require that comparisons between it and the post-scaling terrestrial rates be interpreted with appropriate caution.

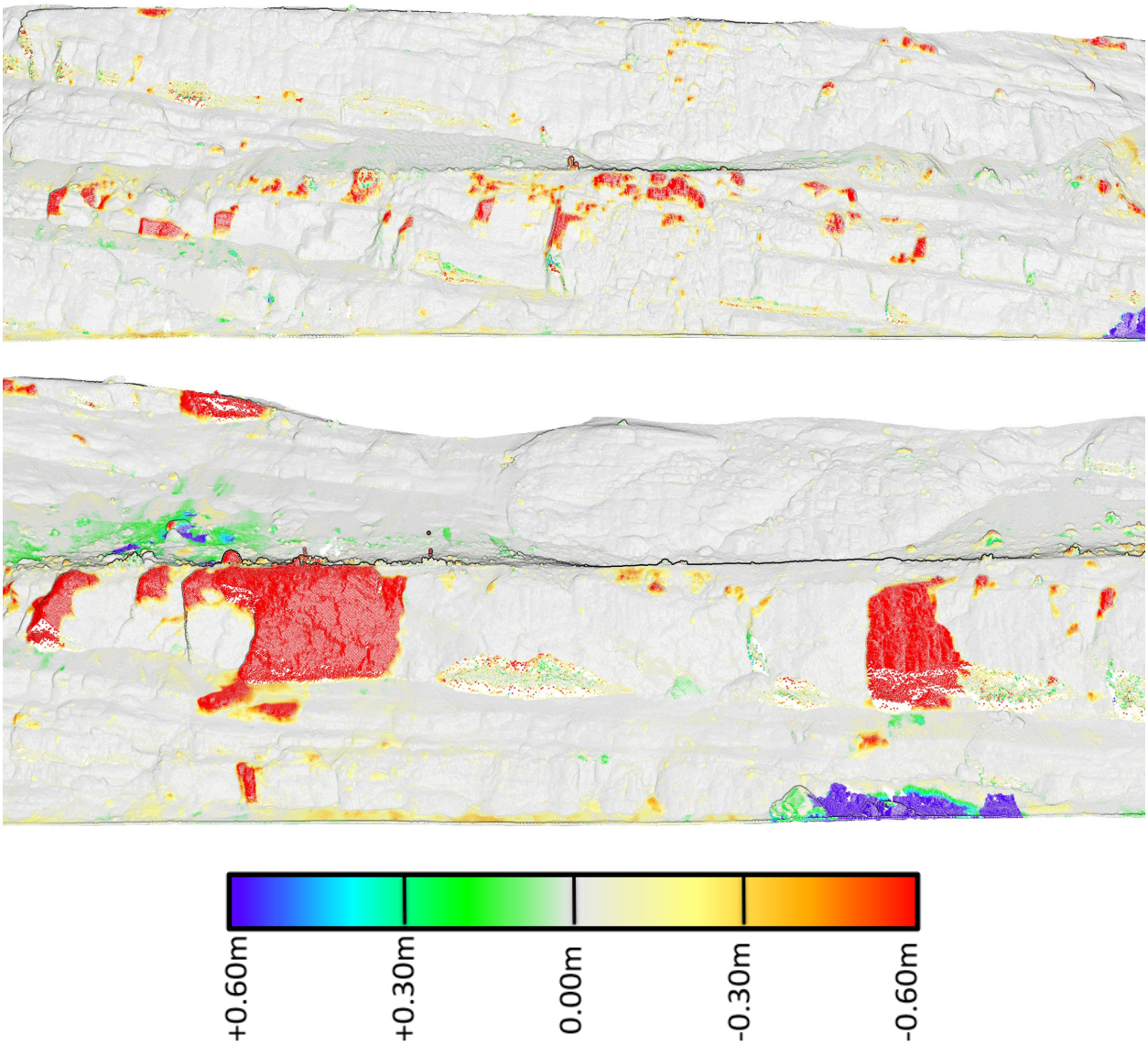

Figure 9.5. Changes to the rock slope resulting from the scaling operation. (6/1/2023 vs 10/12/2023).

Figure 9-6 presents the overall activity rate over time, referenced to the scaling operation. The post-scaling rate in the first monitoring epoch is approximately 0.26%/yr, substantially above the mobile lidar baseline of 0.128%/yr, reflecting the elevated activity associated with adjustment of the freshly exposed slope surface following scaling. This elevated initial rate is consistent with the pattern observed at the Rumble Pit sites and at SR14 MP73, where the period immediately following scaling is characterized by accelerated detachment of loosened and newly destabilized material before the slope stabilizes at a lower activity level. In subsequent epochs the overall rate declines toward and below the mobile lidar baseline, suggesting that the slope achieved a post-scaling activity level comparable to or lower than the pre-treatment condition, at least within the monitoring period. A modest rebound in the final monitoring epoch is evident in Figure 9-6, a

pattern also observed at other sites in this study and discussed further in the context of the GG241 long-term monitoring data in Chapter 9.

Figure 9-7 presents the per-class activity rates over time, disaggregated by RAI morphological class. All classes show declining rates over approximately the first 200 days following scaling, consistent with the initial post-treatment adjustment period identified across the study sites. The cantilevered overhang class exhibits the highest initial activity rate and subsequently declines, though it shows a renewed increase in the later monitoring epochs. Under the Section 6.1.2 evaluation framework, a sustained post-mitigation decline in overhang class activity rates would represent the clearest indicator of successful removal of kinematically unstable surface material. The partial rebound in cantilevered overhang activity in the later epochs at Siskiyou Pass may reflect the progressive exposure of new overhang features as supporting material beneath existing overhangs continues to weather and erode, or it may reflect improved scan coverage of previously occluded overhang zones as the slope geometry evolves. Distinguishing between these interpretations would require field verification of the locations contributing to the elevated late-period overhang activity rates.

Cumulative erosion volume provides a complementary means of quantifying rockfall activity across the monitoring period. For the Siskiyou Pass site, the first monitoring epoch encompasses the scaling operation itself, so no direct comparison of pre- and post-scaling erosion rates is possible from the terrestrial lidar record. Nonetheless, the temporal evolution of cumulative erosion volume following the initial scaling epoch is informative. Figure 9-8 shows cumulative rockfall for various volume bins across the monitoring period. Larger rockfall events; that is, those exceeding approximately 0.01 m^3, account for the majority of total volume change, a pattern that distinguishes Siskiyou Pass from the Rumble Pit sites, where smaller events contributed a more comparable proportion of total erosion volume. This difference likely reflects the larger scale of the Siskiyou Pass slope and the more structurally controlled character of its rock mass, which produces a size distribution weighted toward larger block failures relative to the more finely fragmented Rumble Pit material.

The bottom panel of Figure 9-8 presents the ratio of post-scaling to during-scaling erosion rates across volume bins. All size bins show a substantial reduction in erosion rate following the scaling epoch, with the largest reductions occurring in the larger volume bins. This pattern is the strongest slope performance signal available for the Siskiyou Pass site and directly relevant to ODOT's maintenance and operations planning. A modest rebound in small rockfall rates in the later monitoring epochs is evident, consistent with the progressive re-establishment of background surface activity as freshly exposed material weathers. However, the larger volume bins remain suppressed relative to the during-scaling epoch through the full monitoring period, suggesting that the strategic removal of large precarious sources at Siskiyou Pass produced a more durable effect on the size distribution of rockfall than on the overall rate of surface activity.

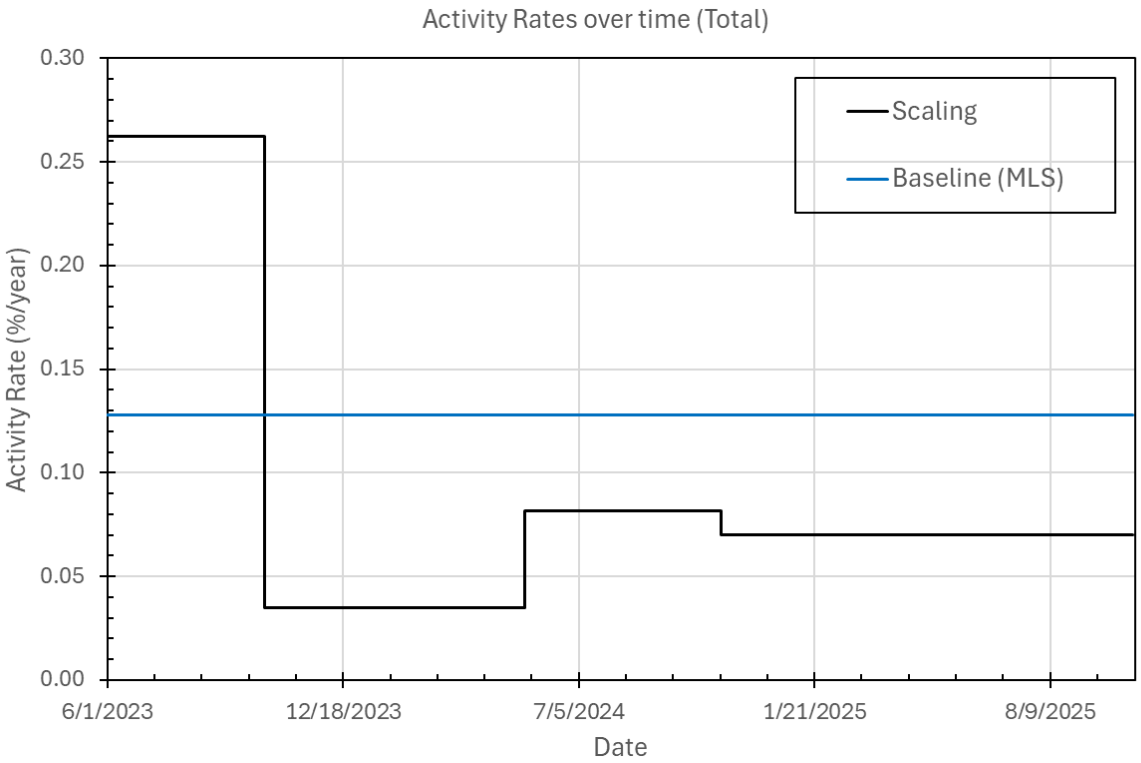

Figure 9.6. Changes in the overall activity rate over time.

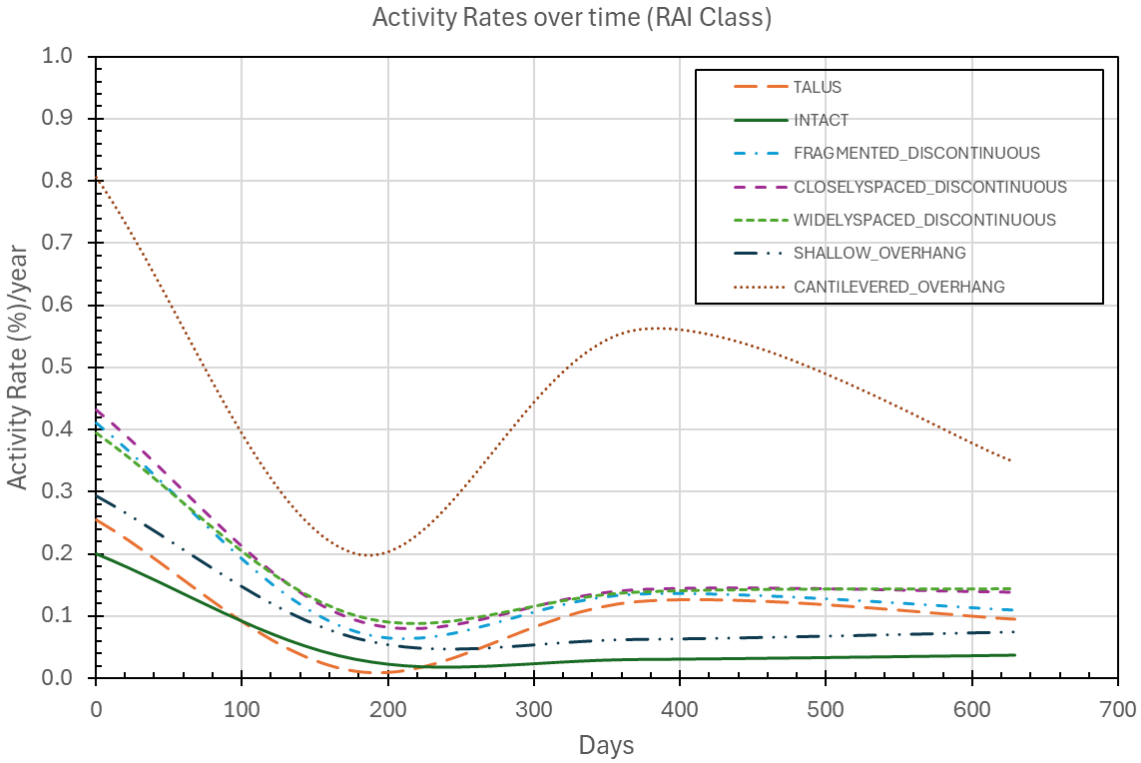

Figure 9.7. Changes in the activity rate over time by RAI class.

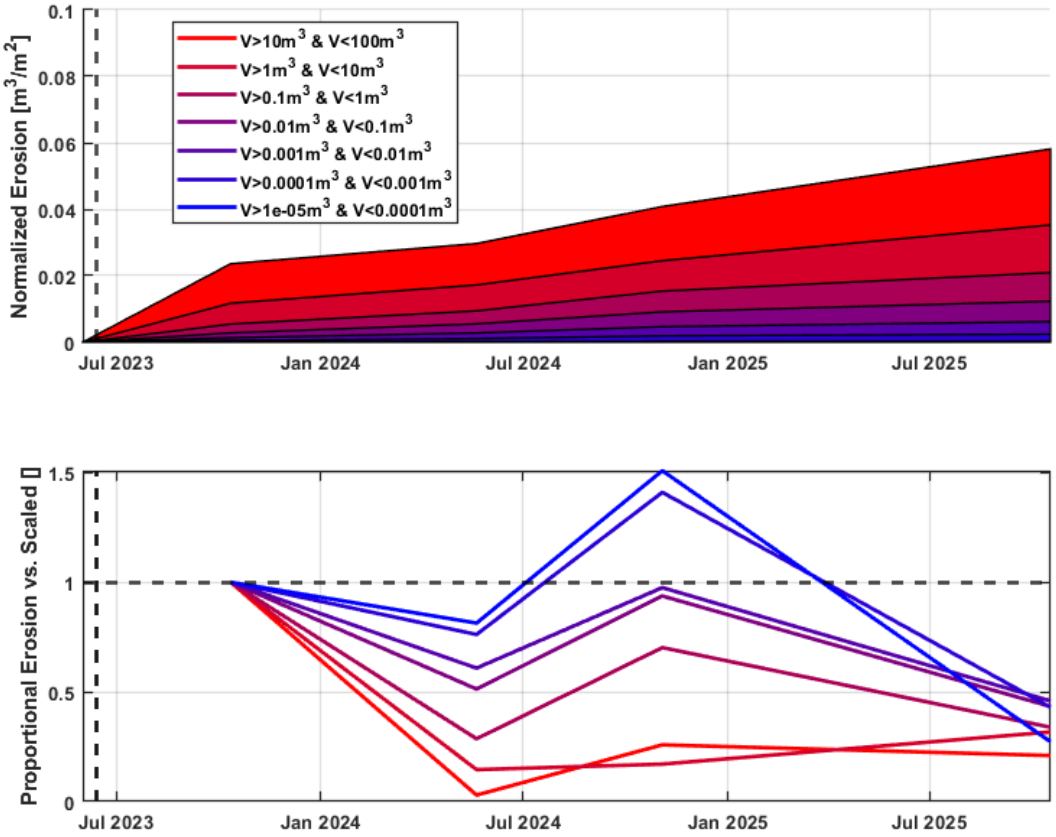

Figure 9.8. (Top Panel) Cumulative normalized erosion of Siskiyou Pass over period of monitoring. Each shaded area represents cumulative normalized erosion volume stemming from various rockfall sizes. (Bottom Panel) Ratio of cumulative volume from Scaled rockfall rates at Siskiyou Pass to post-scaling rates.

9.1.3 Volume-Frequencies

Magnitude-frequency relationships provide a scale-independent characterization of the statistical distribution of rockfall event sizes at the Siskiyou Pass site and serve as a key metric for evaluating whether the scaling operation altered the overall rate or size distribution of rockfall events, as defined in Section 6.1.3. Figure 9-9 presents the M-F curves for the Siskiyou Pass site, with post-scaling epochs shown in green and the during-scaling epoch shown in black.

Because terrestrial lidar monitoring at Siskiyou Pass commenced at the time of the scaling operation, no pre-scaling terrestrial M-F curve is available to serve as a baseline reference. The during-scaling epoch curve therefore serves as the reference against which post-scaling distributions are compared. The apparent post-scaling reduction in large-event frequency relative to the during-scaling curve therefore likely overstates the true mitigation effect. The mobile lidar baseline activity rate of 0.128%/yr provides a partial surrogate for the pre-treatment condition, but it does not support direct M-F parameterization at the resolution required for comparison of β and α values as defined in Section 6.1.3.

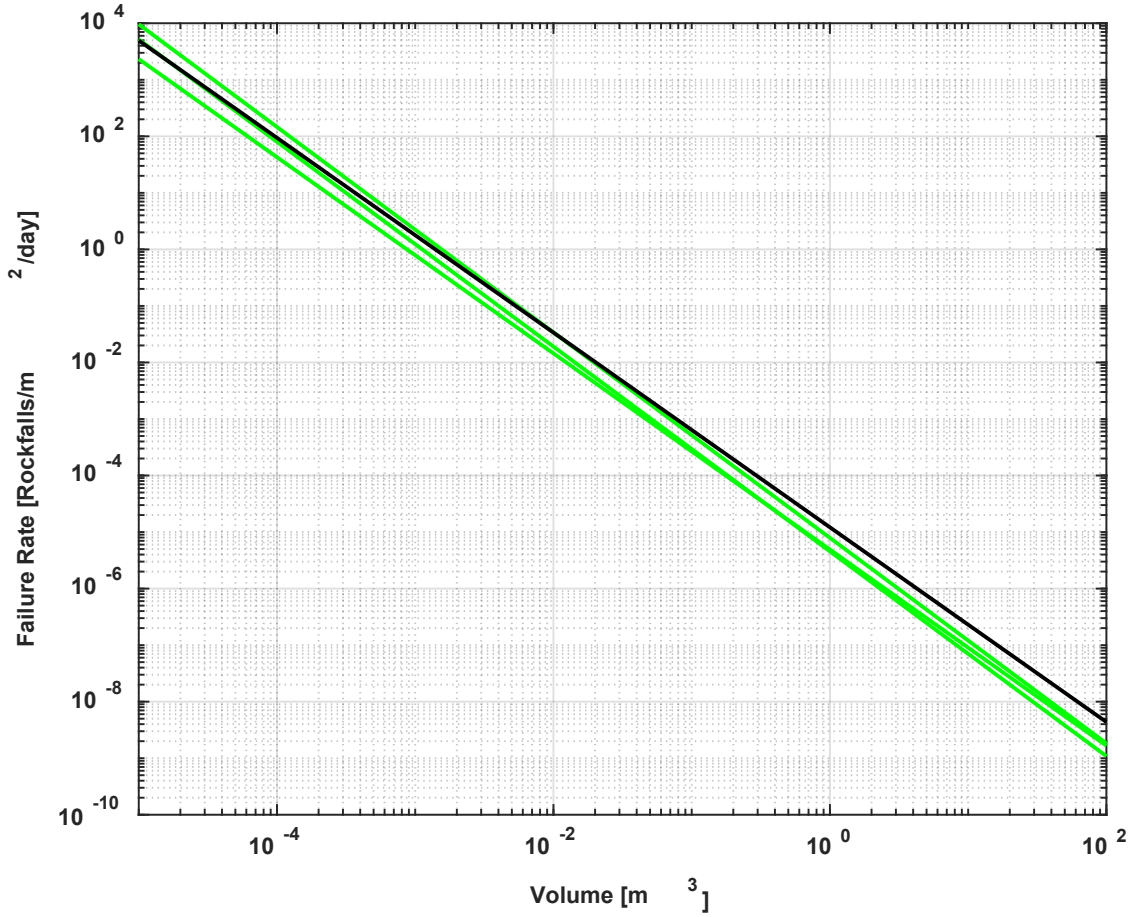

Figure 9.9. Volume-frequency relationships for both post-scaling (green) and scaled (black) rockfall for Siskiyou Summit. During this period, the scaled rockslope shows a modest decrease in the frequency of larger rockfalls.

The Figure 9-9 post-scaling curves are shifted downward and to the left relative to the during-scaling curve for events exceeding approximately 10^{-3} m³, indicating a reduction in the frequency of larger rockfall events in the period following scaling. This reduction in the activity parameter β is consistent with the removal of large, structurally unstable blocks during the scaling operation and with the cumulative erosion volume data presented in Section 9.1.2, which show sustained suppression of the larger volume bins across the post-scaling monitoring period. The convergence of the post-scaling and during-scaling curves at smaller event volumes indicates that the frequency of smaller events was less affected by the scaling operation, a pattern consistent with the Section 6.1.3 interpretation that smaller, more frequent events driven by surface weathering and raveling are less sensitive to scaling than larger, structurally controlled failures.

The scaling parameter α appears broadly similar across the during-scaling and post-scaling epochs, suggesting that the relative dominance of large versus small events did not change substantially due to the scaling operation. Under the Section 6.1.3 framework, an unchanged α in conjunction with a reduced β indicates that scaling reduced the overall frequency of rockfall activity without fundamentally altering the size distribution of events — that is, the slope

continues to produce rockfall with a similar proportional mix of large and small events, but at a lower overall rate. This finding is physically consistent with a scaling operation that removed specific large precarious sources without substantially modifying the structural character of the residual slope surface, and it distinguishes Siskiyou Pass from sites where scaling preferentially removes overhang and widely spaced discontinuous material to expose a fundamentally different surface morphology.

The modest magnitude of the post-scaling shift in the M-F curves at Siskiyou Pass, relative to the more pronounced shifts observed at Sites A and B in Chapter 8 and at GG241 in Chapter 10, is consistent with the scale and structural complexity of this site. At a large operational highway slope with multiple discontinuity sets and ongoing weathering under an active climate, the background rate of rockfall activity is governed by a broad range of structural and environmental factors that a single scaling operation cannot fully address. The M-F data at Siskiyou Pass are therefore best interpreted as evidence of a partial and time-limited reduction in large-event frequency rather than a comprehensive suppression of rockfall activity across all size classes.

9.1.4 Trajectory Analysis

Note that the RTA analysis was the focus of trajectory modeling for this site owing to its sheer size and computational expense. The PTA analysis is computationally expensive for a site of this size. Ideally, more powerful computing or parallelization will enable analysis of trajectories at this site using the PTA.

9.1.4.1 Retrospective Trajectory Analysis (RTA)

As shown in Figure 9-10, the RTA demonstrates that rockfall sizes vary considerably for the Siskiyou Pass. Rockfalls that are higher in elevation have more potential to travel away from the slope owing to impacts with talus piles and outward facing slopes below. Many rockfall also remain on slope ledges owing to their gentle nature.

These analyses demonstrate the associated starting and ending locations inferred from actual rockfall sources at the site, as well as associated kinetic energy upon final impact (assumed to be when velocity nears zero or the lowest elevation in the DEM). Different than the Rumble Pit rockslopes, rockfall at Siskiyou Pass tend to have a larger travel length to height, where more than 80% of rockfall travel more than half the height of their source location. Further, approximately 30% travel as far away from their source as their height, suggesting that the geometry of the slope (steep, outward faces) may result in notable mobility. Again, knowing this distribution of travel lengths provides a semi-empirical means of determining how mobile rockfall can be given a site's morphology and rockfall sizes.

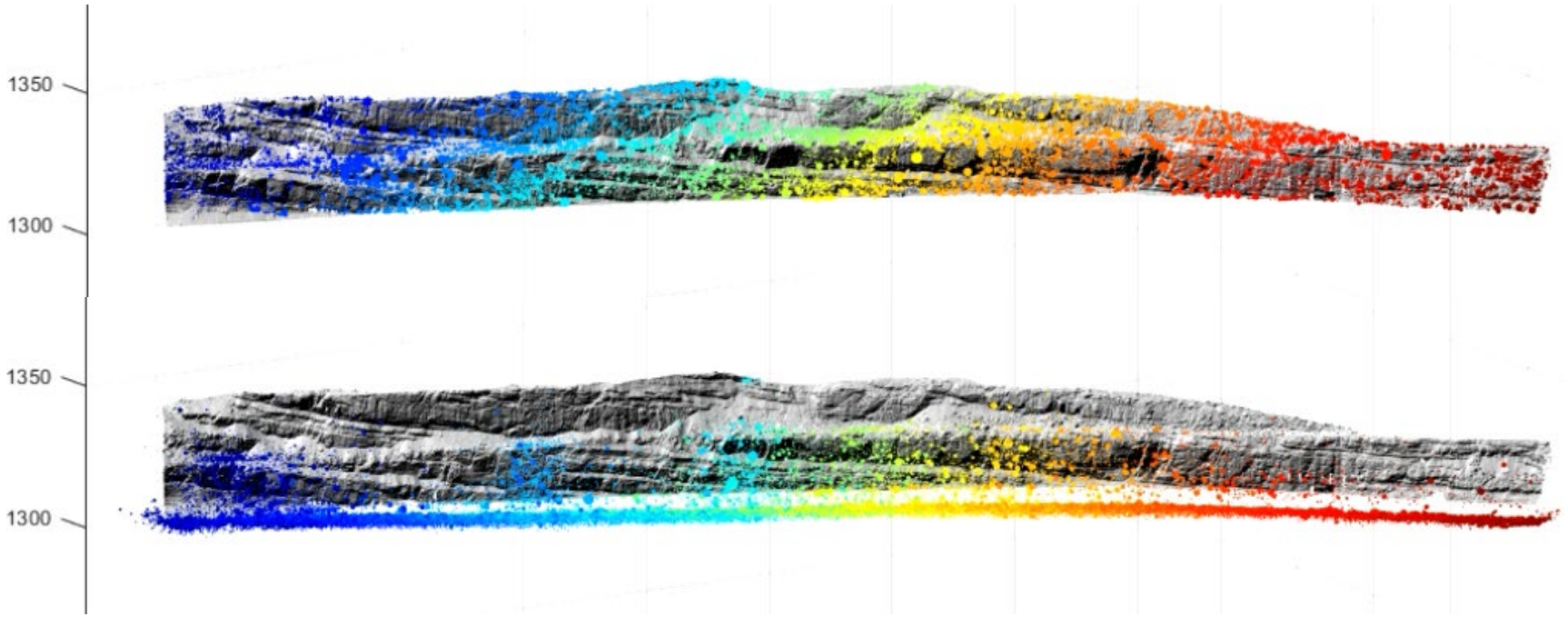

Figure 9.10. Starting and ending rockfall locations for all rockfall sources and volumes for Siskiyou Pass for all epochs.

This analysis again enables a means of quantifying the role of scaling on rockfall mitigation. For example, in Figure 9-11(b), there appears to be a very modest, decreased probability of exceedance in rockfall reach for the site after scaling versus the conditions at scaling. These modest decreases in potential for exceedance for rockfalls for travel length to source height ratios appears to span all values. Once again, it is not an equal comparison to compare scaling and post-scaling conditions directly, but continued observation may result in more reliable evaluation of scaling efficacy. Further, for Siskiyou Pass, scaling appears to result in a minor, decreased likelihood to exceed certain levels of kinetic energy, as shown in Figure 9-11(c). However, the change is rather negligible, as is its relevance.

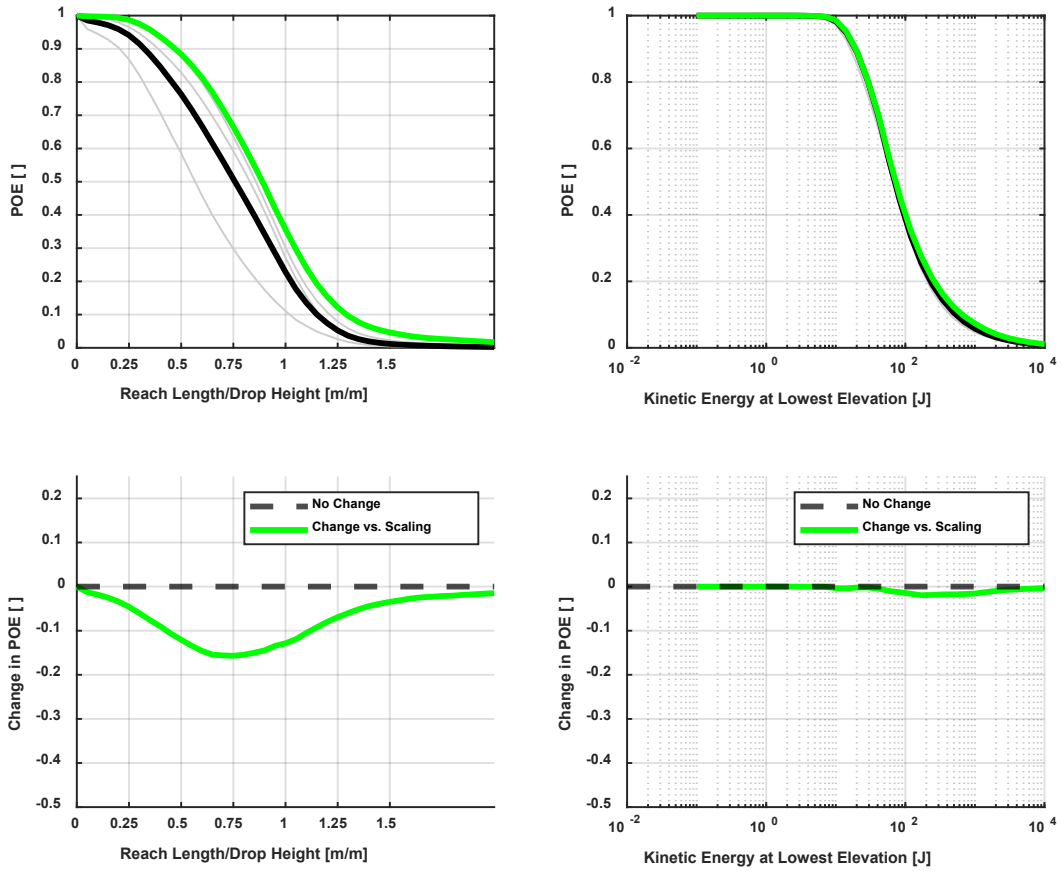

Figure 9.11. Top Left (a): Probability of exceedance of reach length to drop height ratio (m/m) for scaled conditions on Siskiyou Pass (green) and post-scaling conditions (black). Bottom Left (b): Change in probability of exceedance of reach length to drop height ratio (m/m) for post-scaling conditions (black). Top Right (c): Probability of exceedance of kinetic energy at lowest elevation for pre-scaling for scaled conditions on Siskiyou Pass (green) and post-scaling conditions (black), where gray lines represent individual epochs, black line represents mean. Bottom Left (d): Change in probability of exceedance of kinetic energy at lowest elevation for scaled conditions on Siskiyou Pass (green).

9.1.5 Summary

The I-5 Siskiyou Pass site provides a substantive but data collection constrained evaluation of scaling effectiveness at an operational highway rock slope. The morphological, activity rate, and magnitude-frequency data collectively indicate that the scaling operation produced a measurable reduction in rockfall hazard over the monitoring period, with the most evidence residing in the sustained suppression of large rockfall volumes and the consistent morphological improvements documented in the RAI classification data. At the same time, the absence of a pre-scaling terrestrial lidar baseline and a paired control slope prevents the full application of the Section 6 comparative framework.

The RAI morphological analysis documents a post-scaling slope surface that is more dominated by intact rock and less characterized by overhang and highly fragmented discontinuous material than the pre-scaling condition. The reduction in fragmented discontinuous rock and the associated Df-to-Dw transition provide evidence of reduced surface fragmentation that is independent of the overhang metrics and consistent with the removal of the most kinematically active surface material. The temporal stability of the intact rock and overhang classes across successive post-scaling monitoring epochs suggests that these morphological improvements were maintained within the observation window, though the sustained growth of the talus class through the monitoring period indicates that material flux from the slope continued at a measurable rate following treatment.

Activity rates at Siskiyou Pass declined from an elevated initial post-scaling level to values at or below the mobile lidar baseline of 0.128%/yr, before exhibiting a modest rebound in the final monitoring epoch. This trajectory is broadly consistent with the post-scaling activity rate patterns observed at the Rumble Pit sites and at SR14 MP73, where an initial period of elevated surface adjustment gives way to a reduced but gradually recovering background rate. The per-class rate data identify a partial rebound in cantilevered overhang activity in the later monitoring epochs as the feature of greatest interpretive interest at this site — one that warrants continued monitoring to determine whether it reflects the development of new overhang features or improved scan coverage of previously occluded areas.

The magnitude-frequency analysis indicates that the primary effect of scaling at Siskiyou Pass was a reduction in the activity parameter β, a decrease in the overall frequency of rockfall events across size classes, most pronounced for larger events, without a substantive change in the scaling parameter α. This finding suggests that the scaling operation reduced the rate of rockfall production without fundamentally altering the structural character or size distribution of the residual slope surface. The sustained suppression of larger volume bins in the cumulative erosion data, persisting across multiple years of post-scaling monitoring, is the strongest available evidence that scaling at this site produced a durable reduction in the frequency of the events most consequential for road safety and maintenance operations.

This site supports the interpretation that strategic scaling of a large, structurally complex operational highway slope can produce measurable and at least partially durable reductions in rockfall hazard, particularly with respect to larger, structurally controlled failure events.

9.2 OR66 GREEN SPRING

Figure 9-12 presents a change analysis of the OR66 Green Spring site. Color-coded regions indicate varying levels of activity or instability along the face. Most of the slope is characterized by relatively low-intensity values (shown in grey), suggesting generally stable conditions. However, localized zones of elevated activity (yellow to red) are evident, with the most prominent concentration occurring toward the right-central portion of the image. These high-intensity areas likely represent zones of increased deformation, material loss, or potential instability. Annotated regions labeled “Collapse” correspond to areas where significant material failure has occurred or is actively occurring. The contrast between these localized high-activity zones and the surrounding stable regions highlights the heterogeneous nature of the slope response, with instability concentrated in discrete sections rather than uniformly distributed across the face.

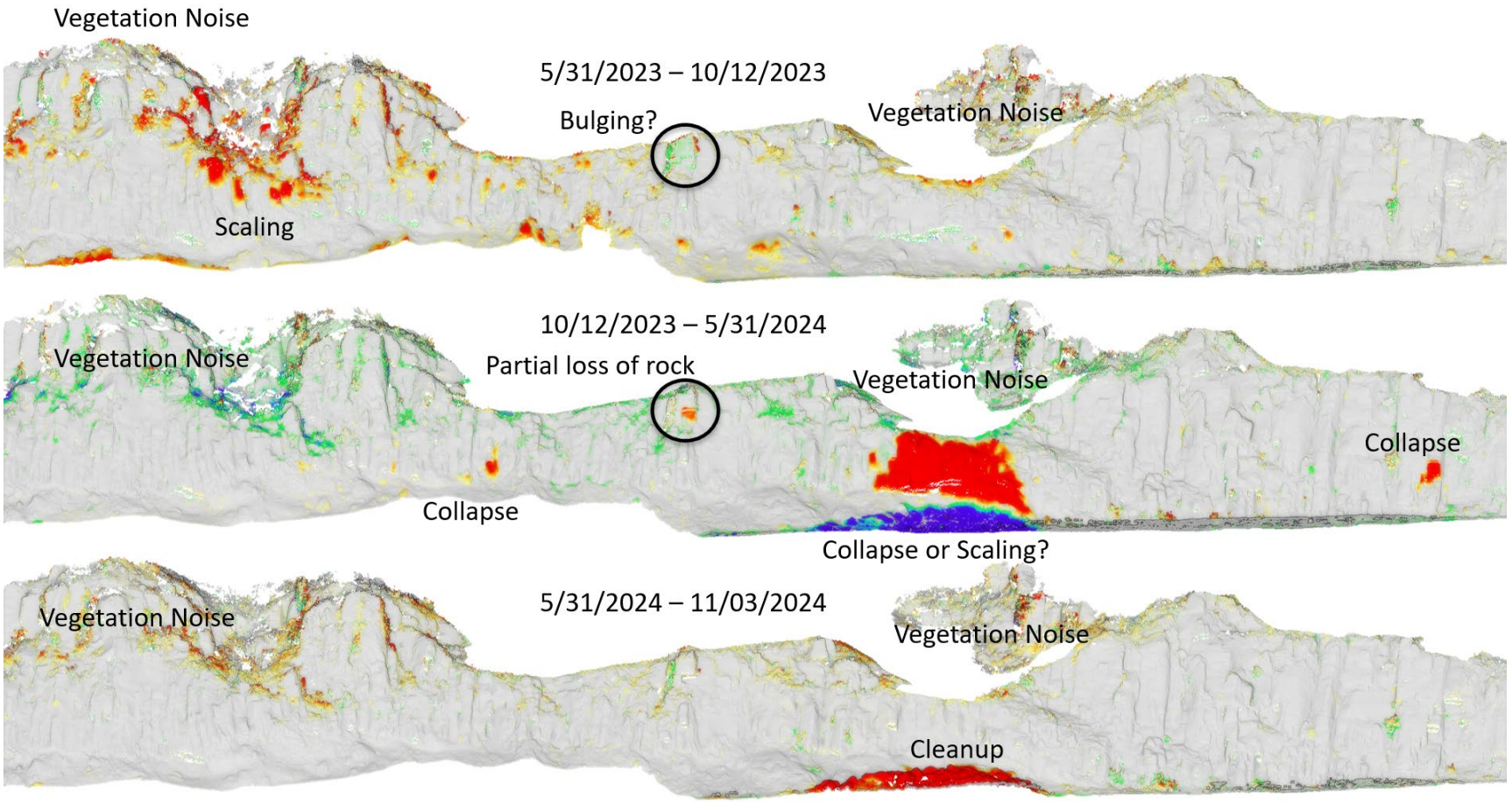

Figure 9.12. Changes observed at the OR66 site during the monitoring period for a portion of the slope.

9.3 SR14 MP73 (WASHINGTON)

9.3.1 RAI Analysis

The SR14 MP73 site along Washington State Route (SR) 14 in the Columbia River Gorge was the subject of an extensive scaling operation conducted between February and August 2022, targeting cantilevered overhangs that dominated the upper portion of the slope face. Unlike the Siskiyou Pass site, pre- and post-scaling terrestrial lidar surveys are available for SR14 MP73, enabling direct morphological comparison against an established baseline and full application of the Section 6.2 morphological classification metrics. The slope face is developed in Columbia River Basalt, a lithology characterized by well-defined columnar jointing that produces large, structurally controlled block failures. This is a geologic setting that is distinctly different from both the Rumble Pit sites and Siskiyou Pass.

The RAI classification maps before and after scaling are presented in Figure 9-13, with the corresponding slope gradient maps in Figure 9-14 and the net change in class areas quantified in Table 9-1 and Figure 9-15. The morphological response to scaling at SR14 MP73 is the most pronounced documented at any site in this study. The cantilevered overhang class decreased from 11,462 m² to 270.6 m² (a reduction of 97.6%) representing the near-complete removal of the cantilevered overhang system that constituted the primary hazard at this site prior to treatment. Under the Section 6.2 evaluation framework, which identifies a measurable post-mitigation reduction in cantilevered and shallow overhang area as one of the most direct and consequential indicators of successful scaling, the SR14 MP73 result is unambiguous: the scaling operation achieved its primary morphological objective to a degree that substantially exceeds the overhang reductions documented at any of the Rumble Pit sites or at Siskiyou Pass.

Intact rock area increased from 2,254 m² to 20,632 m², a gain of approximately 815% in absolute terms and from 19.7% to 43.3% of total classified slope area. This increase is of a fundamentally different character than the modest intact rock gains observed at the Rumble Pit sites, where increases of approximately 2–4% of slope area were attributed to the exposure of relatively competent material beneath removed surface debris. At SR14 MP73, the scale of the intact rock increase reflects the exposure of the massive, unjointed basalt interiors of the columnar joint system following removal of the overhanging cap rock, a structural consequence of the basalt geology that would not be expected in more uniformly jointed or foliated rock masses. The RAI classification maps in Figure 9-14 illustrate this shift spatially: the post-scaling map is dominated by the green tones of intact rock across the central and upper portions of the slope, in marked contrast to the pre-scaling condition in which red overhang tones were distributed broadly across the upper face.

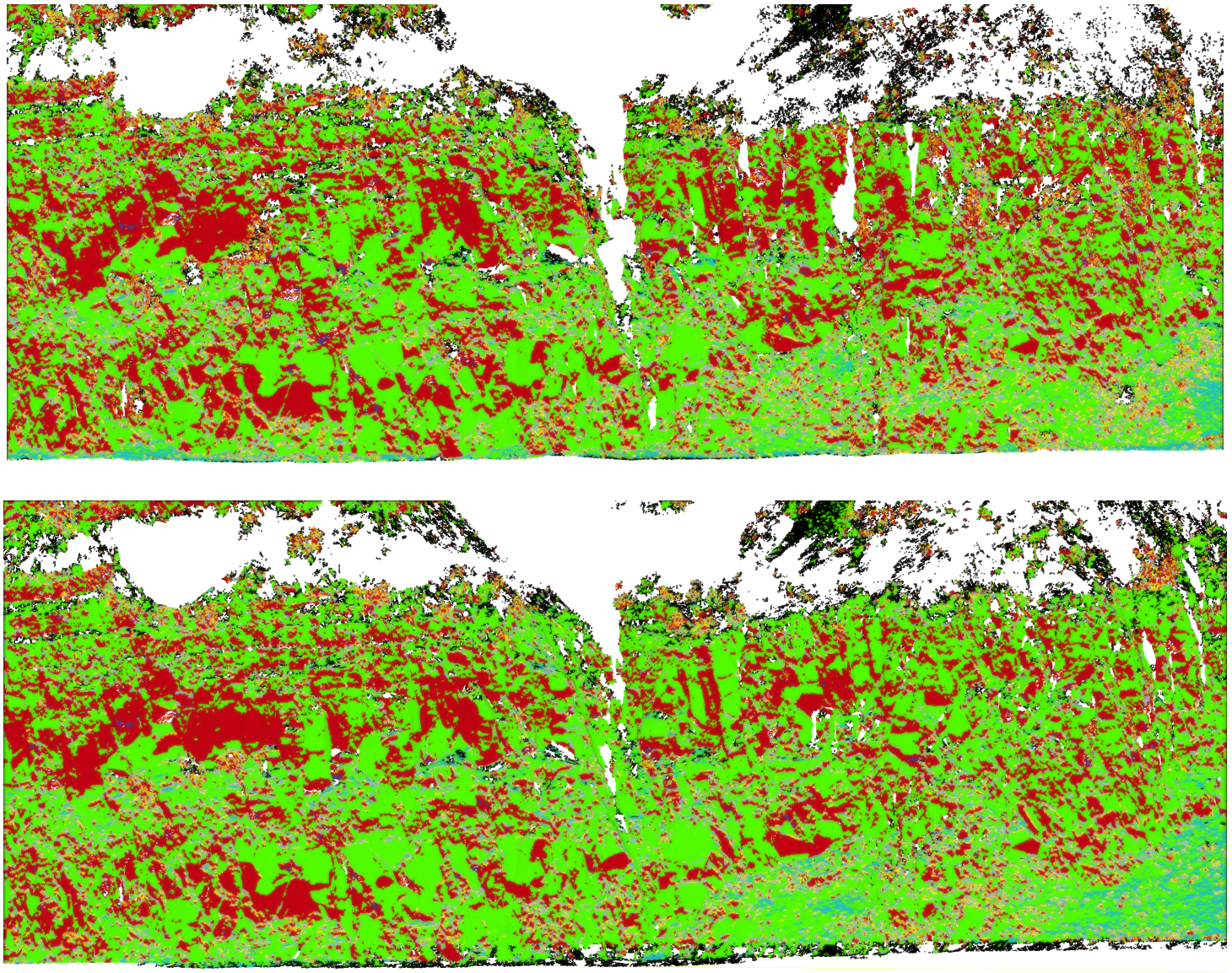

Figure 9.13. RAI classification map of the SR14 MP73 site (a) before and (b) after scaling.

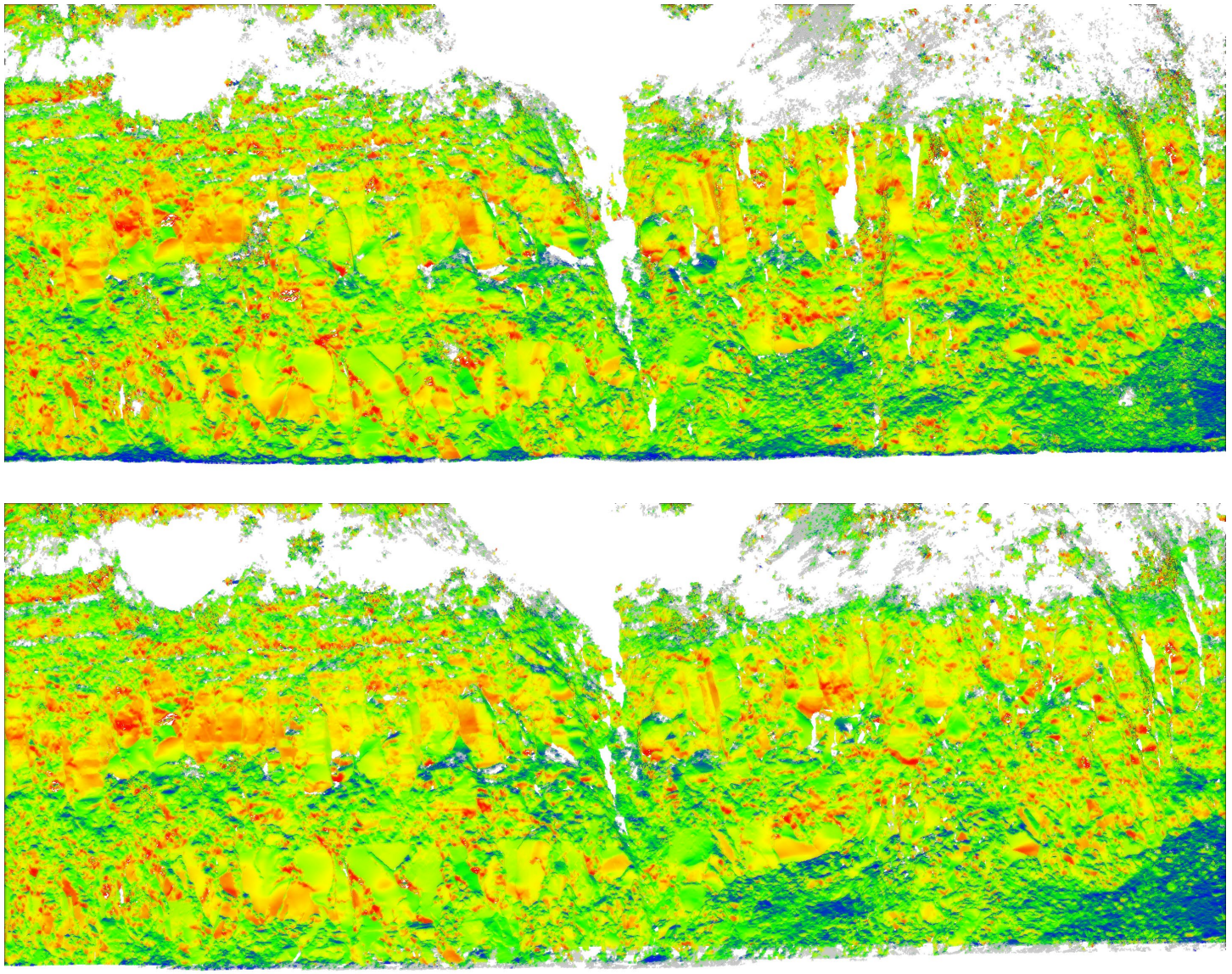

Figure 9.14. Slope map of the SR14 MP73 site (a) before and (b) after scaling.

Table 9.1. Summary of RAI class areas for SR14 MP73.

RAI Class Description	Area (m^2) Before (2/22)	Area (m^2) After (8/15)	Percentage (%) Before (2/22)	Percentage (%) After (8/15)
Talus	605.9	4271.9	5.3%	9.0%
Intact	2253.7	20631.5	36.6%	43.3%
Fragmented Discontinuous	15506.9	5142.2	12.1%	10.8%
Closely-spaced Discontinuous	5107.2	4625.8	12.2%	9.7%
Widely-spaced Discontinuous	5151.9	1516.5	4.7%	3.2%
Shallow Overhang	1976.9	10808.0	27.1%	22.7%
Cantilevered Overhang	11462.0	270.6	0.7%	0.6%

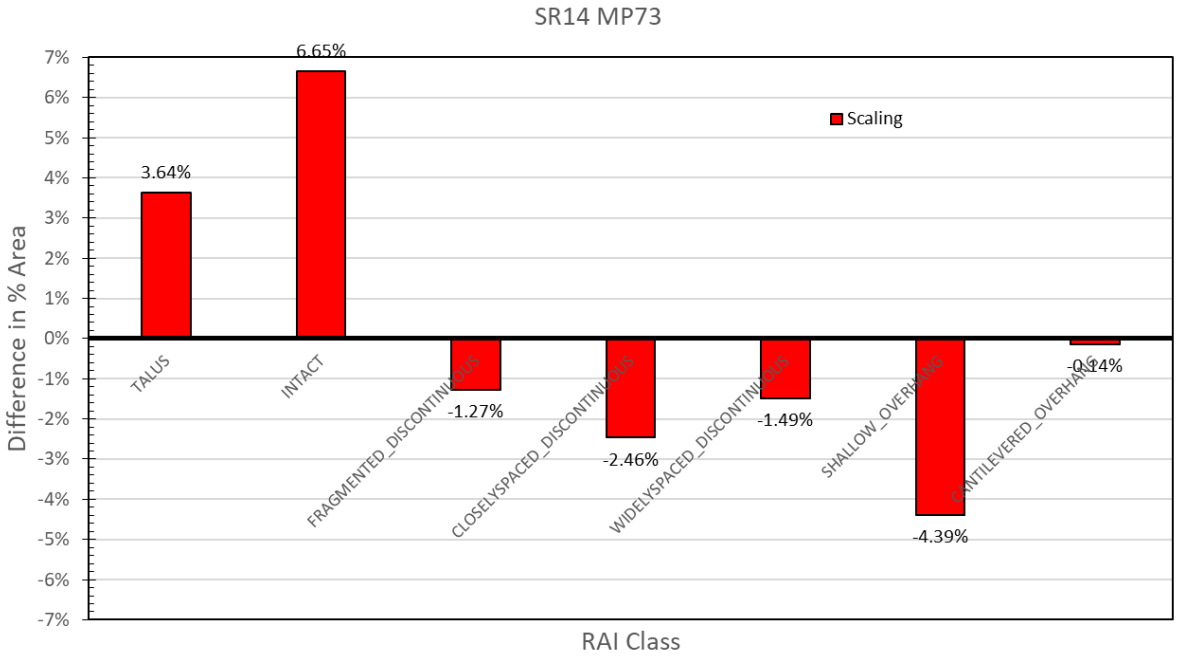

Figure 9.15. Changes in RAI classifications due to scaling at SR14 MP73.

The three discontinuous rock sub-classes [fragmented discontinuous (Df), closely spaced discontinuous (Dc), and widely spaced discontinuous (Dw)] each declined in areal extent following scaling, with Dw showing the largest absolute reduction from 5,152 m² to 1,517 m². Under the Section 6.2 Df-to-Dw transition criterion, this pattern requires interpretation. Rather than a transition from finer to coarser discontinuous material, all three discontinuous sub-classes declined simultaneously while the intact class increased. This indicates that the dominant morphological shift at SR14 MP73 was not a reorganization within the discontinuous rock classes but a transition from discontinuous and overhanging material to intact rock.

Talus area increased from 606 m² to 4,272 m², reflecting the accumulation of debris generated during the large-scale block removals. The surface roughness maps presented in Figure 9-14 provide a complementary perspective on the post-scaling surface character: the post-scaling map shows a substantial increase in low-roughness area, indicated by blue tones, at locations corresponding to the newly exposed intact basalt surfaces. This reduction in surface roughness is physically consistent with the RAI intact rock classification and provides independent corroboration that the scaling operation exposed coherent, relatively unweathered rock faces rather than simply redistributing fragmented surface material.

Figure 9-16 presents the temporal evolution of RAI class distributions across the post-scaling monitoring period, from February 2022 through July 2024. The intact rock class remains the dominant classification throughout the post-scaling record, with a gradual and modest decline over time that is consistent with progressive weathering of the exposed basalt surfaces and the development of new surface discontinuities under the potential influence of freeze-thaw cycling and other environmental forcing. The cantilevered overhang class remains near zero throughout the monitoring record (Note that at no Rumble Pit site or at Siskiyou Pass does the overhang class maintain such a sustained suppression following scaling). This persistence indicates that the morphological improvements achieved by the SR14 MP73 scaling operation were not temporary but were maintained across the full duration of the available monitoring record.

The RAI site score increased from 167,571 kJ before scaling to 180,606 kJ after scaling. As discussed in Section 6.1.1, an increase in the total RAI site score following mitigation does not necessarily indicate a deterioration in slope safety conditions; it may instead reflect an expansion of the classified slope area between surveys. In this case, the total classified area increased from approximately 43,886 m² to 48,010 m² — an increase of approximately 9.4% — that accounts for the apparent rise in the summed RAI score. When the per-class RAI scores in Table 9-1 are examined individually, the physically meaningful changes are evident: the cantilevered overhang class score declined from 564 kJ to 423 kJ, and the widely spaced discontinuous class declined from 51,036 kJ to 45,207 kJ, despite the expanded scan coverage. These class-level reductions, occurring against a backdrop of increasing total classified area, provide the most reliable evidence of genuine hazard reduction within the RAI site score metric and underscore the importance of area normalization when interpreting site-level RAI scores across surveys of differing spatial extent.

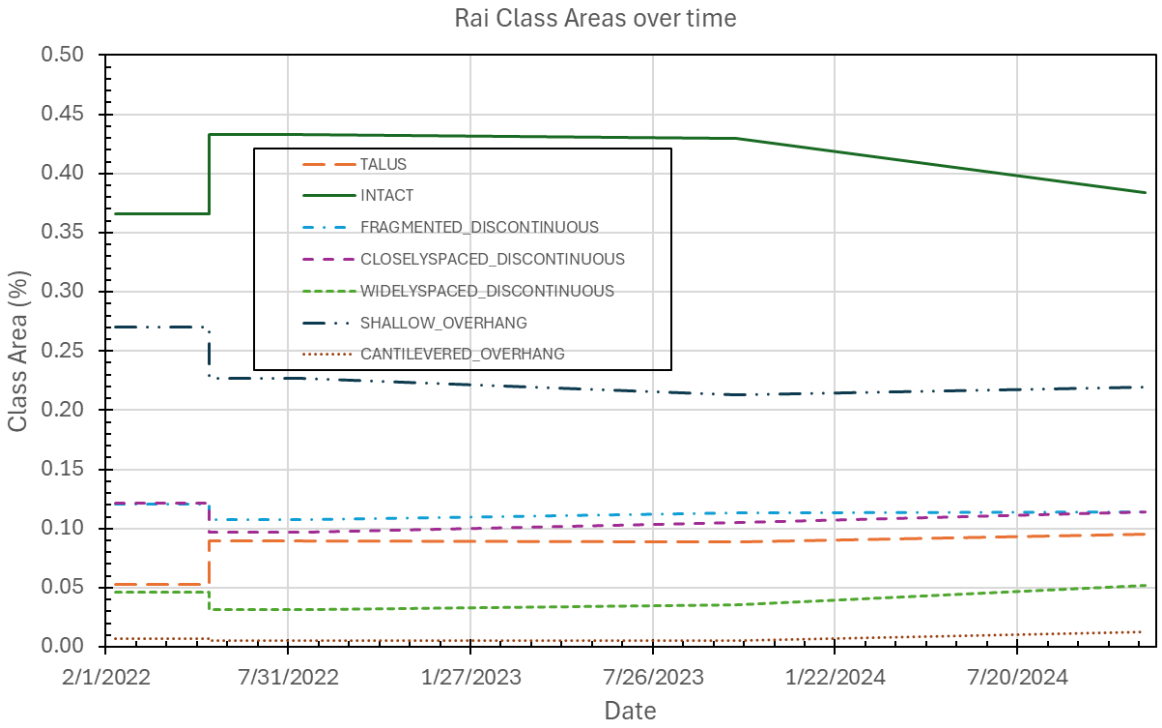

Figure 9.16. Changes in the percent area of RAI classes at site SR14 MP73 over time.

9.3.2 Rates and Volumes

Pre-scaling rockfall activity rates derived from temporally resolved terrestrial lidar data are not available for the SR14 MP73 site, as the monitoring program began at the same time as the scaling operation. The analysis of rates and volumes is therefore based on three monitoring epochs that span the scaling operation and the subsequent post-scaling period, summarized in Table 9-2 and presented graphically in Figure 9-17 to Figure 9-19. While the absence of a pre-scaling terrestrial baseline limits direct before-after rate comparison in the manner possible at the Rumble Pit sites and at GG241, the three-epoch sequence provides an internally consistent record of post-scaling slope evolution that supports several conclusions about the trajectory and durability of the scaling effect.

Table 9.2. Activity rates and failure depths observed for the SR14 MP73 Site.

Start	End	Activity Rate (%/yr)	Ave. Failure Depth (m)	Std. Dev. Failure Depth (m)
2/11/2022	8/15/2022	0.933	0.260	0.306
8/15/2022	10/17/2023	0.161	0.079	0.094
10/17/2023	11/23/2024	0.299	0.076	0.097

The first monitoring epoch, spanning February through August 2022, encompasses the scaling operation itself and yielded an overall activity rate of 0.933%/yr — the highest rate recorded at any site in this study outside of the immediate post-scaling periods at the Rumble Pit sites. This elevated rate reflects two overlapping processes: the direct mechanical removal of large rock volumes during the scaling operation, which registers as surface change in the lidar differencing analysis, and the accelerated adjustment of the freshly exposed slope face as stress conditions redistribute following the removal of the cantilevered overhang system. Figure 8-16 presents the change detection map for this initial epoch, illustrating the spatially extensive and volumetrically significant character of the surface modifications. Areas of material loss are distributed across the full height and lateral extent of the slope face, consistent with a scaling operation that addressed the overhang system across its full spatial extent rather than selectively targeting individual features.

The second monitoring epoch, spanning August 2022 through October 2023, recorded an overall activity rate of 0.161%/yr, a reduction of approximately 83% relative to the first epoch. This is the most pronounced activity rate reduction documented at any site in this study and provides the strongest quantitative evidence of scaling effectiveness at SR14 MP73. Under the Section 6.1.2 evaluation framework, this reduction reflects the shift from the large-volume, mechanically induced removals of the scaling operation to the lower-intensity, weathering-driven surface erosion characteristic of a stabilized post-treatment slope. The magnitude of the reduction is consistent with the scale of the morphological changes documented in Section 9.3.1: the near-complete removal of the cantilevered overhang system, which carries the highest default instability rates of any RAI class, produces a correspondingly large reduction in overall slope activity once the direct effects of the scaling operation have subsided.

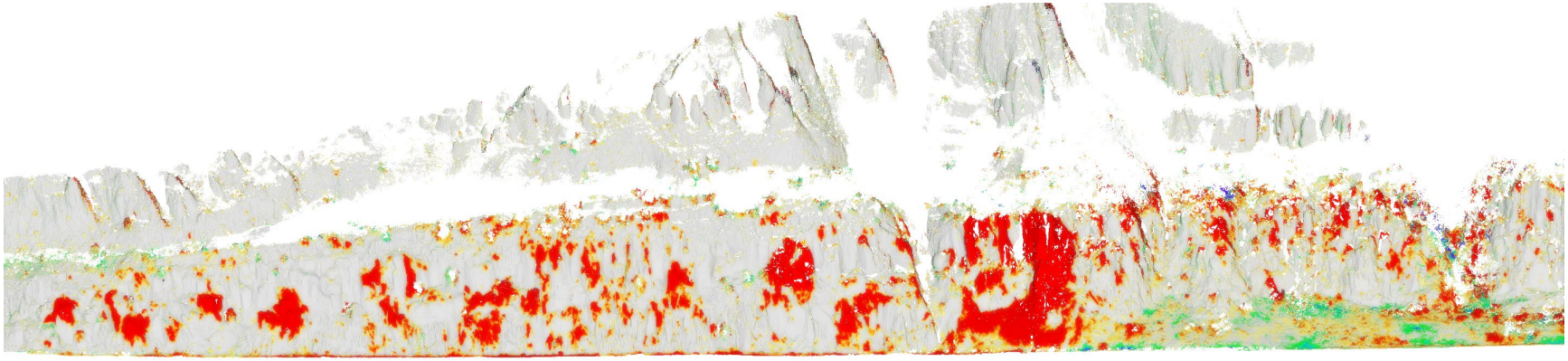

Figure 9.17. Change analysis of Site SR14 MP73 from scaling.

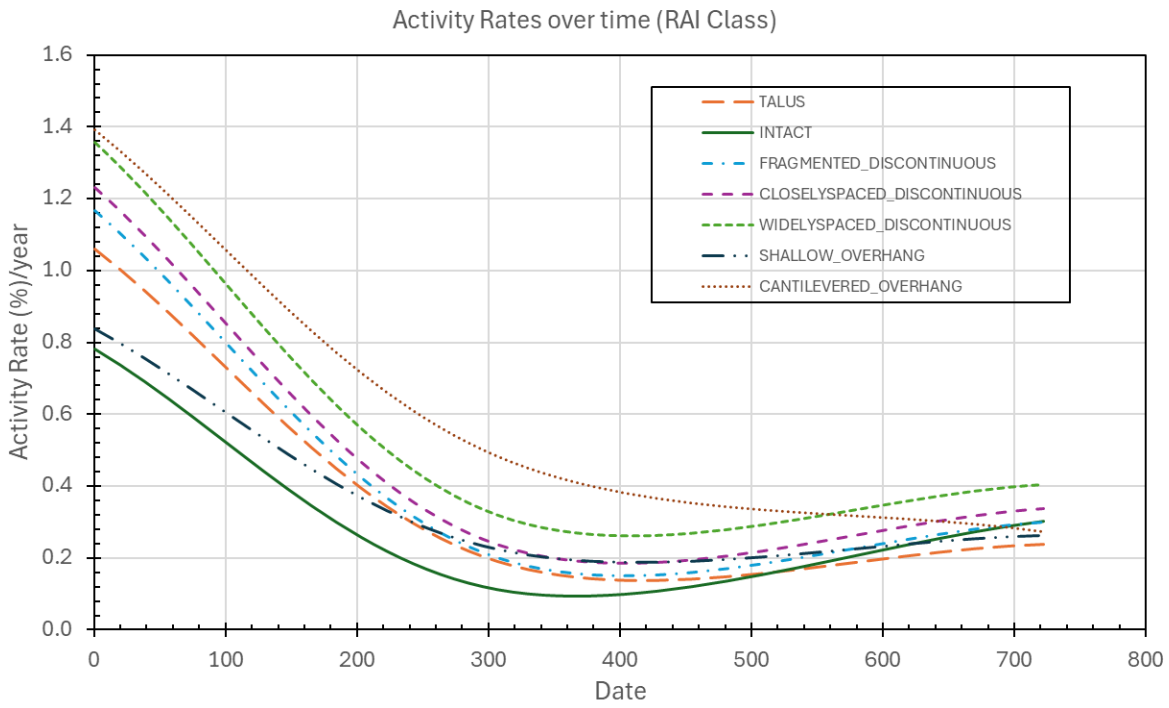

Figure 9.18. Changes in RAI classes over time at Site SR14 MP73.

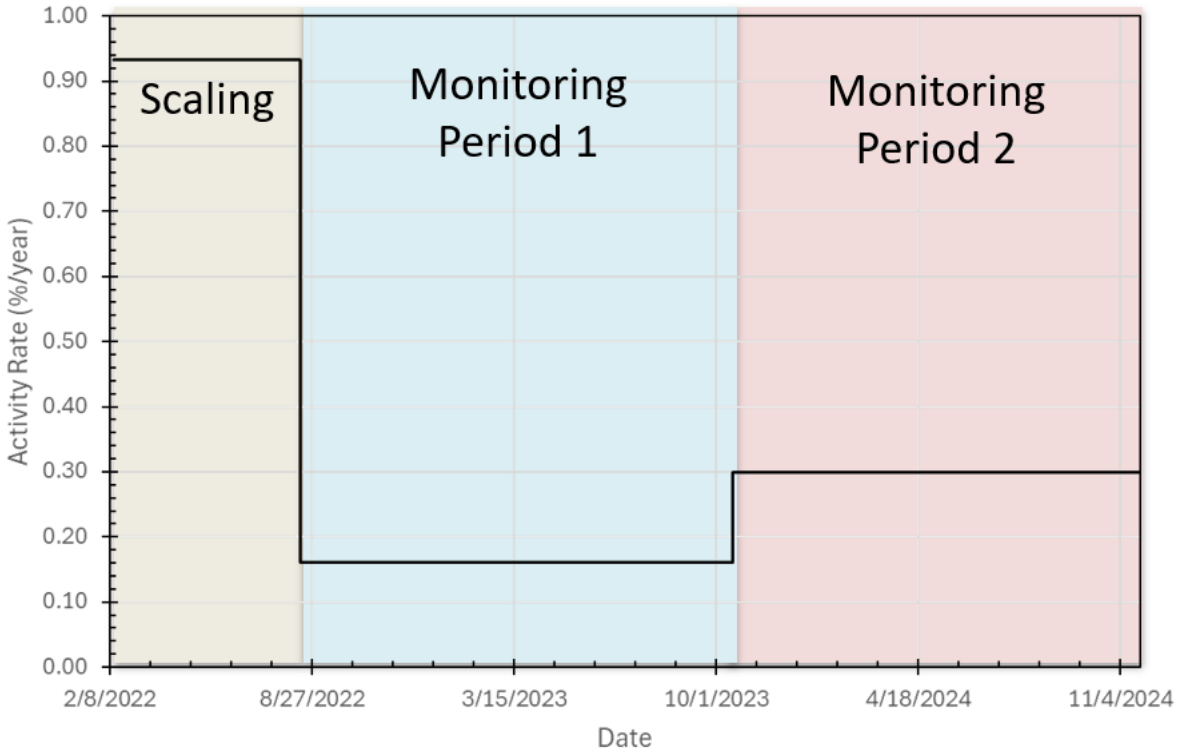

Figure 9.19. Changes in activity rates over time at Site SR14 MP73

The third monitoring epoch, spanning October 2023 through November 2024, yielded an activity rate of 0.299%/yr, an increase of approximately 86% relative to the second epoch, though still approximately 68% below the scaling-epoch rate. This partial rebound in activity is consistent with the post-scaling recovery trajectories observed at the Rumble Pit sites and at Siskiyou Pass, where an initial period of reduced activity following the post-scaling adjustment phase gives way to a gradually recovering background rate as weathering and environmental cycling act on the freshly exposed slope surface. The rebound at SR14 MP73 is larger in proportional terms than those observed at Sites A and B in Chapter 7, which may reflect the more extensive area of freshly exposed intact basalt at this site. The large intact rock surfaces revealed by overhang removal provide a substantial area of newly exposed, relatively unweathered material that is subject to progressive joint opening and surface spalling under the thermal and moisture cycling characteristic of the Columbia River Gorge climate.

Figure 9-18 presents the per-class activity rates over time for all RAI morphological classes. Several features of this figure are informative under the Section 6.1.2 evaluation framework. All classes show sharply declining rates over approximately the first 200 days following the initiation of monitoring, reflecting the transition from scaling-epoch conditions to the post-treatment stabilization period. The cantilevered overhang class, which exhibited the highest initial activity rate consistent with the large-volume block removals during scaling, declines rapidly and remains at near-zero levels through the later monitoring epochs. This is a direct consequence of the near-complete elimination of this class from the slope morphology documented in Section 9.3.1. This sustained suppression of cantilevered overhang activity is the per-class signal most directly predicted by the Section 6.1.2 framework and represents the clearest indicator that the scaling operation successfully addressed the primary failure mechanism at this site.

The widely spaced discontinuous class shows the highest activity rates among the remaining classes in the later monitoring epochs, a pattern consistent with the progressive activation of the columnar joint surfaces exposed by overhang removal. As the newly exposed basalt faces weather and joint apertures widen under freeze-thaw cycling, the widely spaced discontinuous class becomes the dominant contributor to ongoing slope activity. This transition from overhang-dominated to widely spaced discontinuous-dominated activity represents a change in the failure mechanism governing slope behavior at SR14 MP73, from sudden, large-volume tensile fracture of cantilevered slabs to the more gradual, smaller-volume joint-controlled failures characteristic of the Dw class.

Average failure depths, presented in Table 9-2, provide complementary evidence of this mechanical transition. During the scaling epoch, the mean failure depth was 0.260 m with a standard deviation of 0.306 m, values reflecting the large, variable block sizes removed during the operation. In the second and third monitoring epochs, the mean failure depth declined to 0.079 m and 0.076 m respectively, with standard deviations of 0.094 m and 0.097 m. The reduction in both the mean and standard deviation of failure depth across the post-scaling epochs is among the more significant quantitative findings at this site. Under the Section 6.1.2 framework, a sustained reduction in failure depth indicates that scaling altered the scale of individual failure events, shifting from large block removals to surface-scale erosion. The consistency of this reduced failure depth across both post-scaling epochs, with essentially no change between the second and third epochs despite the increase in overall activity rate, indicates

that the character of the failure mechanism stabilized even as the rate of activity partially recovered.

9.3.3 Summary

The SR14 MP73 site provides the most complete morphological and activity rate dataset available among the operational highway sites analyzed in this study, and the results offer clear quantitative evidence of scaling effectiveness across multiple metric categories defined in Section 6. The scaling operation produced morphological changes of a magnitude and character that substantially exceed those documented at any Rumble Pit site, and the post-scaling monitoring record is sufficient in temporal extent to support conclusions about both the immediate response and the medium-term trajectory of slope behavior following treatment.

The RAI morphological analysis documents a post-scaling slope surface that is fundamentally different in character from the pre-scaling condition. The near-complete removal of the cantilevered overhang system, which declined from 11,462 m² to 270.6 m², eliminated the primary high-risk morphological feature at the site and produced a corresponding large increase in intact rock area from 2,254 m² to 20,632 m². These changes satisfy the most consequential morphological criteria defined in Section 6.2 and do so at a scale that is not approached at any other site in the study. The temporal stability of these morphological improvements across the full post-scaling monitoring record, with the cantilevered overhang class remaining near zero and the intact rock class declining only gradually, indicates that the morphological gains achieved by the scaling operation were maintained over the approximately two and a half years of available post-scaling observation.

Activity rate data from the three monitoring epochs provide consistent and mutually reinforcing evidence of the scaling effect. The overall rate declined from 0.933%/yr during the scaling epoch to 0.161%/yr in the first post-scaling epoch, a reduction of approximately 83% that represents the largest inter-epoch rate reduction documented in this study. The partial rebound to 0.299%/yr in the third epoch is consistent with the post-scaling recovery trajectories observed at other sites and does not diminish the overall finding of substantially reduced slope activity relative to the scaling epoch. The per-class rate data identify the mechanism underlying this trajectory: the cantilevered overhang class, which drove the elevated scaling-epoch rates, remains suppressed throughout the post-scaling record, while the gradually increasing rates in the later epochs are attributable primarily to the widely spaced discontinuous class acting on the newly exposed basalt joint surfaces.

The failure depth data in Table 9-2 add an important dimension to the activity rate findings. The decline in mean failure depth from 0.260 m during the scaling epoch to approximately 0.077 m in both post-scaling epochs, maintained consistently across two successive monitoring intervals, indicates that the character of individual failure events changed fundamentally following scaling. The partial rebound in overall activity rate in the third epoch therefore represents an increase in the frequency of smaller, lower-energy events rather than a return to the large-block failure regime that characterized the pre-treatment slope. This distinction has direct practical significance for infrastructure management: a slope producing more frequent but smaller and lower-energy events presents a qualitatively different maintenance and safety challenge than one producing less frequent but larger and more energetic failures.

The primary analytical limitation at SR14 MP73 is the absence of a pre-scaling terrestrial lidar baseline and a paired control slope. The first monitoring epoch encompasses the scaling operation itself, so the scaling-epoch rate serves as an approximate upper bound on pre-treatment activity rather than as a true pre-mitigation baseline. Without a control slope, natural temporal variability in rockfall activity cannot be separated from the scaling effect, and the observed rate reductions could in principle reflect background fluctuations rather than a treatment response. These constraints are noted not to undermine the findings but to accurately characterize their evidential basis. The consistency of the observed rate reductions with the morphological data, the failure depth data, and the post-scaling trajectories observed at sites with more complete experimental designs provides reasonable grounds for attributing the documented improvements to the scaling operation rather than to background variability alone.

The SR14 MP73 results support the conclusion that extensive, targeted scaling of a large cantilevered overhang system in Columbia River Basalt produced substantial, measurable, and at least medium-term reductions in rockfall hazard as characterized by the Section 6 metrics. The site demonstrates that the RAI framework and associated metrics are capable of documenting scaling effectiveness at operational highway scales and under the analytical constraints typical of agency-managed monitoring programs, where pre-treatment baseline data and paired control sites are not always available.

10.0 LONG-TERM MONITORING: GLITTER GULCH MILEPOST 241 (GG241)

10.1 SITE OVERVIEW

The geological characterization of the GG241 site draws on field observations and site descriptions reported by Marohl (2019), supplemented by the foundational geological mapping and characterization of the Healy area by Wahrhaftig (1968) and Wahrhaftig and Black (1958), which together provide the primary basis for the formation-level and structural descriptions presented here.

The GG241 site is located along the George Parks Highway (Alaska Route 3) near milepost 241 in the Glitter Gulch area of the Nenana River Valley, within the Alaska Range. The slope is part of an arcuate hillside that represents a segment of Mount Healy separated by the incising Nenana River. The site lies within the Yukon-Tanana Terrane, one of the oldest accreted terranes in Alaska, whose basement rocks are exposed on hillslopes and in roadcuts near the intersection of the east-west trending Hines Creek Fault, a strand of the Denali fault system, with the northward-draining Tanana River drainage (Marohl, 2019). Alaska is a geologically active region in which the northward subduction of the Pacific Plate and the Yakutat Microplate translates motion onto a series of major fault systems including the Chugach, Border Ranges, and Denali faults, producing the high relief and tectonic complexity that characterizes the Alaska Range (Marohl, 2019).

The rock exposed at the GG241 site is the Healy Schist, a local subunit of the Birch Creek Schist of the Yukon-Tanana Terrane. The Birch Creek Schist is a metasedimentary unit of marine shale and sandstone origin whose original sedimentary structures have been obliterated during regional metamorphism; its mapped thickness of greater than 3,000 meters is measured perpendicular to the axial plane cleavage rather than representing a true stratigraphic thickness (Wahrhaftig, 1968). The Healy Schist specifically is a quartz-sericite schist or phyllite with interbedded quartzite that is locally carbonaceous and contains perfect cubic pyrite crystals up to approximately 6 mm in diameter (Wahrhaftig and Black, 1958). The unit is very fine grained and highly anisotropic, with a strong foliation defined by the preferred orientation of mica minerals. Near-vertical and irregular joints trending generally north-south are present throughout the unit, and some of these joints contain basaltic intrusions (Wahrhaftig and Black, 1958). The composition is predominantly quartz with sericite, calcite, and trace albite and microcline, reflecting a protolith of mixed siliceous and pelitic marine sediments that experienced metamorphism during the Cretaceous collision with the North American Plate and subsequent localized contact metamorphism from basaltic and granitic intrusions (Wahrhaftig, 1968; Marohl, 2019).

The rock mass at GG241 presents as a competent, near-vertical outcrop approximately 30 meters tall and 245 meters wide, forming a prominent roadcut along the highway (Marohl, 2019). The mechanical behavior of the rock mass is strongly controlled by the pronounced planar foliation,

which is oriented parallel to subparallel to the slope face. This geometric relationship is mechanically significant because it creates persistent, planar discontinuities along which slab-like failures can be initiated, particularly where pore water pressures develop along foliations or where freeze-thaw cycling progressively widens foliation-parallel openings (Wahrhaftig and Black, 1958). Widely spaced, high-persistence joints that cross-cut the foliation provide the lateral release surfaces necessary to define discrete failure blocks, and the quartzite-rich portions of the rock mass, which exhibit substantially higher intact strength than the more micaceous zones, generate large and potentially massive block geometries when failure does occur (Marohl, 2019). Weathering is variable across the slope face, with oxidation staining present on approximately 75 percent of the exposed surface and micaceous talus accumulating on ledges where the weaker, more phyllitic portions of the unit have degraded preferentially (Marohl, 2019). The intact rock strength estimated from field observation ranges from weak to very weak where schist mineralogy dominates to strong to extremely strong where quartzite veining is prevalent, reflecting the pronounced compositional heterogeneity of the Healy Schist at the outcrop scale (Marohl, 2019). Slope failures in this unit have been documented in connection with the adjacent Alaska Railroad corridor and are typically associated with freeze-thaw cycling, elevated pore water pressure along foliations, and in more severe cases, the decomposition of micaceous material into clay-rich zones that retain water within the slope and reduce effective stress along failure planes (Wahrhaftig and Black, 1958).

10.2 SURVEY HISTORY

The site was selected for long-term monitoring because of its demonstrated rockfall hazard, its role in ongoing highway maintenance activities, and the availability of pre-mitigation lidar data extending back to 2010. TLS surveys were conducted annually between 2010 and 2022, with the exception of 2016, when mitigation activities precluded acquisition of a post-season scan. Table 10-1 summarizes the TLS registration adjustment results for this site.

Mitigation at GG241 was performed in 2016 through a combination of manual scaling and controlled blasting. The dataset therefore encompasses approximately five years of pre-mitigation baseline monitoring (2010 through 2015) and approximately five years of post-mitigation monitoring (2017 through 2022), providing the longest paired pre- and post-treatment record among all sites examined in this study. This monitoring duration is sufficient to assess both the immediate morphological response to mitigation and the longer-term trajectory of slope behavior, including any return toward pre-treatment conditions. Portions of the adjacent site GG239 were not subject to mitigation and provide a partial control comparison, though the two sites differ in their specific geologic structure and degree of pre-existing discontinuity development, which limits direct quantitative comparison.

The analyses presented in this chapter apply the full suite of Section 6.0 metrics, including RAI site score, per-class instability rates and failure depths, magnitude-frequency relationships, morphological classification assessment, and slope performance metrics. The long monitoring record at GG241 is particularly well suited to evaluating the durability of mitigation effectiveness and the timescale over which post-treatment conditions evolve relative to the pre-treatment baseline.

Table 10.1. Summary of quality control metrics from the registration for Site GG241.

Observation Type	Mean	Median	Std. Dev.	Min	Max	RMS	N
CC Hor Angle (“)	0.1	-0.6	33.9	-362.9	286.7	33.9	4221
Target Hor Angle (“)	0.0	0.0	7.9	-38.8	44.1	7.9	256
CC Hor Dist (m)	0.0002	-0.0006	0.0085	-0.0375	0.0470	0.0085	4298
Target Hor Dist (m)	-0.0018	-0.0018	0.0044	-0.0149	0.0132	0.0047	256
CC Elevation (m)	0.0003	-0.0003	0.0083	-0.0497	0.0595	0.0083	4298
Target Elevation (m)	0.0000	0.0000	0.0034	-0.0140	0.0101	0.0034	256
SP GNSS X (m)	-0.0011	-0.0011	0.0139	-0.0398	0.0256	0.0139	128
SP GNSS Y (m)	-0.0005	-0.0007	0.0128	-0.0334	0.0610	0.0128	128
SP GNSS Z (m)	0.0059	0.0039	0.0303	-0.0647	0.1169	0.0307	128

10.3 RAI ANALYSIS

10.3.1 Morphological Classification

Pre-mitigation RAI classifications at GG241 reflect the highly discontinuous character expected of a steeply dipping, foliated schist slope with a multi-decade exposure history. The slope surface was dominated by fragmented discontinuous and closely spaced discontinuous classes, with substantial areal extents of shallow and cantilevered overhang, particularly along zones where foliation planes intersect the slope face at adverse angles. Intact rock comprised a comparatively minor fraction of the classifiable slope area prior to treatment, consistent with the advanced state of surface weathering and stress-relief fracturing typical of this geologic setting.

Figure 10-1 shows the RAI classifications at GG241 before and after the 2016 mitigation. The post-mitigation scan reveals a clear reduction in the areal extent of overhang classes and an increase in intact rock classification across the treated portions of the slope, most pronounced in the western wedge area where the most intensive intervention was concentrated. Fragmented and closely spaced discontinuous classes also decreased in the immediate post-treatment period, consistent with the removal of the most kinematically active surface material. Figure 10-2 presents the corresponding slope morphology maps, illustrating the spatial redistribution of high-angle facets following mitigation, particularly in the zones targeted by controlled blasting where surface geometry was substantially modified.

Figure 10-3 summarizes the net change in RAI class proportions attributable to the 2016 mitigation. Shallow overhang area decreased by approximately 2 to 3 percent of total slope area, while intact rock increased by a similar margin. Fragmented discontinuous rock showed a decrease of roughly 1 to 2 percent. These shifts are directionally consistent with the expected morphological signature of effective scaling and blasting, as described in Section 6.2. The magnitude of the changes at GG241 exceeds that observed at the smaller Rumble Pit sites, which reflects both the greater intensity of the mitigation operation at GG241 and the larger proportion of the slope face that was treated.

The time-series evolution of RAI class proportions over the full monitoring record is shown in Figure 10-4. Intact rock area increased at the time of mitigation and remained elevated relative to

pre-treatment levels through approximately 2019, after which a gradual decline toward pre-mitigation proportions is apparent. This pattern is consistent with the progressive re-establishment of discontinuous surface fabric through weathering and stress-release fracturing of the freshly exposed schist. Shallow overhang area showed a transient increase in the first one to two post-treatment epochs before stabilizing at a level below the pre-treatment baseline; this behavior likely reflects the development of new foliation-parallel overhang features from the freshly exposed rock faces, a process that is structurally controlled by the foliation dip and the anisotropic weathering characteristics of the schist. By the end of the monitoring period, most RAI classes had returned to within approximately one to two percentage points of their pre-treatment values, suggesting that the surface morphological effects of the 2016 mitigation attenuated over a timescale of three to five years at this site.

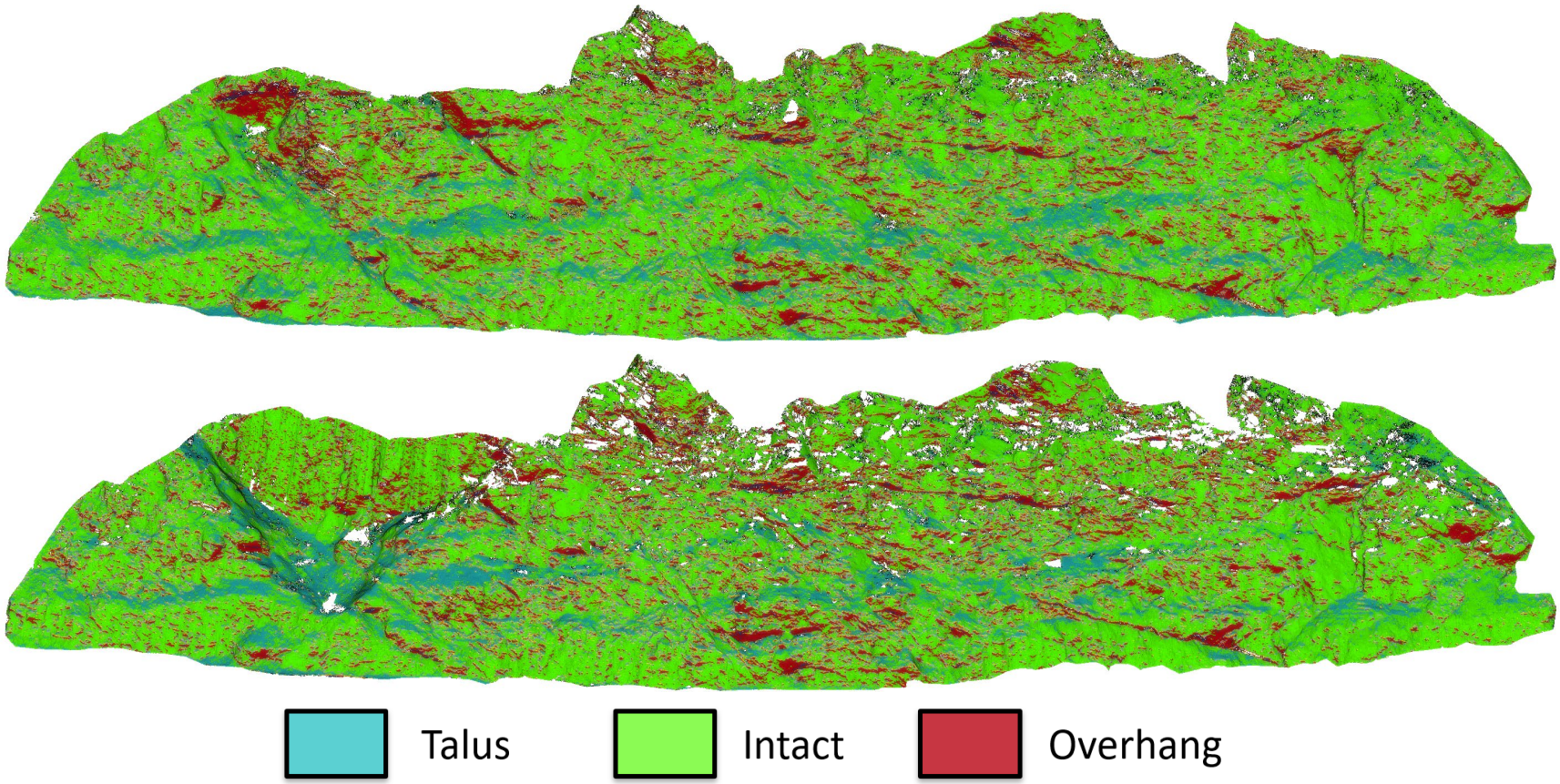

Figure 10.1. RAI classifications at Site GG241 before (a) and after (b) scaling operations.

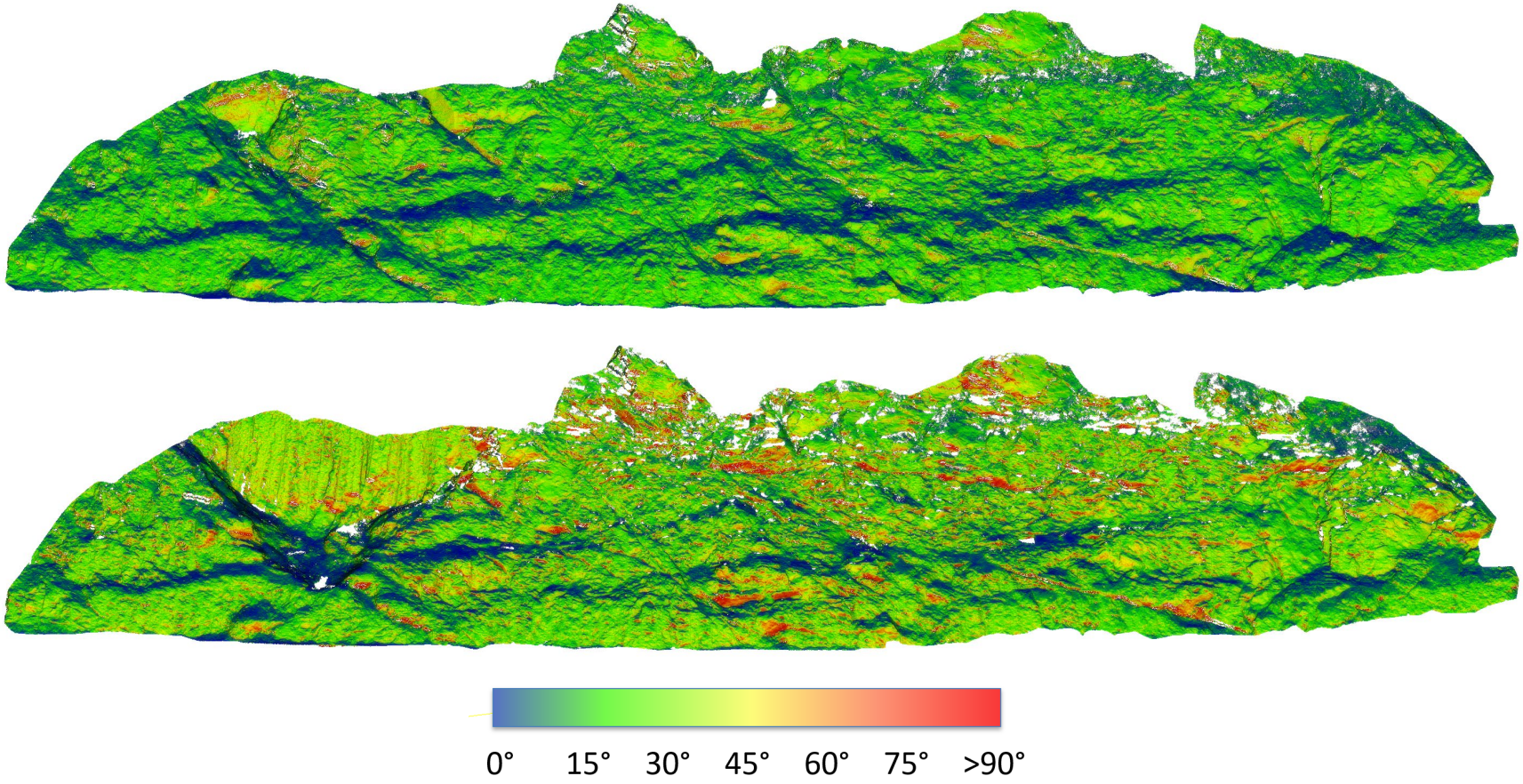

Figure 10.2. Slope morphology at site GG241 before (a) and after (b) scaling operations.

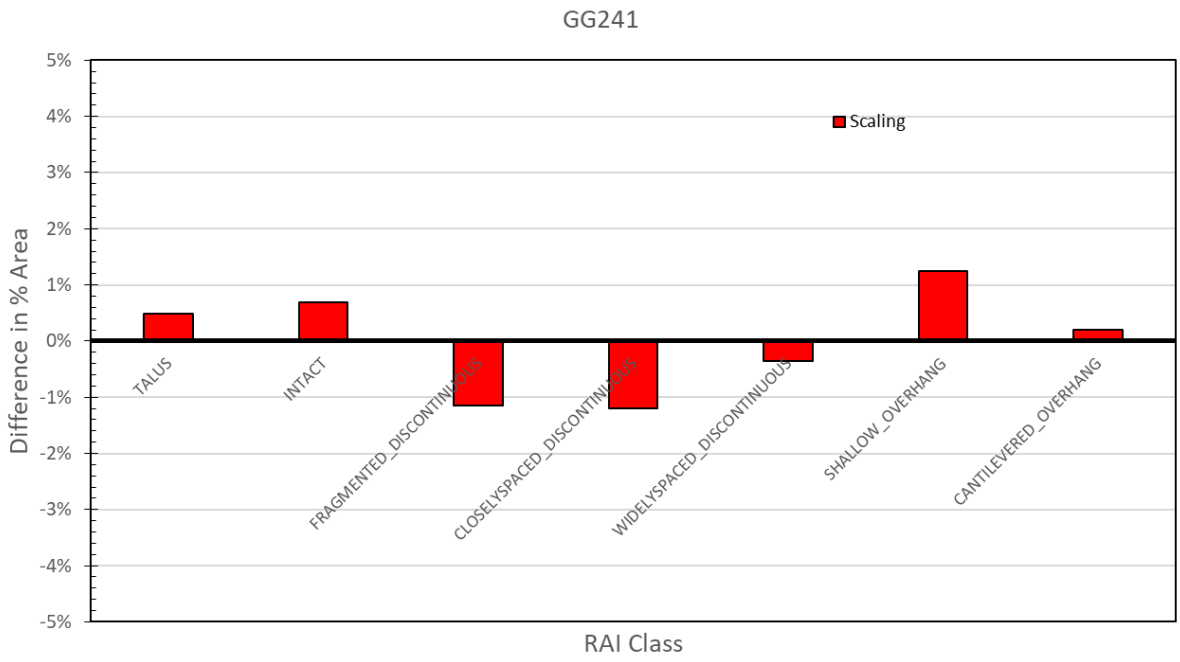

Figure 10.3. Changes in RAI classifications due to scaling operations at site GG241.

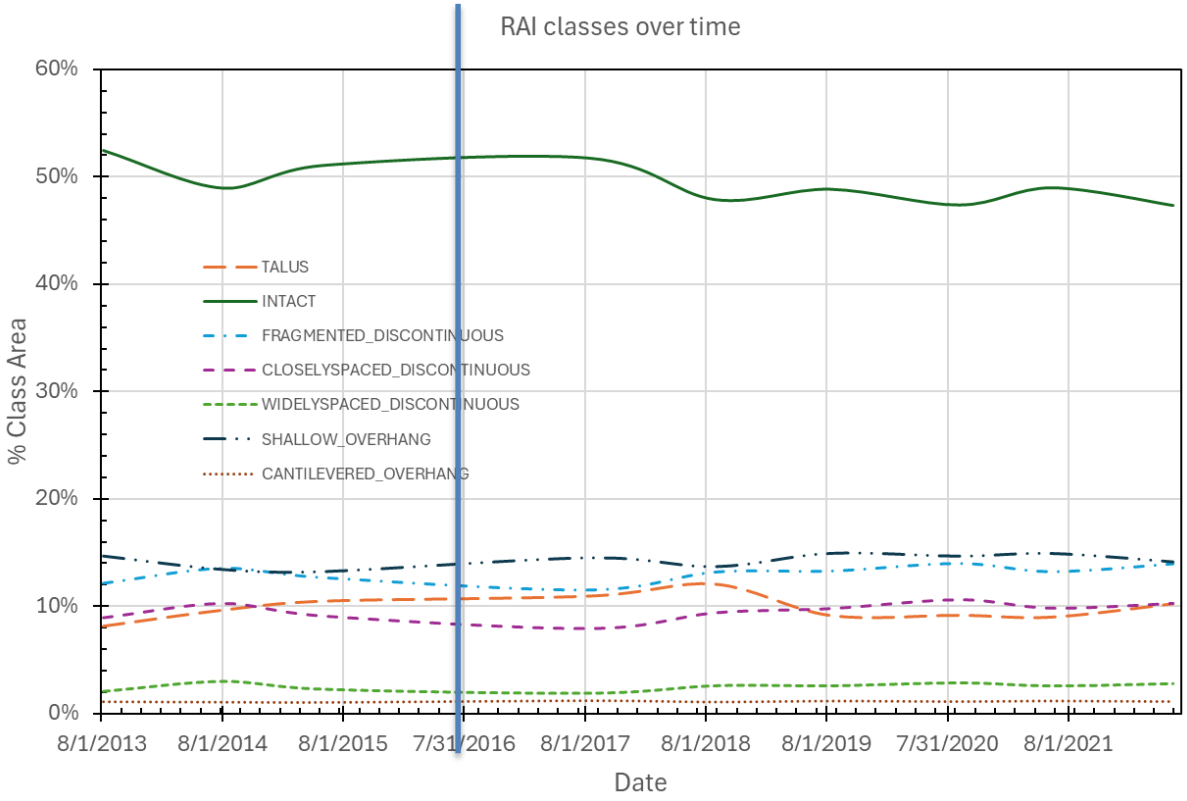

Figure 10.4. Changes in percent area of RAI classes at site GG241 over time. The Blue Line is the approximate scaling date.

10.3.2 RAI Site Score

The RAI site score, defined as the estimated annual kinetic energy delivered along discrete 1-m bins of the slope face, provides a height-weighted measure of hazard that integrates both morphological class distribution and the spatial position of active material on the slope. At GG241, the RAI site score decreased substantially immediately following the 2016 mitigation, reflecting the combined effect of overhang removal from upper portions of the slope and the conversion of a significant area of high-instability-rate discontinuous and overhang material to intact rock classification. As noted in Section 6.1.1, changes in the RAI score that result from material removed near the crest of a tall slope produce disproportionately large reductions relative to equivalent volumes removed near the toe, owing to the height-squared dependence of kinetic energy on release elevation. This effect amplifies the score reduction at GG241 relative to what would be predicted from the change in classified area alone, because a portion of the controlled blasting targeted material in the upper reaches of the slope.

Figure 10-1 illustrates this reduction in the post-treatment RAI score for the western wedge zone, where the most concentrated improvements were implemented. Consistent with the temporal evolution of RAI class proportions described in Section 9.2.1, the site score showed a partial recovery trend over the post-treatment monitoring period as newly exposed rock surfaces progressively developed discontinuous fabric. The magnitude and rate of this recovery are consistent with the attenuation timescale estimated from the class proportion data, with the score remaining below pre-treatment levels through the end of the monitoring record. Direct numerical quantification of the site score trajectory is presented in the associated technical appendices.

10.4 PER-CLASS INSTABILITY RATES AND FAILURE DEPTHS

Activity rates for each RAI class at GG241 over the full monitoring record are shown in Figure 10-5. Prior to mitigation, activity rates were elevated across all classes, with particularly high rates in the overhang and fragmented discontinuous categories, consistent with the advanced discontinuity development of the pre-treatment slope. A sharp decline in activity rates across most classes is apparent at the time of the 2016 mitigation, with post-treatment rates for the overhang classes approximately half of their pre-treatment values in the first post-mitigation monitoring epoch. The intact class, which carries the lowest default instability rate among the non-talus categories (Dunham et al., 2017), expanded in proportion following mitigation, contributing to the overall reduction in weighted site activity.

The overall activity rate time series is shown in Figure 10-6. The pre-treatment period (approximately 2010 through 2015) exhibits a gradual decline in total activity rate, suggesting that the slope was experiencing natural adjustment prior to the intervention. The mitigation produces a pronounced step reduction in the overall rate, which then remains at approximately half its pre-treatment level through the subsequent five years of monitoring. This sustained reduction distinguishes GG241 from the Rumble Pit sites, where activity rates converged toward control-site levels within approximately five months following scaling. The longer duration of the rate reduction at GG241 likely reflects the greater intensity and spatial extent of the 2016 treatment, which included controlled blasting capable of restructuring slope morphology at a scale beyond what manual scaling achieves.

Per-class failure depths, evaluated against the revised default values from Markus et al. (2023), showed a post-treatment reduction in the overhang classes consistent with the removal of the thickest, most precarious overhanging material. The intact class failure depth remained consistent with the default empirical reference throughout the monitoring period, indicating that the newly exposed rock surface eroded at rates comparable to intact rock at other well-monitored sites. The fragmented discontinuous class showed a modest post-treatment reduction in failure depth, which is interpretable as the consequence of removing the most deeply fractured near-surface material during mitigation, leaving a residual surface with somewhat lower per-event failure depth. Temporal trends in failure depth across post-treatment epochs showed no systematic recovery toward pre-treatment values over the monitoring period, providing additional evidence that the mitigation effect persisted beyond the timescale over which activity rates partially recovered.

Discontinuous material at GG241 showed a gradual post-treatment increase beginning approximately two to three years after mitigation, consistent with the progressive re-establishment of foliation-parallel fracture networks in the freshly exposed schist. This trend indicates that while the 2016 treatment effectively removed the existing discontinuous surface fabric, the anisotropic weathering characteristics of the schist promote relatively rapid regeneration of new discontinuities, and any assessment of long-term mitigation durability at foliated metamorphic sites must account for this lithologic tendency.

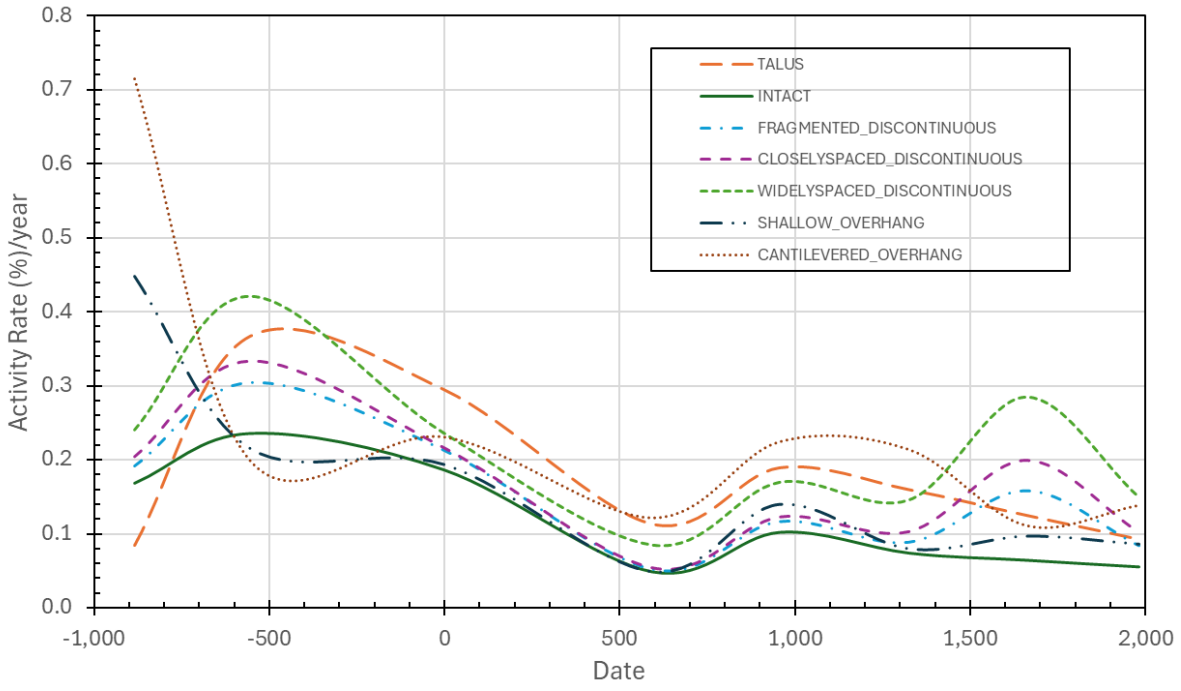

Figure 10.5. Activity rates for all RAI classes over time at site GG241. ***Assuming significant changes of 0.014 m or larger.***

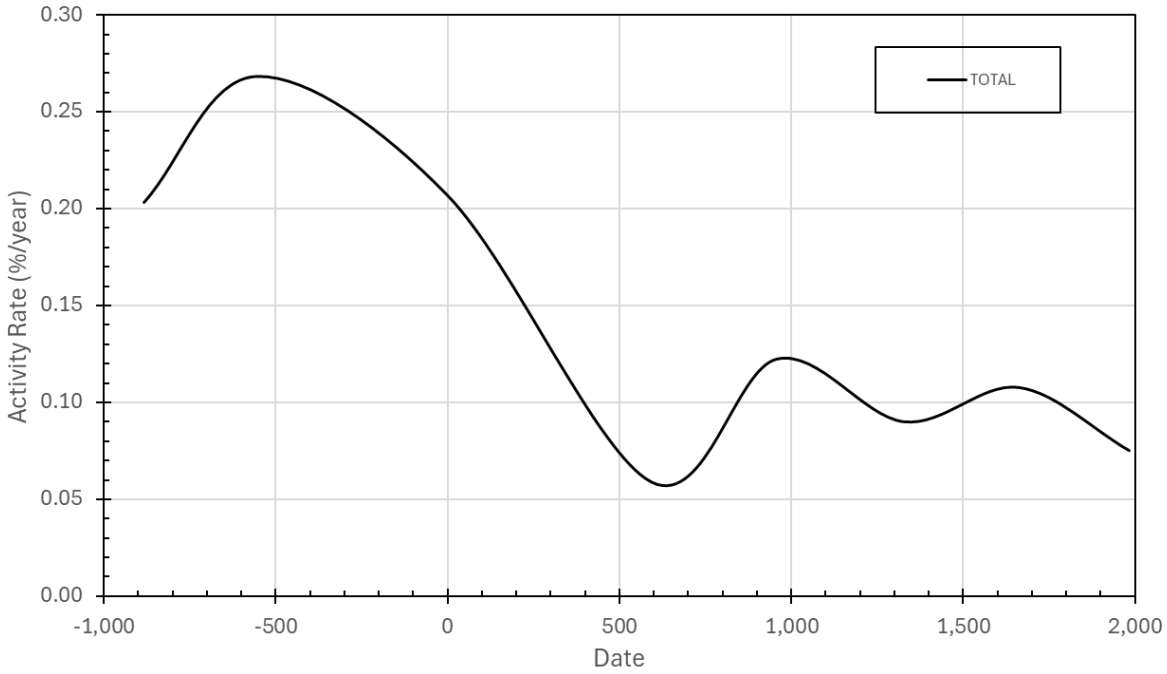

Figure 10.6. Overall activity rates over time at site GG241. ***Assuming significant changes of 0.014 m or larger.***

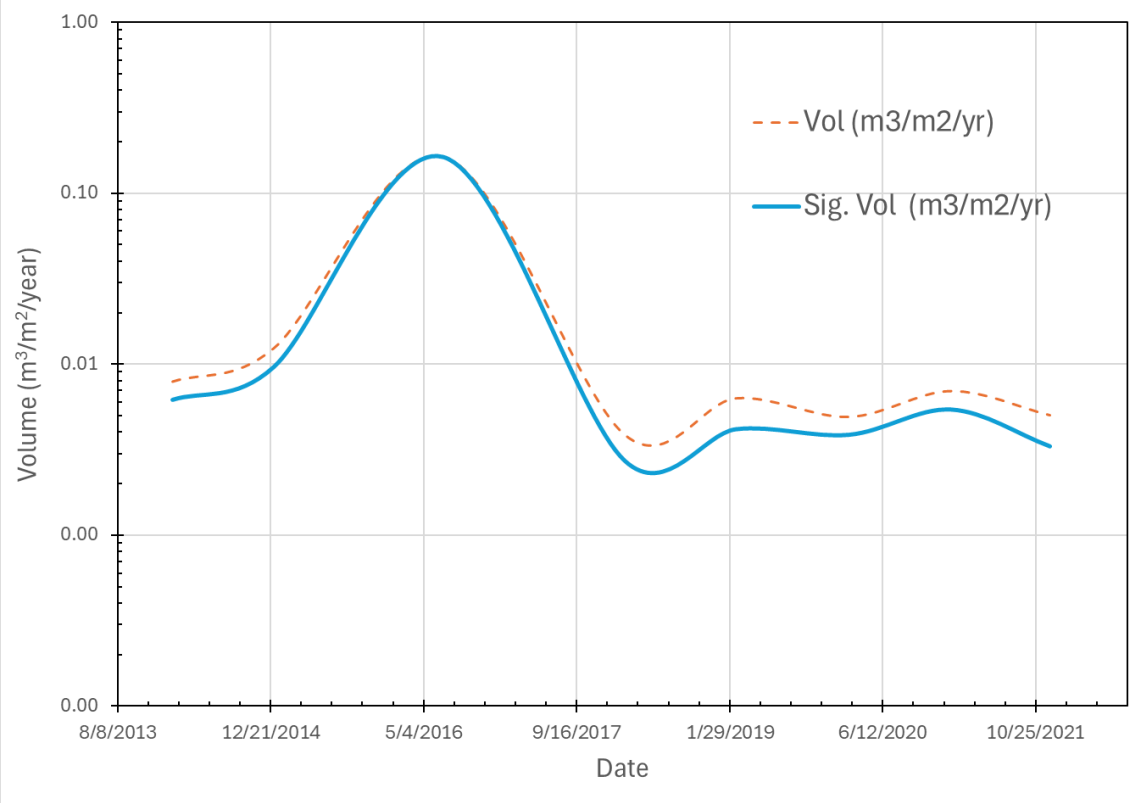

Figure 10.7. Volume and significant volume change observed at site GG241 over time. ***Assuming significant changes of 0.014 m or larger.***

10.5 RATES AND VOLUMES

10.5.1 Cumulative Erosion Volume

Cumulative normalized erosion volume at GG241 over the full monitoring record is shown in Figure 10.8. Total erosion volume is expressed as a time-integrated rockfall rate normalized by rockslope surface area, partitioned into volume bins to resolve the contributions of different event size classes to the overall sediment budget.

As at the Rumble Pit sites and Siskiyou Summit, larger rockfalls (V greater than 0.01 m^3) account for the majority of total volume change at GG241. Unlike the smaller Rumble Pit sites, however, GG241 maintains a relatively steady and substantial proportion of rockfalls in the intermediate size range (0.01 m^3 to 1 m^3) throughout the monitoring record, a pattern that likely reflects the combined influence of slope scale and geologic structure. The schist foliation promotes the development of tabular block geometries with a wider range of failure volumes than is typical of the more uniform basaltic exposure at the Rumble Pit.

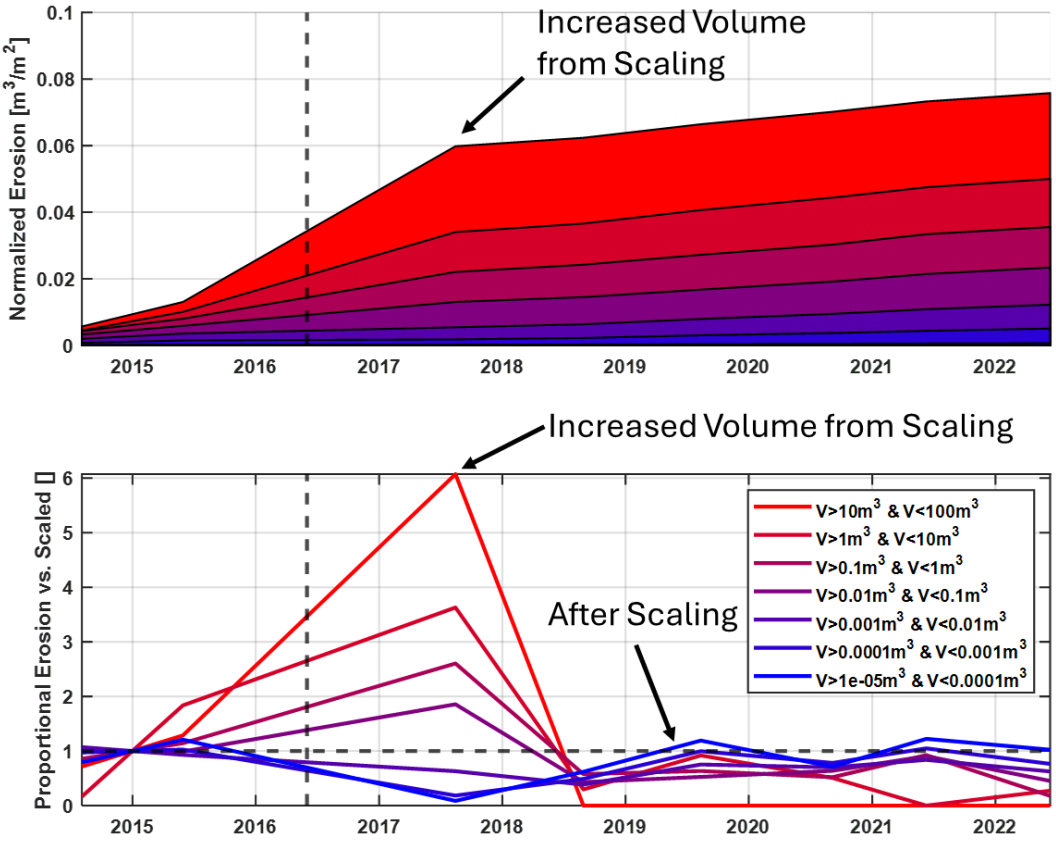

Figure 10.8. (Top Panel) Cumulative normalized erosion of GG241 over period of monitoring. Each shaded area represents cumulative normalized erosion volume stemming from various rockfall sizes. (Bottom Panel) Ratio of cumulative volume from pre-scaled rockfall rates at GG241 to post-scaling rates.

The mitigation event in 2016 is clearly expressed in the cumulative volume record as a large step increase associated with the removal of approximately 3,600 m³ of material from the slope during scaling and blasting. For context, the change in volume between the 2015 and 2017 surveys was approximately 3,710 m³, with the modest difference attributable to natural rockfall occurring during the intervening period. Following the mitigation, cumulative volume accumulation rates declined substantially across all size bins. The average annual erosion volume decreased from approximately 80 m³ per year in the pre-treatment period to approximately 40 m³ per year in the post-treatment period, representing a reduction of approximately fifty percent. This reduction was most pronounced for larger rockfalls (V greater than 0.01 m³), which showed the steepest decline in both frequency and cumulative contribution.

The bottom panel of Figure 10-8 presents the ratio of post-scaling to pre-scaling cumulative erosion volume across all monitoring epochs. This ratio is consistently below 1.0 for the larger size bins throughout the post-treatment period, confirming a sustained reduction in large-rockfall

volume relative to pre-treatment rates. A modest rebound in small rockfall volume ($V < 0.001$ m^3) is evident in the later post-treatment epochs, with rates for this size class approaching and, in some intervals, exceeding the pre-treatment baseline. The rebound in small rockfall is consistent with the progressive re-exposure of fresh, unweathered schist surfaces that subsequently generate small-scale raveling as they begin to develop fracture fabric. Larger rockfall events, by contrast, remained at rates less than 80 percent of pre-treatment values and more commonly at rates less than 60 percent throughout the monitoring period, supporting the interpretation that the strategic removal of large, precarious blocks during the 2016 treatment produced a durable reduction in large-event frequency that persisted for at least five years.

10.5.2 Volume-Frequency Relationships

Volume-frequency relationships normalized by rockslope area and monitoring duration are shown in Figure 10-9 for the pre-scaling period, the scaling operation itself, and the post-scaling period. All three distributions follow the inverse power-law form described in Section 6.1.3. The post-scaling distribution lies below the pre-scaling distribution across all volume ranges, indicating an overall decrease in rockfall activity frequency at the site following mitigation. This reduction is most pronounced for larger rockfall volumes (V greater than 0.01 m^3), where the post-scaling curve is displaced downward relative to both the pre-scaling and scaling-event curves by approximately one-half to one order of magnitude in failure rate.

The distribution corresponding to the scaling event itself is shifted upward relative to both pre- and post-scaling distributions for large volumes, reflecting the concentrated removal of larger precarious blocks during the intervention. This upward shift for the scaling distribution is expected and does not represent an increase in ongoing natural hazard; rather, it documents the intended consequence of the operation, namely the deliberate evacuation of kinematically unstable material.

Changes in the power-law parameters between the pre- and post-mitigation periods are informative in the context of the Section 6.1.3 framework. The post-mitigation activity parameter β is reduced relative to its pre-treatment value, consistent with an overall decrease in rockfall frequency across the slope. The post-mitigation scaling parameter α is modestly steeper, indicating that smaller events govern the post-treatment size distribution more strongly than before mitigation. This shift toward a steeper post-treatment power-law slope is the expected signature of preferential removal of large, structurally controlled blocks, which alters the relative balance of large and small events without eliminating the background supply of small rockfall from surface weathering. Together, these parameter changes confirm that the 2016 treatment altered not only the rate but also the character of rockfall activity at GG241, in the manner anticipated by Section 6.1.3 for an effective mitigation.

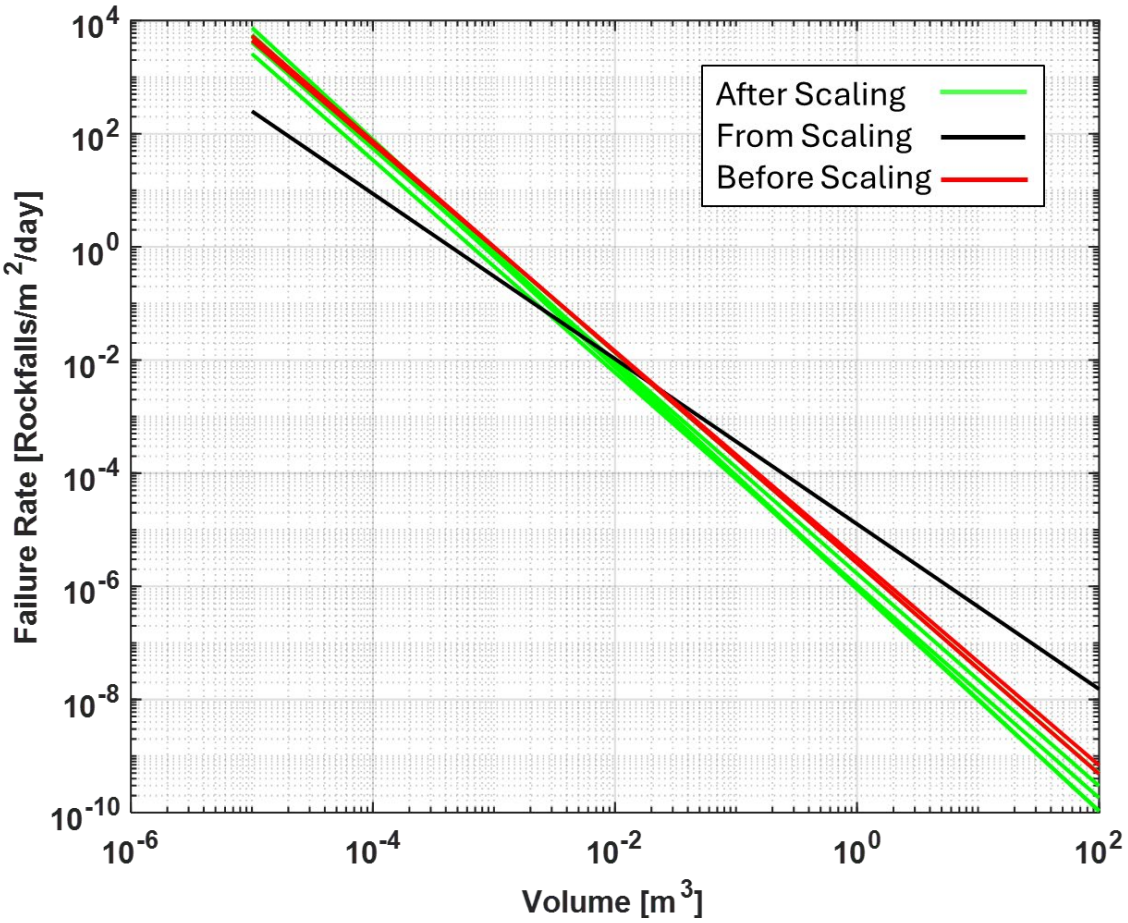

Figure 10.9. Volume-frequency relationships for both post-scaling (green), scaled (black), and pre-scaling rockfall for GG241. During this period, the scaled rockslope shows a notable decrease in the frequency of larger rockfalls.

9.5 Trajectory Analysis

Note that the RTA analysis was the focus of trajectory modeling for this site owing to its sheer size and computational expense. The PTA analysis is computationally expensive for a site of this size. Ideally, more powerful computing or parallelization will enable analysis of trajectories at this site using the PTA.

9.5.1 Retrospective Trajectory Analysis (RTA)

As shown in Figure 10-10, the RTA demonstrates that rockfall sizes vary considerably for the GG241. Rockfalls that are higher in elevation have more potential to travel away from the slope owing to impacts with talus piles and outward facing slopes below.

These analyses demonstrate the associated starting and ending locations inferred from actual rockfall sources at the site, as well as associated kinetic energy upon final impact (assumed to be when velocity nears zero or the lowest elevation in the DEM). Different than the Rumble Pit rockslopes, rockfall at GG241 tend to have a larger travel length to height, where more than 80% of rockfall travel more than half the height of their source location. Further, approximately 20% travel as far away from their source as their height, suggesting that the geometry of the slope (steep, outward faces) may result in notable mobility, especially with the outward dip of the rock faces, which serve as overhang sources for rockfalls and adverse facies for rockfall bouncing and sliding.

This analysis again enables a means of quantifying the role of scaling on rockfall mitigation. For example, in Figure 10-11, there appears to be a notable, decreased probability of exceedance in rockfall reach for the site after scaling versus the conditions prior to scaling. These modest decreases in potential for exceedance for rockfalls for travel length to source height ratios appears to be most pronounced at ratios ranging 50%-100% of height. Further, for GG241, scaling appears to result in a notable decreased likelihood to exceed certain levels of kinetic energy, as shown in Figure 10-11. These factors demonstrate that scaling appears to have decreased both the energy and the observed travel distance of rockfall for the multi-year period following mitigation.

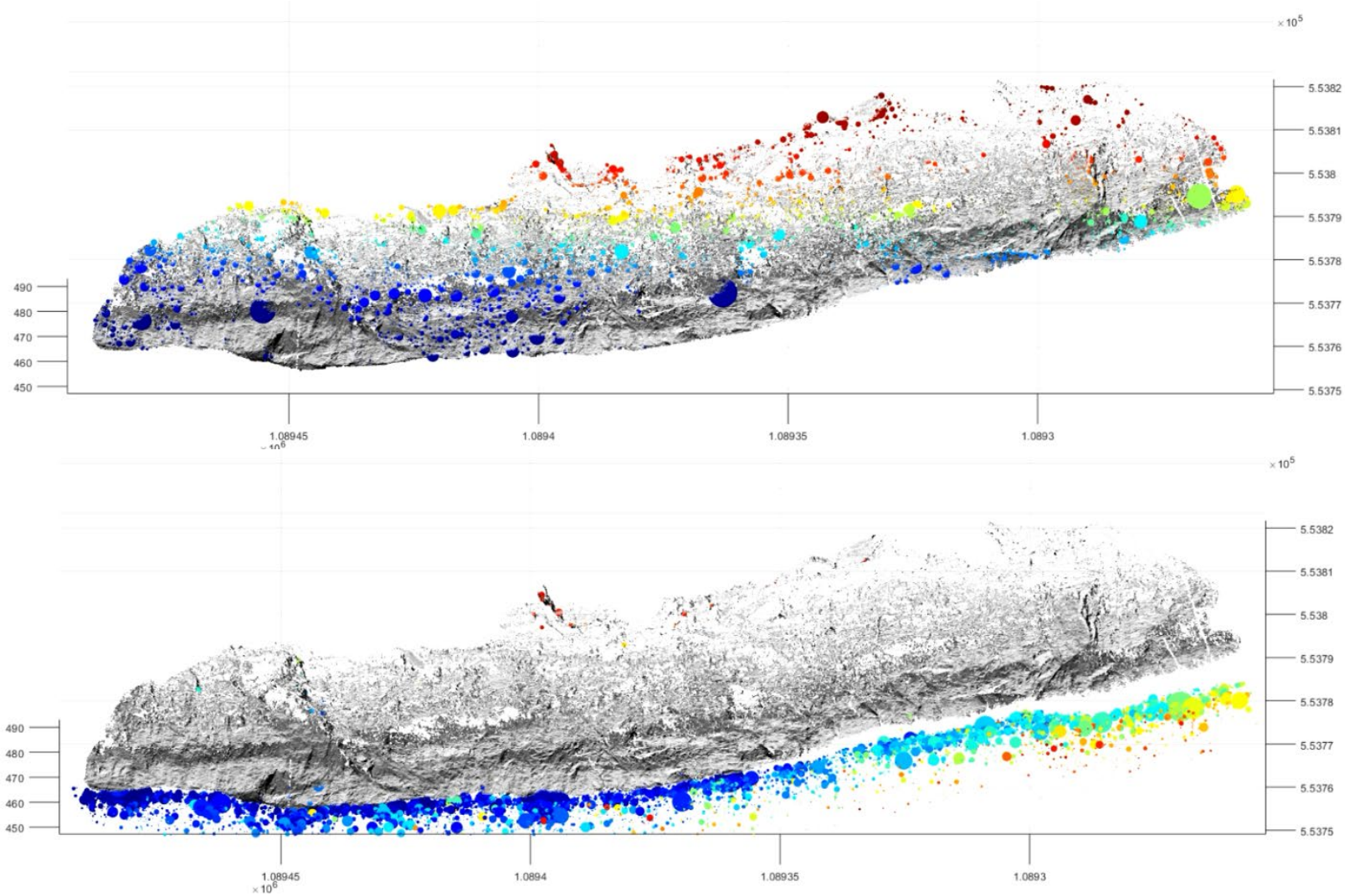

Figure 10.10. Ending rockfall locations for all rockfall sources and volumes GG241 for all epochs.

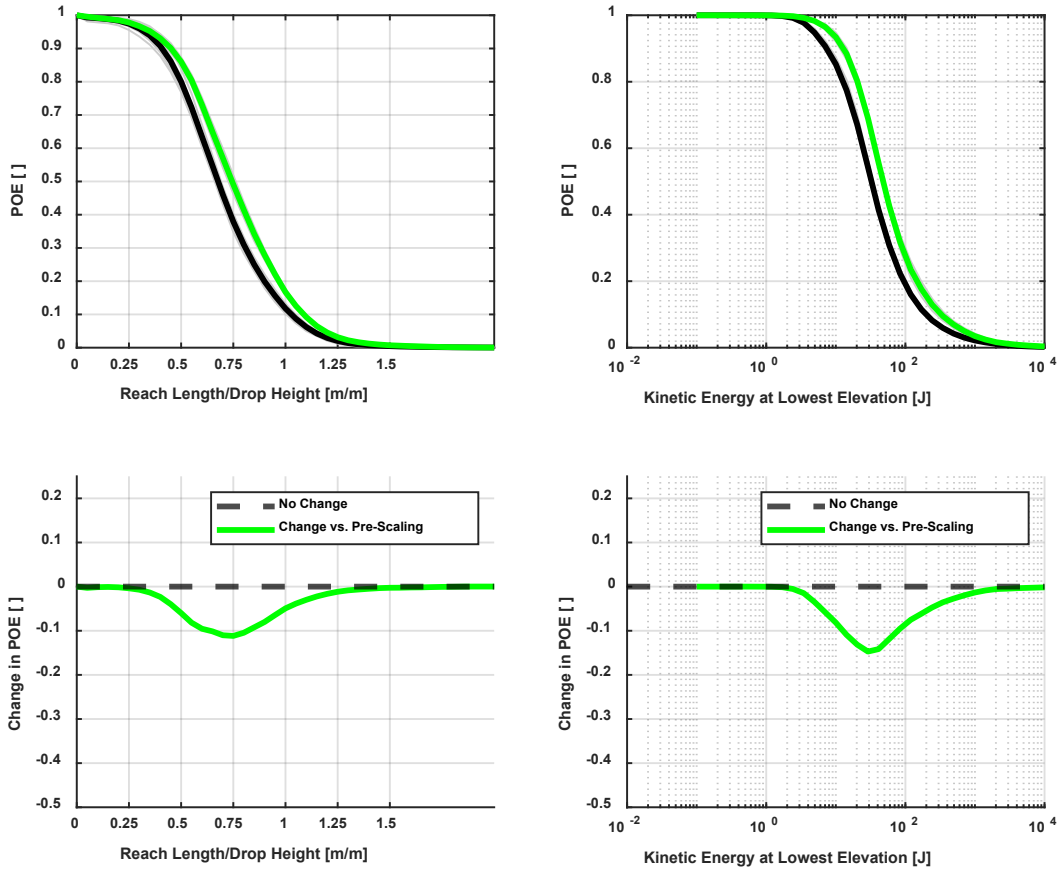

Figure 10.11. Top Left (a): Probability of exceedance of reach length to drop height ratio (m/m) for pre-scaling conditions on GG241 (green) and post-scaling conditions (black). Bottom Left (b): Change in probability of exceedance of reach length to drop height ratio (m/m) for post-scaling conditions (black). Top Right (c): Probability of exceedance of kinetic energy at lowest elevation for pre-scaling conditions on GG241 (green) and post-scaling conditions (black), where gray lines represent individual epochs, black line represents mean. Bottom Right (d): Change in probability of exceedance of kinetic energy at lowest elevation for scaled conditions on GG241 (green).

10.6 SLOPE PERFORMANCE

Talus accumulation at slope benches and at the toe provides a direct measure of the ongoing material flux from the slope face that is relevant to ODOT maintenance planning. At GG241, talus accumulation on the primary catch bench increased immediately following the 2016 mitigation, reflecting the deposition of material dislodged during the scaling and blasting operations. In subsequent monitoring epochs, the rate of new talus accumulation declined relative to the pre-treatment period, consistent with the overall reduction in rockfall activity rates documented in Section 10.3. The spatial distribution of deposited material also shifted toward the immediate slope toe in the post-treatment epochs, consistent with the trajectory analysis finding that the probability of rockfalls traveling beyond half their source height decreased following mitigation. This concentration of debris closer to the slope base indicates both a reduction in event magnitude and a decrease in the kinetic energy of individual failures and has direct implications for the design and required maintenance frequency of catch structures at the site.

An increase in talus classified as derived from previously intact rock material was observed on benches in the later post-treatment monitoring epochs. The RAI classification framework attributes this accumulation to raveling of newly exposed, unfractured schist surfaces that begin to develop foliation-parallel fracture networks over time. As noted by Markus et al. (2023), talus at highway cut sites may also be influenced by maintenance activities that periodically remove material from the slope toe, and any interpretation of post-treatment talus metrics at GG241 must account for this dynamic. The available monitoring record does not permit precise quantification of maintenance-related talus removal, and this uncertainty should be acknowledged in any operational planning that relies on the GG241 debris accumulation data.

10.7 SYNTHESIS AND CROSS-METRIC ASSESSMENT

Across all Section 6.0 metrics, GG241 provides the most complete and internally consistent evidence of scaling effectiveness among the sites examined in this study. The RAI morphological classification, per-class instability rates, magnitude-frequency parameters, cumulative erosion volumes, trajectory exceedance probabilities, and talus accumulation patterns all change in directions consistent with a reduction in rockfall hazard following the 2016 treatment, and the direction and approximate magnitude of these changes are mutually consistent across metrics.

The cross-metric pattern at GG241 also illustrates several dynamics that were less clearly resolved at shorter-duration sites. The most consequential of these is the differentiated response by rockfall size class: large rockfall events (V greater than 0.01 m^3) show a persistent reduction in frequency and cumulative volume throughout the post-treatment period, while small rockfall (V less than 0.001 m^3) shows a partial rebound toward pre-treatment rates beginning approximately two to three years after mitigation. This size-class divergence is physically coherent. The 2016 treatment targeted and removed large, kinematically unstable blocks, depleting the inventory of precarious material that could source large events. Small rockfall, by contrast, is driven primarily by surface weathering processes that operate continuously on newly exposed schist faces; these processes are not substantially altered by a single mitigation event and recover on a timescale governed by the rate of fracture development in the freshly exposed rock mass.

The temporal evolution of RAI class proportions, per-class activity rates, and cumulative volume together indicate that the morphological effects of the 2016 treatment attenuated over approximately three to five years, with most metrics returning to within the range of pre-treatment variability by the end of the monitoring record. This timescale is substantially longer than the five-month convergence observed at Rumble Pit Site A and reflects both the greater intensity of the GG241 treatment and the difference in scale between the two sites. However, the persistence of a reduction in large-rockfall frequency beyond the period of morphological recovery suggests that the depletion of structurally controlled precarious blocks has a more durable hazard-reduction effect than morphological metrics alone would indicate. This finding has practical implications for maintenance planning: the reduction in large-event frequency may justify longer intervals between mitigation treatments at sites with similar geologic structure, even if surface morphology metrics suggest a return toward pre-treatment conditions.

Two limitations govern the confidence that can be attached to these conclusions. First, the absence of a fully paired, unmitigated control site with equivalent geology and monitoring history at GG241 limits the ability to separate the effect of the 2016 treatment from temporal trends in rockfall activity that may have occurred independent of mitigation. The partial comparison afforded by GG239 is useful but not sufficient to replace a dedicated control site. Second, the exclusion of the 2016 survey epoch from the dataset means that the immediate post-treatment morphological condition cannot be directly observed; the 2017 survey represents the first post-treatment scan and encompasses one full year of post-treatment evolution. Despite these limitations, the convergence of evidence across multiple independent metrics over a five-year post-treatment record supports the conclusion that the 2016 mitigation at GG241 produced a measurable and durable reduction in rockfall hazard, with the largest and most consequential reductions concentrated in the large-event size classes that pose the greatest risk to highway infrastructure.

10.8 SUMMARY

Site GG241 at Glitter Gulch provides the most conclusive evidence of rockfall scaling effectiveness among all sites examined in this study. The 2016 mitigation, combining manual scaling and controlled blasting, produced immediate reductions in overhang and fragmented discontinuous rock classification, an increase in intact rock proportion, a decrease in per-class instability rates of approximately fifty percent, and a reduction in average annual erosion volume from approximately 80 m^3 per year to approximately 40 m^3 per year. Volume-frequency analysis confirmed a reduction in the frequency of large rockfall events accompanied by a modest steepening of the power-law slope, consistent with the preferential removal of large, structurally controlled blocks. Trajectory analysis demonstrated decreased probabilities of exceedance for both reach length and kinetic energy delivery in the post-treatment period, with the most pronounced reductions at reach ratios between 0.5 and 1.0 of source height.

Morphological effects of the treatment attenuated over approximately three to five years, with most RAI class proportions returning toward pre-treatment levels by the end of the monitoring record. However, the reduction in large-rockfall frequency was sustained throughout the five-year post-treatment period, suggesting that block depletion effects persist beyond the timescale of morphological recovery. A modest rebound in small-rockfall frequency was observed beginning two to three years after treatment, reflecting the progressive development of fracture fabric in freshly exposed schist surfaces. The highly foliated nature of the schist at GG241 promotes relatively rapid regeneration of discontinuous surface morphology, and future treatment planning at this site should account for this lithologic tendency when estimating the expected service life of a mitigation operation. Taken together, the GG241 dataset demonstrates that scaling, when applied at sufficient intensity to structurally controlled rockfall sources at high elevation on a slope, can produce a reduction in large-event frequency that persists for multiple years and constitutes a meaningful decrease in hazard to adjacent infrastructure.

11.0 CONCLUSIONS

This study evaluated the effectiveness of rock slope scaling using quantitative, repeatable metrics derived from multi-temporal terrestrial laser scanning, morphological change analysis, and Rockfall Activity Index (RAI) analysis. Together, morphological analysis and RAI metrics proved effective in quantifying scaling-induced changes in rockfall activity and provided an objective framework for assessing mitigation performance across a range of site conditions. The results demonstrate that scaling can reduce rockfall hazard under certain conditions; however, its performance is highly site-specific and governed by slope geometry, structural controls, and prevailing geomorphic processes. No single metric adequately captures mitigation effectiveness across all sites. Instead, a suite of complementary indicators, including activity rates, volume–frequency relationships, block size distributions, prevalence of precarious overhangs, and associated potential energy, was necessary to characterize slope response and hazard evolution.

Activity rates were particularly informative but were sensitive to the selected significant-change thresholds and monitoring intervals. Immediate post-scaling reductions in RAI scores and overall activity were observed at several sites, reflecting the removal of unstable material. Scaling commonly reduced failures associated with overhangs and structurally adverse features, and this reduction was frequently accompanied by a corresponding increase in the proportion of slope surface classified as intact rock, indicating that more competent material was exposed following removal of the most discontinuous and overhanging material. However, smaller rockfalls appeared less sensitive to scaling and often returned to rates near baseline levels within a period ranging from several months to approximately one year, depending on site characteristics and the volume of material removed during treatment. These observations indicate that scaling provides measurable short-term benefits, particularly in reducing higher-magnitude events, while having limited influence on ongoing background rockfall processes.

Site-specific findings illustrate both the potential and the constraints of scaling as a mitigation technique. At the Rumble Pit controlled field site, Sites A and B showed measurable but time-limited reductions in rockfall activity following hand-tool scaling, with effects persisting for approximately five to six months. Site B produced the strongest response among the Rumble Pit sites, with approximately a 65 percent reduction in the probability of exceedance of kinetic energy relative to pre-scaling conditions. Site C, in contrast, yielded a null result attributable to the already-disaggregated character of the basalt column structure at that location, which left little structurally coherent material for scaling to remove. This within-site variability demonstrates that structural geology is a primary control on scaling effectiveness and that sites sharing similar gross lithology may respond very differently to the same mitigation treatment.

At the SR14 MP73 site along the Columbia River Gorge, scaling produced the most pronounced morphological response documented in this study. Cantilevered overhang area was reduced by 98 percent following the scaling operation, and the overall activity rate was lower in the first post-scaling epoch. Average failure depth decreased from approximately 0.260 m prior to scaling to approximately 0.077 m following treatment and remained stable across two subsequent

monitoring epochs, indicating that the scaling operation successfully removed the most kinematically unstable surface material and that the resulting slope surface did not revert rapidly to pre-scaling failure modes.

GG241, a highway rock cut in Alaska, provided the most conclusive evidence of durable scaling effectiveness among the study sites. Activity rates at GG241 declined by approximately half following scaling, and the average annual rockfall volume decreased from approximately 80 m^3/yr prior to treatment to approximately 40 m^3/yr in the post-scaling period. These reductions persisted across more than five years of post-scaling monitoring, a duration substantially greater than the multi-month effects observed at the Rumble Pit. At GG241, the frequency of smaller rockfall events returned to near-baseline conditions within approximately one year of scaling, while suppression of larger-magnitude events was sustained over the full monitoring period. This pattern suggests that the duration of post-scaling activity suppression is related to the size of material removed during treatment, with removal of larger precarious sources producing more durable reductions in the higher-magnitude portion of the rockfall size distribution.

The I-5 Siskiyou Pass site showed sustained suppression of larger rockfall volumes over multiple post-scaling years. Interpretation of results at this site is constrained by the absence of a pre-scaling terrestrial laser scan baseline, which limits the ability to directly attribute observed post-scaling conditions to the scaling operation relative to other factors. This limitation underscores the importance of obtaining pre-mitigation baseline surveys prior to treatment, particularly at sites where subsequent monitoring data are intended to serve as evidence of mitigation effectiveness.

Across the sites studied, scaling appeared most effective where precarious geologic conditions—including overhanging rock, adverse bedding orientations, and facies directed toward the travel lane—were present and where slope dimensions permitted generation of larger blocks. The relationship between removed block size and the durability of suppression is consistent across the Rumble Pit, SR14 MP73, and GG241 findings and supports a strategy of targeted removal of large, structurally controlled sources to achieve sustained hazard reduction. Smaller-scale rockfall, which is prevalent at all site sizes and is less responsive to scaling, requires complementary mitigation measures such as catch ditches, rockfall barriers, mesh, or surface stabilization to manage the residual hazard.

Trajectory-based analyses strengthened the evaluation by translating observed morphological changes into hazard-relevant metrics. Retrospective Trajectory Analysis (RTA) integrates observed change detection and identified source zones into rockfall modeling, enabling quantification of reach length, impact energy distributions, and probability of exceedance before and after scaling, and provides a defensible index of mitigation efficacy applicable across site scales. Probabilistic Trajectory Analysis (PTA), which treats all slope locations as potential sources and incorporates empirical magnitude–frequency relationships, offers more comprehensive hazard characterization but is computationally intensive. PTA was applied primarily to the smaller Rumble Pit sites, where it demonstrated how slope morphology, block size, and event frequency collectively shape downslope energy distributions and can support strategic identification of precarious source zones. For larger slopes, RTA offers a practical and data-driven approach for evaluating mitigation-induced changes and communicating outcomes to asset managers.

The integration of multi-temporal morphological analysis, RAI metrics, and trajectory modeling provides a more objective and repeatable framework for assessing mitigation effectiveness than qualitative inspection alone. Scaling produces variable effects depending on rockfall mechanisms and structural context, typically reducing overhang-driven failures while having limited influence on smaller, more frequent events. Short-term improvements are clearly measurable at appropriately characterized sites; long-term effectiveness under ongoing weathering and geomorphic evolution remains an area for continued study. Expanded monitoring datasets and longer observation windows will further refine understanding of temporal patterns and the conditions under which scaling performance is sustained.

Uncertainties associated with climatic variability, geologic heterogeneity and survey precision, are inherent in field-based assessments of this kind and must be acknowledged in the interpretation of results. The findings nonetheless demonstrate that strategic scaling, particularly the targeted removal of large, precarious sources, can reduce rockfall hazard for a sustained, though finite, period. When integrated with complementary mitigation measures and ongoing monitoring, the quantitative tools developed and applied in this study support improved decision-making and long-term management of rockfall-prone transportation corridors.

11.1 KEY TAKEAWAYS

The following key takeaways summarize principal findings relevant to implementation of the research findings by transportation agencies.

- **Rock slope scaling can reduce hazard, but effectiveness is site-specific.** Scaling reduced activity rates and the occurrence of larger rockfall events at most sites studied and for variable time periods. Performance depends significantly on slope geometry, structural geology, and geomorphic processes. Sites with already-disaggregated surface material, such as the Rumble Pit Site C, may yield no measurable benefit from scaling.

- **The duration of post-scaling suppression appears related to the size of material removed.** At the Rumble Pit, where hand-tool scaling removed modest block sizes, activity reductions relative to control conditions persisted for approximately five to six months. At GG241, where larger precarious sources were removed, suppression of higher-magnitude events was sustained across more than five years of monitoring. Targeted removal of large, structurally controlled sources offers greater potential for durable hazard reduction than removal of smaller, more disaggregated material.

- **No single metric is sufficient to evaluate mitigation effectiveness.** A combination of metrics—activity rates, magnitude–frequency relationships, block size distributions, overhang characteristics, and potential energy—is needed to meaningfully characterize post-scaling slope behavior and to distinguish between transient post-treatment adjustment and sustained mitigation response.

- **Quantitative, repeatable metrics improve confidence in mitigation decisions.** Morphological change analysis using terrestrial laser scanning provides an objective framework for evaluating scaling outcomes and reduces reliance on subjective, qualitative

assessments. Pre-mitigation baseline surveys are essential; their absence, as at I-5 Siskiyou Pass, limits the ability to attribute post-scaling conditions directly to the treatment.

- **Scaling outcomes are time-dependent and require multi-epoch monitoring.** Post-mitigation slopes continue to evolve, and activity rates for smaller rockfall events may return to near-baseline conditions within months to approximately one year of treatment. Multi-temporal monitoring is essential to distinguish initial post-scaling adjustment from sustained response and to inform the timing and frequency of maintenance interventions.

- **Trajectory analyses link morphological change to actionable hazard indicators.** Integrating change detection with RTA enables evaluation of runout behavior, impact energies, and probability of exceedance before and after scaling, providing a defensible and communicable index of mitigation efficacy. PTA offers more comprehensive hazard characterization for smaller sites and can support strategic identification of precarious source zones prior to treatment.

- **Engineering judgment remains important in the application of quantitative methods.** Quantitative metrics improve transparency, consistency, and repeatability in the assessment of scaling effectiveness, but do not replace site-specific judgment in identifying structurally adverse conditions, interpreting monitoring data in the context of local geology and climate, and selecting among complementary mitigation alternatives. The methods presented here provide a more defensible basis for those judgments and for communicating outcomes to agency decision-makers.

1.2 FUTURE RESEARCH

The results of this study demonstrate the potential value of rockfall scaling as a proactive slope-maintenance and risk-reduction strategy, while also identifying several areas where additional research is needed to better quantify its effectiveness, longevity, and cost benefits. In particular, future work should focus on understanding how site geology and environmental conditions influence the duration of scaling benefits, improving methods for quantifying changes in rockfall activity, and translating these findings into agency maintenance, contracting, and funding practices.

- **Long-term monitoring:** Determine the appropriate post-scaling monitoring period and how long reductions in rockfall activity persist. Anecdotal observations suggest some sites may return toward baseline activity within approximately two years, but longer datasets are needed to quantify longer term-trends, particularly across different geologies.

- **Geologic controls on effectiveness:** Evaluate how lithology, degree of weathering, fracture characteristics, rock mass strength, and Geological Strength Index (GSI) influence scaling effectiveness and treatment longevity. Particular attention should be given to slopes where weathering is a primary control.

- **Freeze-thaw and climatic effects:** Quantify the influence of freeze-thaw cycles, precipitation, snowmelt, and seasonal temperature changes on post-scaling rockfall activity and deterioration rates.

- **Designed and blasted slopes:** Extend long-term monitoring to designed and blasted rock slopes to better understand how construction methods affect long-term rockfall activity and future scaling needs.

- **3D monitoring methods:** Evaluate point clouds, photogrammetric meshes, lidar, UAS, and other 3D approaches for efficiently documenting rockfall source areas, changes in slope condition, and treatment performance.

- **Scaling quantities and contracting:** Investigate methods for better estimating scaling quantities, particularly on highly weathered slopes where removal of unstable material can expose substantially larger volumes than anticipated.

- **Rockfall loading on culverts:** Evaluate rockfall impact and debris loading on culverts and other transportation infrastructure, building on examples and experience from agencies.

- **Economic benefits:** Develop methods to quantify the benefits of scaling in terms of reduced rockfall activity, emergency response, closures, maintenance, and infrastructure damage. Improved quantification could strengthen justification for FHWA and other federal funding.

- **Implementation into operations:** Develop practical procedures for incorporating scaling effectiveness, repeat monitoring, and 3D change analysis into routine slope inspections, asset management, maintenance planning, and treatment prioritization.

12.0 REFERENCES

Abellán, A., Calvet, J., Vilaplana, J.M. and Blanchard, J., 2010. Detection and spatial prediction of rockfalls by means of terrestrial laser scanner monitoring. Geomorphology, 119(3-4), pp.162-171.

Abellán, A., Vilaplana, J. M., Calvet, J., García-Sellés, D., & Asensio, E. (2011). Rockfall monitoring by Terrestrial Laser Scanning–case study of the basaltic rock face at Castellfollit de la Roca (Catalonia, Spain). *Natural Hazards and Earth System Sciences*, *11*(3), 829-841.

Abellán, A., Oppikofer, T., Jaboyedoff, M., Rosser, N. J., Lim, M., & Lato, M. J. (2014). Terrestrial laser scanning of rock slope instabilities. *Earth surface processes and landforms*, *39*(1), 80-97.

Agliardi, F., Crosta, G.B. and Frattini, P., 2009. Integrating rockfall risk assessment and countermeasure design by 3D modelling techniques. Natural Hazards and Earth System Sciences, 9(4), p.1059.

Al-Rawabdeh, A., He, F., Moussa, A., El-Sheimy, N. and Habib, A., 2016. Using an unmanned aerial vehicle-based digital imaging system to derive a 3D point cloud for landslide scarp recognition. Remote sensing, 8(2), p.95.

Anderson, S., Vessely, M., Dowling, C. and Carter, R. Geotechnical Asset Management Program, WisDOT ID no. 0092-21-06.

Arosio, D., Longoni, L., Mazza, F., Papini, M. and Zanzi, L., (2013), Freeze-thaw cycle and rockfall monitoring. In Landslide science and practice (pp. 385-390). Springer, Berlin, Heidelberg.

Badger, T. C., & Lowell, S. M. (1992). Rockfall control in Washington state. *Transportation research record*, (1343).

Barlow, J., Lim, M., Rosser, N., Petley, D., Brain, M., Norman, E. and Geer, M., 2012. Modeling cliff erosion using negative power law scaling of rockfalls. Geomorphology, 139, pp.416-424.

Barton, N., & Choubey, V. (1977). The shear strength of rock joints in theory and practice. *Rock mechanics*, *10*, 1-54.

Battulwar, R., Zare-Naghadehi, M., Emami, E., Sattarvand, J., (2021). A state-of-the-art review of automated extraction of rock mass discontinuity characteristics using three-dimensional surface models, Journal of Rock Mechanics and Geotechnical Engineering, 13(4), 920-936. https://doi.org/10.1016/j.jrmge.2021.01.008

Beckstrand, D. L., Mines, A. E., George, B. A., & Black, B. A. (2020). *Estimating and Contracting Rock Slope Scaling Adjacent to Highways* (No. Project 20-05, Topic 50-13)

Bemis, S.P., Micklethwaite, S., Turner, D., James, M.R., Akciz, S., Thiele, S.T. and Bangash, H.A., 2014. Ground-based and UAV-based photogrammetry: A multi-scale, high-resolution mapping tool for structural geology and paleoseismology. Journal of Structural Geology, 69, pp.163-178.

Berti, M., Corsini, A. and Daehne, A., 2013. Comparative analysis of surface roughness algorithms for the identification of active landslides. Geomorphology, 182, pp.1-18.

Bestland, E. A. (1987). Volcanic stratigraphy of the Oligocene Colestin Formation in the Siskiyou Pass area of southern Oregon. Oregon Geology, 49(7), 79–86.

Bobet, A., & Einstein, H. H. (2011). Tunnel reinforcement with rockbolts. *Tunnelling and Underground Space Technology*, *26*(1), 100-123.

Bouali, E.H., Oommen, T., Vitton, S., Escobar-Wolf, R. and Brooks, C., 2017. Rockfall hazard rating system: benefits of utilizing remote sensing. Environmental and Engineering Geoscience, 23(3), pp.165-177.

Budetta, P., 2004. Assessment of rockfall risk along roads. Natural Hazards and Earth System Science, 4(1), pp.71-81.

Buzzi, O., Leonarduzzi, E., Krummenacher, B., Volkwein, A., & Giacomini, A. (2015). Performance of high strength rock fall meshes: effect of block size and mesh geometry. *Rock Mechanics and Rock Engineering*, *48*, 1221-1231.

Caduff, R., Schlunegger, F., Kos, A. and Wiesmann, A., 2014. A review of terrestrial radar interferometry for measuring surface change in the geosciences. Earth surface processes and landforms, 40(2), pp.208-228.

Calvetti, F., & Di Prisco, C. (2012). Rockfall impacts on sheltering tunnels: real-scale experiments. *Géotechnique*, *62*(10), 865-876.

Campbell, Ian., A., (2016). Massive rock falls on Tyee Road | News | nrtoday.com. [ONLINE] Available at: https://www.nrtoday.com/news/massive-rock-falls-on-tyee-road/article_b966e6b0-dd33-11e5-b595-5fc7cc02bfd4.html. [Accessed 25 February 2018].

Carlà, T., Farina, P., Intrieri, E., Botsialas, K. and Casagli, N., 2017. On the monitoring and early-warning of brittle slope failures in hard rock masses: Examples from an open-pit mine. Engineering Geology, 228, pp.71-81.

Carlà, T., Farina, P., Intrieri, E., Ketizmen, H. and Casagli, N., 2018. Integration of ground-based radar and satellite InSAR data for the analysis of an unexpected slope failure in an open-pit mine. Engineering Geology, 235, pp.39-52.

Carlà, T., Intrieri, E., Farina, P. and Casagli, N., 2017. A new method to identify impending failure in rock slopes. International Journal of Rock Mechanics and Mining Sciences, 93, pp.76-81.

Carrea, D., Abellan, A., Derron, M.H. and Jaboyedoff, M., 2015. Automatic rockfalls volume estimation based on terrestrial laser scanning data. In Engineering Geology for Society and Territory-Volume 2 (pp. 425-428). Springer, Cham.

Cunningham, K., Olsen, M.J., O'Banion, M., Wartman, J., Rault, C. and Hall, M., Unmanned aircraft system assessments of landslide safety for transportation corridors.

Cunningham, K., Olsen, M.J., Wartman, J., Leshchinsky, B., O'Banion, M., (2017), Transportation corridor resiliency in the face of a changing climate, Final Project report, PacTrans Report No 2013-M-UAF-0042

D'Amato, J., Guerin, A., Hantz, D., Rossetti, J.P. and Jaboyedoff, M., 2015. Investigating Rock Fall Frequency and Failure Configurations Using Terrestrial Laser Scanner. In Engineering Geology for Society and Territory-Volume 2 (pp. 1919-1923). Springer, Cham.

Daghigh, H., Tannant, D.D., Daghigh, V., Lichti, D.D., Lindenbergh, R., (2022). A critical review of discontinuity plane extraction from 3D point cloud data of rock mass surfaces, Computers and Geosciences, 169, 105241. https://doi.org/10.1016/j.cageo.2022.105241

De Miranda, S., Gentilini, C., Gottardi, G., Govoni, L., Mentani, A., & Ubertini, F. (2015). Virtual testing of existing semi-rigid rockfall protection barriers. *Engineering Structures*, *85*, 83-94.

Dorren, L. K., & Berger, F. (2006). Stem breakage of trees and energy dissipation during rockfall impacts. *Tree physiology*, *26*(1), 63-71.

Duffy, J. D. (2018). Rock Slope Scaling Investigative Approach and Volume Estimation Method. In *69th Highway Geology SymposiumHighway Geology Symposium*.

Dunham, L., Wartman, J., Olsen, M.J., O'Banion, M. and Cunningham, K., 2017. Rockfall Activity Index (RAI): A lidar-derived, morphology-based method for hazard assessment. Engineering Geology, 221, pp.184-192.

Eberhardt, E. (2003). Rock slope stability analysis–utilization of advanced numerical techniques. *Earth and Ocean sciences at UBC*, *41*.

Eltner, A., Kaiser, A., Castillo, C., Rock, G., Neugirg, F. and Abellán, A., 2016. Image-based surface reconstruction in geomorphometry–merits, limits and developments. Earth Surface Dynamics, 4(2), pp.359-389.

Evans, S.G. and Hungr, O., 1993. The assessment of rockfall hazard at the base of talus slopes. Canadian geotechnical journal, 30(4), pp.620-636.

Fanos, A. M., & Pradhan, B. (2018). Laser scanning systems and techniques in rockfall source identification and risk assessment: a critical review. *Earth Systems and Environment*, *2*(2), 163-182.

Feng, L., Intrieri, E., Pazzi, V., Gigli, G., & Tucci, G. (2021). A framework for temporal and spatial rockfall early warning using micro-seismic monitoring. *Landslides*, *18*, 1059-1070.

Fernández, T., Pérez, J.L., Cardenal, F.J., López, A., Gómez, J.M., Colomo, C., Delgado, J. and Sánchez, M., 2015. Use of a light UAV and photogrammetric techniques to study the evolution of a landslide in Jaén (southern Spain). The International Archives of Photogrammetry, Remote Sensing and Spatial Information Sciences, 40(3), p.241.

Gabet, E.J. and Mudd, S.M., (2009), A theoretical model coupling chemical weathering rates with denudation rates. Geology, 37(2), pp.151-154.

Gigli, G., Morelli, S., Fornera, S. and Casagli, N., 2014. Terrestrial laser scanner and geomechanical surveys for the rapid evaluation of rock fall susceptibility scenarios. Landslides, 11(1), pp.1-14.

Gischig, V. S., Hungr, O., Mitchell, A., & Bourrier, F. (2015). Pierre3D: a 3D stochastic rockfall simulator based on random ground roughness and hyperbolic restitution factors. *Canadian Geotechnical Journal*, *52*(9), 1360-1373.

Graber, A., & Santi, P. (2022). Power law models for rockfall frequency-magnitude distributions: review and identification of factors that influence the scaling exponent. *Geomorphology*, *418*, 108463.

Green et al. (numerous authors), 2016. Rockfall: Design considerations for passive protection structures. Publsihed by the Ministriy of Business, Innovation, & Employment, New Zealand Geotechinial Society, Inc., and the NZ Transport Agency. https://www.building.govt.nz/assets/Uploads/building-code-compliance/b-stability/b1-structure/rockfall-design-consideration/rockfall-design-passive-protection-structures.pdf

Greenwood, W., Zekkos, D., Lynch, J., Bateman, J., Clark, M.K. and Chamlagain, D., 2016, June. UAV-Based 3-D characterization of rock masses and rock slides in Nepal. In 50th US Rock Mechanics/Geomechanics Symposium. American Rock Mechanics Association.

Hearn, G., Barrett, R. K., & Henson, H. H. (1995). Development of effective rockfall barriers. *Journal of transportation engineering*, *121*(6), 507-516.

Heckmann, T., Bimböse, M., Krautblatter, M., Haas, F., Becht, M. and Morche, D., 2012. From geotechnical analysis to quantification and modelling using LiDAR data: a study on rockfall in the Reintal catchment, Bavarian Alps, Germany. Earth Surface Processes and Landforms, 37(1), pp.119-133.

Heltzen, A. M. (1979, June). Shotcrete-An Effective Resource Against Rock Fall In Spalling Rock. In *20th US Symposium on Rock Mechanics (USRMS)*. OnePetro.

Highland, L.M., Bobrowsky, P., 2008, The Landslide Handbook—A Guide to Understanding Landslides, United States Geological Survey, Appendix C, part 2.

Hoek, E., & Bray, J. D. (1981). *Rock slope engineering*. CRC press.

Hoek, E., & Brown, E. T. (2019). The Hoek–Brown failure criterion and GSI–2018 edition. *Journal of Rock Mechanics and Geotechnical Engineering*, *11*(3), 445-463.

Hoek, E., Bray, J.W., 1981. Rock Slope Engineering (Revised Third Edition). Institute of Mining and Metallurgy, London, p. 358

Hren, M.T., Hilley, G.E. and Chamberlain, C.P., (2007), The relationship between tectonic uplift and chemical weathering rates in the Washington Cascades: field measurements and model predictions. American Journal of Science, 307(9), pp.1041-1063.

Huang, S.L., Darrow, M.M. and Calvin, P., 2009. Unstable Slope Management Program: Background Research and Program Inception (No. FHWA-AK-RD-09-04).

Jaboyedoff, M., Metzger, R., Oppikofer, T., Couture, R., Derron, M.H., Locat, J. and Turmel, D., 2007, May. New insight techniques to analyze rock-slope relief using DEM and 3D-imaging cloud points: COLTOP-3D software. In Rock mechanics: Meeting Society's Challenges and demands (Vol. 1, pp. 61-68).

Jaboyedoff, M., Oppikofer, T., Abellán, A., Derron, M.H., Loye, A., Metzger, R. and Pedrazzini, A., 2012. Use of LIDAR in landslide investigations: a review. Natural hazards, 61(1), pp.5-28.

James, M.R. and Robson, S., 2012. Straightforward reconstruction of 3D surfaces and topography with a camera: Accuracy and geoscience application. Journal of Geophysical Research: Earth Surface, 117(F3).

James, M.R., Robson, S. and Smith, M.W., 2017. 3-D uncertainty-based topographic change detection with structure-from-motion photogrammetry: precision maps for ground control and directly georeferenced surveys. Earth Surface Processes and Landforms, 42(12), pp.1769-1788.

Kakavas, M.P.; Nikolakopoulos, K.G.; Kyriou, A.; Koukouvelas, I. The Influence of the DSM Spatial Resolution in Rockfall Simulation and Validation with In Situ Data. Geosciences 2023, 13, 57. https://doi.org/10.3390/geosciences13020057

Kashani, A.G., Olsen, M.J., Parrish, C.E. and Wilson, N., 2015. A review of LiDAR radiometric processing: From ad hoc intensity correction to rigorous radiometric calibration. Sensors, 15(11), pp.28099-28128.

Keller, E.A., (2011), Environmental geology, Boston: Pearson Prentice Hall

Kemeny, J. and Turner, K., 2008. Ground based LIDAR. Rock Slope Mapping and Assessment. Federal Highway Administration. Office of Federal Lands Highway. Central Federal Lands Highway Division., University of Arizona.

Kemeny, J., Norton, B. and Turner, K., 2006. Rock slope stability analysis utilizing ground-based LiDAR and digital image processing. Felsbau, 24(3).

Kothari, U.C. and Momayez, M., 2018. New approaches to monitoring, analyzing and predicting slope instabilities. Journal of Geology and Mining Research, 10(1), pp.1-14.

Krautblatter, M. and Moser, M., (2009), A nonlinear model coupling rockfall and rainfall intensity-based newline on a four-year measurement in a high Alpine rock wall (Reintal, German Alps). Natural Hazards and Earth System Sciences, 9(4), p.1425.

Kulatilake, P.H.S.W., Wang, L., Tang, H. and Liang, Y., 2011. Evaluation of rock slope stability for Yujian River dam site by kinematic and block theory analyses. Computers and Geotechnics, 38(6), pp.846-860.

Laimer, H. J., Müllegger, M., & Darsow, A. (2022). A New Engineering-Geological Classification Method for the Determination of Rock-Scaling Intervals Along Railways. *Rock Mechanics and Rock Engineering*, 1-13.

Lambert, S. and Bourrier, F., 2013. Design of rockfall protection embankments: a review. Engineering geology, 154, pp.77-88.

Lambert, S., Bourrier, F. and Toe, D., 2013. Improving three-dimensional rockfall trajectory simulation codes for assessing the efficiency of protective embankments. International Journal of Rock Mechanics and Mining Sciences, 60, pp.26-36.

Lan, H., Martin, C.D. and Lim, C.H., 2007. RockFall analyst: A GIS extension for three-dimensional and spatially distributed rockfall hazard modeling. Computers & Geosciences, 33(2), pp.262-279.

Lan, H., Martin, C.D., Zhou, C. and Lim, C.H., 2010. Rockfall hazard analysis using LiDAR and spatial modeling. Geomorphology, 118(1-2), pp.213-223.

Lato, M., Gauthier, D., Quinn, P., Hutchinson, D.J., Kromer, R.A., Edwards, T. and Riopel, J., 2015. 3D data collection for rapid rock fall response situations. Proceedings of GEOQuébec, p.513.

Lato, M., Hutchinson, J., Ball, D. and Harrap, R., 2009. Engineering monitoring of rockfall hazards along transportation corridors: using mobile terrestrial LiDAR. Natural Hazards and Earth System Sciences, 9(3), p.935.

Lee, E.M. and Jones, D.K., 2004. Landslide risk assessment. Thomas Telford.

Leine, R. I., Schweizer, A., Christen, M., Glover, J., Bartelt, P., & Gerber, W. (2014). Simulation of rockfall trajectories with consideration of rock shape. *Multibody System Dynamics*, *32*, 241-271.

Li, C. C. (2010). Field observations of rock bolts in high stress rock masses. *Rock Mechanics and Rock Engineering*, *43*(4), 491-496.

Li, C., & Stillborg, B. (1999). Analytical models for rock bolts. *International Journal of Rock Mechanics and Mining Sciences*, *36*(8), 1013-1029.

Li, L., & Lan, H. (2015). Probabilistic modeling of rockfall trajectories: a review. *Bulletin of Engineering Geology and the Environment*, *74*, 1163-1176.

Li, Z.H., Huang, H.W., Xue, Y.D. and Yin, J., 2009. Risk assessment of rockfall hazards on highways. Georisk, 3(3), pp.147-154.

Luo, L., Ma, W., Zhang, Z., Zhuang, Y., Zhang, Y., Yang, J., Cao, X., Liang, S. and Mu, Y., 2017. Freeze/Thaw-induced deformation monitoring and assessment of the slope in permafrost based on terrestrial laser scanner and GNSS. Remote Sensing, 9(3), p.198.

Ma, Y., Knowles, J. N., & Evans, T. M. (2020, June). Numerical Simulation of Gabion Rockfall Barrier Subjected to Extreme Loads. In *54th US Rock Mechanics/Geomechanics Symposium*. OnePetro.

Manousakis, J., Zekkos, D., Saroglou, F. and Clark, M., 2016. Comparison of UAV-enabled photogrammetry-based 3D point clouds and interpolated DSMs of sloping terrain for rockfall hazard analysis. The International Archives of Photogrammetry, Remote Sensing and Spatial Information Sciences, 42, p.71.

Markus, S. J., Wartman, J., Olsen, M., & Darrow, M. M. (2023). Lidar-Derived Rockfall Inventory—An Analysis of the Geomorphic Evolution of Rock Slopes and Modifying the Rockfall Activity Index (RAI). Remote Sensing, 15(17), 4223. https://doi.org/10.3390/rs15174223

Marohl, K., 2019, Using the Rockfall Activity Index to assess the impact of scaling on rock fall activity at Glitter Gulch, Alaska: University of Washington Master of Science report, Earth and Space Sciences: Applied Geosciences, MESSAGe Technical Report Number 079, 39 p.

Maruyama, K. and Kozima, S., 1994. A proposal of the warning criterion for the landslide crisis depended on the observation data of sliding distance. Landslides, 31(1), pp.45-51_1.

Mason, D., Brabhaharan, P. & Saul, G. (2017) Performance of road networks in the 2016 Kaikōura earthquake: Observations on ground damage and outage effects. Proc. 20th NZGS Geotechnical Symposium. Eds. GJ Alexander & CY Chin

Massey, C., Olsen, M.J., Wartman, J., Senogles, A., Lukovic, B., Leshchinsky, B., Archibald, G., Litchfield, N., Van Dissen, R., de Vilder, S., and Holden, C. (2022). Rockfall activity

rates before, during and after the 2010/11 Canterbury Earthquake Sequence, AGU Journal of Geophysical Research, Earth Surface. 127, e2021JF006400. DOI: 10.1029/2021JF006400

Masuya, H., Amanuma, K., Nishikawa, Y., & Tsuji, T. (2009). Basic rockfall simulation with consideration of vegetation and application to protection measure. *Natural Hazards and Earth System Sciences*, *9*(6), 1835-1843.

Matasci, B., Jaboyedoff, M., Loye, A., Pedrazzini, A., Derron, M.H. and Pedrozzi, G., 2015. Impacts of fracturing patterns on the rockfall susceptibility and erosion rate of stratified limestone. Geomorphology, 241, pp.83-97.

Matasci, B., Stock, G.M., Jaboyedoff, M., Carrea, D., Collins, B.D., Guérin, A., Matasci, G. and Ravanel, L., 2017. Assessing rockfall susceptibility in steep and overhanging slopes using three-dimensional analysis of failure mechanisms. Landslides, pp.1-20.

Mateos, R.M., García-Moreno, I. and Azañón, J.M., (2012), Freeze–thaw cycles and rainfall as triggering factors of mass movements in a warm Mediterranean region: the case of the Tramuntana Range (Majorca, Spain). Landslides, 9(3), pp.417-432.

Matsuoka, N. and Sakai, H., (1999), Rockfall activity from an alpine cliff during thawing periods. Geomorphology, 28(3-4), pp.309-328.

Mavrouli, O., Corominas, J. and Jaboyedoff, M., 2015. Size distribution for potentially unstable rock masses and in situ rock blocks using LiDAR-generated digital elevation models. Rock mechanics and rock engineering, 48(4), pp.1589-1604.

Mentani, A., Govoni, L., Gottardi, G., Lambert, S., Bourrier, F., & Toe, D. (2016). A new approach to evaluate the effectiveness of rockfall barriers. *Procedia Engineering*, *158*, 398-403.

Metzger, A.T., Olsen., Wartman, J., Dunham, L., Stuedlein, A., 2014, Platform for risk-based assessment of unstable slopes using mobile lidar, PACTRANS technical report# 2012-M-0002

Michoud, C., Horton, P., Jaboyedoff, M., Baillifard, F.J., Loye, A., Nicolet, P., Pedrazzini, A. and Queyrel, A., 2012. Rockfall hazard and risk assessments along roads at a regional scale: example in Swiss Alps. Natural Hazards and Earth System Sciences, 12(3), p.615.

Miller, P.E., Mills, J.P., Barr, S.L., Lim, M., Barber, D., Parkin, G., Clarke, B., Glendinning, S. and Hall, J., 2008. Terrestrial laser scanning for assessing the risk of slope instability along transport corridors. International Archives of Photogrammetry, Remote Sensing and Spatial Information Sciences, 37(B5), pp.495-500.

Miller, P.K., Vessely, M., Olson, L.D. and Tinkey, Y., 2013. Slope stability and rock-fall monitoring with a remote interferometric radar system. In Geo-Congress 2013: Stability and Performance of Slopes and Embankments III (pp. 304-318).

Mitchell, S.G., Ehlers, T.A., Reiners, P.W., Montgomery, D.R. and Greenberg, H., 2001, December. Surface Uplift and Exhumation Trends of the Washington Cascade Range From Warping of the Grande Ronde Basalt and Apatite (U-Th)/He Ages. In AGU Fall Meeting Abstracts.

Mitri, H. and Vennes, I., 2014. Rock Slope Surface Monitoring Technologies with Focus on Ground-Based Synthetic Aperture Radar. In Mine Planning and Equipment Selection (pp. 1251-1263). Springer, Cham.

National Academies of Sciences, Engineering, and Medicine (NASEM) 2022. Design Practices for Rock Slopes and Rockfall Management. Washington, DC: The National Academies Press. https://doi.org/10.17226/26636.

Nicolson, D.T., 2004, Introduction to the RDA (Rockslope Deterioration Assessment. Published at: http://www.dawntnicholson.org.uk/. Accessed 03/16/2018

Niethammer, U., James, M.R., Rothmund, S., Travelletti, J. and Joswig, M., 2012. UAV-based remote sensing of the Super-Sauze landslide: Evaluation and results. Engineering Geology, 128, pp.2-11.

O'Neil-Dunne, J.P.M., and Estabrook, E., (2019). The integration of unmanned aircraft systems to increase safety and decrease costs of transportation projects and related tasks, Report # FHWA-NH-RD-26962J.

ODOT, 2001, ODOT Landslide & Rockfall Pilot Study (Final Report)

ODOT, 2003, Highway Design Manual, Section 10

ODOT, 2016, Geotechnical design manual, section 12 Rock Cuts – Analysis, Design, and Mitigation

Olsen, M.J., 2011, October. Seacliff erosion analysis using 3D laser scanning. In 2011 GSA Annual Meeting in Minneapolis.

Olsen, M.J., 2013. Guidelines for the use of mobile LIDAR in transportation applications (Vol. 748). Transportation Research Board.

Olsen, M.J., Chen, Z., Hutchinson, T. and Kuester, F., 2013. Optical techniques for multiscale damage assessment. Geomatics, Natural Hazards and Risk, 4(1), pp.49-70.

Olsen, M.J., Johnstone, E., Driscoll, N., Ashford, S.A. and Kuester, F., 2009. Terrestrial laser scanning of extended cliff sections in dynamic environments: Parameter analysis. Journal of Surveying Engineering, 135(4), pp.161-169.

Olsen, M.J., Massey, C., Senogles, A., Leshchinsky, B.A., and Wartman, J. (2020). Predicting seismically induced rockfall hazard for targeted site mitigation, ODOT SPR809 Final Report.

Olsen, M.J., Wartman, J., McAlister, M., Mahmoudabadi, H., O'Banion, M.S., Dunham, L. and Cunningham, K., 2015. To fill or not to fill: sensitivity analysis of the influence of resolution and hole filling on point cloud surface modeling and individual rockfall event detection. Remote Sensing, 7(9), pp.12103-12134.

Olsen, M.J., Wartman, J., McAlister, M., Mahmoudabadi, H., O'Banion, M.S., Dunham, L. and Cunningham, K., 2015. To fill or not to fill: sensitivity analysis of the influence of resolution and hole filling on point cloud surface modeling and individual rockfall event detection. Remote Sensing, 7(9), pp.12103-12134.

Oregon Department of Transportation. 2016. Repairs to ease rockfall threat start Tuesday on I-84 near Hood River . [ONLINE] Available at: https://content.govdelivery.com/accounts/ORDOT/bulletins/161266e. [Accessed 25 March 2018]

OregonLive.com. 2017. US 30 to be closed for weeks after rockslide, officials say | OregonLive.com. [ONLINE] Available at: http://www.oregonlive.com/pacific-northwest-news/index.ssf/2017/05/us_30_to_be_closed_for_weeks_a.html. [Accessed 25 March 2018].

Pierson, L.A, 1992. Rockfall hazard rating system. Transportation Research Record, pp.6-6.

Pierson, Lawrence A., and Ronald G. Chassie. *Rockfall catchment area design guide*. No. FHWA-OR-RD-02-04m; SPR-3 (032). Oregon. Dept. of Transportation, 2001.

Rabatel, A., Deline, P., Jaillet, S. and Ravanel, L., 2008. Rock falls in high-alpine rock walls quantified by terrestrial lidar measurements: A case study in the Mont Blanc area. Geophysical Research Letters, 35(10).

Raghuvanshi, T.K., 2017. Plane failure in Rock slopes–A review on stability analysis techniques. Journal of King Saud University-Science.

Reiners, P.W., Ehlers, T.A., Mitchell, S.G. and Montgomery, D.R., 2003. Coupled spatial variations in precipitation and long-term erosion rates across the Washington Cascades. Nature, 426(6967), p.645.

Richards, L. 2012. Port Hills Rockfall:Rockfall mitigation – design strategy, Project Memo 2 to Ted Malan, Geotechnical Advisor, Port Hills White Zone Recovery Project, Christchurch City Council. https://www.ccc.govt.nz/assets/Documents/Environment/Land/rockfalldesignstrategy-new.pdf

Riebe, C.S., Kirchner, J.W., Granger, D.E. and Finkel, R.C., (2001), Strong tectonic and weak climatic control of long-term chemical weathering rates. Geology, 29(6), pp.511-514.

Romana, M., 1985, September. New adjustment ratings for application of Bieniawski classification to slopes. In Proceedings of the international symposium on role of rock mechanics, Zacatecas, Mexico (pp. 49-53).

Romana, M., 1988, July. Practice of SMR classification for slope appraisal. In Proc. 5th Int. Symp. on Landslides, Balkema, Rotterdam (pp. 1227-1229).

Romana, M., 1991, January. SMR classification. In 7th ISRM Congress. International Society for Rock Mechanics.

Rosenblad, B.L., Gilliam, J., Gomez, F., Loehr, J.E., 2015, Ground-based Interferometric Radar for Rockfall Hazard Monitoring. Report# MATC-MU: 278 Final Report

Rosser, N.J., Petley, D.N., Lim, M., Dunning, S.A. and Allison, R.J., 2005. Terrestrial laser scanning for monitoring the process of hard rock coastal cliff erosion. Quarterly Journal of Engineering Geology and Hydrogeology, 38(4), pp.363-375.

Santana, D., Corominas, J., Mavrouli, O. and Garcia-Sellés, D., 2012. Magnitude–frequency relation for rockfall scars using a Terrestrial Laser Scanner. Engineering geology, 145, pp.50-64.

Scaioni, M., 2015, Modern Technologies for Landslide Monitoring and Prediction, Springer Natural Hazards, Springer, New York

Shakoor, A., & Admassu, Y. (2010). *Rock slope design criteria* (No. FHWA/OH-2010/11). Ohio. Dept. of Transportation. Office of Research and Development.

Sherrod, David R., and James G. Smith. Geologic Map of Upper Eocene to Holocene Volcanic and Related Rocks of the Cascade Range, Oregon. U.S. Geological Survey, 2000. Geologic Investigations Series Map I-2569.

Snavely, P.D., MacLeod, N.S., Wagner, H.C., and Rau, W.W., 1976, Geologic map of the Yaquina and Toledo Quadrangles, Lincoln County, Oregon: Reston, Va., U.S. Geological Survey Miscellaneous Investigations Map I-867, scale 1:62,500.

Snavely, Parke D., Jr., et al. *Geologic Map of the Yaquina and Toledo Quadrangles, Lincoln County, Oregon*. U.S. Geological Survey, 1976. Miscellaneous Investigations Series Map I-867.

Snavely, Parke D., Jr., Norman S. MacLeod, and Holly C. Wagner. "Miocene Tholeiitic Basalts of Coastal Oregon and Washington and Their Relations to Coeval Basalts of the Columbia Plateau." *Geological Society of America Bulletin*, vol. 84, no. 2, Feb. 1973, pp. 387-424.

Stevens, W. D. (1998). *RocFall, a tool for probabilistic analysis, design of remedial measures and prediction of rockfalls* (Doctoral dissertation).

Stille, H., Holmberg, M., & Nord, G. (1989, January). Support of weak rock with grouted bolts and shotcrete. In *International Journal of Rock Mechanics and Mining Sciences & Geomechanics Abstracts* (Vol. 26, No. 1, pp. 99-113). Pergamon.

Sturzenegger, M. and Stead, D., 2009. Close-range terrestrial digital photogrammetry and terrestrial laser scanning for discontinuity characterization on rock cuts. Engineering Geology, 106(3-4), pp.163-182.

Taherynia, M.H., Mohammadi, M. and Ajalloeian, R., (2014), Assessment of Slope Instability and Risk Analysis of Road Cut Slopes in Lashotor Pass, Iran. Journal of Geological Research, 2014.

Tebbens, S. F. (2020). Landslide scaling: A review. Earth and Space Science, 7, e2019EA000662, https://doi.org/10.1029/2019EA000662

Telling, J., Lyda, A., Hartzell, P. and Glennie, C., 2017. Review of earth science research using terrestrial laser scanning. Earth-Science Reviews, 169, pp.35-68.

Terzaghi, R.D., 1965. Sources of error in joint surveys. Geotechnique, 15(3), pp.287-304.

Tonini, M. and Abellan, A., 2014. Rockfall detection from terrestrial LiDAR point clouds: A clustering approach using R. Journal of Spatial Information Science, 2014(8), pp.95-110.

Turner, A.K. and Jayaprakash, G.P., 2013. NEW TRB PUBLICATION: Rockfall: Characterization and Control. TR News, (284).

Turner, A.K., & Schuster, R.L. (2012). Rockfall : characterization and control. TRB.

Turner, D., Lucieer, A. and De Jong, S.M., 2015. Time series analysis of landslide dynamics using an unmanned aerial vehicle (UAV). Remote Sensing, 7(2), pp.1736-1757.

Vandewater, C.J., Dunne, W.M., Mauldon, M., Drumm, E.C. and Bateman, V., 2005. Classifying and assessing the geologic contribution to rockfall hazard. Environmental & Engineering Geoscience, 11(2), pp.141-154.

Volkwein, A. (2005). Numerical simulation of flexible rockfall protection systems. In *Computing in Civil Engineering (2005)* (pp. 1-11).

Volkwein, A., Schellenberg, K., Labiouse, V., Agliardi, F., Berger, F., Bourrier, F., ... & Jaboyedoff, M. (2011). Rockfall characterisation and structural protection–a review. *Natural Hazards and Earth System Sciences*, *11*(9), 2617-2651.

Wahrhaftig, C., 1968, Schists of the Central Alaska Range: U.S. Geological Survey Bulletin 1254, 22 p.

Wahrhaftig, C., and Black, R.F., 1958, Quaternary geology of the Nenana River valley and adjacent parts of the Alaska Range; Engineering geology along part of the Alaska Railroad: U.S. Geological Survey Professional Paper 293, 118 p.

Wang, I.T. and Lee, C.Y., 2010. Influence of slope shape and surface roughness on the moving paths of a single rockfall. World Acad Sci Eng Technol, 65, pp.1021-1027.

Whadcoat, S.K., (2017) Numerical modelling of rockfall evolution in hard rock slopes, Durham theses, Durham University. Available at Durham E-Theses Online: http://etheses.dur.ac.uk/11994/

Wieczorek, G.F., Snyder, J.B., Waitt, R.B., Morrissey, M.M., Uhrhammer, R.A., Harp, E.L., Norris, R.D., Bursik, M.I. and Finewood, L.G., (2000), Unusual July 10, 1996, rock fall at Happy Isles, Yosemite National Park, California. Geological Society of America Bulletin, 112(1), pp.75-85.

Wilkinson, M.W., Jones, R.R., Woods, C.E., Gilment, S.R., McCaffrey, K.J.W., Kokkalas, S. and Long, J.J., 2016. A comparison of terrestrial laser scanning and structure-from-motion photogrammetry as methods for digital outcrop acquisition. Geosphere, 12(6), pp.1865-1880.

Williams, J. G., Rosser, N. J., Hardy, R. J., & Brain, M. J. (2019). The importance of monitoring interval for rockfall magnitude-frequency estimation. *Journal of Geophysical Research: Earth Surface*, *124*(12), 2841-2853.

Wyttenberg, K., Griffith, A., Williams, J., & Lynde, M. (2002). Aggregate resource inventory and needs forecast study: Final report (Report No. SPR 314). Oregon Department of Transportation Research Group; Federal Highway Administration.

Young, A.P., Olsen, M.J., Driscoll, N., Flick, R.E., Gutierrez, R., Guza, R.T., Johnstone, E. and Kuester, F., 2010. Comparison of airborne and terrestrial lidar estimates of seacliff erosion in southern California. Photogrammetric Engineering & Remote Sensing, 76(4), pp.421-427.